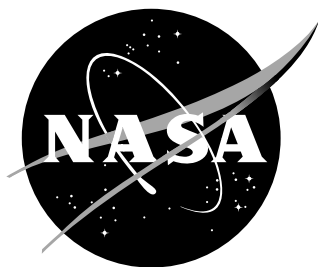# Technical Report Series on Global Modeling and Data Assimilation, Volume 38

Randal D. Koster, Editor

The Quick Fire Emissions Dataset (QFED): Documentation of versions 2.1, 2.2 and 2.4

Anton S. Darmenov, Arlindo da Silva

Since its founding, NASA has been dedicated to the advancement of aeronautics and space science. The NASA scientific and technical information (STI) program plays a key part in helping NASA maintain this important role.

The NASA STI Program operates under the auspices of the Agency Chief Information Officer. It collects, organizes, provides for archiving, and disseminates NASA's STI. The NASA STI Program provides access to the NASA Aeronautics and Space Database and its public interface, the NASA Technical Report Server, thus providing one of the largest collection of aeronautical and space science STI in the world. Results are published in both non-NASA channels and by NASA in the NASA STI Report Series, which includes the following report types:

- TECHNICAL PUBLICATION. Reports of completed research or a major significant phase of research that present the results of NASA programs and include extensive data or theoretical analysis. Includes compilations of significant scientific and technical data and information deemed to be of continuing reference value. NASA counterpart of peer-reviewed formal professional papers, but having less stringent limitations on manuscript length and extent of graphic presentations.

- TECHNICAL MEMORANDUM. Scientific and technical findings that are preliminary or of specialized interest, e.g., quick release reports, working papers, and bibliographies that contain minimal annotation. Does not contain extensive analysis.

- CONTRACTOR REPORT. Scientific and technical findings by NASA-sponsored contractors and grantees.

- CONFERENCE PUBLICATION. Collected papers from scientific and technical conferences, symposia, seminars, or other meetings sponsored or co-sponsored by NASA.

- SPECIAL PUBLICATION. Scientific, technical, or historical information from NASA programs, projects, and missions, often concerned with subjects having substantial public interest.

- TECHNICAL TRANSLATION. English-language translations of foreign scientific and technical material pertinent to NASA's mission.

Specialized services also include creating custom thesauri, building customized databases, and organizing and publishing research results.

For more information about the NASA STI Program, see the following:

- Access the NASA STI program home page at *http://www.sti.nasa.gov*

- E-mail your question via the Internet to help@sti.nasa.gov

- Fax your question to the NASA STI Help Desk at 443-757-5803

- Phone the NASA STI Help Desk at 443-757-5802
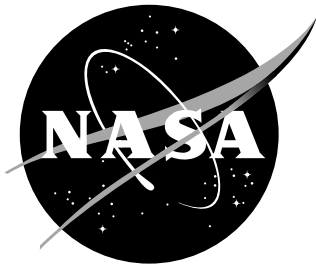
Technical Report Series on Global Modeling and Data Assimilation, Volume 38

Randal D. Koster, Editor

The Quick Fire Emissions Dataset (QFED): Documentation of versions 2.1, 2.2 and 2.4

Anton S. Darmenov
NASA Goddard Space Flight Center, Greenbelt, MD

Arlindo da Silva
NASA Goddard Space Flight Center, Greenbelt, MD

Abstract

Biomass burning is an important source of particulates and trace gases and a major element of the terrestrial carbon cycle. Well constrained emissions from vegetation fires are needed to model direct and indirect effects of biomass burning aerosols, to model homogeneous and heterogeneous chemistry in the atmosphere, and to perform credible Earth system analysis, and climate and air pollution studies. To improve the performance of NASA Goddard Earth Observing System Model (GEOS) in the areas of atmospheric constituent modeling with a focus on biomass burning we developed the Quick Fire Emissions Dataset (QFED). The QFED emissions are based on the fire radiative power (top-down) approach and draw on the cloud correction method developed in the Global Fire Assimilation System (GFAS). Location and fire radiative power of fires are obtained from the Moderate Resolution Imaging Spectroradiometer (MODIS) Level 2 fire products (MOD14 and MYD14) and the MODIS Geolocation products (MOD03 and MYD03). QFED strengths are high spatial and temporal resolutions and near-real time availability. Daily mean emissions are available at 0.3125×0.25 degrees and in recent versions also at 0.1×0.1 degrees. QFED provides emissions of black carbon, organic carbon, sulfur dioxide, carbon monoxide, carbon dioxide, $PM_{2.5}$, ammonia, nitrogen oxides, methyl ethyl ketone, propylene, ethane, propane, n- and i-butane, acetaldehyde, formaldehyde, acetone and methane. Two QFED product systems are maintained by the NASA Global Modeling and Assimilation Office (GMAO): one that produces near real-time daily emissions used operationally in the GEOS-5 Data Assimilation System, and one that produces an extended historical dataset with daily emissions from March 2000 to the present. The historical dataset also provides monthly mean and monthly climatological emissions.

Contents

List of Tables

List of Figures

1 Introduction

1.1 Background

Open combustion of non-fossilized vegetative or organic fuel, also referred to as biomass burning, releases a mixture of compounds (Akagi et al., 2011; Andreae and Merlet, 2001) that include important atmospheric constituents such as carbon dioxide, black carbon, organic carbon, sulfur dioxide, ammonia and nitrogen oxides. The composition of the mixture is determined by the fuel make-up, environmental conditions and ultimately by the physical processes and chemical reactions taking place during all stages of a fire. Changing the amount of dry fuel burned M_{dry} but holding all other factors constant, results in releasing a proportional amount M_s of species s:

$$M_s \propto M_{dry}.$$

The amount of particulate or trace gas species s released in the atmosphere per unit dry fuel burned is called the emission factor (β_s). From this definition it follows that:

$$M_s = \beta_s M_{dry}. \tag{1}$$

Fire processes, including primary emissions of aerosols and trace gases, operate at subgrid-scales when considered within the context of the current generation of regional and global models. Emissions from well quantified individual fires need to be aggregated at spatial and temporal scales of a few kilometers to hundreds of kilometers and from hours to weeks and months in order to create datasets that are suitable for use in numerical models. However, detailed information about fuel type, conditions and amount consumed are not available on a global scale. Instead, a common approach is to simplify plant diversity and variability of emissions factors by using a reduced vegetation classification, for example, one based on terrestrial biomes. The total emitted mass of species s can be then computed as the sum of the mass emitted from fires in each biome, i.e.:

$$M_s = \sum_b \beta_{b,s} M_{b,dry}, \tag{2}$$

where the index b indicates the dependence of the emission factor on the biome type.

1.2 Quantifying fire emissions

Quantifying emissions from fires with high fidelity remains a challenging problem despite the simple relationship between emissions and consumed dry fuel (see Equations 1 and 2). One of the sources of uncertainty in estimating biomass burning emissions is the natural variation of the emission factors (van Leeuwen and van der Werf, 2011). Emission factors measured in a controlled environment might not well represent the emission factors of naturally occurring fires because it is difficult to recreate realistic fuel composition, fire stages and combustion conditions. Hence, there might be significant differences between the emission factors derived from lab measurements and those derived from in situ measurements near wild fires or prescribed burns. As a result of natural variability and measurement difficulties, the reported emission factors can vary significantly, in some cases by over 50% as can be seen from Table 1. Table 1 contains the best estimates and uncertainties or range of measured values of emission factors of selected pyrogenic species released from tropical forest, extratropical forest, savanna and grassland fires. The values were compiled and reported by Andreae and Merlet (2001) and Akagi et al. (2011).

The amount of fuel burned is the other important and highly uncertain quantity needed to calculate biomass burning emissions. Two approaches are commonly employed to determine the fuel burned. The first one is based on the burned area. The second approach utilizes thermal energy measured at the top of the atmosphere by passive remote sensing instruments.

Table 1: Emission factors and their uncertainties for selected species emitted from biomass burning of tropical forest, extratropical forest, savanna and grassland vegetation. Values in the table are in units $g\,kg^{-1}$. QFED uses the emission factors compiled by Andreae and Merlet (2001).

Species	Tropical Forest	Extratropical Forest	Savanna and Grassland
Andreae and Merlet (2001)			
Carbon Dioxide (CO_2)	1580 ± 90	1569 ± 131	1613 ± 95
Carbon Monoxide (CO)	104 ± 20	107 ± 37	65 ± 20
Sulfur Dioxide (SO_2)	0.57 ± 0.23	1.0	0.35 ± 0.16
Organic Carbon (OC)	5.2 ± 1.5	8.6–9.7	3.4 ± 1.4
Black Carbon (BC)	0.66 ± 0.31	0.56 ± 0.19	0.48 ± 0.18
Ammonia (NH_3)	1.30	1.40 ± 0.8	0.6–1.5
$PM_{2.5}$	9.1 ± 1.5	13.0 ± 7.0	5.4 ± 1.5
Methane (CH_4)	6.80	4.70	2.30
Nitrogen Oxides (NO_x as NO)	1.6 ± 0.7	3.00 ± 1.4	3.9 ± 2.4
Methyl Ethyl Ketone (C_4H_8O)	0.43	0.17–0.74	0.26
Propylene (C_3H_6)	0.55	0.59 ± 0.16	0.26 ± 0.14
Ethane (C_2H_6)	0.5–1.9	0.60 ± 0.15	0.32 ± 0.16
Propane (C_3H_8)	0.15	0.25 ± 0.11	0.09 ± 0.03
n-Butane (C_4H_{10})	0.041	0.069 ± 0.038	0.019 ± 0.09
i-Butane (C_4H_{10})	0.015	0.022 ± 0.009	0.006 ± 0.003
Acetaldehyde (CH_3CHO)	0.65	0.48–0.52	0.50 ± 0.39
Formaldehyde (HCHO)	1.40	2.2 ± 0.5	0.26–0.44
Acetone (C_3H_6O)	0.62	0.52–0.59	0.25–0.62
Akagi et al. (2011)			
Carbon Dioxide (CO_2)	1643 ± 58	1509 ± 98	1686 ± 38
Carbon Monoxide (CO)	93 ± 27	122 ± 44	63 ± 17
Sulfur Dioxide (SO_2)	0.40 ± 0.19	–	0.48 ± 0.27
Organic Carbon (OC)	4.71 ± 2.73	$8.6 - 9.7$	2.62 ± 1.24
Black Carbon (BC)	0.52 ± 0.28	0.56 ± 0.19	0.37 ± 0.2
Ammonia (NH_3)	1.33 ± 1.21	2.46 ± 2.35	0.52 ± 0.35
$PM_{2.5}$	9.1 ± 3.5	15 ± 7.5	7.17 ± 3.42
Methane (CH_4)	5.07 ± 1.98	5.68 ± 3.24	1.94 ± 0.85
Nitrogen Oxides (NO_x as NO)	2.55 ± 1.40	1.12 ± 0.69	3.9 ± 0.8
Methyl Ethyl Ketone (C_4H_8O)	0.50 ± 0.21	0.22	–
Propylene (C_3H_6)	0.64 ± 0.43	1.11 ± 0.61	0.79 ± 0.56
Ethane (C_2H_6)	0.71 ± 0.28	1.70 ± 1.05	0.66 ± 0.41
Propane (C_3H_8)	0.126 ± 0.06	0.42 ± 0.18	0.10 ± 0.067
n-Butane (C_4H_{10})	0.038 ± 0.023	0.069 ± 0.038	0.019 ± 0.09
i-Butane (C_4H_{10})	0.011 ± 0.009	0.042	0.0043 ± 0.0027
Acetaldehyde (CH_3CHO)	1.55 ± 0.75	–	0.57 ± 0.30
Formaldehyde (HCHO)	1.73 ± 1.22	0.73 ± 0.62	1.92 ± 1.14
Acetone (C_3H_6O)	0.63 ± 0.17	0.75	0.16 ± 0.13

1.2.1 Burned area (bottom-up) approach

In the burned area (bottom-up) approach, fire emissions are determined by estimating the dry mass of the consumed fuel and applying Equation 1. The mass of the burned vegetation can be computed as the product of the burned area A, the fuel load ρ_f and the combustion completeness γ. Therefore, the emitted mass of species s is:

$$M_s = \beta_s \gamma \rho_f A \tag{3}$$

Equation 3 can be generalized to account for combustion from different vegetation types in a manner similar to Equation 2. Burned area A, fuel load ρ_f and the combustion completeness γ vary spatially and temporally. Quantifying each on a global scale remains challenging, and each contributes to the uncertainties in the burned area/bottom-up emissions estimates. The burned area approach is used by several fire emissions datasets, including the Global Fire Emissions Database (GFED) (Giglio et al., 2006; van der Werf et al., 2006, 2010) and the Fire Locating and Modeling of Burning Emissions (FLAMBE) program (Reid et al., 2009).

1.2.2 Fire radiative power (top-down) approach

Thermal energy measured by passive remote sensing instruments provides a more direct means of detecting fires and fire intensity globally. The connection between the rate of radiative energy emitted by active fires and the rate of combustion was proposed by Kaufman et al. (1996). Numerous studies have used fire radiative power measurements from spaceborne platforms to improve the characterization of fires (e.g., Ichoku et al. (2008); Schroeder et al. (2010); Wooster and Zhang (2004); Wooster et al. (2005); Zhang et al. (2014)) and fire emissions on regional and global scales (e.g., Ellicott et al. (2009); Kaiser et al. (2012); Whitburn et al. (2015); Zhang et al. (2012)). The linear relationship between the energy released as radiation (fire radiative energy) and the mass of the fuel consumed during combustion has been experimentally demonstrated by Wooster (2002). This simple relationship can be explained by the empirical evidence that burning a given amount of dry vegetation releases a similar amount of energy regardless of the vegetation type (Wooster et al., 2005). On the other hand, one can use a conceptual model of the fire processes in which a fraction of the chemical energy released during combustion is transferred into the environment due to conductive, evaporative and convective processes. The remaining energy is released primarily as infrared (IR) radiation. Under the assumption that the energy released as IR radiation is approximately proportional to the total energy, one can relate the amount of fuel burned with the time-integrated fire radiative energy (FRE). Therefore, the amount of pyrogenic species s emitted from a fire that resulted in the release of total radiative energy $\mathscr{E}$ is:

$$M_s = \alpha \beta_s \mathscr{E} = \alpha \beta_s \int_{t_1}^{t_2} F(t) dt \tag{4}$$

where $F(t)$ is the Fire Radiative Power, namely, the instantaneous rate of fire radiative energy in units $J\,s^{-1}$ or W, and α is an empirical constant relating the FRE to the amount of dry mass consumed. Equation 4 can be written in a form that is more suitable for use in chemical transport models:

$$E_s = \frac{\Delta M_s}{A \Delta t} = \alpha \beta_s \frac{F}{A}, \tag{5}$$

that is, the emission rate E_s of species s per unit area is proportional to the product of the emission factor β_s and the fire radiative power (FRP) area density (F/A), where A is the area of the satellite pixel.

Notice that the emission coefficient α convolves the simplified treatment of the fire processes in the conceptual model with the remote sensor sensitivity and performance characteristics (e.g., resolution, bands and signal saturation levels) used to measure the FRP. The emission coefficient can be determined by calibrating FRP based emissions against a known set of fire emissions. Another calibration strategy is to employ a chemical transport model to simulate aerosol and gas constituents and find the optimal emission coefficient that minimizes the differences between the model and observational datasets. Although the goal of the two calibration approaches is to determine the unknown emission coefficient, they are conceptually very different. The model based approach is constructed to yield the *perceived emissions* by a particular model that are tailored to the specific model parameterizations, whereas the direct calibration will result in emissions that are similar to a reference emission dataset. Implementation details and results applying these two approaches are presented in Sections 2.3 and 2.4.

Among the advantages of the top-down approach are global coverage and high spatial and temporal resolutions when FRP data from modern satellite instruments such as the MODerate Resolution Imaging Spectroradiometer (MODIS) are used. Moreover, FRP data is available in near real-time, which makes the FRP-based emissions well suited for operational use. The FRP method suffers from limitations pertinent to remote sensing of fires, including difficulties in detecting small fires (e.g., the MODIS instrument is limited in detecting fires smaller than $100\,\mathrm{m}^2$) or fires with weak thermal signature (e.g, smoldering and peat fires), and attenuation of signal from fires by clouds. A methodology to account for fires obscured by clouds was originally proposed and implemented by Kaiser et al. (2009, 2012). Because of these limitations, FRP retrievals are likely underestimated. Any attempt to calibrate FRP-based emissions to produce realistic aerosol/trace gases simulations will result in an overestimation of the emission factors in order to compensate for the absence of emissions from undetected fires.

1.3   Document organization

This document is organized as follows: Section 1 introduces the basic concepts used to quantify emissions of particulates and trace gases from fires. Section 2 contains detailed description of the Quick Fire Emissions Dataset (QFED). Section 3 includes comparison of the QFED dataset to the Global Fire Emissions Database (GFED), the Global Fire Assimilation System (GFAS) and the Fire Locating and Modeling of Burning Emissions (FLAMBE) datasets. Acronyms used in this document are listed in Appendix A. Supplementary information used in the development of QFED is included in appendices B and C. Appendix D contains results from the regional comparison of QFED with GFAS, GFED, and FLAMBE. Appendix E contains the QFED file specification.

2 Description of the QFED

The QFED uses satellite observations of FRP to estimate gridded fire emissions globally. The QFED dataset comprises two globally gridded (Level 3) products. The principal QFED product, Level 3a, contains daily-mean FRP data, stratified by biome. The Level 3b product provides biomass burning emissions for several species, including carbon monoxide (CO), carbon dioxide (CO_2), sulfur dioxide (SO_2), organic carbon (OC), black carbon (BC) and fine particular matter ($PM_{2.5}$), also stratified by biome. The QFED Level 3 products are available at $0.3125° \times 0.25°$ spatial resolution. Level 3 products in QFED-2.4 are also produced at $0.1° \times 0.1°$ degrees spatial resolution for use in global meso-scale simulations.

The QFED fire emissions are produced in near real-time on a daily basis and are used in the operational Goddard Earth Observing System Model (GEOS)-5 data assimilation system. QFED uses MODIS measurements of FRP to calculate biomass burning emissions. Near real-time MODIS Level 2 fire and geo-location products (MOD14/MYD14 and MOD03/MYD03) are obtained from the Land Atmosphere Near Real-time Capability for EOS (LANCE, http://lance-modis.eosdis.nasa.gov/). In addition to the near real-time emissions, a longer historical record dataset is also maintained based on data from the MODIS Adaptive Processing System (MODAPS) Service (http://modaps.nascom.nasa.gov/services/). This historical product is updated on a monthly basis and uses a more complete set of MOD14/MYD14 and MOD03/MYD3 data. The historical dataset is available from March 2000 to the present and is primarily used for model development, reanalyses and scientific research applications. Information on how to access the near real-time and historical emissions datasets can be found in the QFED web page at http://geos5.org/wiki/index.php?title=Quick_Fire_Emission_Dataset_(QFED). The current processing is based on MODIS Collection 5.

In the next sections we present the methodology and data used to calculate the QFED fire radiative power and emissions products. We describe the similarities and the differences in our approaches between versions 2.1, 2.2 and 2.4.

2.1 Methodology and data

The QFED biomass burning emissions are calculated using the FRP (top-down) approach (Wooster, 2002; Wooster et al., 2005). The fire radiative power and location of the fires are obtained from the MODIS Collection 5 Active Fire product (MOD14 and MYD14) and the MODIS Geolocation product (MOD03 and MYD03). The location of the fires in conjunction with a vegetation classification dataset is used to determine the type of the vegetation category, select the emission factor, and assign the FRP to the corresponding QFED vegetation class. The emission factors are from Andreae and Merlet (2001)[1]. The area and FRP of MOD14 and MYD14 pixels are binned onto a global grid and used to calculate the total and stratified by biome biomass burning emissions.

2.1.1 The MODIS active fire product

The QFED global gridded FRP product is derived from the MODIS Level 2 fire product (Giglio, 2010). In cloud free conditions, the twin MODIS sensors on board the sun-synchronous polar orbiting satellites Terra (descending node, 10:30 AM) and Aqua (ascending node, 1:30 PM) typically can sample a fire hotspot with temporal resolution of about four times in 24 hours. The MODIS fire product is collected daily at $1\,km \times 1\,km$ resolution at nadir and includes an active fire mask, a pixel-level quality assurance data layer, and a fire-pixel table with radiometric data.

---

[1]Emission factors for selected pyrogenic species are reprinted in Table 1.

Table 2: Mapping of the IGBP land cover classification to the biome types used in QFED. The tropics region is defined as the zone from 30°S to 30°N latitude.

QFED biome	IGBP land cover class	Note
Tropical Forests	Evergreen Broadleaf Forest	The tropics
Extratropical Forests	Evergreen Needleleaf Forest	
	Evergreen Broadleaf Forest	Latitudes beyond the tropics
	Deciduous Needleleaf Forest	
	Deciduous Broadleaf Forest	
	Mixed Forest	
Savanna	Closed Shrublands	
	Open Shrublands	
	Woody Savannas	
	Savannas	
Grassland	Grasslands	
	Permanent Wetlands	
	Croplands	
	Urban and Built-Up	
	Cropland/Natural Vegetation Mosaic	
	Snow and Ice	
	Barren or Sparsely Vegetated	
	Water Bodies	

2.1.2 Vegetation classification

Information about the vegetation type is obtained from the IGBP-INPE dataset that includes 17 land cover classes. The IGBP-INPE data is based on the International Geosphere-Biosphere Programme (IGBP) database and contains an improved representation of the vegetation in the tropical forests of Brazil (Saulo Freitas, personal communication). Horizontal resolution of the IGBP-INPE dataset is $1\,\mathrm{km}\times1\,\mathrm{km}$. The IGBP-INPE classes were aggregated into four basic vegetation types: Tropical Forest, Extra-tropical Forest, Savanna and Grassland. This mapping was dictated by the vegetation types for which emission factors are reported in the literature. The QFED tropical forest class includes the IGBP-INPE evergreen broadleaf forest class limited to latitudes between 30°S and 30°N. The QFED extratropical forest class aggregates all of the IGBP-INPE forest classes north of 30°N and south of 30°S. The IGBP-INPE savanna and shrubland classes are aggregated into the QFED savanna class. The QFED grassland class aggregates the rest of the IGBP-INPE types. Table 2 contains the detailed mapping scheme of the IGBP land cover classes to the QFED biome types.

2.1.3 Treatment of pixels obscured by clouds

The top-down approach relies on the direct link between emission flux and FRP density (Equation 5). Clouds hinder FRP retrievals and therefore emissions from pixels obscured by clouds need to be treated explicitly. Let us consider a grid box with area A which is observed with one or multiple overpasses from a remote sensing platform. Fractions of the area can be cloud-free, cloudy, covered by water, or not observed (orbital gaps); see Figure 1. FRP is an additive quantity, therefore the FRP

density φ can be expressed in terms of the fractional FRP densities:

$$\varphi = \frac{\varphi_{o,l}A_{o,l} + \varphi_{o,w}A_{o,w} + \varphi_{*,l}A_{*,l} + \varphi_{\#}A_{\#}}{A_{o,l} + A_{o,w} + A_{*,l} + A_{\#}} \tag{6}$$

where the symbols o, $*$ and $\#$ are used to denote cloud-free (observed), obscured by clouds, and not observed, and where the subscripts l and w denote land and water, respectively. At the nominal QFED resolution, the orbital geometries of the MODIS/Aqua and MODIS/Terra granules result in good observability, hence the terms $\varphi_{\#}A_{\#}$ and $A_{\#}$ in Equation 6 can generally be neglected. A grid box that is entirely unobserved results in zero emissions at this location.

Equation 6 can be further simplified accounting for the fact that the fire emissions from water bodies are zero, thus:

$$\varphi = \frac{\varphi_{o,l}A_{o,l} + \varphi_{*,l}A_{*,l}}{A_{o,l} + A_{o,w} + A_{*,l}} \tag{7}$$

The FRPs from areas that are obscured by clouds cannot be directly observed and hence $\varphi_{*,l}$ is unknown. Different approaches can be employed to estimate the $\varphi_{*,l}$ based on how the fires in the areas obscured by clouds are treated:

1) Explicit (no data – no fires) approach
A lower bound for the FRP density φ can be computed under the assumption that there are no fires in the areas obscured by clouds, i.e., $\varphi_{*,l} = 0$. Therefore:

$$\varphi = \frac{\varphi_{o,l}A_{o,l}}{A_{o,l} + A_{o,w} + A_{*,l}} \tag{8}$$

This method will perform well in regions where clouds and fires are strongly anticorrelated, however one can expect that it will likely underestimate the FRP density and emissions globally.

2) Extrapolation (GFAS) approach
On the other hand, one can hypothesize that conditions in the observed and obscured areas are similar and therefore the FRP density in the cloudy areas can be approximated by the FRP mean density in the cloud free areas. This approach was originally proposed by Kaiser et al. (2009) and adopted in the GFAS system cloud correction algorithm (Kaiser et al., 2012). In this case, $\varphi_{*,l} = \varphi_{o,l}$ and then from Equation 7 we get

$$\varphi = \frac{\varphi_{o,l}(A_{o,l} + A_{*,l})}{A_{o,l} + A_{o,w} + A_{*,l}} \tag{9}$$

If the similarity hypothesis is applied to both the cloudy and unobserved areas, that is $\varphi_{*,l} = \varphi_{\#} = \varphi_{o,l}$, then Equation 6 simplifies to:

$$\varphi = \varphi_{o,l}(1 - f_{water}) \tag{10}$$

where f_{water} is the water fraction in the grid box, which can be considered to be known.

Equations 9 and 10 are not dissimilar. Indeed, the term that includes the ratio of the areas in Equation 9 is similar to the $1 - f_{water}$ term in Equation 10, but the former includes only the water bodies in the area covered by the satellite granules rather than all water bodies in the grid box. In fully observed grid boxes the two results are equivalent. The similarities in the results, however, does not render the requirement for good observability unnecessary. One has to recognize that although the similarity hypothesis provides the means to estimate the emissions from the cloudy and unobserved areas of the grid box, the fidelity of the results weakens as the area of the non-observed

Table 3: Methodology and tuning reference datasets used in the QFED versions.

QFED version	FRP density method	Tuning Reference Dataset
2.1	Extrapolation (GFAS) approach	GFED-v2
2.2	Extrapolation (GFAS) approach	MODIS AOT
2.4	Sequential approach	MODIS AOT

or obscured by clouds pixels increases. This approach becomes problematic when the observed area is much smaller than the grid box area. For example, if a fire occurs in this small observed area, extrapolating this behavior to the full grid box will likely overestimate the emissions.

3) Sequential approach

The explicit and extrapolation approaches rely entirely on the current observations to estimate the current grid box mean FRP density. In the sequential approach an attempt is made to utilize the previous as well as the latest observations. This is done with a model that predicts the FRP density from the previously obtained FRP density and a blending scheme that combines the current observations with the predicted values to calculate a new estimate of the FRP density in the obscured by clouds areas. The new estimate $\varphi_{*,l}$ is calculated from the predicted (a first-guess value) $\varphi_{*,l}^b$ and the observed $\varphi_{o,l}$ FRP densities as:

$$\varphi_{*,l} = \varphi_{*,l}^b + \mathcal{K}\left(\varphi_{o,l} - \varphi_{*,l}^b\right) \tag{11}$$

where the scalar gain $\mathcal{K}$ is parametrized as:

$$\mathcal{K} = \frac{A_{o,l}}{A_{o,l} + A_{*,l}} \tag{12}$$

The formulation of $\mathcal{K}$ implicitly assumes that the error variance of the observed and obscure FRP densities are inversely proportional to the corresponding areas. When the grid box is well observed ($A_{o,l} \gg A_{*,l}$), the scalar gain $\mathcal{K}$ approaches 1 and $\varphi_{*,l} = \varphi_{o,l}$ (the GFAS limit.) If the grid box is poorly observed ($A_{o,l} \ll A_{*,l}$), the scalar gain $\mathcal{K}$ approaches 0 resulting in $\varphi_{*,l} = \varphi_{*,l}^b$.

The prior $\varphi_{*,l}^b$ is estimated from a damped persistence model (see Section 2.5) based on the previous day FRP density estimates. Once $\varphi_{*,l}^b$ is available, Equations 11 and 12 are used to find $\varphi_{*,l}$. The grid mean FRP density φ can be now calculated from Equation 7.

The sequential model utilizes the current and previous observations. This is also the case in GFAS, however it relies on the Kalman filter technique to assimilate the latest fire observations (Kaiser et al., 2012). In GFAS, the dynamics of the FRP density is described by a persistence model. Daily variability is not explicitly modeled; it is instead accounted for by inflating the variance of the last available FRP density estimate.

The extrapolation approach was used in QFED versions 2.1 and 2.2, whereas QFED-v2.4 relied on the sequential approach. The main characteristics of the different QFED versions are summarized in Table 3 and explained in greater detail in the next sections.

2.2 The QFED Level 3a products

The principal QFED product is the Level 3a global gridded daily-mean FRP and pixel areas. It contains FRP from fires in the four biomes as well as the areas of cloud-free, cloudy, and water
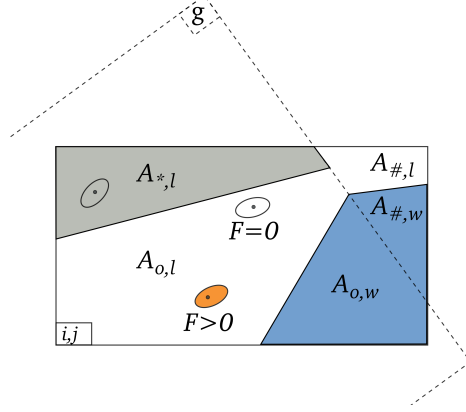
Figure 1: Schematic of gridding and merging remotely sensed fire data in QFED. The outlines of a MODIS granule g are shown as dashed lines. The ovals represent individual MODIS pixels with $F \geq 0$. Water and cloudy portions of a grid cell with indexes (i, j) are filled with blue and gray, respectively.

MODIS pixels. Pixels from day- and night-time granules from each of the MODIS instruments are aggregated on a daily basis to compute the daily mean FRP and areas. Merging of the derived gridded daily mean FRP products is done during the calculation of the emissions. This approach ensures robustness of the QFED products if there are gaps in the input data caused by interruptions in one of the MODIS satellite product streams.

The MODIS pixels areas are calculated from the pixel sample index (Giglio, 2010). The geolocation and type of the pixels are used to calculate the daily mean gridded values of the total area of all pixels of the same type, that is:

$$A(i, j) = \sum_g \sum_p A_p \tag{13}$$

where the set $\{p\}$ includes the pixels of the same type in the set of granules $\{g\}$ that intersect the grid cell with indexes (i, j). The observed FRPs are gridded and aggregated in a similar manner:

$$F(i, j) = \sum_g \sum_p F_p \tag{14}$$

The sum over the pixels can be reduced to include only the pixels with positive FRP ($F > 0$) because the non burning pixels do not contribute to the gridded FRP value.

Common to the three approaches discussed earlier (Equations 8, 9 and 12) is the need to provide the FRP density of the cloud free pixels. The daily gridded $\varphi_{o,l}(i, j)$ value is computed as:

$$\varphi_{o,l}(i, j) = \frac{F(i, j)}{A_{o,l}(i, j)} \tag{15}$$

The FRPs are binned and stored for each biome type in order to apply the biome specific emission factors. The binning of the FRP and areas is done independently for the MODIS/Terra and MODIS/Aqua fire product granules. The variables included in the QFED Level 3 products are listed in Appendix E. The QFED Level 3a data from the two MODIS instruments are merged at the emissions calculation step to create the QFED Level 3b global gridded fire emissions product. The specifics are described next.

2.3 QFED version 2.1

The main objective of QFED version 2.1 was to generate a high resolution dataset with global fire emissions that agreed well on a global scale with the GFED-v2 dataset. This version used the extrapolation method to estimate the FRP density and fire emissions. A two step calibration process was employed to calculate the emissions. In the first step, an initial value[2] $\alpha_0 = 1.37 \times 10^{-6}\,\mathrm{kg\,J^{-1}}$, as reported in Kaiser et al. (2009), was selected for the emission coefficient in Equation 16. Using this emission factor and the QFED Level 3a FRP product we calculated biomass burning emissions independently for MODIS/Terra and MODIS/Aqua. Following the extrapolation approach, the emissions were calculated under the assumption that the FRP density of the unobserved and obscured by clouds areas are equal to the FRP density of the observed (including land and water) areas. In the next, reference dataset correction step of the calibration, the global monthly GFED-v2 and QFED emissions for the years 2003–2007 were calculated. The pre-calibrated QFED Level 3b/Terra and Level 3b/Aqua emissions were calculated independently merging only granules from the same MODIS instrument. A linear regression model was used to find a new set of emission coefficients:

$$E^{GFED} = \chi_m E_m^{QFED}$$

where the index m specifies the MODIS product (MOD14 or MYD14), and E^{GFED} and E^{QFED} are the global monthly mean emissions from the GFED and the pre-calibration QFED datasets, respectively. The linear regression was performed with the log-transformed emissions, i.e., χ_m was calculated as:

$$\chi_m = exp\left(\overline{log(E^{GFED})} - \overline{log(E_m^{QFED})}\right)$$

where the overline indicates an average over time. The coefficients χ_m were used to update the corresponding emission coefficients α_m:

$$\alpha_m = \chi_m \alpha_0$$

Finally, the corrected emission coefficients α_m were used to merge MODIS/Aqua and MODIS/Terra FRP data and calculate the QFED Level 3b emissions product:

$$E_s(i,j) = \frac{\sum_m \alpha_m \sum_b \beta_{b,s} F_{m,b}(i,j)}{\sum_m A_{o,m}(i,j)} \tag{16}$$

Here the index m denotes one of the MODIS fire products, e.g., $m = \{\text{MOD14, MYD14}\}$, and $A_o(i,j)$ is the gridded area of the observed (land and water) pixels. The QFED emissions are calculated using the Andreae and Merlet (2001) emission factors listed in Table 1.

The result of the calibration process described above using biomass burning emissions of CO is shown in Figure 2. The GFED-v2 and QFED global monthly mean emissions are plotted using log-log scale graphs. The horizontal axis shows the QFED emissions computed using the initial emission coefficient α_0 and FRP from MODIS/Terra (left) and MODIS/Aqua (right). The vertical axis in both panels shows the GFED-v2 emissions. The dashed lines show the one-to-one relationship. The solid lines show the best linear fit between the log-transformed GFED and QFED data sets.

The scatter plots indicate that with respect to GFED, the initial QFED Level 3b/Terra emissions are biased low, whereas the initial QFED Level 3b/Aqua emissions are biased high. To adjust the QFED Level 3b/Terra bias the emission coefficient needs to be scaled up by a factor of $\chi_{MOD14} =$

---

[2]The value of α_0 is not of great importance. We could have used $\alpha_0 = 0.37 \times 10^{-6}\,\mathrm{kg\,J^{-1}}$ reported by Wooster et al. (2005) or any other value of order $10^{-6}\,\mathrm{kg\,J^{-1}}$.
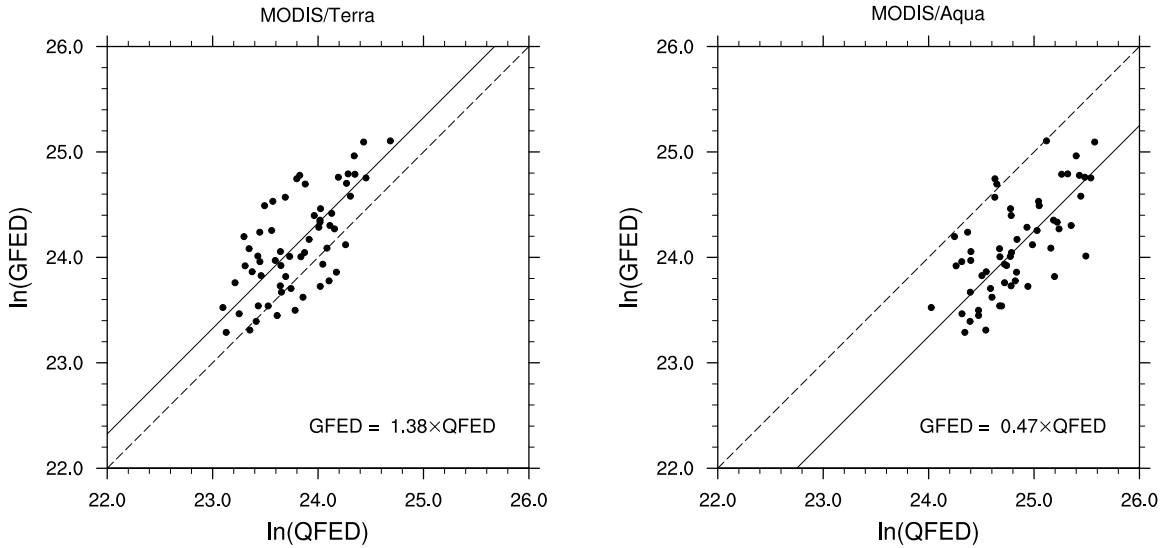
Figure 2: Calibration of QFED Level 3b/Terra (left) and QFED Level 3b/Aqua (right) against the GFED-v2 dataset. A log-log graph is used to show the global monthly mean emissions of CO (Tg/yr) for the 2003–2007 period. The linear regression and the one-to-one relationship are shown as solid and dashed lines, respectively. Also shown are the linear regression coefficients.

1.38. The QFED Level Level 3b/Aqua emissions needs to be scaled down by a factor of $\chi_{MYD14} = 0.47$. Hence, the corrected emissions coefficients are $\alpha_{MOD14} = 1.89 \times 10^{-6}\,\mathrm{kg\,J^{-1}}$ and $\alpha_{MYD14} = 0.644 \times 10^{-6}\,\mathrm{kg\,J^{-1}}$. The differences in the MODIS/Aqua and MODIS/Terra emissions coefficients can be explained by the natural peak in fire emissions intensity, which typically occurs a few hours after local noon time, which coincides with the overpass of the Aqua (EOS PM) satellite.

The performance of the merged MODIS/Aqua and MODIS/Terra QFED emissions was examined to verify if the candidate Level3b emissions remain in agreement with the reference calibration dataset. A scatter plot of QFED against the GFED-v2 emissions is shown in Figure 3. A linear regression between the global monthly mean emissions of CO from the GFED-v2 and QFED-v2.1 yielded a slope of 1.01 confirming that the emissions product remained in agreement with GFED. The final QFED-v2.1 emissions were calculated with the derived above MODIS/Aqua and MODIS/Terra emission coefficients.

The emission factors used in GFED-v2 and the QFED-v2.1 are based on (Andreae and Merlet, 2001), and therefore one can expect that the emission coefficients we derived based on analysis of CO emissions should also work well for other biomass burning species. On the other hand, one can argue that GFED-v2 and QFED-v2.1 rely on different vegetation datasets. However on a global scale the resulting differences in the emissions should be small. Indeed, performing the same calibration procedure but using emissions for different pyrogenic species resulted in virtually the same emission coefficients.

2.4 QFED version 2.2

Analysis of aerosol optical thickness (AOT) from GEOS-5 simulations with QFED-v2.1 fire emissions revealed that, much like GFED-v2, there is a low bias over the regions affected by smoke from fires. Kaiser et al. (2012) reached similar conclusions when they evaluated AOT modeled with the global Monitoring Atmospheric Composition and Change (MACC) system using emis-
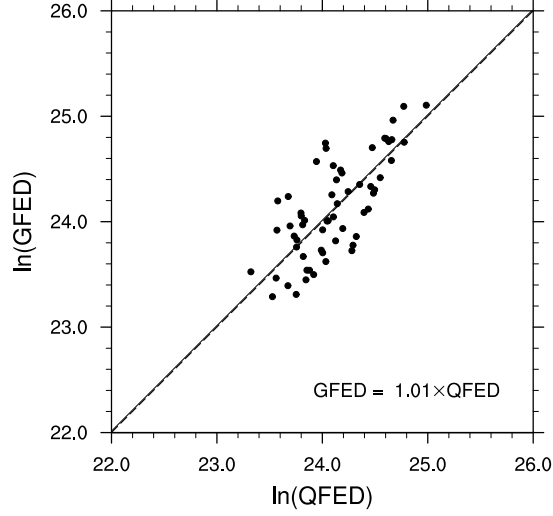
Figure 3: Scatter plot of global monthly mean CO emissions (Tg/yr) from the QFED-v2.1 and GFED-v2 datasets.

sions from the GFAS dataset, which is also calibrated against GFED emissions. The development of QFED-v2.2 aimed to improve the GEOS-5 model simulations in terms of AOT in the major biomass burning regions by refining the strength of the fire emissions.

Our approach was to introduce biome dependent emission coefficients and determine their best values by minimizing discrepancies between modeled and satellite-retrieved AOT. The continuity equation that governs the evolution of the aerosol components can be written as

$$\frac{\partial q}{\partial t} + \mathbf{v} \cdot \nabla q = E + P - L \tag{17}$$

where q is the aerosol mass mixing ratio, $\mathbf{v}$ is the velocity field, E and P are the terms describing the primary emissions and production processes, and L is the term describing the loss processes. The total emissions can be decomposed as the sum of the contributions from different type of sources, for example:

$$E = E_{BB} + E_{AN} + E_N \tag{18}$$

where E_{BB} stands for the biomass burning emissions, E_{AN} are the anthropogenic emissions, and E_N are the remaining emissions from natural sources. The processes on the right hand side of Equation 17 are largely linear with respect to q, and therefore an approximate solution can be found that is a superposition of the solutions of Equation 17 obtained by setting the emissions term E to the contributions from the fire, anthropogenic and natural sources:

$$q = q_{BB} + q_{AN} + q_N \tag{19}$$

Because the aerosol extinction is proportional to the mass mixing ratio q it follows that aerosol optical depth τ can be decomposed in a similar manner:

$$\tau = \tau_{BB} + \tau_{AN} + \tau_N \tag{20}$$

The linearity of the model response to the emissions means that if the contributions to the total emissions are scaled by some factors, i.e.:

$$E' = \chi_{BB} E_{BB} + \chi_{AN} E_{AN} + \chi_N E_N \tag{21}$$

18

we can expect that the model response will be

$$\tau' = \chi_{BB}\tau_{BB} + \chi_{AN}\tau_{AN} + \chi_N\tau_N \tag{22}$$

The focus here is to estimate χ_{BB}, but given that other emissions may have deficiencies we will attempt to estimate scaling for both biomass burning and anthropogenic emissions. With this in mind, we fix the χ_N coefficient to 1 and scale the anthropogenic and the stratified by biome biomass burning emissions:

$$E' = \sum_b \chi_b E_{BB,b} + \chi_{AN}E_{AN} + E_N \tag{23}$$

$$\tau' = \sum_b \chi_b \tau_{BB,b} + \chi_{AN}\tau_{AN} + \tau_N \tag{24}$$

where the subscript b denotes the biome type.

The established above relationship between the scaled emissions and the model response in terms of aerosol optical depth is the basis for deriving biomass emissions in QFED-v2.2. One can determine the optimal scaling coefficients by minimizing the differences between the observed and modeled aerosol depth and apply them to adjust the emissions by scaling their strength by the same factor. In the case of the biomass burning emissions, one can interpret the scaling procedure as a correction to the emission coefficients α_m in Equation 16. Rather than use a global emission coefficient (as in QFED-v2.1), now we have the means to determine and apply biome dependent emission coefficients that represent better the connection between the remotely sensed FRPs from the spaceborne instruments and the fires from the different biomes. To some degree, the derived scaling coefficients also account for weaknesses in the underlying chemical transport model. This would make the results and specifically the corrected (perceived by the underlying model) biomass burning emissions model dependent. Using the biomass burning emissions in other models requires caution and an understanding of this aspect of the results.

Different strategies can be employed to determine the scaling coefficients. One approach is to perform a regression analysis of the observed and modeled aerosol optical depth. If this analysis is done globally the correlations between the emissions from the biomes might affect the results. Rather than solving a global minimization problem we adopted the following heuristic technique. The regression model:

$$\tau \sim \chi_{BB}\tau_{BB} + \chi_{AN}\tau_{AN} + \tau_N \tag{25}$$

was performed regionally across an extensive list of regions affected by biomass burning. The results were carefully examined and systematized by the biome type primarily contributing to the aerosol extinction to determine four global biome specific scaling factors. To obtain the τ_{BB}, τ_{AN} and
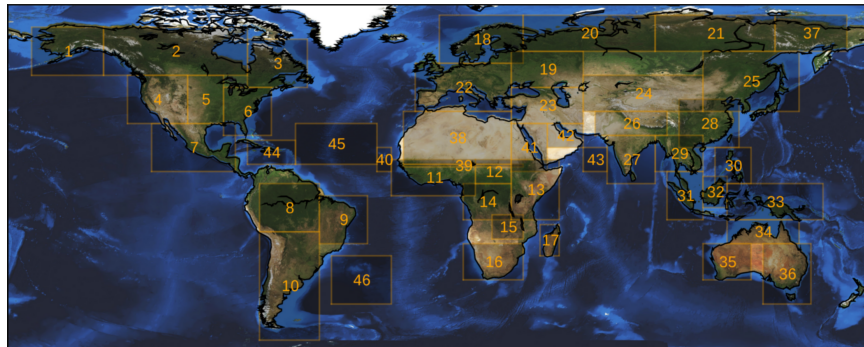
Figure 4: Map with the outlines of the geographical regions used in the development of QFED-v2.2.

19

τ_N we performed a GEOS-5 model run with the full suite of emissions, a run with biomass burning emissions set to zero and another run with anthropogenic emissions set to zero. The biomass burning emissions were from the QFED-v2.1 dataset. The aerosol optical depth due to biomass burning τ_{BB} was calculated as the difference between the model aerosol optical depth of the run with the full suite of emissions and that of the run with biomass burning emissions set to zero. The contributions from the anthropogenic and natural sources were calculated in a similar manner. The observational dataset included bias corrected (NNR) MODIS aerosol optical depth over land and water.

2.4.1 Regional analysis of aerosol optical thickness

The bilinear regression (Equation 25) was performed using regional mean values of aerosol optical depth. For our analysis we adopted (with small modifications) the regions defined by Ichoku et al. (2008) and complemented them with several additional regions. A map with the outline of the regions is shown in Figure 4, and their names and geographical extents are listed in Table 4.

Table 4: Names and geographical extents of the regions used in the development of QFED-v2.2.

Region			Longitude		Latitude	
Number	Name	Abbreviation	min	max	min	max
North America						
1	Alaska	NAmer_Alsk	-170	-140	50	70
2	Canada	NAmer_Cana	-140	-80	50	70
3	Quebec	NAmer_Queb	-80	-55	45	65
4	US (West)	NAmer_USW	-130	-105	30	50
5	US (Central)	NAmer_USC	-105	-90	30	50
6	US (East)	NAmer_USE	-90	-70	25	45
South America and Mexico						
7	Mexico	SAmm_Mex	-120	-85	10	30
8	Brazil (Forest)	SAmm_Brazf	-75	-50	-15	5
9	Brazil (Cerrado)	SAmm_Brazc	-50	-30	-20	0
10	Argentina	SAmm_Argen	-75	-50	-60	-15
Africa						
11	Africa (West)	Afri_West	-20	15	0	15
12	Africa (Central)	Afri_Central	15	30	5	15
13	Africa (East)	Afri_East	30	50	-10	15
14	Congo	Afri_Congo	10	30	-10	5
15	Zambia	Afri_Zamb	22	35	-18	-8
16	Africa (South)	Afri_South	10	35	-35	-20
17	Madagascar	Afri_Madag	42	50	-25	-12
Europe and Siberia						
18	Scandinavia	Eusi_Scan	0	35	55	75
19	Moscow	Eusi_Mosc	30	60	45	60
20	Siberia (West)	Eusi_Sibw	35	90	60	75
21	Siberia (East)	Eusi_Sibe	90	140	60	75
22	Europe (West)	Eusi_Eurw	-10	30	35	55

<div align="center">Continued</div>

Region			Longitude		Latitude	
Number	Name	Abbreviation	min	max	min	max
23	Middle East	Eusi_Mide	30	60	30	45
Asia						
24	Asia (Central)	Asia_Cent	60	110	35	50
25	China (East)	Asia_Chine	110	150	35	60
26	Nepal	Asia_Nepal	65	95	25	35
27	India	Asia_India	70	90	5	25
28	China (South)	Asia_Chins	100	125	20	40
29	Indochina	Asia_Indchn	90	110	10	25
Australia and South Asia						
30	The Philippines	Ausa_Philip	115	130	5	20
31	Sumatra	Ausa_Sumatra	95	110	-10	10
32	Borneo	Ausa_Borneo	110	120	-5	8
33	Indonesia and PNG	Ausa_Indpng	120	160	-10	5
34	Australia (North)	Ausa_Ausn	120	150	-20	-10
35	Australia (West)	Ausa_Ausw	110	130	-35	-20
36	Australia (East)	Ausa_Ause	135	155	-45	-20
Additional regions						
37	Siberia (Far East)	Eusi_Sibfe	140	170	60	75
38	Sahara	Afri_Sahara	-15	30	13	35
39	Sahel	Afri_Sahel	-15	35	12	13
40	Cape Verde	Afri_CapVerd	-26	-20	10	20
41	Red Sea	Afri_RedSea	30	45	10	30
42	Persian Gulf	Asia_PerGulf	45	60	20	30
43	Arabian Sea	IO_ArabSea	60	70	10	20
44	Caribbean Sea	NAO_Carib	-80	-60	13	23
45	SAL/Dust	NAO_AfrDust	-60	-26	13	30
46	South America BB	SAO_SAmmBB	-45	-20	-45	-25

To facilitate the AOT analysis and the interpretation of the results from the regression model we created diagnostic plots for all regions (see Appendixes B and C). An example of these plots is shown in Figure 5. From top to bottom, the first panel shows time series of the observed (black) and modeled (red) AOTs as well as the modified AOT (blue) after correcting the biomass burning contribution. For this region, the regression of the model against the AOT from the bias corrected NNR/Aqua over land product yielded $\chi_{BB} = 2.2$ and $\chi_{AN} = 4.4$. The second panel shows time series of the biomass burning (red), anthropogenic AOT (gray), and the adjusted biomass burning component $\chi_{BB}\tau_{BB}$ (orange). Contributions from dust (brown), sea-salt (blue), anthropogenic (gray), adjusted biomass burning (orange) and other sources of aerosols (peach) are stacked up and compared against the observed AOT (black) in the third panel. The bottom-left panel shows a scatter plot of the total AOT from the model and the observations, and the one-to-one line. The bottom-right panel includes probability density functions (PDFs) of the observed (black), model (red) and corrected (blue) AOTs after applying a logarithmic transformation $ln(AOT + \varepsilon)$, where $\varepsilon = 0.01$.

The time series of AOT shown in the top plot in Figure 5 indicate that one can expect a better agreement between the model and the observations if the biomass burning emissions are scaled up by a factor of 2.2. Other examples of regions in which enhancing the biomass burning has a positive

impact on the model AOT include: US Central, for which diagnostics are shown in Figure B16; Brazil (Forest) (Figure B19); Zambia (Figure B26); East China (Figure B36); Indochina (Figure B40); East Australia (Figure B47); and Siberia (Far-East) (Figure B48).

The results from the analysis of all regions are summarized in Tables 5 and 6. A map with the derived biomass burning scaling factors is shown in Figure 6. Although there are significant variations in the derived biomass burning scaling factors, the range of values from the regional analyses over land are: 2–3 for tropical forest, 3–5 for extratropical forest, and 1–3 for grassland and savanna biomes. Based on these results we selected the following representative values that can be applied globally: 2.5 for fires from tropical forests, 4.5 for fires from extratropical forests, and 1.8 for savanna and grassland fires. These representative scaling factors (Table 7) were used in QFED-v2.2. Note that only aerosol emissions were enhanced by applying the biome dependent factors. Further investigation is needed to verify if the AOT derived factors can also improve CO, CO_2 and other pyrogenic gas species in the model.

Table 5: Regional parameters estimated using the bilinear regression model described in Section 2.4 and AOT over land. The definition of the regions can be found in Section 2.4.1.

Region		NNR/Aqua			NNR/Terra		
Number	Name	χ_{BB}	χ_{AN}	R^2	χ_{BB}	χ_{AN}	R^2
North America							
1	Alaska	3.0 ± 0.8	0.9 ± 0.5	0.52	4.6 ± 0.7	-0.8 ± 0.5	0.54
2	Canada	4.2 ± 0.5	0.1 ± 0.2	0.75	3.5 ± 0.6	0.1 ± 0.3	0.63
3	Quebec	5.1 ± 0.9	0.7 ± 0.2	0.85	4.5 ± 0.8	0.7 ± 0.2	0.79
4	US (West)	1.6 ± 0.4	0.5 ± 0.1	0.77	1.8 ± 0.5	0.5 ± 0.1	0.75
5	US (Central)	4.5 ± 1.0	0.8 ± 0.2	0.89	3.7 ± 0.9	0.8 ± 0.2	0.88
6	US (East)	4.6 ± 1.3	1.5 ± 0.2	0.91	4.7 ± 1.5	1.3 ± 0.2	0.88
South America and Mexico							
7	Mexico	6.2 ± 0.3	1.4 ± 0.1	0.96	6.5 ± 0.3	1.1 ± 0.1	0.95
8	Brazil (Forest)	1.9 ± 0.2	4.2 ± 0.7	0.88	2.3 ± 0.2	4.0 ± 0.8	0.88
9	Brazil (Cerrado)	2.4 ± 0.4	3.3 ± 0.5	0.85	2.4 ± 0.4	2.6 ± 0.5	0.83
10	Argentina	2.4 ± 0.1	4.4 ± 0.3	0.96	2.4 ± 0.2	3.0 ± 0.4	0.91
Africa							
11	Africa (West)	0.3 ± 0.2	-0.6 ± 0.2	0.09	0.4 ± 0.2	-0.4 ± 0.3	0.05
12	Africa (Central)	-0.6 ± 0.1	-1.1 ± 0.2	0.57	-0.7 ± 0.1	-0.7 ± 0.2	0.52
13	Africa (East)	1.2 ± 0.3	1.7 ± 0.2	0.86	1.1 ± 0.3	2.2 ± 0.2	0.90
14	Congo	0.7 ± 0.1	3.6 ± 0.4	0.94	1.5 ± 0.2	3.4 ± 0.5	0.93
15	Zambia	2.0 ± 0.2	2.1 ± 0.4	0.86	3.2 ± 0.2	1.5 ± 0.4	0.89
16	Africa (South)	1.8 ± 0.1	2.9 ± 0.1	0.96	1.4 ± 0.2	2.6 ± 0.2	0.93
17	Madagascar	3.1 ± 0.9	2.7 ± 1.0	0.69	3.3 ± 0.8	1.4 ± 0.7	0.69
Europe and Siberia							
18	Scandinavia	5.8 ± 0.9	0.1 ± 0.1	0.81	5.8 ± 1.0	0.0 ± 0.1	0.73
19	Moscow	3.6 ± 0.8	0.5 ± 0.1	0.78	2.4 ± 0.6	0.5 ± 0.1	0.76
20	Siberia (West)	3.9 ± 1.0	0.3 ± 0.2	0.82	5.1 ± 1.0	-0.0 ± 0.2	0.81
21	Siberia (East)	4.5 ± 0.4	0.4 ± 0.1	0.92	3.9 ± 0.4	0.3 ± 0.1	0.90
22	Europe (West)	4.2 ± 1.8	0.3 ± 0.2	0.65	6.2 ± 1.8	0.0 ± 0.2	0.62
Continued							

Region		NNR/Aqua			NNR/Terra		
Number	Name	χ_{BB}	χ_{AN}	R^2	χ_{BB}	χ_{AN}	R^2
23	Middle East	-0.8 ± 2.2	1.3 ± 0.3	0.78	-0.1 ± 2.5	0.7 ± 0.3	0.52
Asia							
24	Asia (Central)	4.7 ± 0.9	1.1 ± 0.1	0.92	3.6 ± 1.0	0.8 ± 0.2	0.87
25	China (East)	3.2 ± 0.4	1.3 ± 0.1	0.93	2.9 ± 0.3	1.1 ± 0.1	0.94
26	Nepal	18 ± 1.3	1.6 ± 0.1	0.95	19 ± 1.5	1.4 ± 0.1	0.93
27	India	10 ± 0.9	1.1 ± 0.1	0.95	9.1 ± 1.0	1.6 ± 0.1	0.96
28	China (South)	3.8 ± 0.3	1.8 ± 0.04	0.98	3.5 ± 0.3	1.7 ± 0.0	0.98
29	Indochina	3.2 ± 0.2	1.76 ± 0.07	0.95	3.6 ± 0.2	1.6 ± 0.1	0.95
Australia and South Asia							
30	The Philippines	2.5 ± 0.6	3.3 ± 0.2	0.92	2.9 ± 0.6	2.9 ± 0.2	0.90
31	Sumatra	9.4 ± 0.9	2.9 ± 0.3	0.94	9.8 ± 0.8	2.5 ± 0.2	0.95
32	Borneo	9.2 ± 0.9	4.3 ± 0.6	0.88	11 ± 1.0	4.4 ± 0.6	0.87
33	Indonesia and PNG	5.4 ± 1.2	4.3 ± 0.8	0.74	6.0 ± 1.1	4.0 ± 0.7	0.76
34	Australia (North)	0.9 ± 0.2	6.3 ± 0.5	0.88	0.6 ± 0.2	5.9 ± 0.5	0.82
35	Australia (West)	0.3 ± 0.1	2.9 ± 0.3	0.75	0.4 ± 0.2	2.1 ± 0.4	0.63
36	Australia (East)	1.1 ± 0.3	2.4 ± 0.4	0.78	1.6 ± 0.4	1.4 ± 0.4	0.65
Additional regions							
37	Siberia (Far East)	5.4 ± 0.4	0.4 ± 0.2	0.94	4.1 ± 0.4	0.4 ± 0.2	0.92
38	Sahara	-6.2 ± 0.7	-1.4 ± 0.2	0.85	-6.3 ± 0.7	-1.8 ± 0.2	0.87
39	Sahel	-1.8 ± 0.3	-1.3 ± 0.2	0.68	-2.7 ± 0.3	-0.7 ± 0.2	0.68
40	Cape Verde	*n/a*					
41	Red Sea	-0.3 ± 0.4	0.9 ± 0.1	0.60	-0.3 ± 0.4	0.7 ± 0.1	0.53
42	Persian Gulf	2.8 ± 1.2	0.4 ± 0.2	0.40	-0.9 ± 1.2	0.6 ± 0.2	0.15
43	Arabian Sea	6.8 ± 1.2	1.3 ± 0.2	0.79	4.7 ± 1.3	1.8 ± 0.2	0.86
44	Caribbean Sea	*n/a*					
45	SAL/Dust	*n/a*					
46	South America BB	*n/a*					

Table 6: Regional parameters estimated using the bilinear regression model described in Section 2.4 and AOT over water. The definition of the regions can be found in Section 2.4.1.

Region		NNR/Aqua			NNR/Terra		
Number	Name	χ_{BB}	χ_{AN}	R^2	χ_{BB}	χ_{AN}	R^2
North America							
1	Alaska	6.3 ± 1.9	-1.7 ± 0.8	0.13	7.0 ± 2.4	-2.6 ± 0.8	0.13
2	Canada	6.3 ± 2.1	-1.3 ± 0.7	0.11	6.7 ± 1.9	-1.4 ± 0.7	0.15
3	Quebec	7.2 ± 1.2	-0.1 ± 0.3	0.57	6.8 ± 1.1	-0.1 ± 0.2	0.58
4	US (West)	2.8 ± 1.1	-0.4 ± 0.3	0.12	2.3 ± 1.1	-0.2 ± 0.3	0.11
5	US (Central)	*n/a*					
6	US (East)	2.9 ± 0.9	1.1 ± 0.1	0.90	2.7 ± 0.9	1.0 ± 0.1	0.88
South America and Mexico							

Continued

	Region	NNR/Aqua			NNR/Terra		
Number	Name	χ_{BB}	χ_{AN}	R^2	χ_{BB}	χ_{AN}	R^2
7	Mexico	6.0 ± 0.3	0.4 ± 0.1	0.95	6.3 ± 0.3	0.6 ± 0.1	0.96
8	Brazil (Forest)	*n/a*					
9	Brazil (Cerrado)	2.3 ± 0.4	1.2 ± 0.4	0.78	2.2 ± 0.6	1.6 ± 0.5	0.72
10	Argentina	-0.3 ± 1.0	-2.3 ± 0.5	0.41	-1.9 ± 1.2	-2.0 ± 0.6	0.46
Africa							
11	Africa (West)	2.9 ± 0.2	1.3 ± 0.4	0.89	2.9 ± 0.2	1.5 ± 0.4	0.87
12	Africa (Central)	*n/a*					
13	Africa (East)	2.6 ± 0.7	2.6 ± 0.2	0.90	2.8 ± 0.9	2.8 ± 0.3	0.87
14	Congo	1.5 ± 0.1	5.8 ± 0.4	0.97	1.6 ± 0.1	5.4 ± 0.4	0.97
15	Zambia	*n/a*					
16	Africa (South)	1.5 ± 0.2	1.4 ± 0.2	0.88	1.3 ± 0.2	1.6 ± 0.2	0.87
17	Madagascar	3.7 ± 0.8	0.2 ± 0.8	0.58	3.8 ± 0.9	0.7 ± 0.8	0.64
Europe and Siberia							
18	Scandinavia	9.1 ± 2.9	-0.7 ± 0.3	0.17	9.1 ± 2.6	-0.7 ± 0.3	0.18
19	Moscow	7.2 ± 1.3	0.7 ± 0.2	0.74	4.6 ± 0.9	0.7 ± 0.1	0.83
20	Siberia (West)	8.6 ± 1.8	0.0 ± 0.2	0.67	6.4 ± 1.9	0.1 ± 0.2	0.59
21	Siberia (East)	*n/a*					
22	Europe (West)	4.2 ± 2.0	0.2 ± 0.2	0.50	6.2 ± 2.1	-0.0 ± 0.2	0.48
23	Middle East	3.6 ± 2.2	0.7 ± 0.2	0.78	5.7 ± 2.2	0.5 ± 0.2	0.76
Asia							
24	Asia (Central)	*n/a*					
25	China (East)	5.5 ± 0.6	1.4 ± 0.1	0.93	5.0 ± 0.6	1.2 ± 0.1	0.94
26	Nepal	*n/a*					
27	India	12 ± 1.3	1.0 ± 0.1	0.91	13 ± 1.2	1.5 ± 0.1	0.94
28	China (South)	7.9 ± 1.0	2.4 ± 0.1	0.90	6.0 ± 0.8	2.0 ± 0.1	0.92
29	Indochina	5.5 ± 0.5	1.9 ± 0.1	0.90	5.8 ± 0.5	1.8 ± 0.1	0.91
Australia and South Asia							
30	The Philippines	3.3 ± 0.6	1.4 ± 0.1	0.78	3.4 ± 0.6	1.3 ± 0.2	0.75
31	Sumatra	13 ± 1.4	1.2 ± 0.5	0.88	7.6 ± 0.9	2.4 ± 0.3	0.92
32	Borneo	13 ± 1.4	3.1 ± 0.8	0.83	11 ± 1.2	4.0 ± 0.6	0.88
33	Indonesia and PNG	8.6 ± 0.9	1.8 ± 0.4	0.87	8.5 ± 0.9	2.3 ± 0.5	0.87
34	Australia (North)	2.1 ± 0.2	0.5 ± 0.4	0.79	2.1 ± 0.2	1.0 ± 0.4	0.81
35	Australia (West)	2.3 ± 0.2	-2.7 ± 0.3	0.56	1.9 ± 0.2	-2.3 ± 0.3	0.52
36	Australia (East)	3.5 ± 0.8	-3.9 ± 0.7	0.31	3.2 ± 0.8	-3.0 ± 0.7	0.21
Additional regions							
37	Siberia (Far East)	*n/a*					
38	Sahara	-3.8 ± 2.0	-0.5 ± 0.3	0.51	-3.8 ± 2.1	-0.5 ± 0.3	0.46
39	Sahel	0.0 ± 0.3	-1.5 ± 0.4	0.22	-0.2 ± 0.4	-1.1 ± 0.5	0.10
40	Cape Verde	-1.2 ± 0.6	-2.2 ± 0.3	0.61	-1.3 ± 0.6	-2.0 ± 0.3	0.52
41	Red Sea	3.6 ± 0.8	2.0 ± 0.1	0.88	4.2 ± 0.9	2.4 ± 0.1	0.90
42	Persian Gulf	4.3 ± 1.6	2.1 ± 0.3	0.79	3.3 ± 1.8	2.8 ± 0.3	0.81
43	Arabian Sea	5.5 ± 1.2	0.8 ± 0.2	0.76	4.1 ± 1.1	1.2 ± 0.2	0.82
44	Caribbean Sea	7.3 ± 0.8	-1.1 ± 0.2	0.57	6.9 ± 0.8	-1.3 ± 0.2	0.54

Continued

Region		NNR/Aqua			NNR/Terra		
Number	Name	χ_{BB}	χ_{AN}	R^2	χ_{BB}	χ_{AN}	R^2
45	SAL/Dust	4.1 ± 1.0	-2.4 ± 0.2	0.68	3.6 ± 0.9	-2.2 ± 0.2	0.66
46	South America BB	1.7 ± 1.0	-4.7 ± 0.9	0.39	1.7 ± 0.8	-3.9 ± 0.8	0.34

Table 7: Biome dependent factors used to scale up fire emissions of OC, BC, SO_2, NH_3 and $PM_{2.5}$.

Tropical Forest	Extratropical Forest	Savanna	Grassland
2.5	4.5	1.8	1.8

2.5 QFED version 2.4

The major development in QFED-v2.4 was the adoption of the sequential method that was discussed in Section 2.1.3. This required developing a model to compute a first guess of the FRP density of the areas obscured by clouds. An exploratory analysis of the temporal evolution of FRP densities suggested that a simple exponential relationship can be used to relate the one-day lagged values:

$$\varphi_{o,l}(t+\Delta t) = \varphi_{o,l}(t)exp(-\Delta t/\tau) \tag{26}$$

where $\Delta t = 1$ day and the parameter τ is the characteristic time controlling the fire decay rate. Large τ values describe fires that persist over long time, whereas small τ values describe short lived fires. In the limiting case $\tau >> 1$ the model describes the basic persistence model $\varphi_{o,l}(t+\Delta t) = \varphi_{o,l}(t)$.

We can apply the damped persistence model to estimate the current FRP densities from the known FRP densities from the previous day. The FRP densities predicted in this way serve as the first guess value in the obscured by clouds areas. Equation 11 is next applied to estimate the current FRP densities and these can then be used in turn to make the next prediction and so on.

The joint PDF of the FRP densities for two consecutive days for the tropical forest, extra-tropical forest, savanna and grassland biomes are shown in Figure 7. The shapes of the joint PDFs for the four biomes are similar - they are asymmetrical with respect to the one-to-one line. The asymmetrical joint PDFs reflect the fact that for a given location and day, the FRP density on the next day tends to decrease.

To find the characteristic time τ we used the expression:

$$\Delta t/\tau = \ln\varphi_{o,l}(t) - \ln\varphi_{o,l}(t+\Delta t) \tag{27}$$

which follows directly from Equation 26. The PDF and cumulative distribution function (CDF) of the right-hand side of Equation 27 are shown in the right and left inset graphs included at the top of the four panels in Figure 7. The PDFs for the four biome types are skewed to the right and have similar widths. Likewise, the CDF for the four biomes are remarkably similar. Basic statistical parameters such as mode and median were computed and are included in the PDF and CDF graphs.

For about 80% of the data, parameter τ is in the range 0.4–5, with median values of 0.9, 1.0, 1.0 and 0.9 days for the tropical forest, extra-tropical forest, savanna and grassland biomes. The most frequently observed values (modes) of the parameter τ for the tropical forest, extra-tropical forest, savanna and grassland biomes were found to be 2.9, 3.0, 3.3 and 3.3 days, respectively. Given the
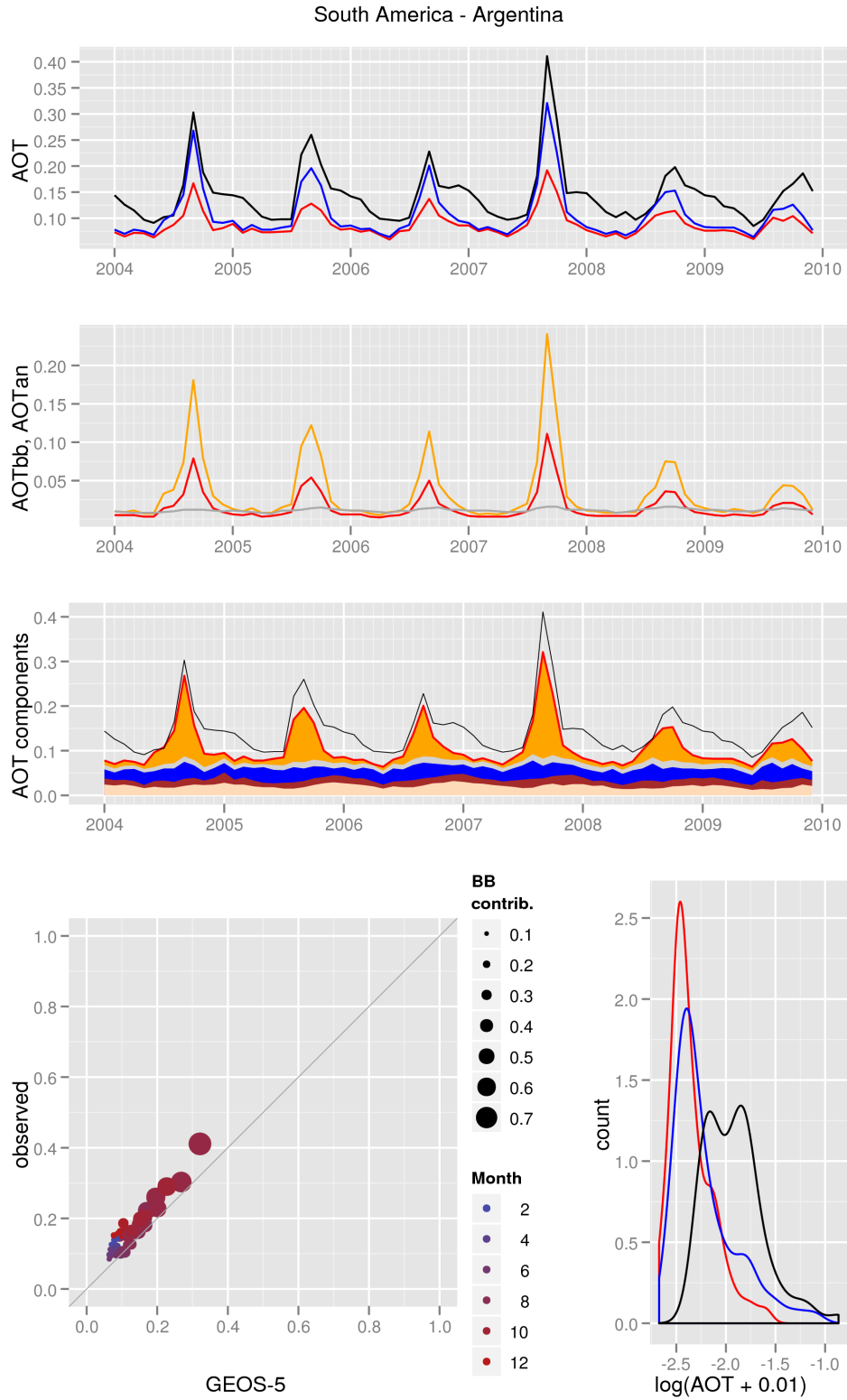
Figure 5: Diagnostic plots for the Argentina (SAmm_Argen) region. The regression coefficients calculated using NNR-AOT/Aqua over land data are $\chi_{BB} = 2.2$ and $\chi_{AN} = 4.4$, the coefficient of determination R^2 is 0.96. Description of the plots shown in the panels can be found in Section 2.4.1.
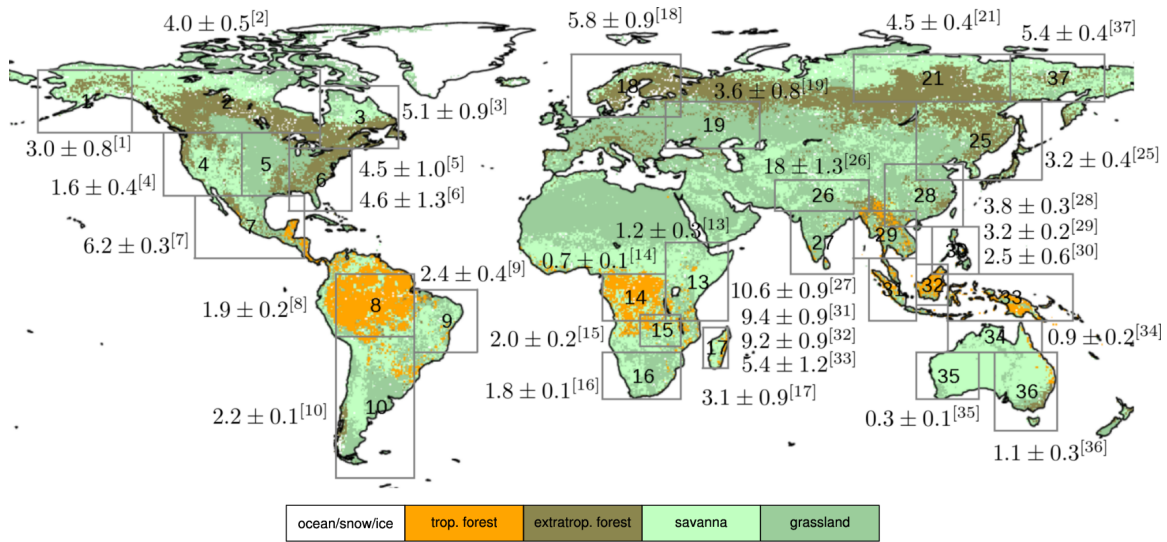
Figure 6: The best estimate and the error of the biomass burning scaling factors for the selected regions. The regional bilinear regressions was performed using NNR-AOT/Aqua(land) data.

observed spread of the data, we adopted the same value $\tau = 3.0$ for all biome types in the emission algorithm.

We would like to point out that the approach developed here and the subsequent analysis are not a substitute for a biomass fire prediction method. The derived value of the parameter τ ensures stability of the emission algorithm, because emissions from fires that are not well observed will exponentially weaken. For example, lapse of observed FRP density data means that the emissions will decrease to about 50% of their initial value in two days, and keep decreasing to about 10% of their initial value in seven days. Global emissions were not affected significantly by the adoption of the sequential method and remained within a few percent of the QFED-v2.2 emissions estimates.
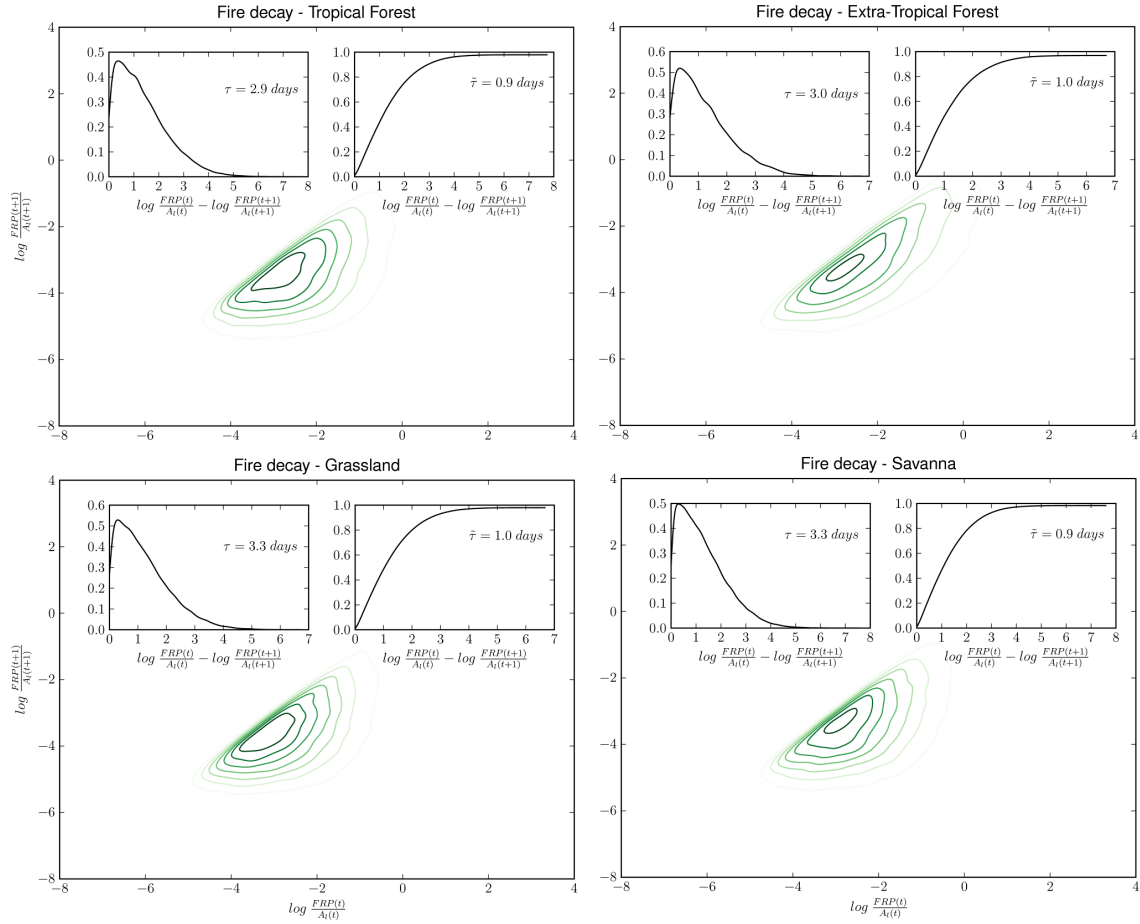
Figure 7: Diagnostic plots of FRP densities for two consecutive days. The panels show the joint PDF of the log-transformed FRP densities ($log\frac{FRP(t)}{A_l(t)}$ and $log\frac{FRP(t+1)}{A_l(t+1)}$ are on the x-axis and y-axis, respectively) for the four biome types. The PDF and CDF of the difference of one-day lagged log-transformed FRP densities ($log\frac{FRP(t)}{A_l(t)} - log\frac{FRP(t+1)}{A_l(t+1)}$) are shown respectively in the left and right embedded plots. Also shown are the most likely (mode) and the median value of the parameter τ.

3 Comparison of QFED with the GFED, GFAS and FLAMBE datasets

To investigate how QFED compares with the GFED (van der Werf et al., 2010), GFAS (Kaiser et al., 2012) and FLAMBE (Reid et al., 2009) we computed monthly mean emissions from fires in the GFED basis regions, which are shown in Figure 8. The regional and global emissions from the GFAS-v1.0, GFED-v2.1 and QFED-v2.2 were computed for years 2003–2010. FLAMBE emissions were computed for years 2003–2008. In our analysis we also included GFAS emissions that were scaled by a factor of 3.4 as recommended by Kaiser et al. (2012). Here, we refer to the scaled up GFAS emissions as enhanced GFAS (GFAS-v1_e); also in the text below we omit the version of the datasets and refer to them using their abbreviated names. For the comparative analysis we created time series, climatologies and scatter plots (with regression lines) of global and regional monthly mean emissions. The results from the linear regressions of BC emissions from the GFED basis regions are listed in Table 8. The monthly time series and climatology of the BC emissions from the QFED, FLAMBE, GFAS and GFED datasets are shown in Figures 9 and 10, respectively.
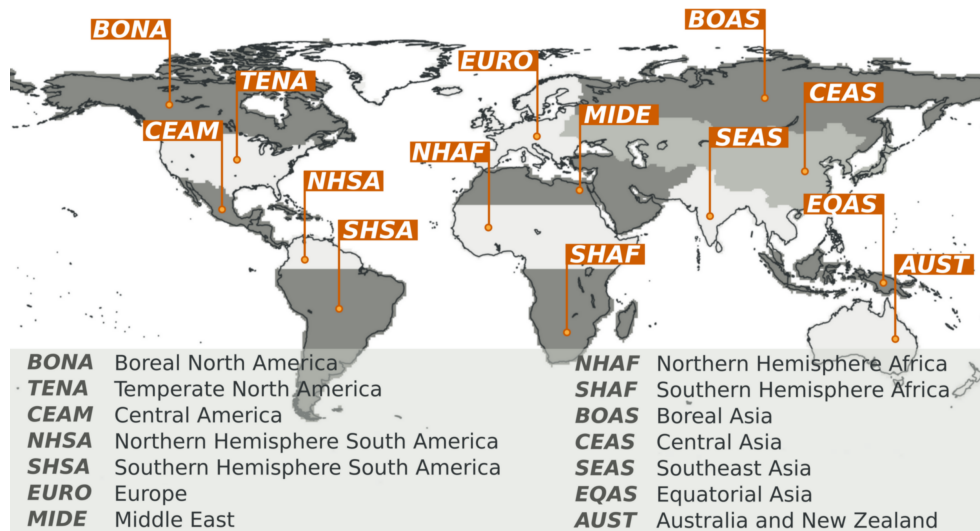
Figure 8: Map of the GFED basis regions.

Globally the QFED emissions are well correlated with the estimates from the other datasets. The correlation is highest between QFED and GFAS with $R^2 = 0.96$, followed by GFED ($R^2 = 0.72$) and FLAMBE ($R^2 = 0.59$). The FLAMBE emission estimates tend to be higher than the QFED emissions throughout the year, except in October, November, December and January. The introduction of biome dependent emission coefficients in QFED-v2.2 results in QFED emissions that are globally larger than the GFED and GFAS-v1.0 estimates. The global emissions have similar seasonal variability across the four datasets - in all cases, maximum of the emissions occurs in JJA driven by strong emissions in the major biomass burning source regions, and less pronounced peaks are seen in the winter and spring seasons. In contrast to the other datasets, GFED climatological emissions are very low in the spring (Figure 10). With respect to QFED, the FLAMBE emissions peak one month early and are much lower in the winter. During the analyzed period there are three years with above average maximum emissions in QFED: 2005, 2007 and 2010. This is also corroborated by time series of the GFED, GFAS and FLAMBE emissions. Globally, the FLAMBE and the enhanced GFAS emissions overestimate QFED estimates by about 20%, whereas GFAS and GFED estimates are lower than the QFED emissions by factors of 3 and 2, respectively (Figure 11 and Table 8).

In the *Australia and New Zealand (AUST)* region all datasets have very similar seasonal patterns, with fire emission reaching a maximum in SON and a weaker secondary peak in MAM. All datasets indicate that there were strong fire seasons in 2003, 2004, 2006 and 2007. In this region, QFED agrees very well with the enhanced GFAS emissions ($R^2 = 0.87$). Although there is a good correlation between QFED and the other datasets in this region, the QFED emissions are about 2 to 4 times larger (Figure D85).

In the *Boreal Asia (BOAS)* region the emissions are mainly from fires in MAM, JJA and SON. The datasets agree that strong fires have occurred in 2003 and 2008. The QFED estimates are larger than the values from FLAMBE, GFAS, and GFED. In this region the enhanced GFAS emissions are about 20% stronger than QFED (Figure D86). The linear regression analysis resulted in R^2 coefficients of 0.78, 0.83 and 0.96 for the correlation of QFED with FLAMBE, GFED and GFAS, respectively.

In the *Boreal North America (BONA)* region the fire season starts in April and peaks in JJA. The QFED, FLAMBE and GFAS suggest an increase of the emissions in October. The emissions estimates from FLAMBE, GFAS and GFED are fairly similar. The estimates from the globally enhanced GFAS are about 30% larger than QFED, whereas the rest of the datasets have emissions that are weaker than QFED (Figure D87). The similar seasonal patterns result in strongly correlated datasets, with $R^2 > 0.8$.

The *Central America (CEAM)* region exhibits weak interannual variability of fire emissions. According to the QFED estimates the strong emissions in 2003 were followed by a less active 2004. There is a very good agreement between the QFED and the enhanced GFAS emissions (Figure D88). In this region GFAS agrees very well with the FLAMBE, whereas GFED has the weakest emissions across the four datasets. QFED is about 3 times stronger than FLAMBE, 5 times stronger than GFED, and about 2.5 times stronger than GFAS. The R^2 values are equal to 0.85, 0.88 and 0.98, respectively.

The time series of the QFED emissions from the *Central Asia (CEAS)* region reveal complex behavior, with large year-to-year and seasonal variability. In some years (e.g., 2003 and 2006) the QFED emissions are clearly bimodal, whereas in other years they are trimodal (e.g., 2004 and 2005). Overall, the GFED emissions are the weakest in this region, followed by GFAS and FLAMBE. QFED agrees well with the enhanced GFAS emissions. The (R^2) values are the lowest among all of the GFED basis regions, reflecting the differences between QFED and the other datasets (D89).

The *Equatorial Asia (EQAS)* region is the only region where QFED is biased low with respect to GFED. The large-scale fires that affected the region in 2006 are clearly seen in the GFED and FLAMBE time series, whereas QFED and GFAS have difficulties capturing the magnitude of this extreme event. This is a good example of the limitations of the FRP based emissions in cases of smoldering and peat fires with low thermal signature. Figure D90 shows that QFED is very well correlated with FLAMBE ($R^2 = 0.97$) and GFAS ($R^2 = 0.97$). The FLAMBE emissions are over 2 times larger than those of QFED. GFAS has the weakest emissions, about 40% of the QFED estimates. The relatively low correlation between QFED and GFED ($R^2 = 0.65$) reflects the difficulties QFED has in reproducing the magnitude and temporal patterns of fire emissions suggested by GFED.

Emissions in the *Europe (EURO)* region have a well defined season cycle, with a maximum in August. QFED, FLAMBE and GFAS also show an increase of fire emissions in March and April likely caused by field burning of agricultural wastes. Time series of QFED and FLAMBE emissions support the connection between the heat waves in 2003, 2005, 2006 and 2007 and elevated fire emissions in this region. GFAS and GFED estimates are very similar. The magnitude of the enhanced GFAS emissions is similar to the FLAMBE estimates. QFED emissions are largest in this region (Figure D91) and are very well correlated with the other datasets ($R^2 > 0.89$). QFED
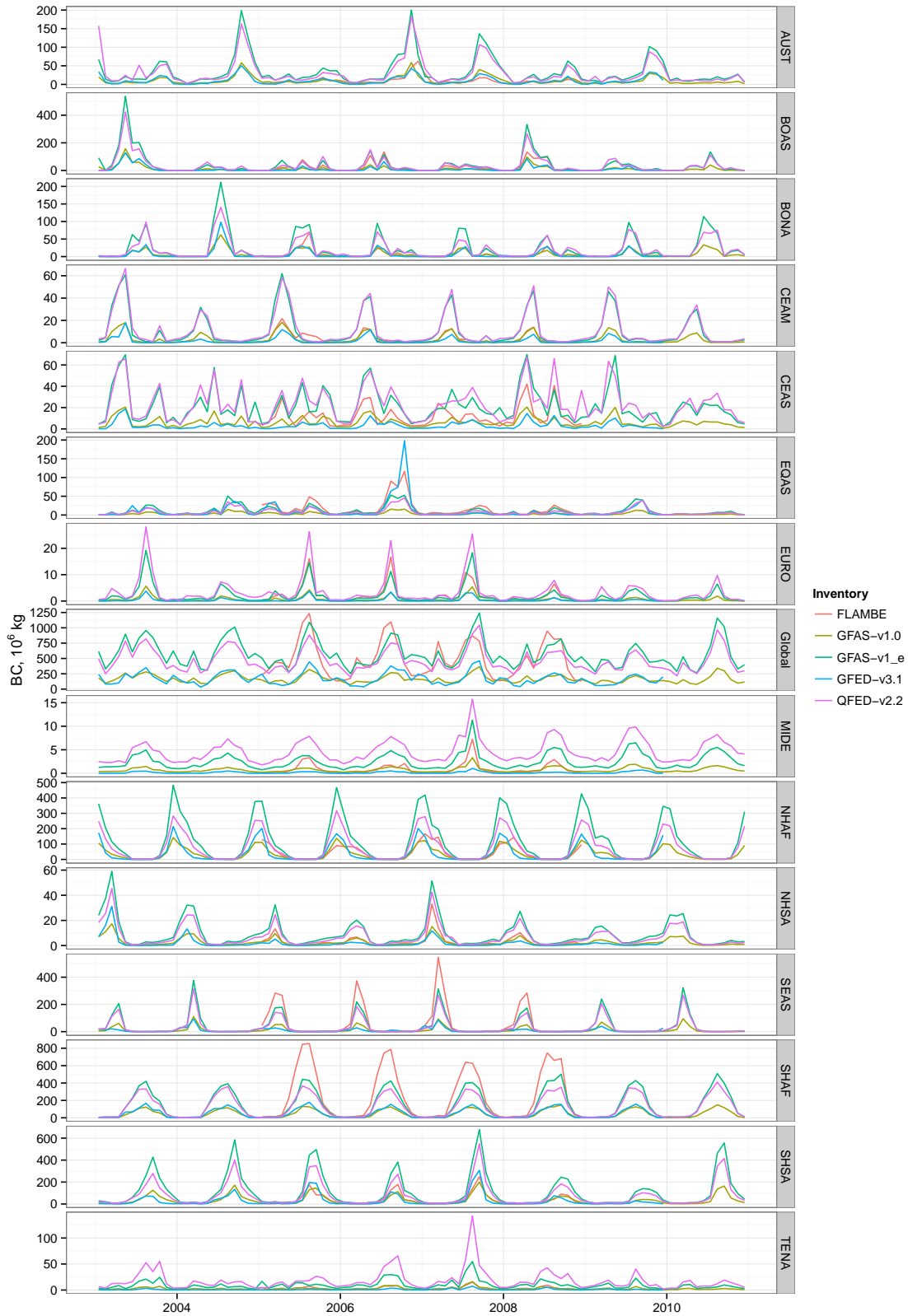
Figure 9: Time series of global and regional BC emissions from the QFED, GFED, GFAS and FLAMBE datasets.

estimates exceed those of FLAMBE by a factor of 1.7, GFED by a factor of 7, GFAS by a factor of 5.5, and the enhanced GFAS by a factor of 1.6.

The fire emissions from the *Middle East (MIDE)* region have weak interannual variability. From 2003 to 2010 there is only one year (2007) with noticeably elevated emissions. The higher than average emissions in 2007 are observed in the QFED time series as well as in the FLAMBE and GFAS datasets. QFED estimates in this region are the largest, followed by those of the enhanced GFAS, FLAMBE, GFAS and GFED. Another feature of the QFED emissions is the apparent large background values. While GFED and FLAMBE have very small emissions in DJF and MAM, the QFED emissions remain relatively high during these seasons. This difference in the QFED behavior is reflected by the negative intercepts of the linear regressions (Figure D92 and Table 8). Some of this bias is likely caused by emissions from flare stacks or other sources with persistent thermal signature that need to be screened out, similarly to the QA procedure in the GFAS system. This is another region for which the datasets are well correlated but have noticeably different estimates for the magnitude of the fire emissions: GFED is over 10 times smaller that QFED; FLAMBE is about 2 times lower that QFED; GFAS is about 5 times lower than QFED.

In the *Northern Hemisphere Africa (NHAF)* region fires occur throughout the year except for the months of June, July, August and September, when all of the datasets are in agreement that the emissions approach zero. In this region the enhanced GFAS estimates are largest. In February, March, April, May and June the QFED emissions are similar to those of FLAMBE. During these months GFED has the lowest estimates, but this changes in October, November, December and February, when GFED emissions are stronger than those of GFAS and FLAMBE, but weaker than those of QFED. These seasonal differences are seen in the scatter plots (D93) and the plotted climatologies (Figure 10). GFAS and QFED are very well correlated with $R^2 = 0.99$, however the QFED emissions are about two times stronger than those of GFAS and 1.5 times weaker than those of the enhanced GFAS.

The temporal patterns of the fire emissions from the *Northern Hemisphere South America (NHSA)* region are consistent across the datasets - in each, there is a minimum in June and a maximum in February or March. The amplitude of the emissions in 2003 and 2007 is noticeable larger than the average for this period. In this region the enhanced GFAS emissions are the strongest, about 30% higher than QFED emissions. GFED has the lowest estimate, whereas FLAMBE is lower than QFED and GFAS is lower than FLAMBE. Overall, the QFED emissions are about 35% stronger than FLAMBE emissions, and about 60% stronger than those of GFED and GFAS. As can be seen from the scatter plots for this region (Figure D94) and the results from the linear regressions (Table 8), QFED is correlated very well with FLAMBE ($R^2 = 0.92$) and GFAS ($R^2 = 0.99$). The R^2 value between QFED and GFED is 0.75.

The fire season in the *Southeast Asia (SEAS)* region lasts from January to June. All datasets agree that the maximum of the emissions is in March. The GFED climatology differs from that of the other datasets, which have distinct unimodal temporal patterns, by having another mode in January. In this region the FLAMBE emissions are the largest, followed by those of the enhanced GFAS, QFED and GFAS. The emissions from GFED are the weakest. The regression analysis (Figure D95) resulted in QFED being about 2 times stronger than FLAMBE. QFED is about 4.5 and 2.8 times stronger than GFED and GFAS, respectively. The enhanced GFAS emissions are about 1.2 times higher than those of QFED. Temporally, QFED agrees best with GFAS ($R^2 = 1.0$) and FLAMBE ($R^2 = 0.99$). QFED is also well correlated with GFED ($R^2 = 0.7$). Based on the QFED time series, 2004, 2007 and 2010 were years with above average seasonal emissions.

The best agreement between the temporal variability of the fire emissions across the datasets is in the *Southern Hemisphere Africa (SHAF)* region (Figures 9 and D94). The fire emissions begin to rapidly increase in April, reach a maximum in July or August, start to decrease in September, and
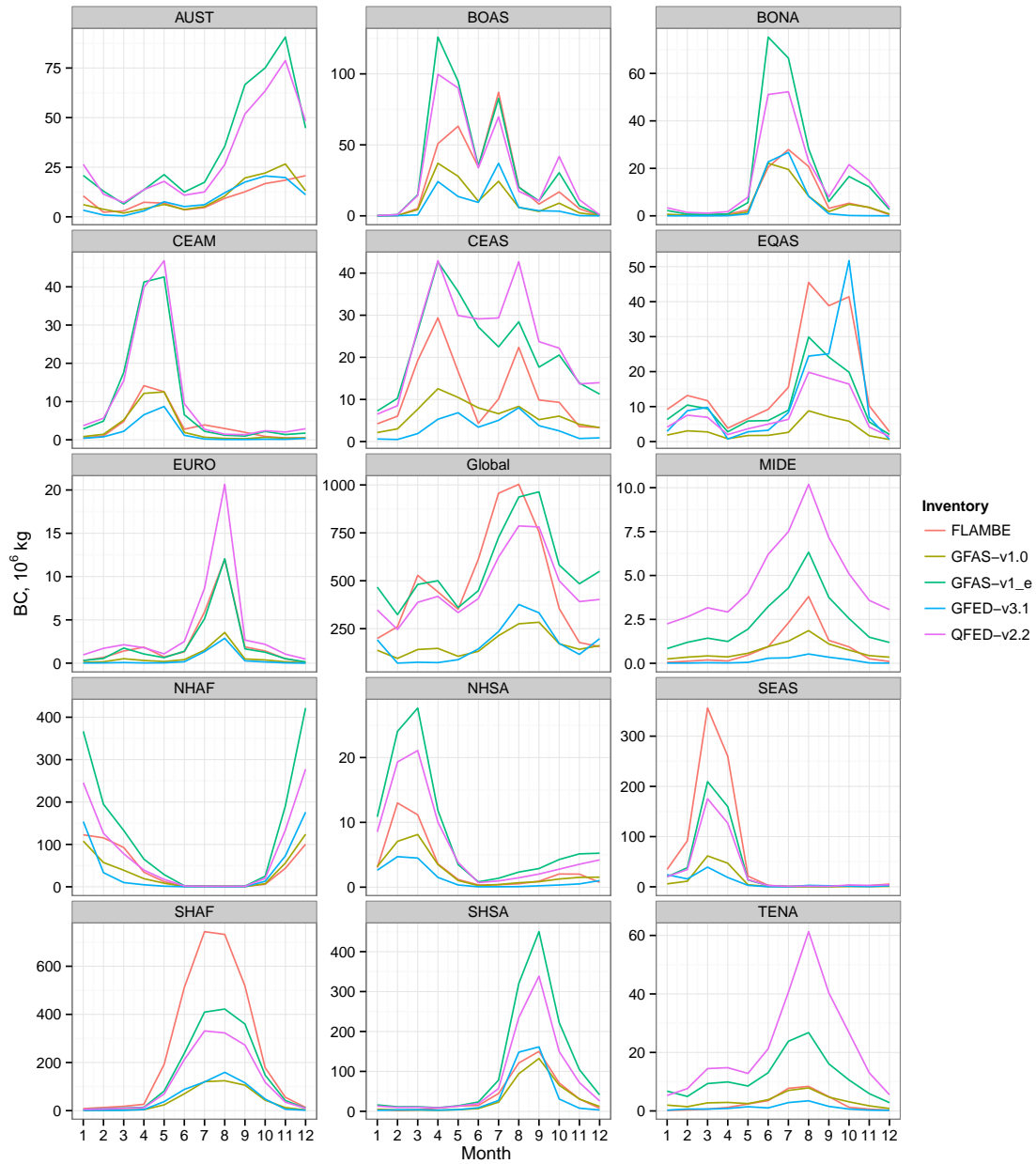
Figure 10: Monthly climatological emissions of black carbon (BC) from the QFED, GFED, GFAS and FLAMBE datasets. Monthly climatological emissions were created using data for years 2003–2008.

reach their minimum in December or January. In this region FLAMBE has the highest estimates, followed by the enhanced GFAS, QFED, GFED and GFAS. FLAMBE and the enhanced GFAS emissions are respectively about 2.2 and 1.2 times stronger than QFED emissions. GFED and GFAS estimates are about 40% and 23% of QFED values. QFED is very well correlated with the other datasets ($R^2 > 0.96$).

The fire emissions in the *Southern Hemisphere South America (SHSA)* have similar intra- and interannual variability across the datasets. In 2007 fires generated more emissions than the climatological mean and were followed by weaker than average fire seasons in 2008 and 2009 (Figure 9). In this region the enhanced GFAS has the maximum amplitude of fire emissions. The enhanced GFAS emissions are about 1.4 time stronger than QFED emissions; QFED estimates are about 1.1, 2.1, and 2.5 times higher, respectively, than FLAMBE, GFED and GFAS estimates (Figure D97). Similarities in the temporal patterns between QFED and GFAS are reflected by a very high R^2 value (0.99). QFED is also very well correlated with FLAMBE and GFED, with R^2 values respectively equal to 0.9 and 0.84.

In the *Temperate North America (TENA)* region QFED and GFAS have nonzero background emissions, which indicate that fires occur there throughout the year. Fire activity in DJF is more conservative in the FLAMBE and GFED datasets, with near zero emissions during this season. According to QFED and GFAS the emissions begin to increase in January and level out in March and April, decrease slightly in May, and then steadily increase until they reach maximum strength in August, followed by a gradual decline of fire activity in SON. QFED has the largest amplitude, followed by the enhanced GFAS, GFAS, FLAMBE and GFED. During the analyzed time period the fire seasons in 2003, 2006 and 2007 in particular were stronger than the climatological mean. The results of the regression analysis (Figure D98 and Table 8) show that QFED is well correlated with GFAS ($R^2 = 0.88$), but overall the QFED emissions are about 8.3 and 2.4 times stronger than those of GFAS and the enhanced GFAS, respectively. FLAMBE ($R^2 = 0.78$) and GFED ($R^2 = 0.7$) emissions need to be scaled up by factors 8.3 and 18.9, respectively, to match the magnitude of the QFED emissions.
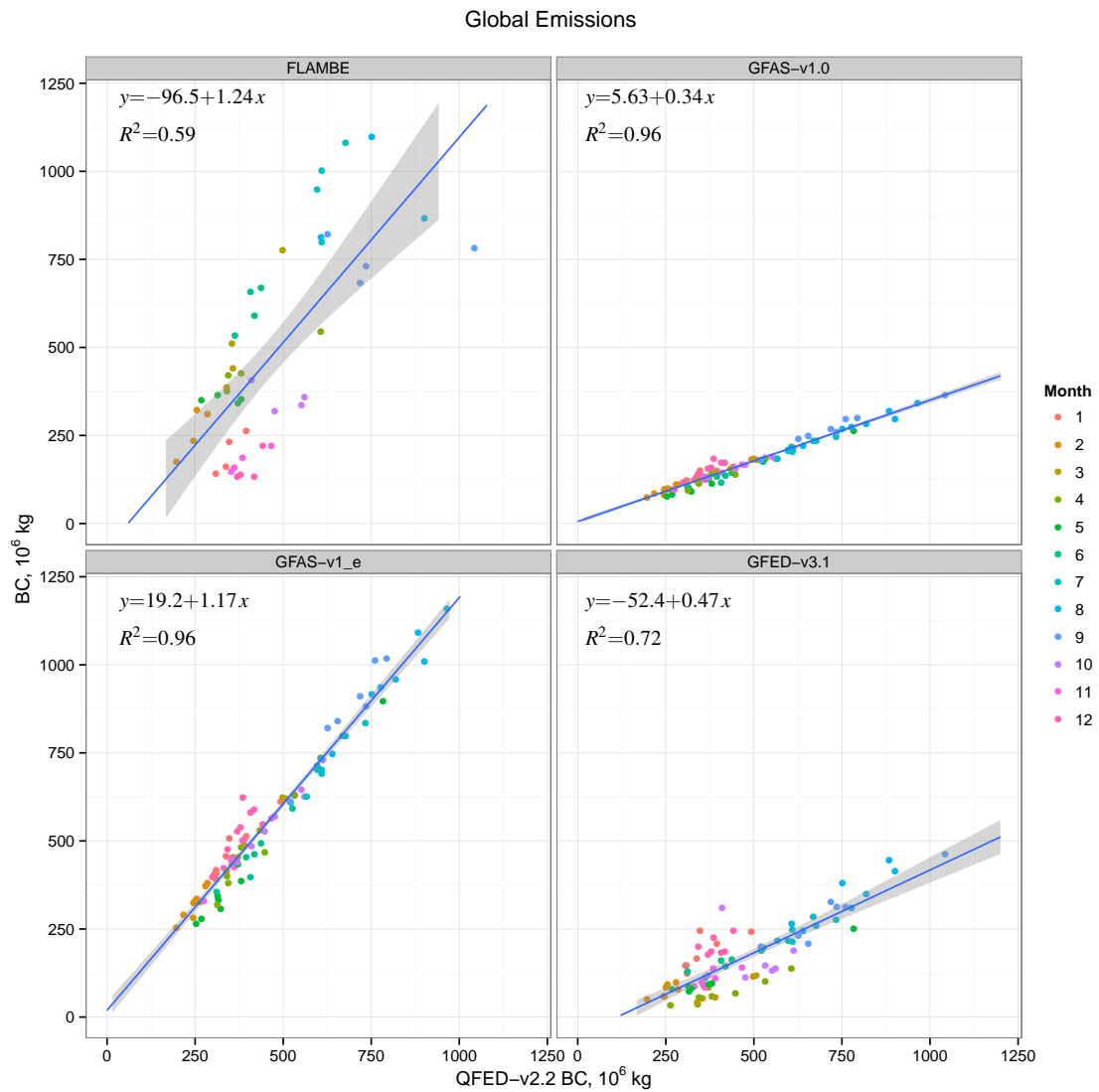
Figure 11: Scatter plots with regression lines of global monthly black carbon (BC) emissions from the FLAMBE, GFAS, GFED and QFED datasets.

Table 8: Regression analysis of global and regional fire emissions. The linear regression analysis was done with the dependent variable equal to the FLAMBE, GFAS or GFED emission estimates and the independent variable being the QFED emissions. The intercept coefficients are in units 10^6 kg-BC.

	Region	intercept	slope	R^2	intercept	slope	R^2
		FLAMBE			GFED		
	Global	-96.54	1.24	0.59	-52.36	0.47	0.72
AUST	Australia and New Zealand	1.75	0.26	0.65	1.31	0.27	0.84
BOAS	Boreal Asia	3.25	0.65	0.78	-1.28	0.32	0.83
BONA	Boreal North America	-1.73	0.56	0.81	-2.62	0.48	0.83
CEAM	Central America	0.59	0.29	0.85	-0.42	0.19	0.88
CEAS	Central Asia	-0.46	0.50	0.63	-1.07	0.18	0.72
EQAS	Equatorial Asia	-1.77	2.40	0.97	-6.48	2.03	0.64
EURO	Europe	0.14	0.57	0.89	-0.15	0.14	0.94
MIDE	Middle East	-1.30	0.45	0.86	-0.187	0.076	0.82
NHAF	N.H. Africa	9.99	0.44	0.71	-9.77	0.61	0.89
NHSA	N.H. South America	-1.02	0.65	0.92	-1.11	0.43	0.75
SEAS	Southeast Asia	-1.55	2.06	0.99	2.52	0.22	0.69
SHAF	S.H. Africa	-6.87	2.20	0.97	-1.18	0.42	0.96
SHSA	S.H. South America	3.45	0.45	0.90	-8.12	0.47	0.84
TENA	Temperate North America	-0.11	0.12	0.78	-0.062	0.053	0.70
		GFAS			enhanced GFAS		
	Global	5.63	0.34	0.96	19.19	1.17	0.96
AUST	Australia and New Zealand	0.81	0.29	0.87	2.76	1.00	0.87
BOAS	Boreal Asia	-0.89	0.36	0.96	-3.03	1.21	0.96
BONA	Boreal North America	-0.86	0.39	0.93	-2.94	1.32	0.93
CEAM	Central America	-0.18	0.29	0.98	-0.61	0.98	0.98
CEAS	Central Asia	0.29	0.26	0.81	0.99	0.88	0.81
EQAS	Equatorial Asia	0.16	0.38	0.97	0.54	1.29	0.97
EURO	Europe	-0.029	0.18	0.96	-0.098	0.627	0.96
MIDE	Middle East	-0.21	0.20	0.95	-0.72	0.69	0.95
NHAF	N.H. Africa	0.29	0.44	0.99	0.98	1.51	0.99
NHSA	N.H. South America	0.044	0.38	0.99	0.15	1.29	0.99
SEAS	Southeast Asia	-0.42	0.36	1.00	-1.4	1.2	1.0
SHAF	S.H. Africa	-0.89	0.36	0.99	-3.04	1.23	0.99
SHSA	S.H. South America	0.39	0.40	0.99	1.32	1.37	0.99
TENA	Temperate North America	0.54	0.12	0.88	1.84	0.42	0.88

References

Akagi, S. K., Yokelson, R. J., Wiedinmyer, C., Alvarado, M. J., Reid, J. S., Karl, T., Crounse, J. D., and Wennberg, P. O.: Emission factors for open and domestic biomass burning for use in atmospheric models, Atmos. Chem. Phys., 11, doi:10.5194/acp-11-4039-2011, 2011.

Andreae, M. O. and Merlet, P.: Emission from trace gases and aerosols from biomass burning, Global Biogeochemical Cycles, 15, 955–966, 2001.

Ellicott, E., Vermote, E., Giglio, L., and Roberts, G.: Estimating biomass consumed from fire using MODIS FRE, Geophysical Research Letters, 36, doi:10.1029/2009GL038581, 113401, 2009.

Giglio, L.: MODIS Collection 5 Active Fire Product User's Guide Version 2.4, Science Systems and Applications, Inc., University of Maryland, Department of Geography, 2010.

Giglio, L., van der Werf, G. R., Randerson, J. T., Collatz, G. J., and Kasibhatla, P.: Global estimation of burned area using MODIS active fire observations, Atmos. Chem. Phys., 6, doi: 10.5194/acp-6-957-2006, 2006.

Ichoku, C., Giglio, L., Wooster, M. J., and Remer, L. A.: Global characterization of biomass-burning patterns using satellite measurements of fire radiative energy, Remote Sensing of Environment, 112, doi:10.1016/j.rse.2008.02.009, 2008.

Kaiser, J. W., Flemming, J., Schultz, M. G., Suttie, M., and Wooster, M. J.: The MACC Global Fire Assimilation System: First Emission Products (GFASv0), ECMWF Tech. Memo., 596, 2009.

Kaiser, J. W., Heil, A., Andreae, M. O., Benedetti, A., Chubarova, N., Jones, L., Morcrette, J.-J., Razinger, M., Schultz, M. G., Suttie, M., and van der Werf, G. R.: Biomass burning emissions estimated with a global fire assimilation system based on observed fire radiative power, Biogeosciences, doi:10.5194/bg-9-527-2012, 2012.

Kaufman, Y. J., Remer, L., Ottmar, R., Ward, D., Li, R.-R., Kleidman, R., Fraser, R. S., Flynn, L., McDougal, D., and Shelton, G.: Relationship between remotely sensed fire intensity and rate of emission of smoke: SCAR-C experiment, Global biomass burning, pp. 685–696, 1996.

Reid, J., Hyer, E. J., Prins, E. M., Westphal, D. L., Zhang, J., Wang, J., Christopher, S. A., Curtis, C. A., Schmidt, C. C., Eleuterio, D. P., Richardson, K. A., and Hoffman, J. P.: Global monitoring and forecasting of biomass-burning smoke: Description of and lessons from the Fire Locating and Modeling of Burning Emissions (FLAMBE) program,, Selected Topics in Applied Earth Observations and Remote Sensing, IEEE Journal of, 2, doi:10.1109/JSTARS.2009.2027443, 2009.

Schroeder, W., Csiszar, I., Giglio, L., and Schmidt, C. C.: On the use of fire radiative power, area, and temperature estimates to characterize biomass burning via moderate to coarse spatial resolution remote sensing data in the Brazilian Amazon, Journal of Geophysical Research: Atmospheres, 115, doi:10.1029/2009JD013769, d21121, 2010.

van der Werf, G. R., Randerson, J. T., Giglio, L., Collatz, G. J., Kasibhatla, P. S., and Arellano, Jr., A. F.: Interannual variability in global biomass burning emissions from 1997 to 2004, Atmos. Chem. Phys., 6, doi:10.5194/acp-6-3423-2006, 2006.

van der Werf, G. R., Randerson, J. T., Giglio, L., Collatz, G. J., Mu, M., Kasibhatla, P. S., Morton, D. C., DeFries, R. S., Jin, Y., and van Leeuwen, T. T.: Global fire emissions and the contribution

of deforestation, savanna, forest, agricultural, and peat fires (1997–2009), Atmos. Chem. Phys., 10, doi:10.5194/acp-10-11707-2010, 2010.

van Leeuwen, T. T. and van der Werf, G. R.: Spatial and temporal variability in the ratio of trace gases emitted from biomass burning, Atmos. Chem. Phys., 11, doi:10.5194/acp-11-3611-2011, 2011.

Whitburn, S., Damme, M. V., Kaiser, J., van der Werf, G., Turquety, S., Hurtmans, D., Clarisse, L., Clerbaux, C., and Coheur, P.-F.: Ammonia emissions in tropical biomass burning regions: Comparison between satellite-derived emissions and bottom-up fire inventories, Atmospheric Environment, pp. –, doi:http://dx.doi.org/10.1016/j.atmosenv.2015.03.015, 2015.

Wooster, M. J.: Small-scale experimental testing of fire radiative energy for quantifying mass combusted in natural vegetation fires, Geophys. Res. Lett., 29, doi:10.1029/2002GL015487, 2002.

Wooster, M. J. and Zhang, Y. H.: Boreal forest fires burn less intensely in Russia than in North America, Geophys. Res. Lett., 31, L20505, doi:10.1029/2004GL020805, 2004.

Wooster, M. J., Roberts, G., Perry, G. L. W., and Kaufman, Y. J.: Retrieval of biomass combustion rates and totals from fire radiative power observations: FRP derivation and calibration relationships between biomass consumption and fire radiative energy release, J. Geophys. Res., 110, doi:10.1029/2005JD006318, 2005.

Zhang, X., Kondragunta, S., Ram, J., Schmidt, C., and Huang, H.-C.: Near-real-time global biomass burning emissions product from geostationary satellite constellation, Journal of Geophysical Research: Atmospheres, 117, doi:10.1029/2012JD017459, d14201, 2012.

Zhang, X., Kondragunta, S., and Roy, D. P.: Interannual variation in biomass burning and fire seasonality derived from geostationary satellite data across the contiguous United States from 1995 to 2011, Journal of Geophysical Research: Biogeosciences, 119, 1147–1162, doi:10.1002/2013JG002518, 2013JG002518, 2014.

Appendix A. Acronyms

AOT   aerosol optical thickness

CDF   cumulative distribution function

FLAMBE Fire Locating and Modeling of Burning Emissions

FRE   fire radiative energy

FRP   fire radiative power

GEOS   Goddard Earth Observing System Model

GFAS   Global Fire Assimilation System

GFED   Global Fire Emissions Database

GMAO   Global Modeling and Assimilation Office

IGBP   International Geosphere-Biosphere Programme

IR   infrared

MACC   Monitoring Atmospheric Composition and Change

MODIS   MODerate Resolution Imaging Spectroradiometer

PDF   probability density function

QFED   Quick Fire Emissions Dataset

Appendix B. Regional diagnostics of GEOS-5 AOT over land

North America - Alaska
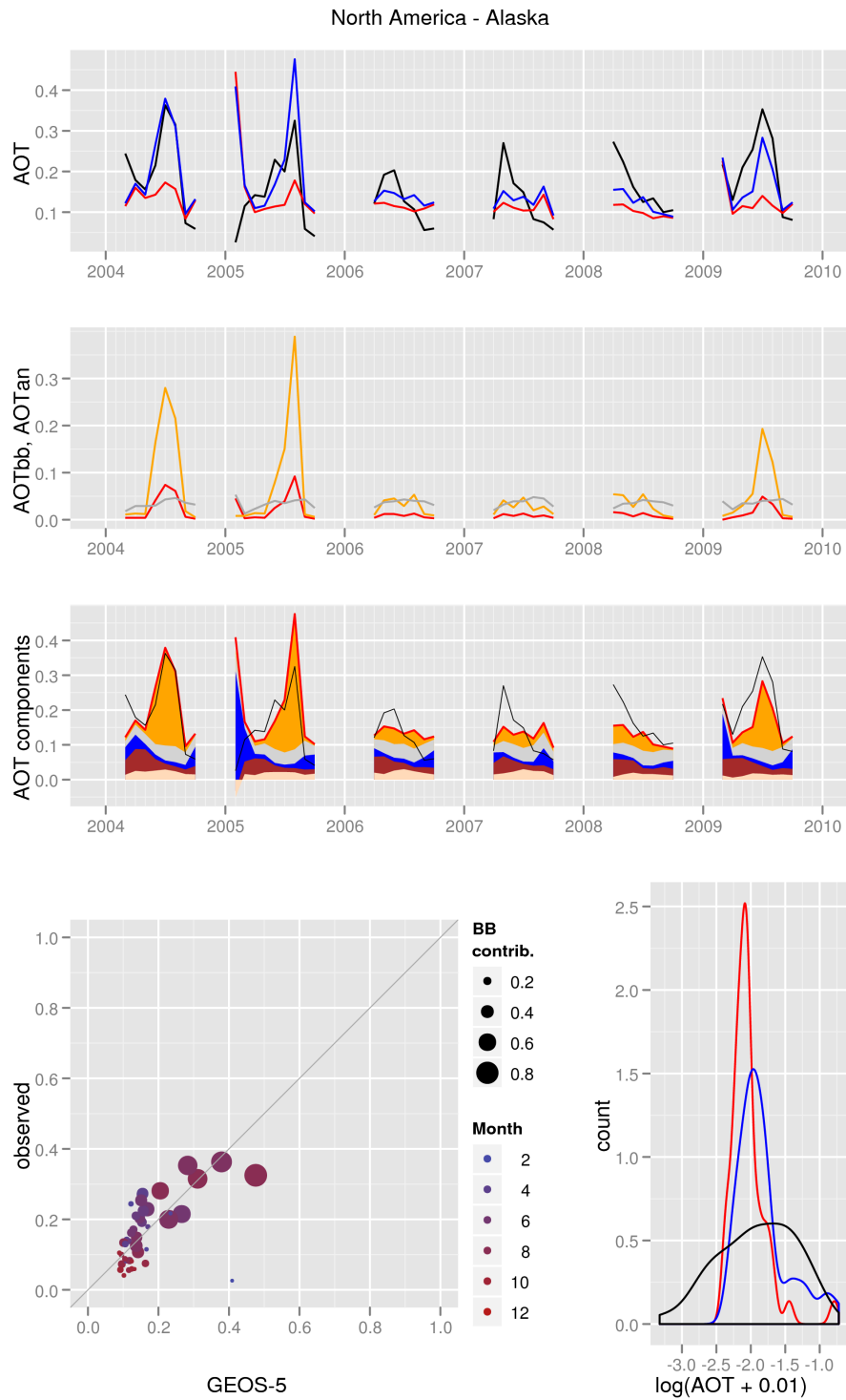
(a) GEOS-5 and NNR-AOT/Aqua

Figure B12: AOT diagnostics for the Alaska region. See the discussion surrounding Figure 5 for explanation.

North America - Alaska

(b) GEOS-5 and NNR-AOT/Terra

41
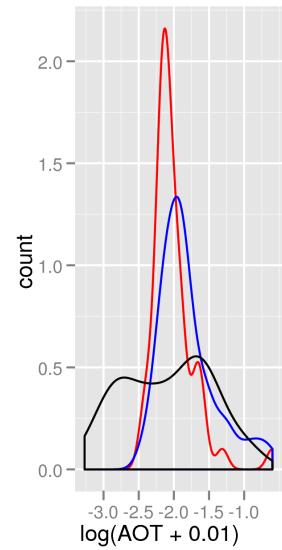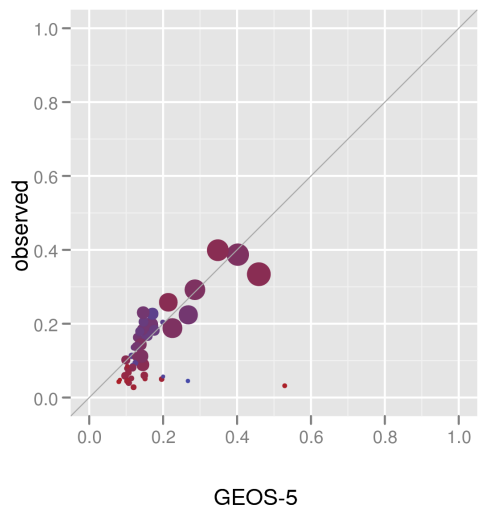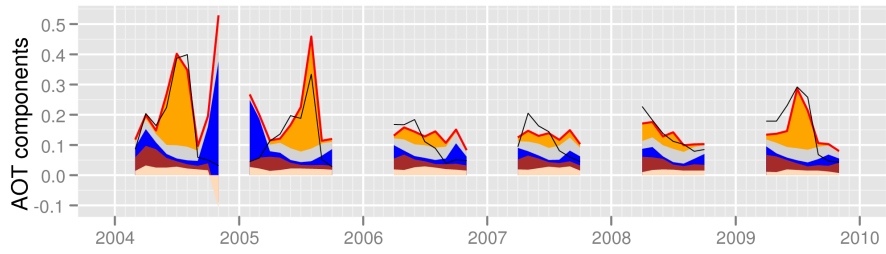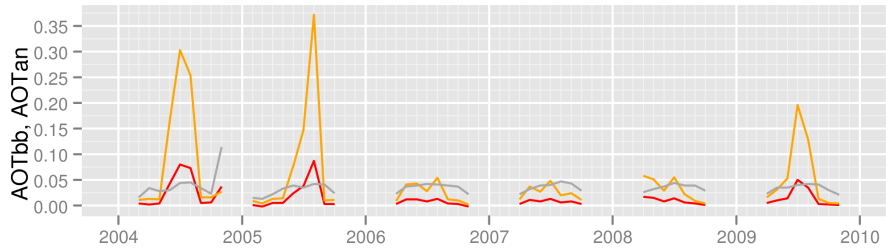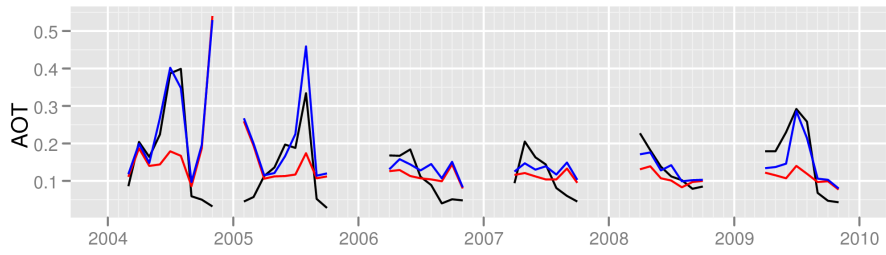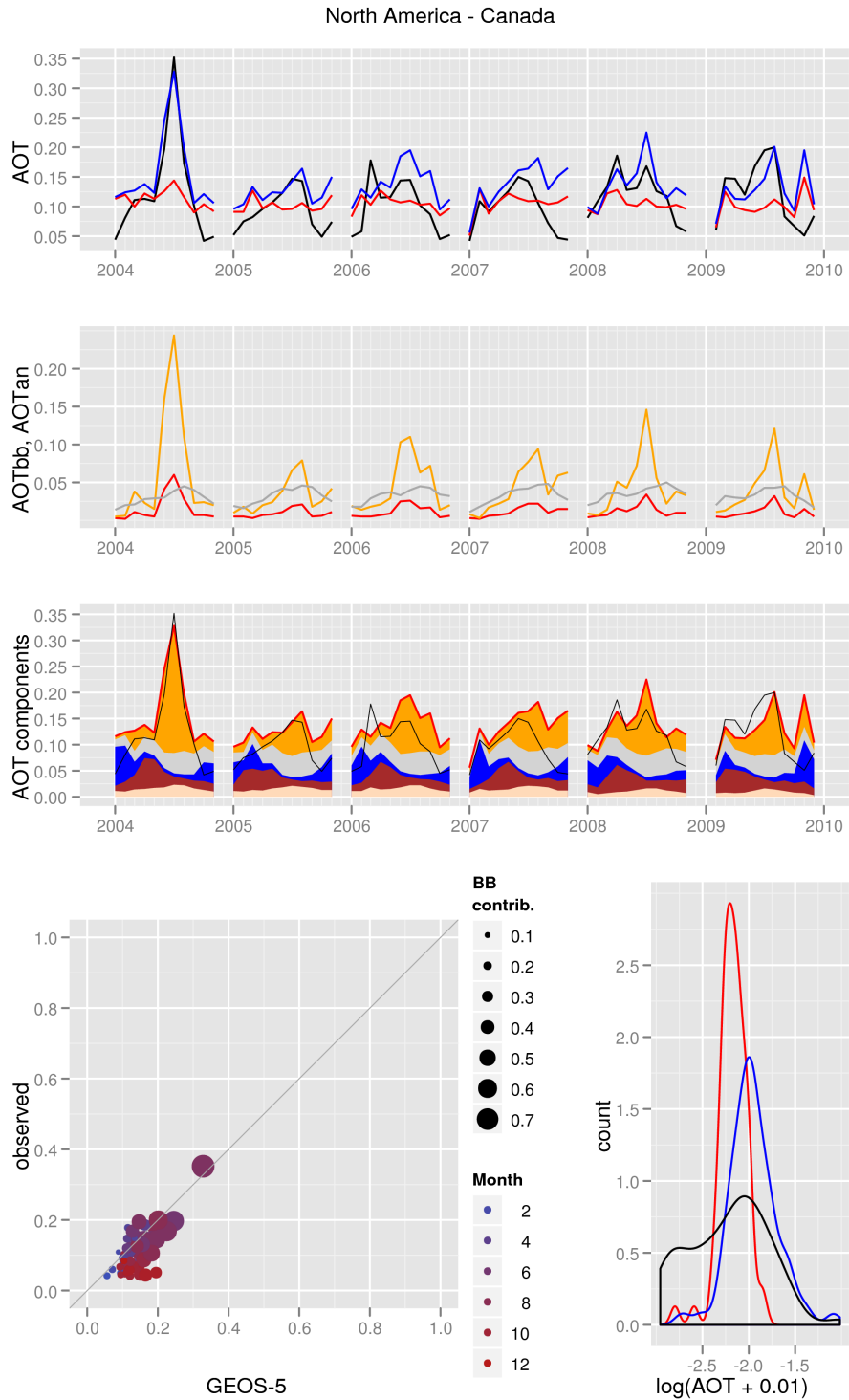
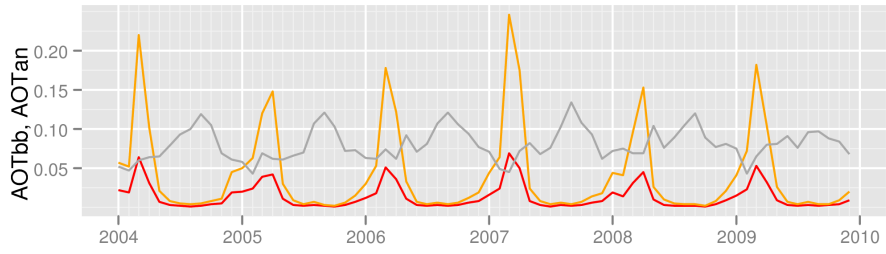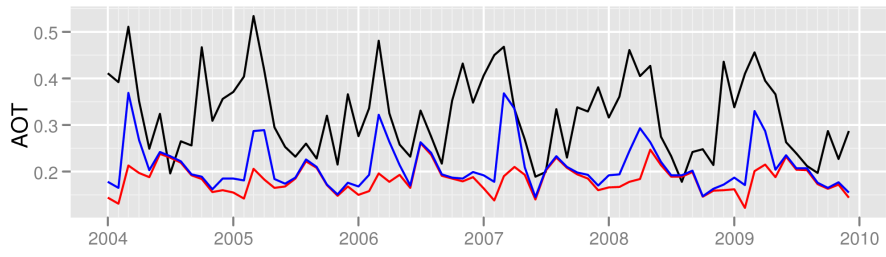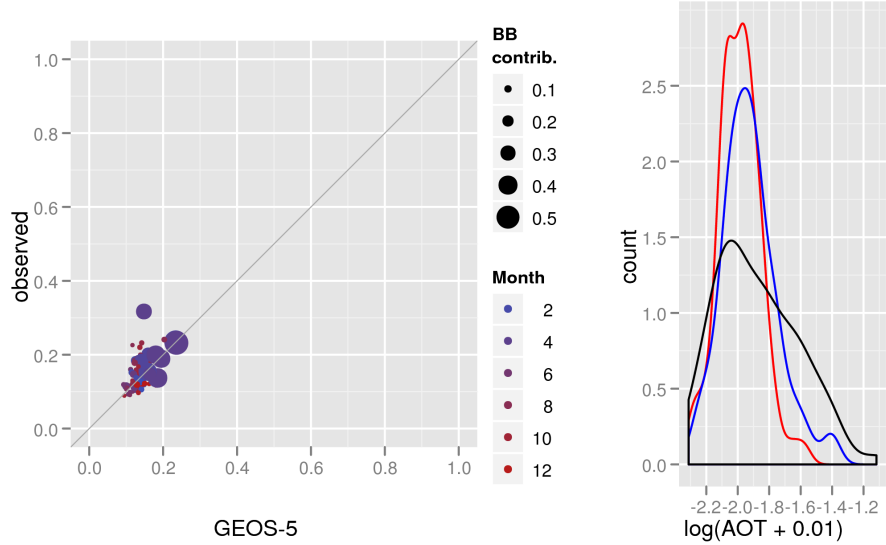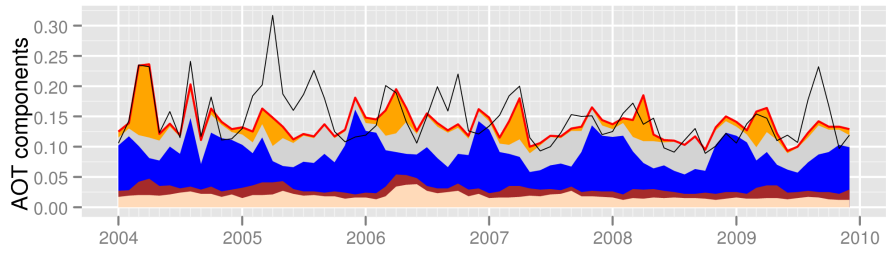(a) GEOS-5 and NNR-AOT/Aqua

Figure B13: AOT diagnostics for the Canada region.

North America - Canada

(b) GEOS-5 and NNR-AOT/Terra
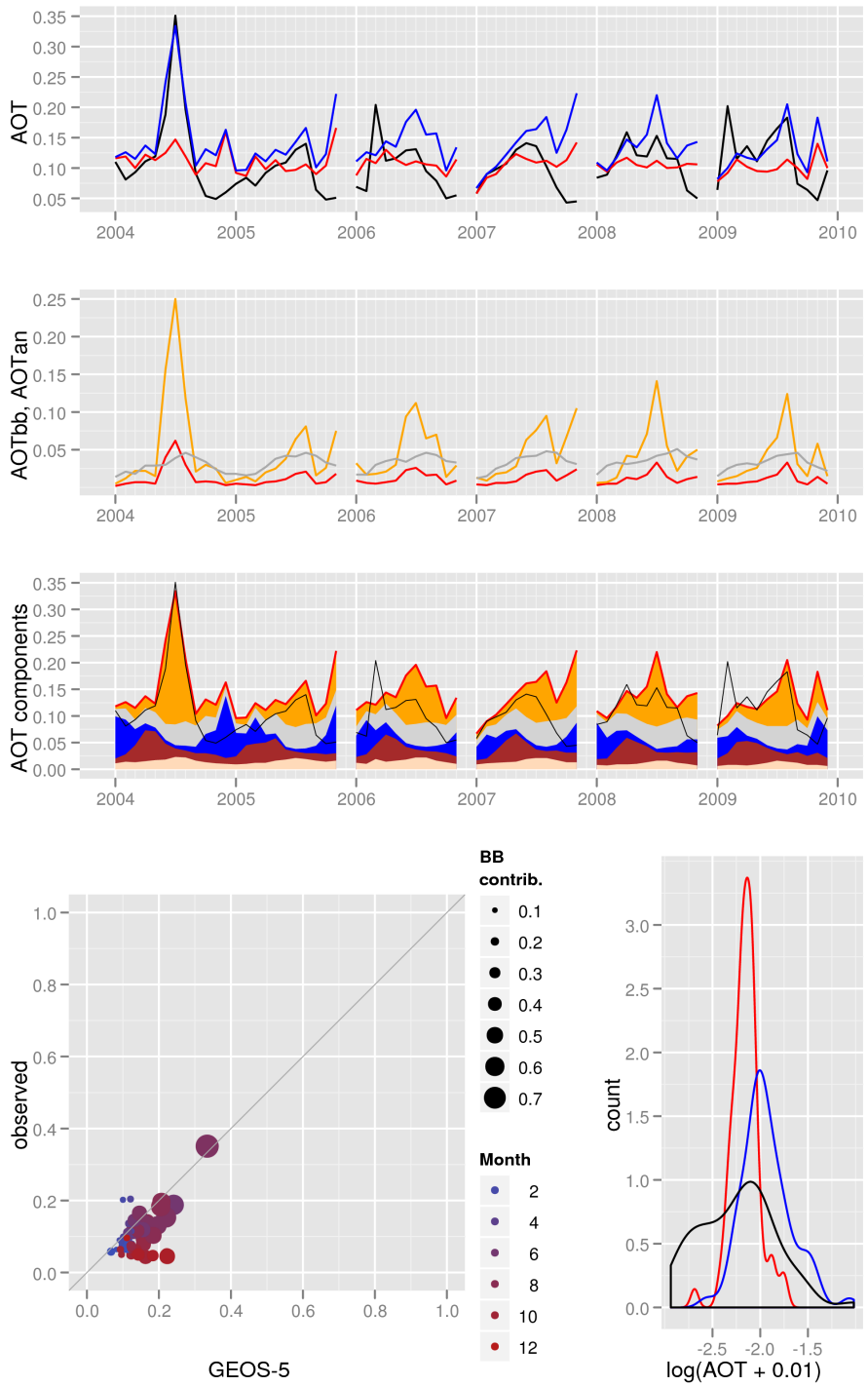
North America - Quebec
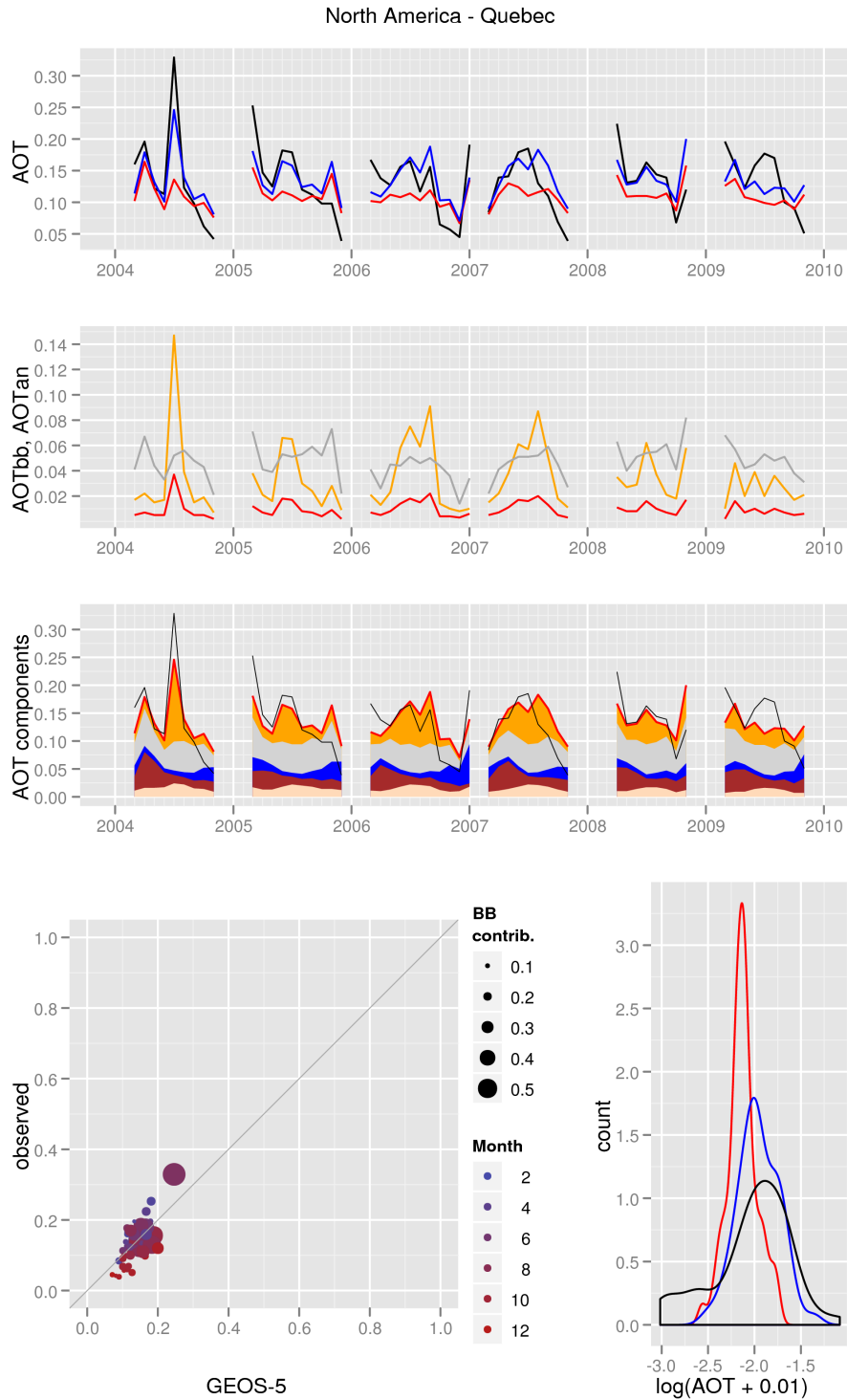
(a) GEOS-5 and NNR-AOT/Aqua

Figure B14: AOT diagnostics for the Quebec region.

North America - Quebec

(b) GEOS-5 and NNR-AOT/Terra

North America - USA(West)
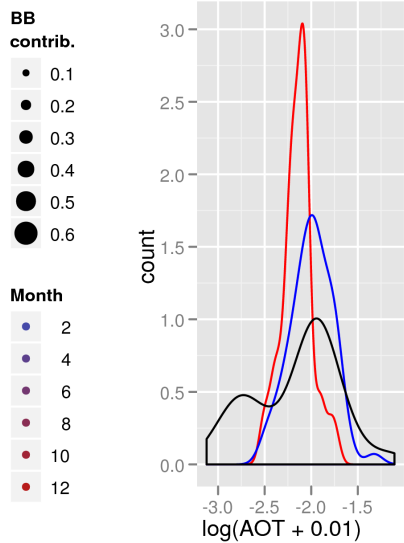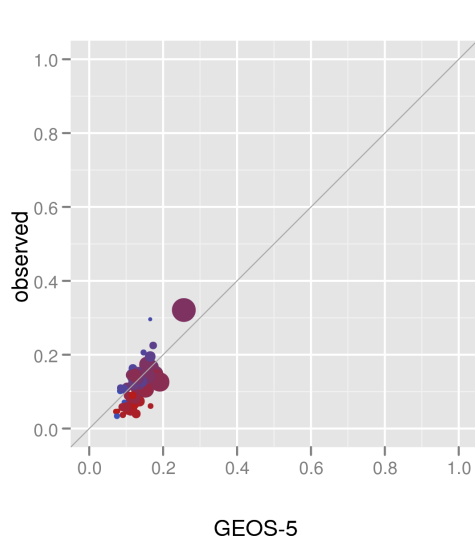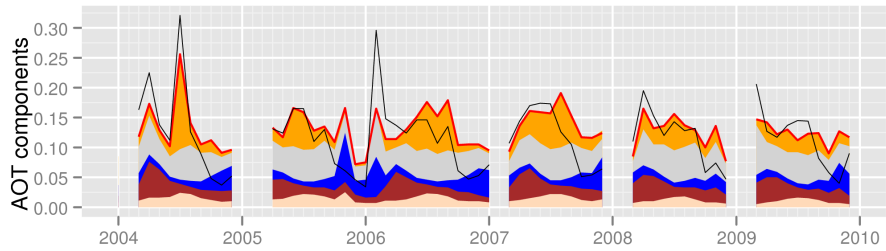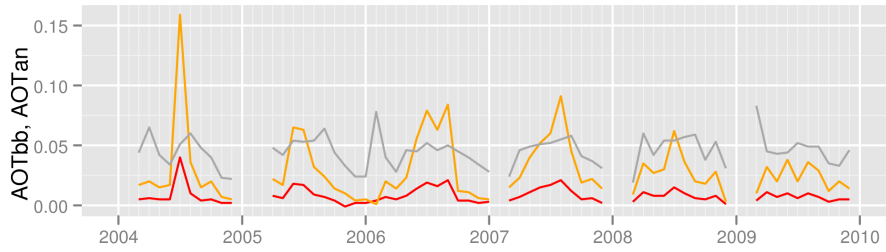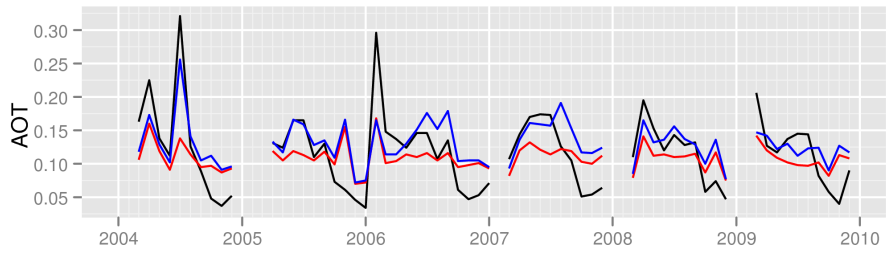
(a) GEOS-5 and NNR-AOT/Aqua
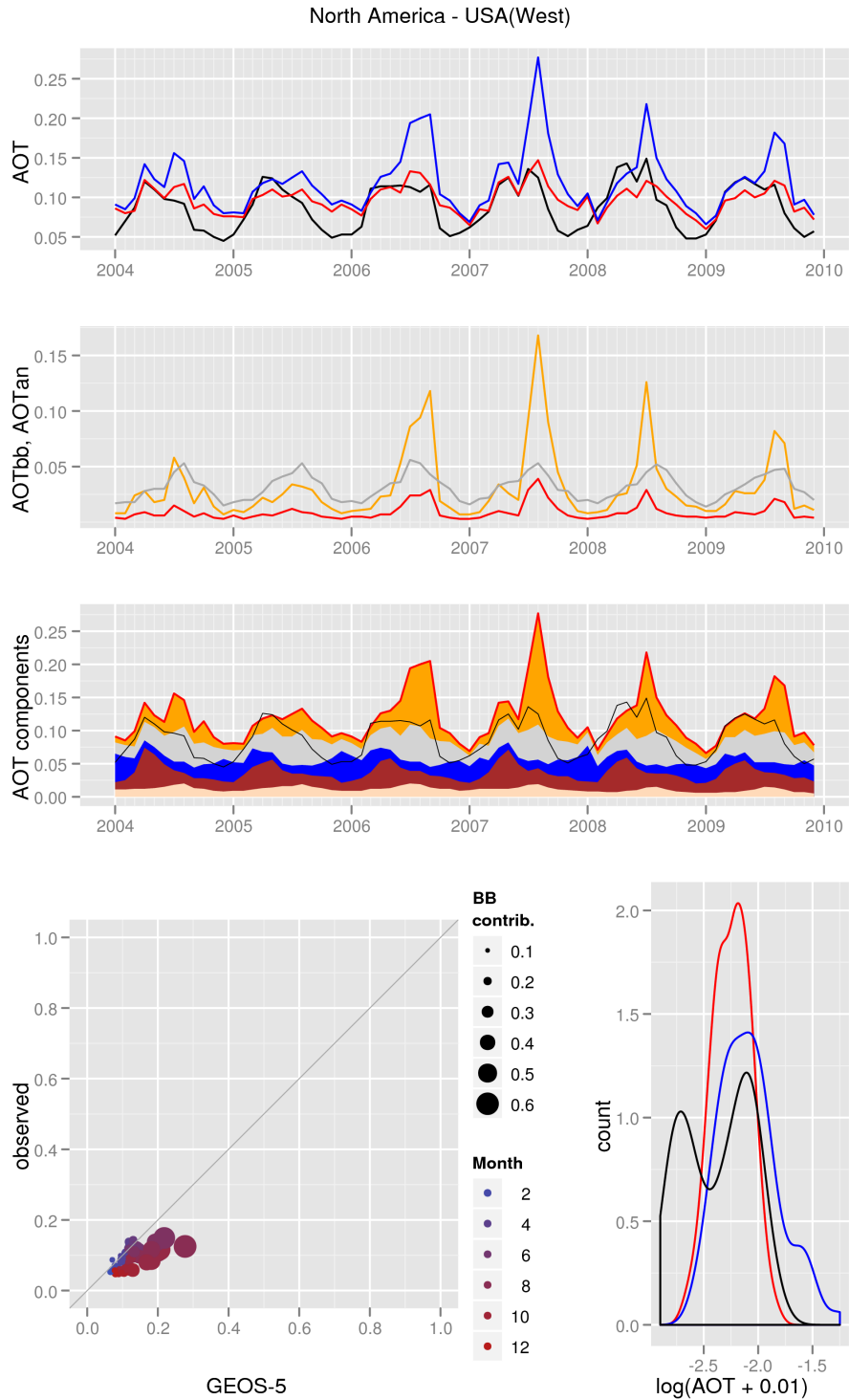
Figure B15: AOT diagnostics for the US West region.

46

North America - USA(West)
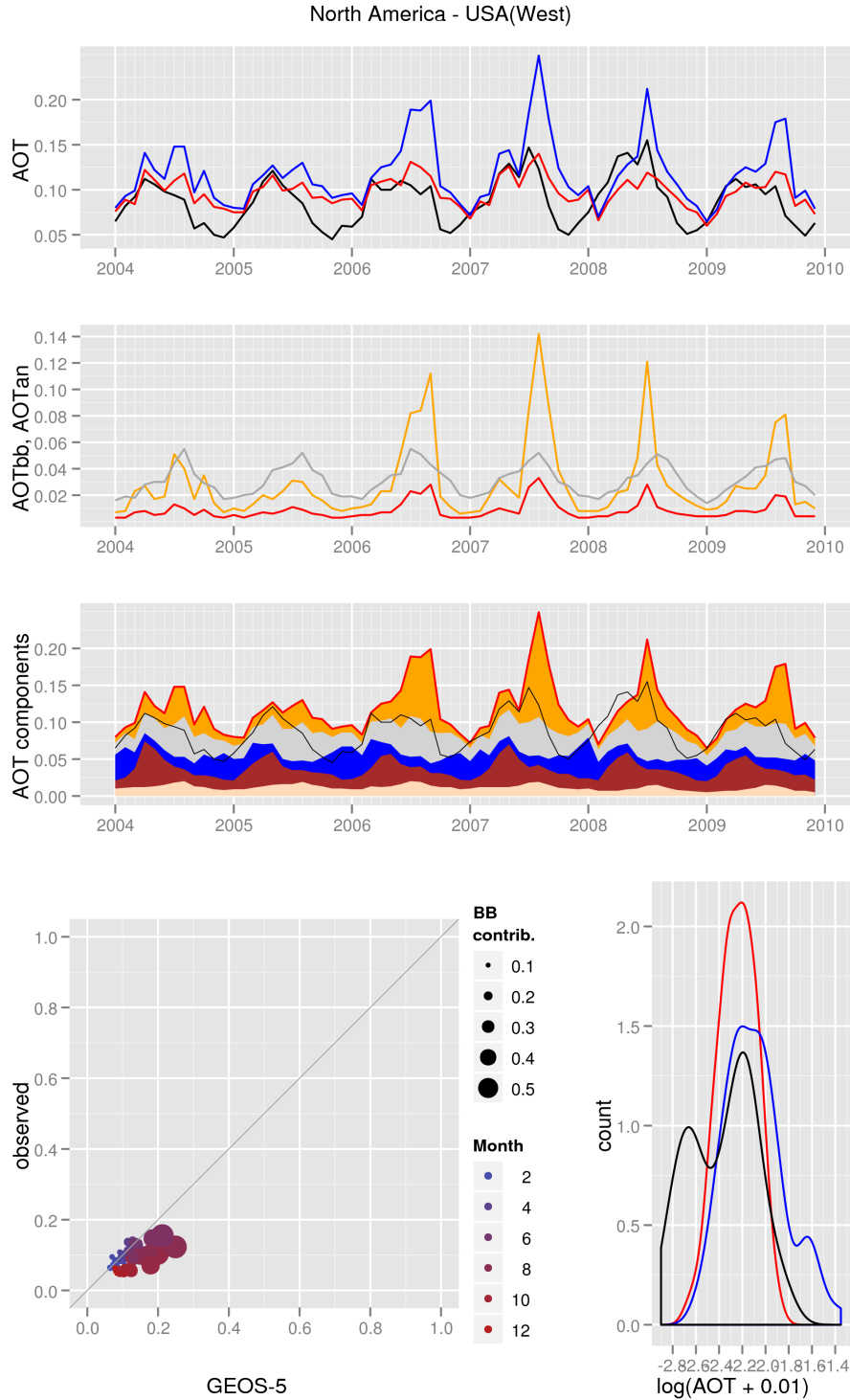
(b) GEOS-5 and NNR-AOT/Terra
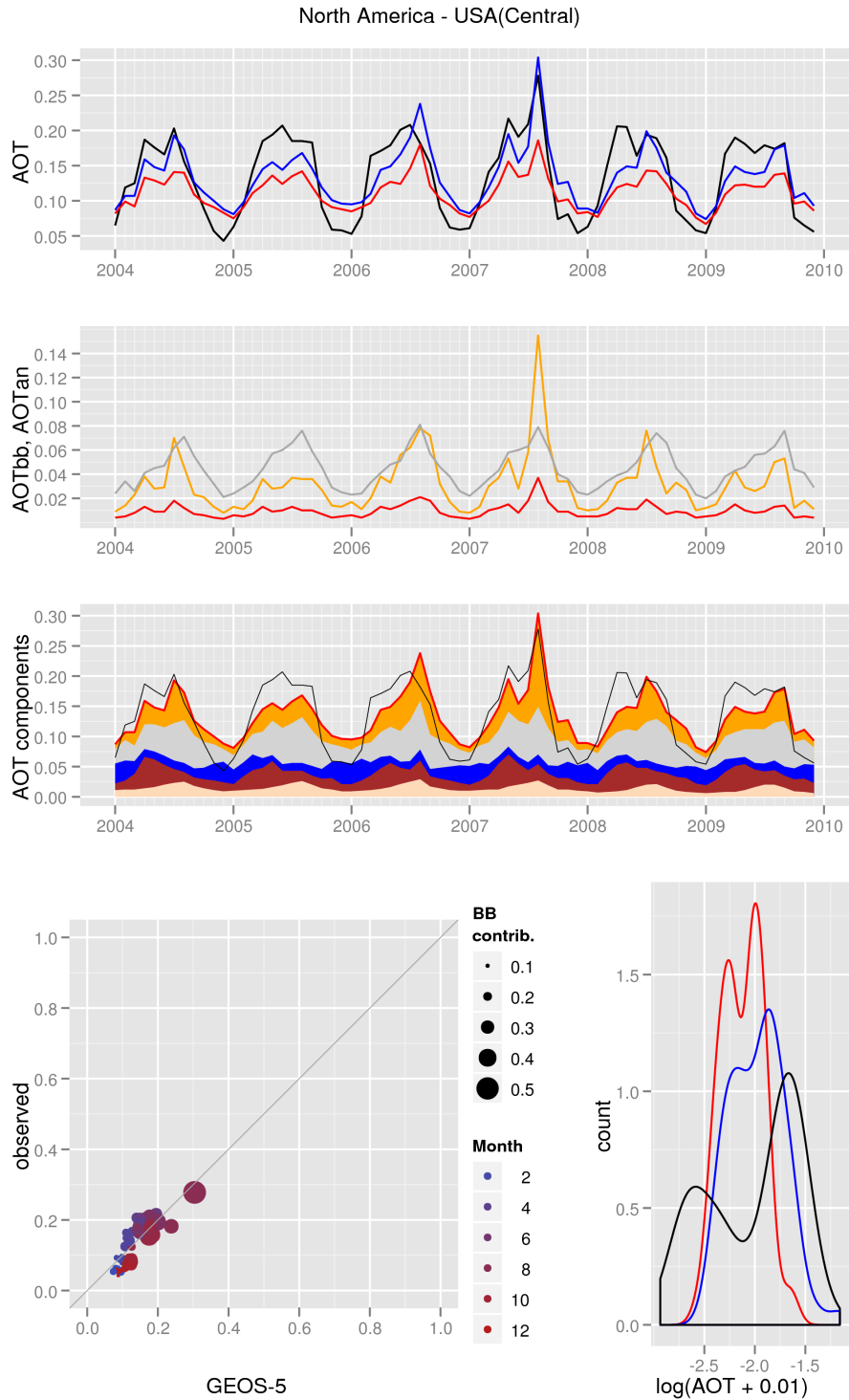
(a) GEOS-5 and NNR-AOT/Aqua

Figure B16: AOT diagnostics for the US Central region.

North America - USA(Central)

(b) GEOS-5 and NNR-AOT/Terra

49

North America - USA(East)

(a) GEOS-5 and NNR-AOT/Aqua

Figure B17: AOT diagnostics for the US East region.

North America - USA(East)

(b) GEOS-5 and NNR-AOT/Terra

(a) GEOS-5 and NNR-AOT/Aqua

Figure B18: AOT diagnostics for the Mexico region.

South America - Mexico

(b) GEOS-5 and NNR-AOT/Terra

53
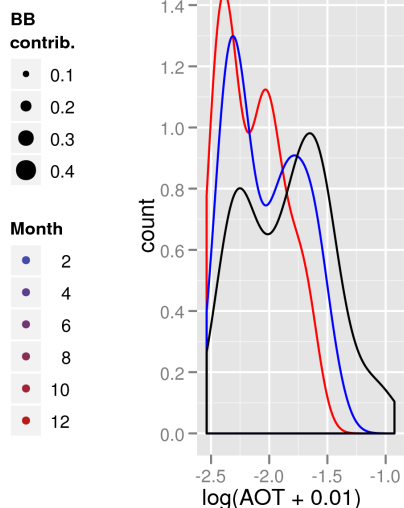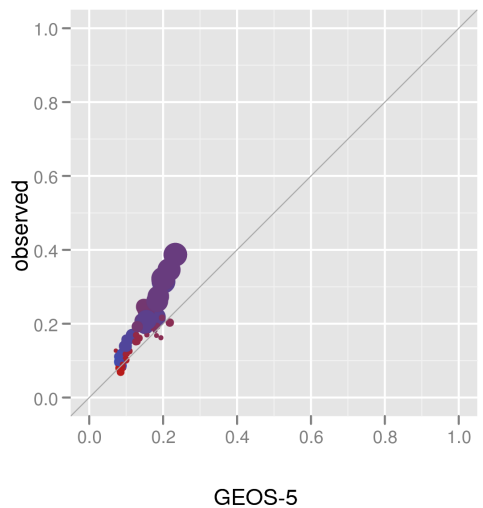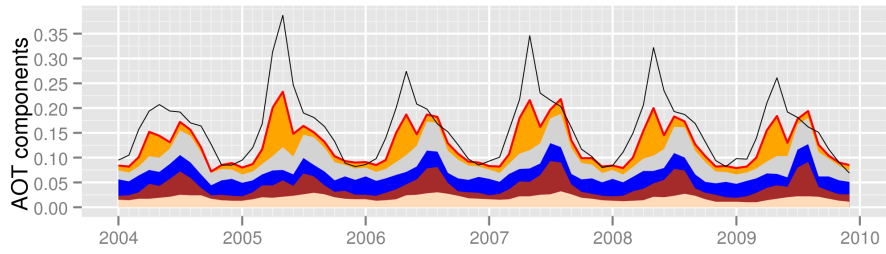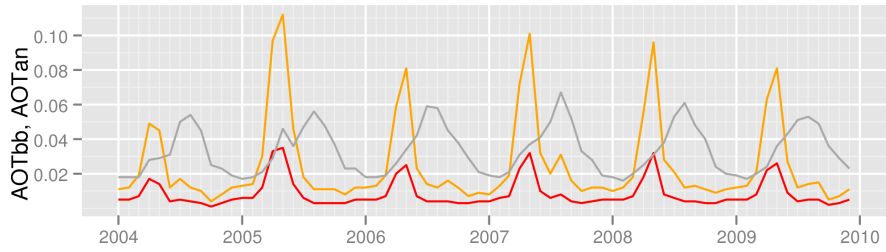
South America - Brazil(Forest)
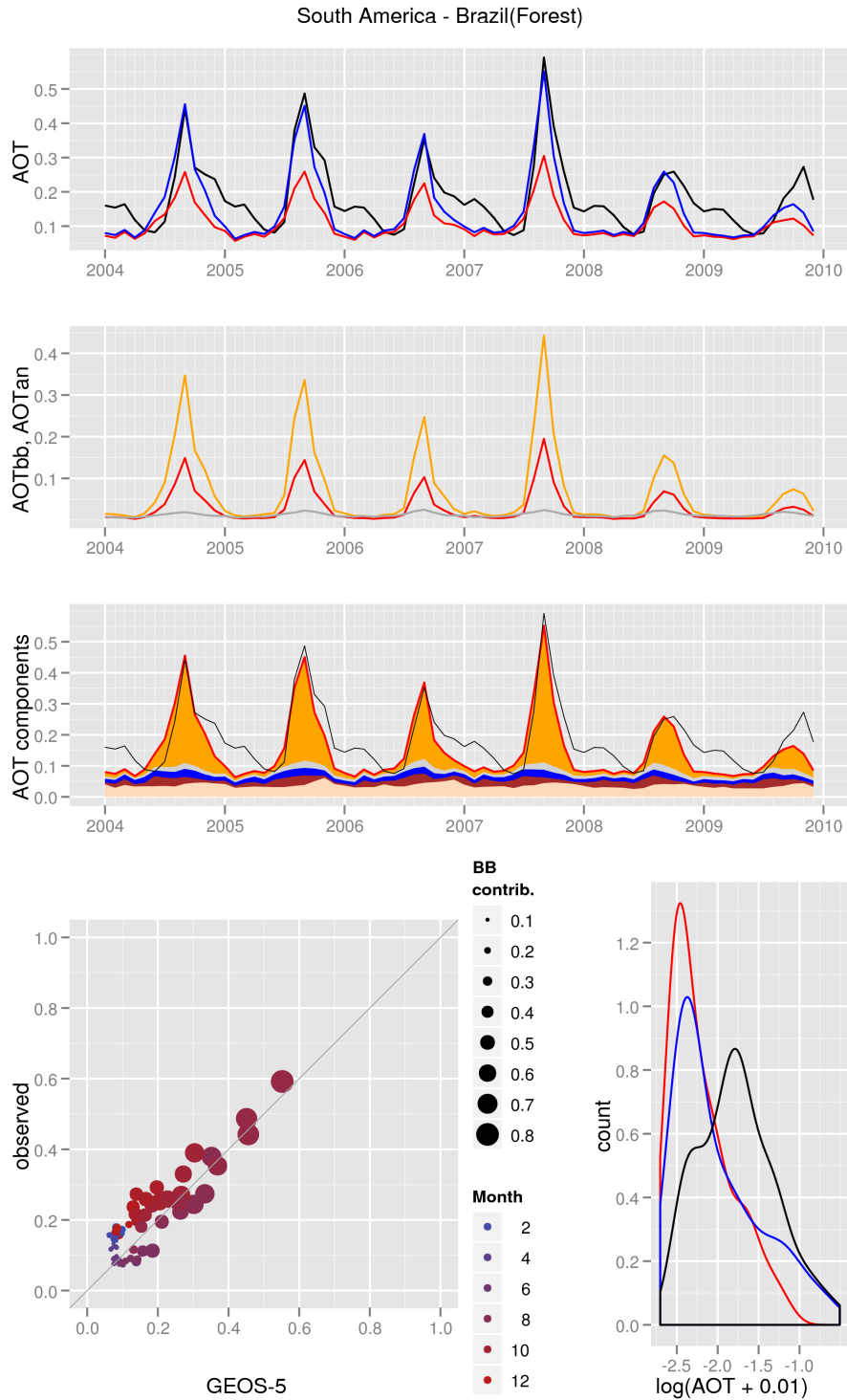
(a) GEOS-5 and NNR-AOT/Aqua

Figure B19: AOT diagnostics for the Brazil-Forest region.

South America - Brazil(Forest)
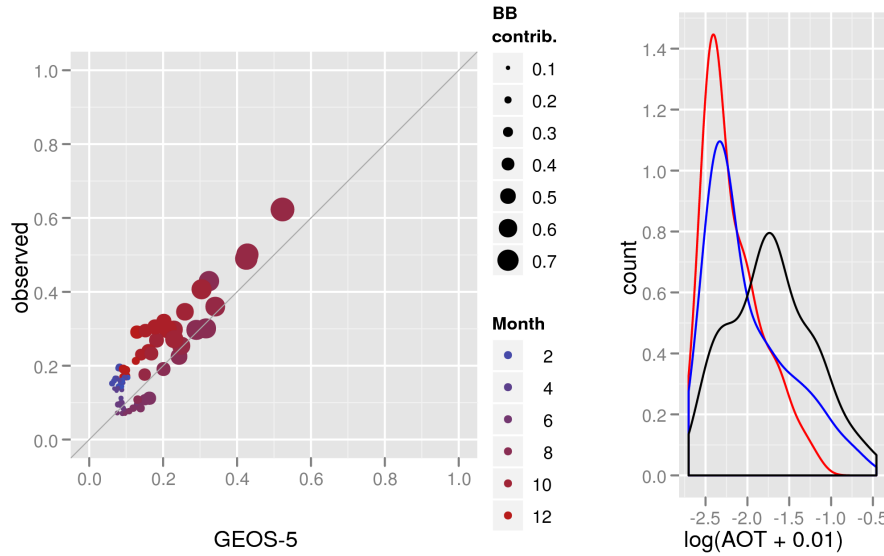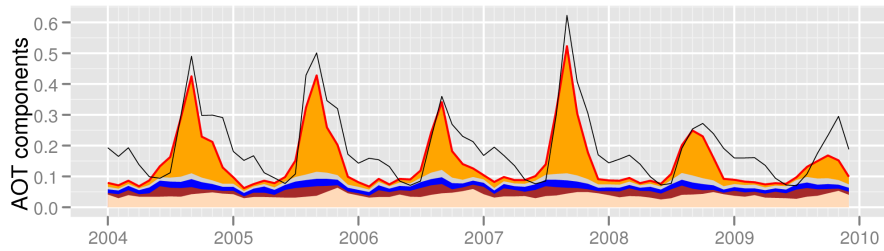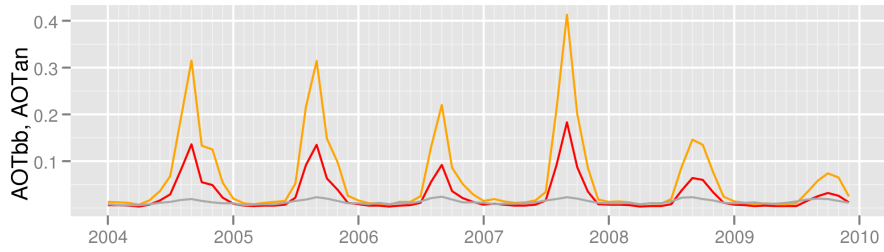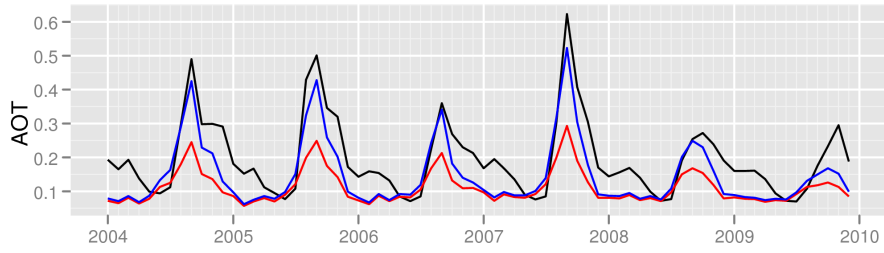
(b) GEOS-5 and NNR-AOT/Terra
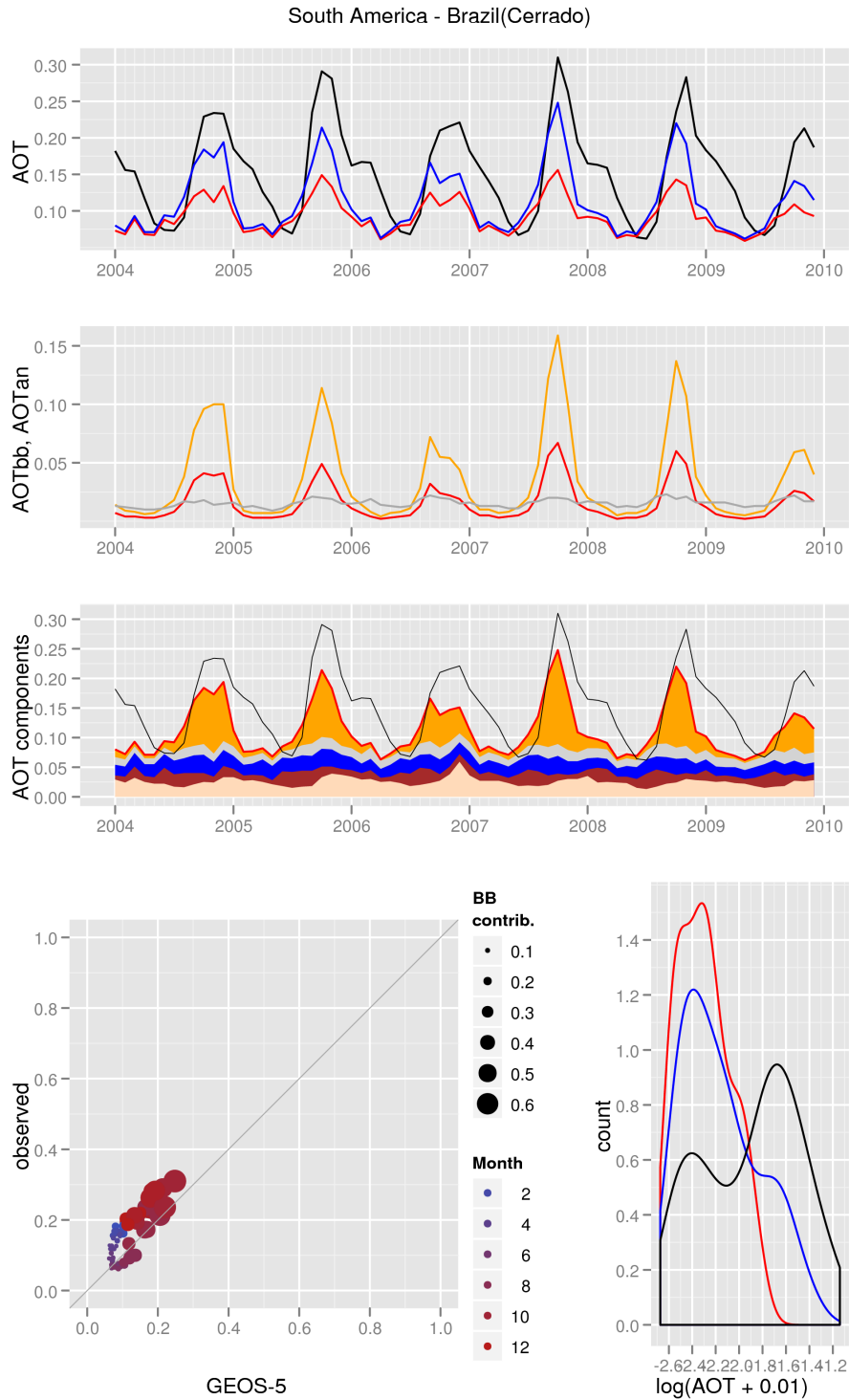
(a) GEOS-5 and NNR-AOT/Aqua

Figure B20: AOT diagnostics for the Brazil-Cerrado region.
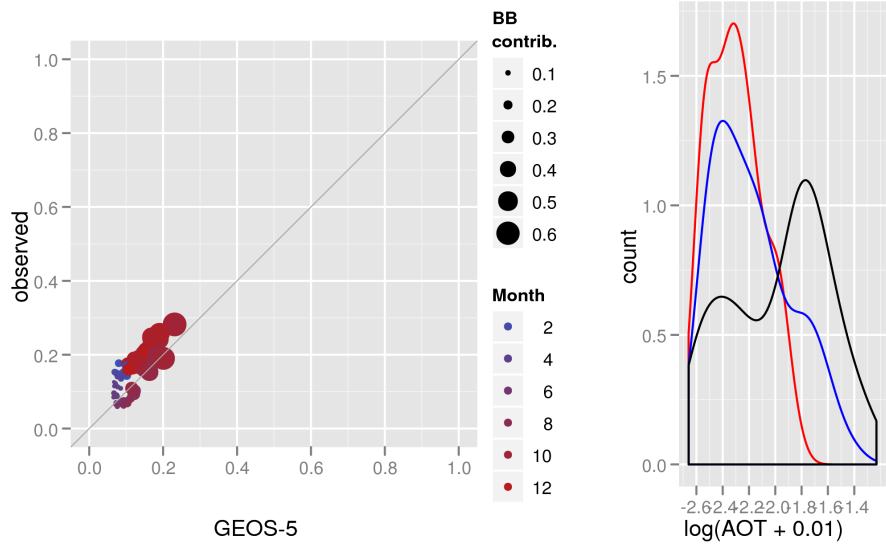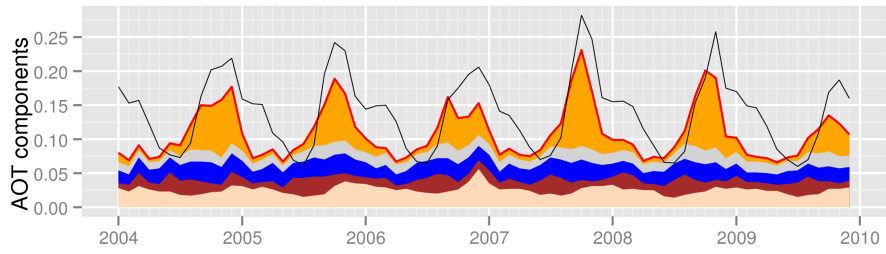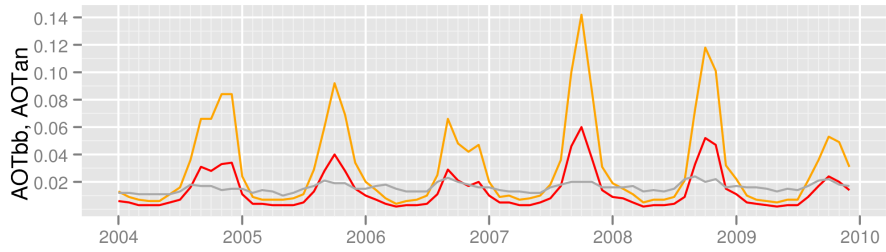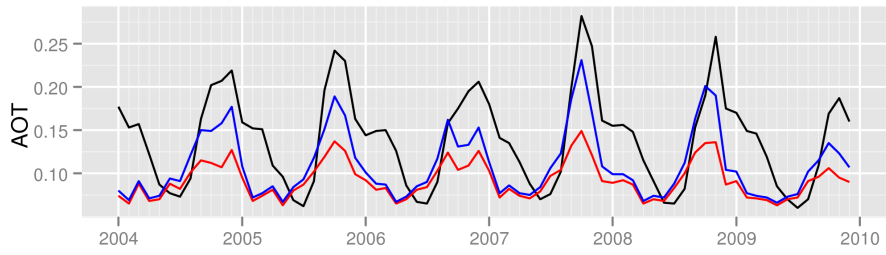
(b) GEOS-5 and NNR-AOT/Terra
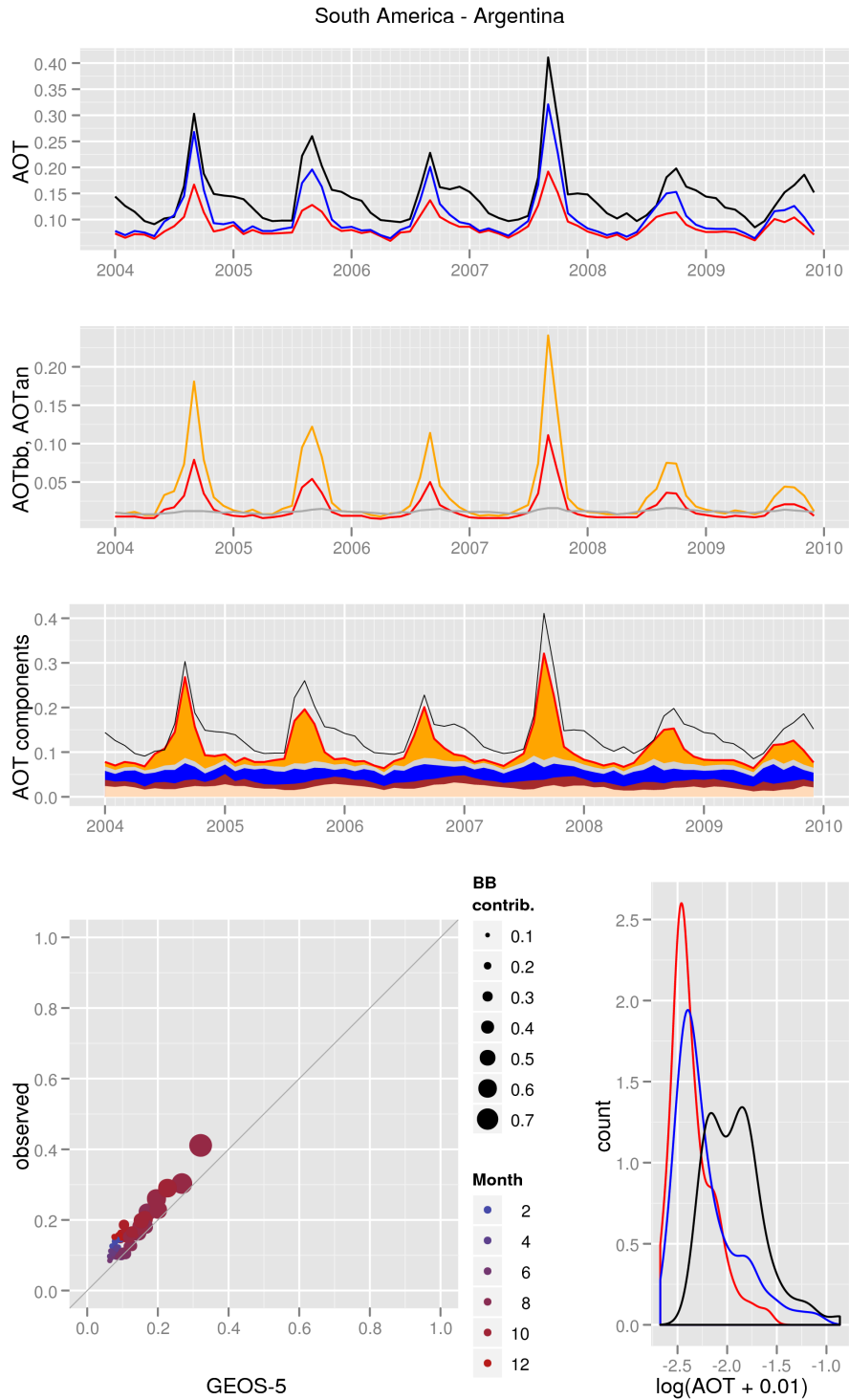
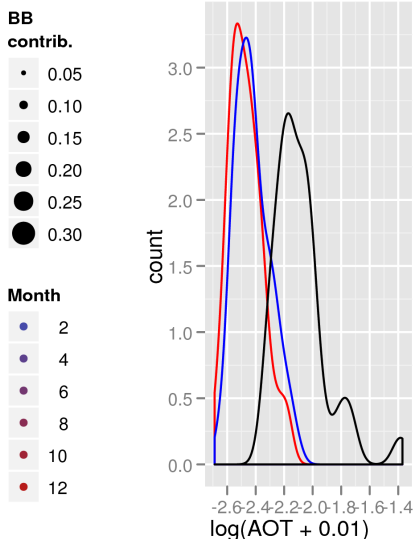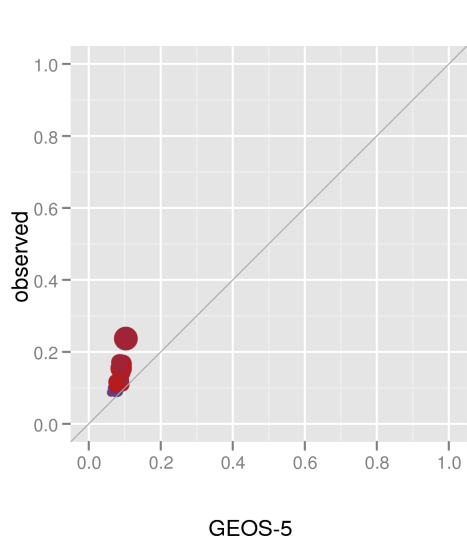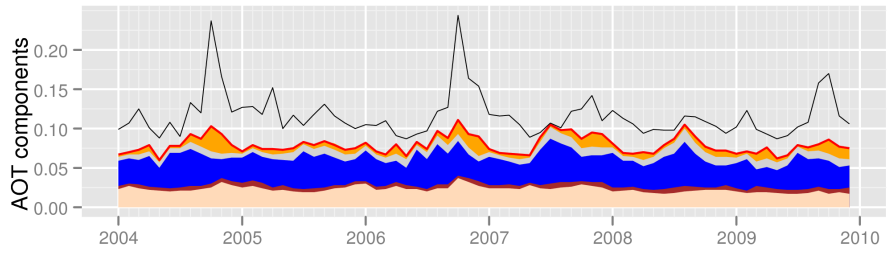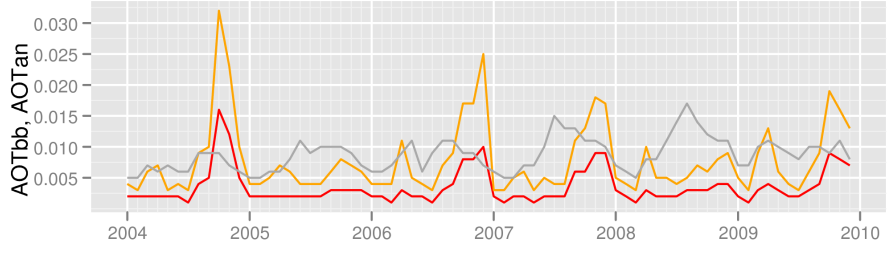(a) GEOS-5 and NNR-AOT/Aqua

Figure B21: AOT diagnostics for the Argentina region.

(b) GEOS-5 and NNR-AOT/Terra

(a) GEOS-5 and NNR-AOT/Aqua

Figure B22: AOT diagnostics for the West Africa region.
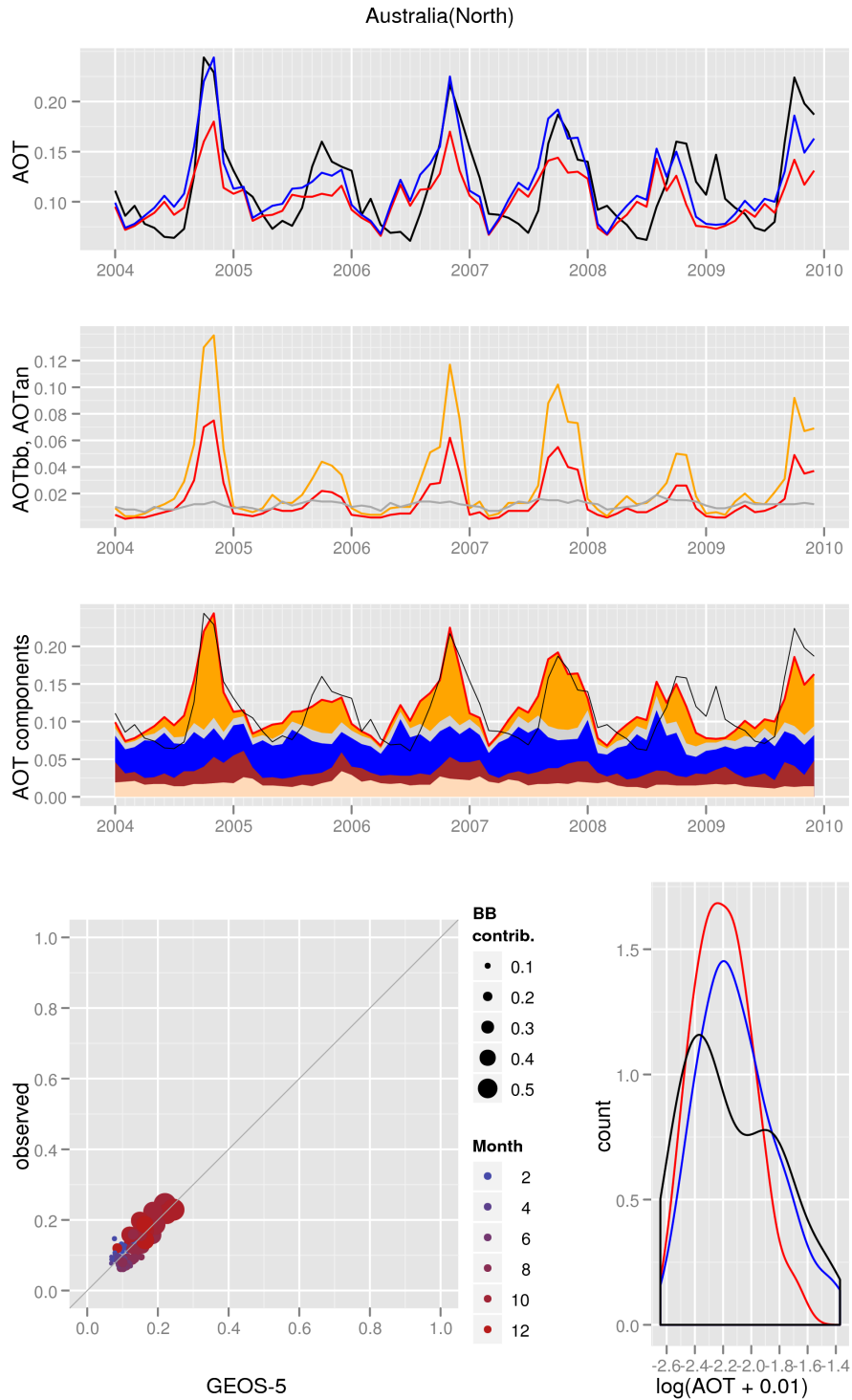
Africa(West)

(b) GEOS-5 and NNR-AOT/Terra

(a) GEOS-5 and NNR-AOT/Aqua

Figure B23: AOT diagnostics for the Central Africa region.

(b) GEOS-5 and NNR-AOT/Terra

63
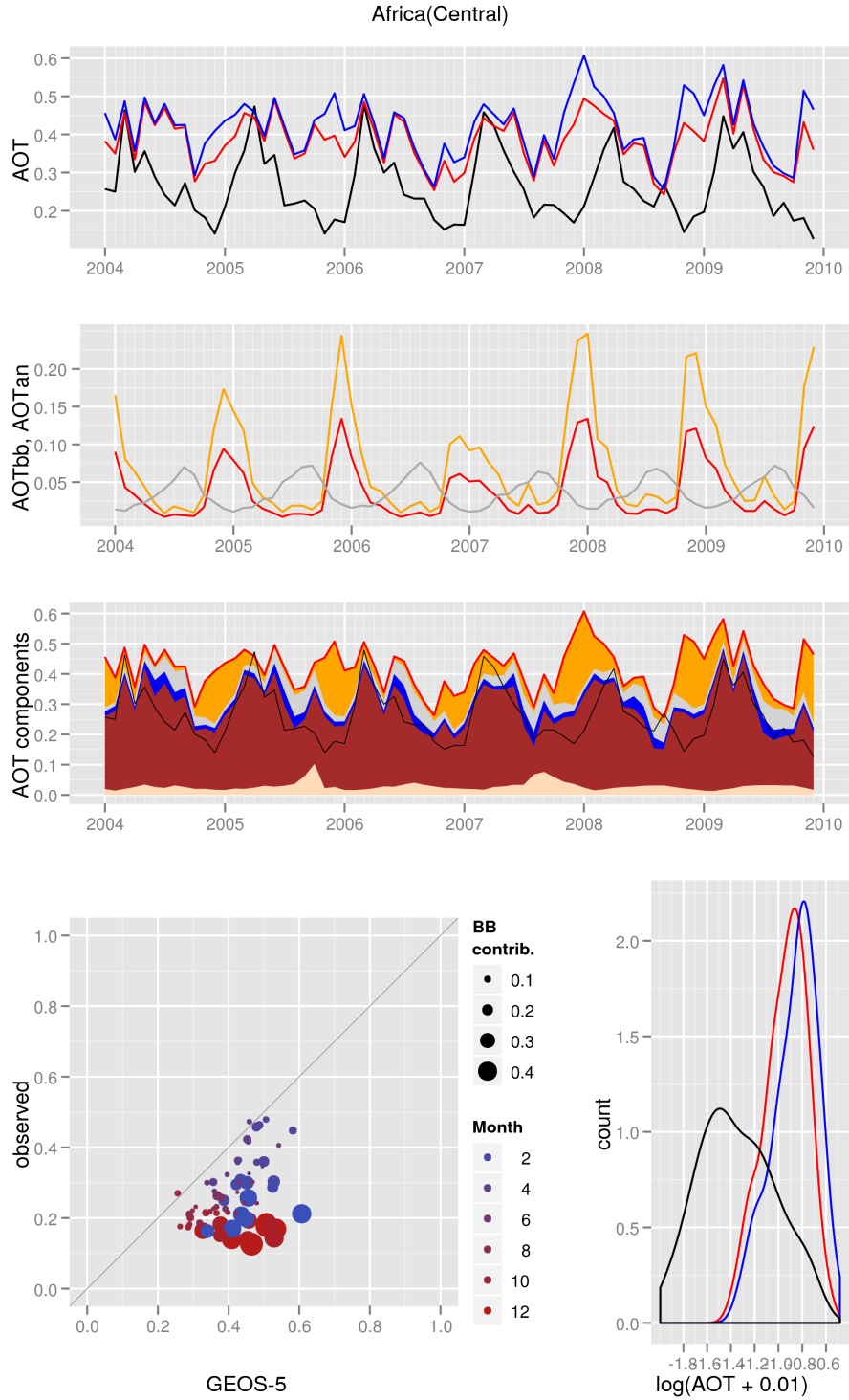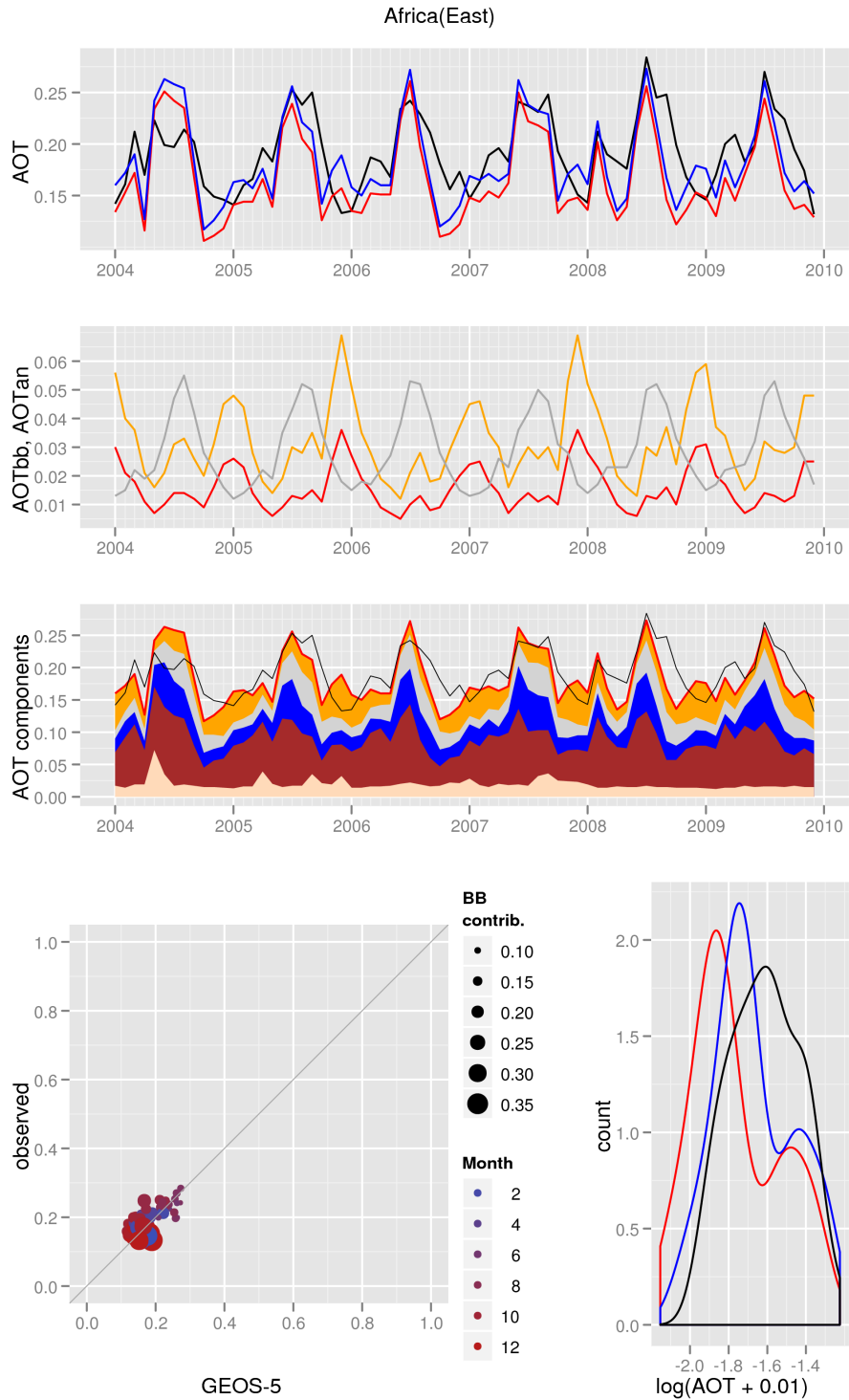
Africa(East)

(a) GEOS-5 and NNR-AOT/Aqua

Figure B24: AOT diagnostics for the East Africa region.

Africa(East)
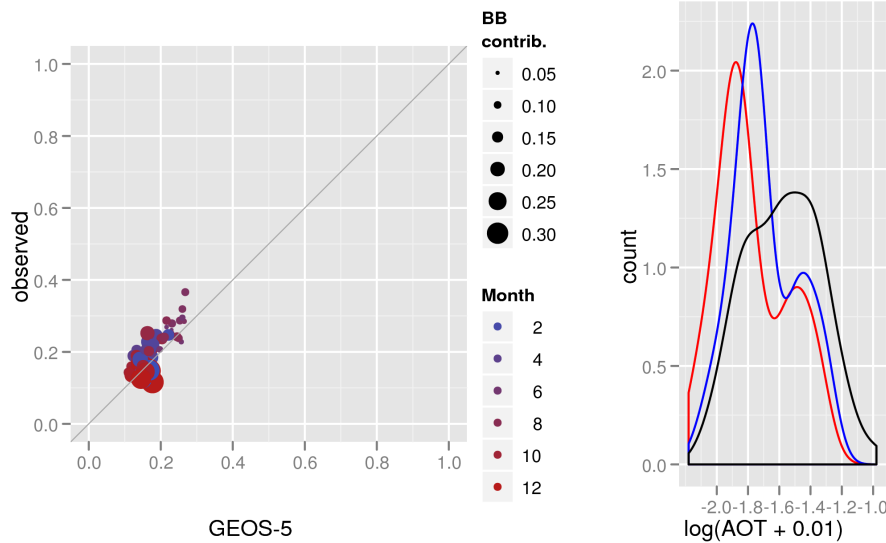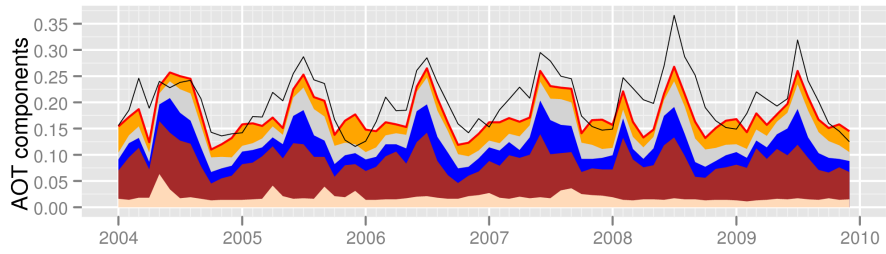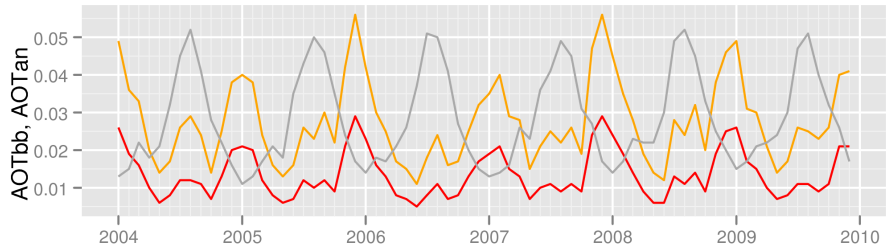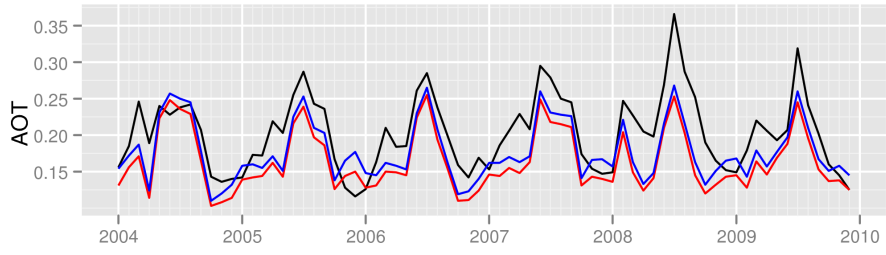
(b) GEOS-5 and NNR-AOT/Terra
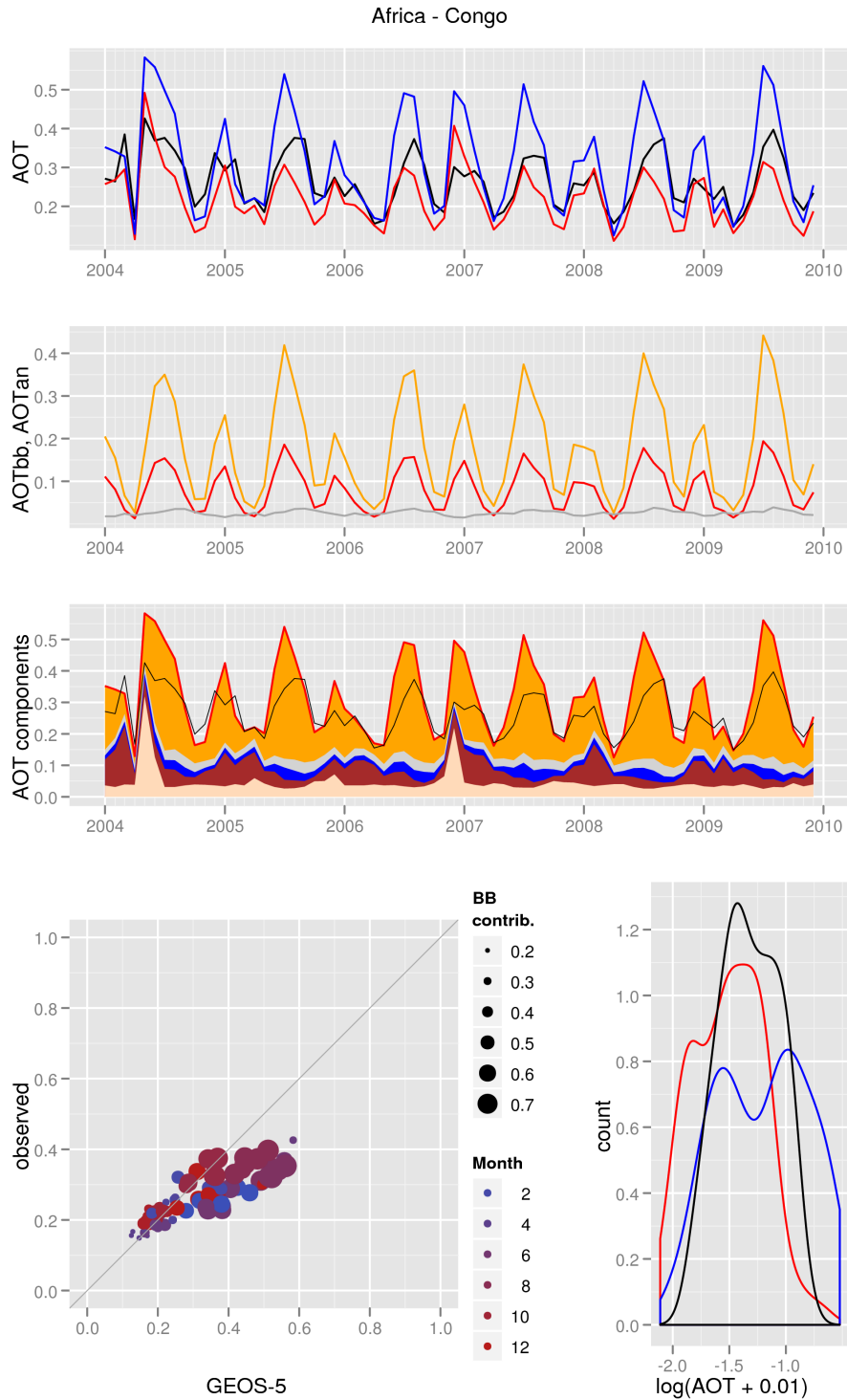
Africa - Congo

(a) GEOS-5 and NNR-AOT/Aqua

Figure B25: AOT diagnostics for the Congo region.

Africa - Congo
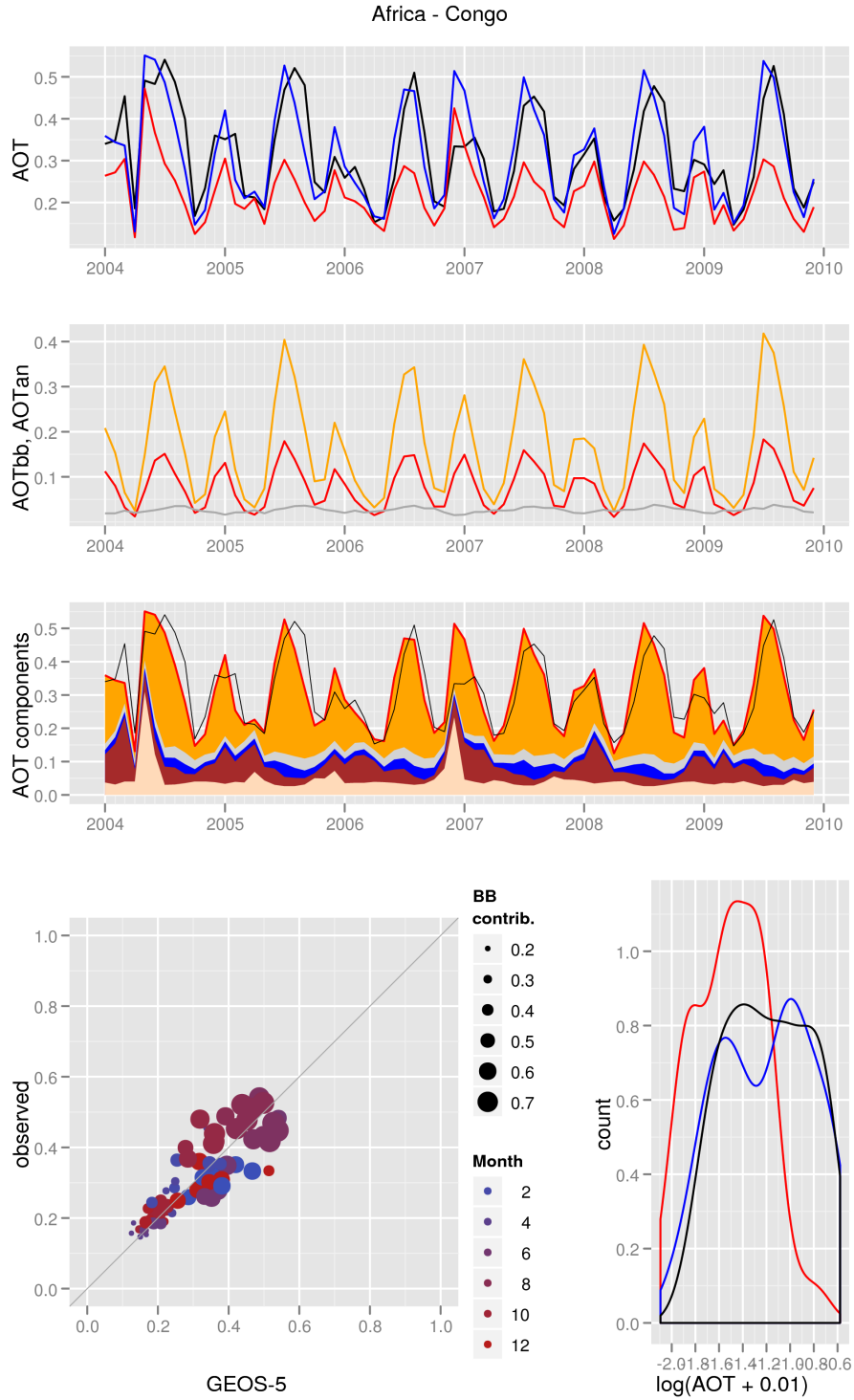
(b) GEOS-5 and NNR-AOT/Terra
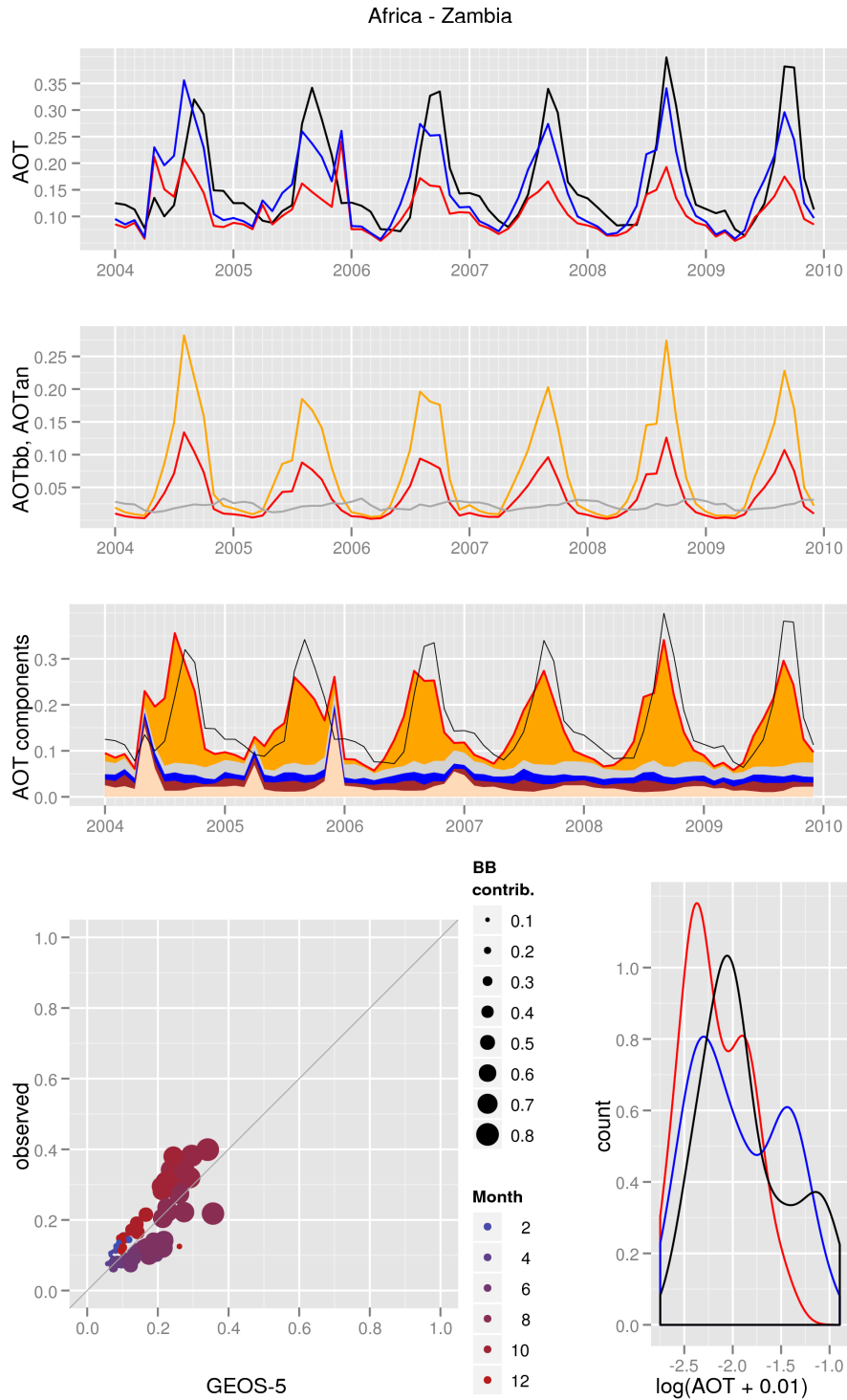
(a) GEOS-5 and NNR-AOT/Aqua
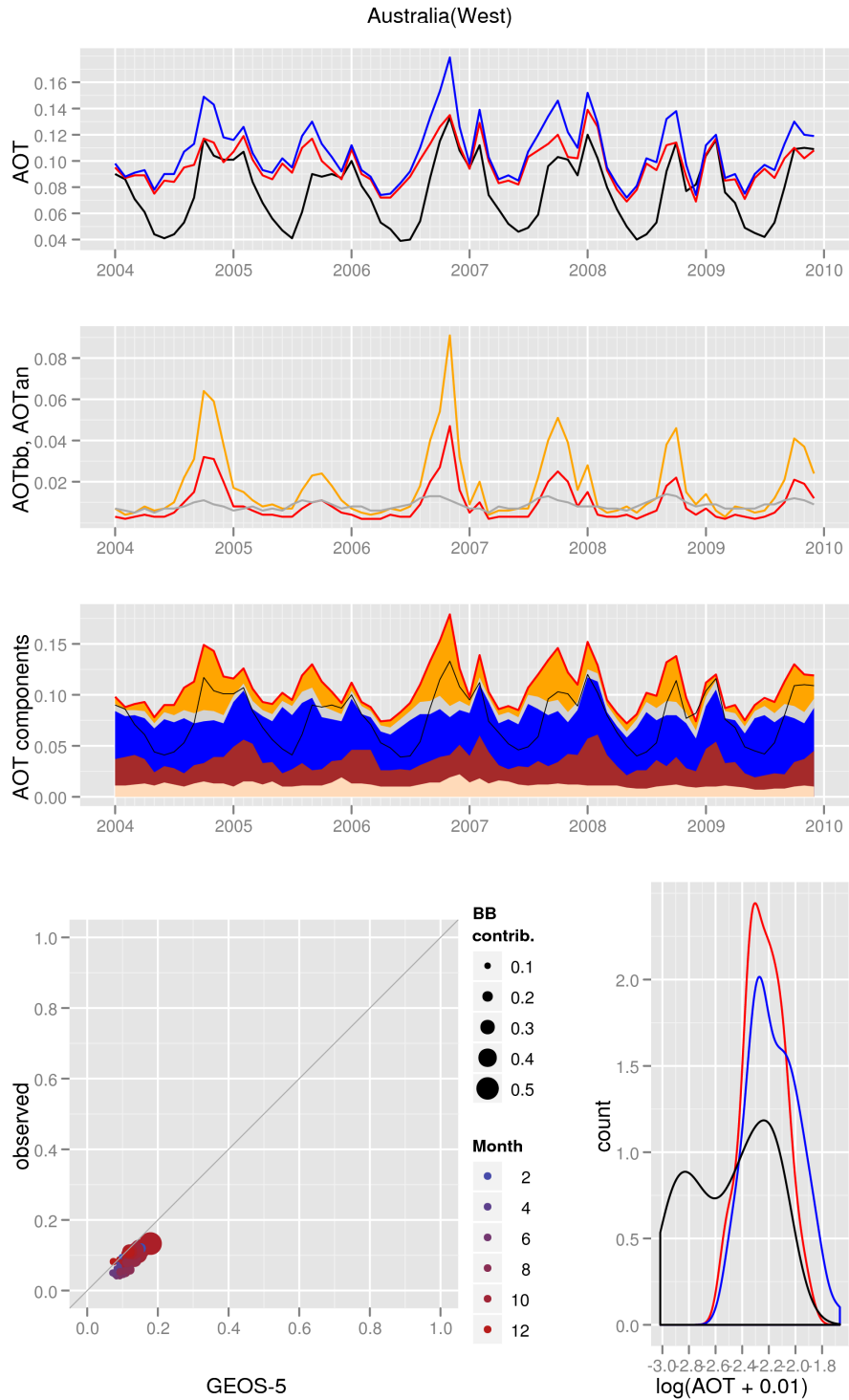
Figure B26: AOT diagnostics for the Zambia region.
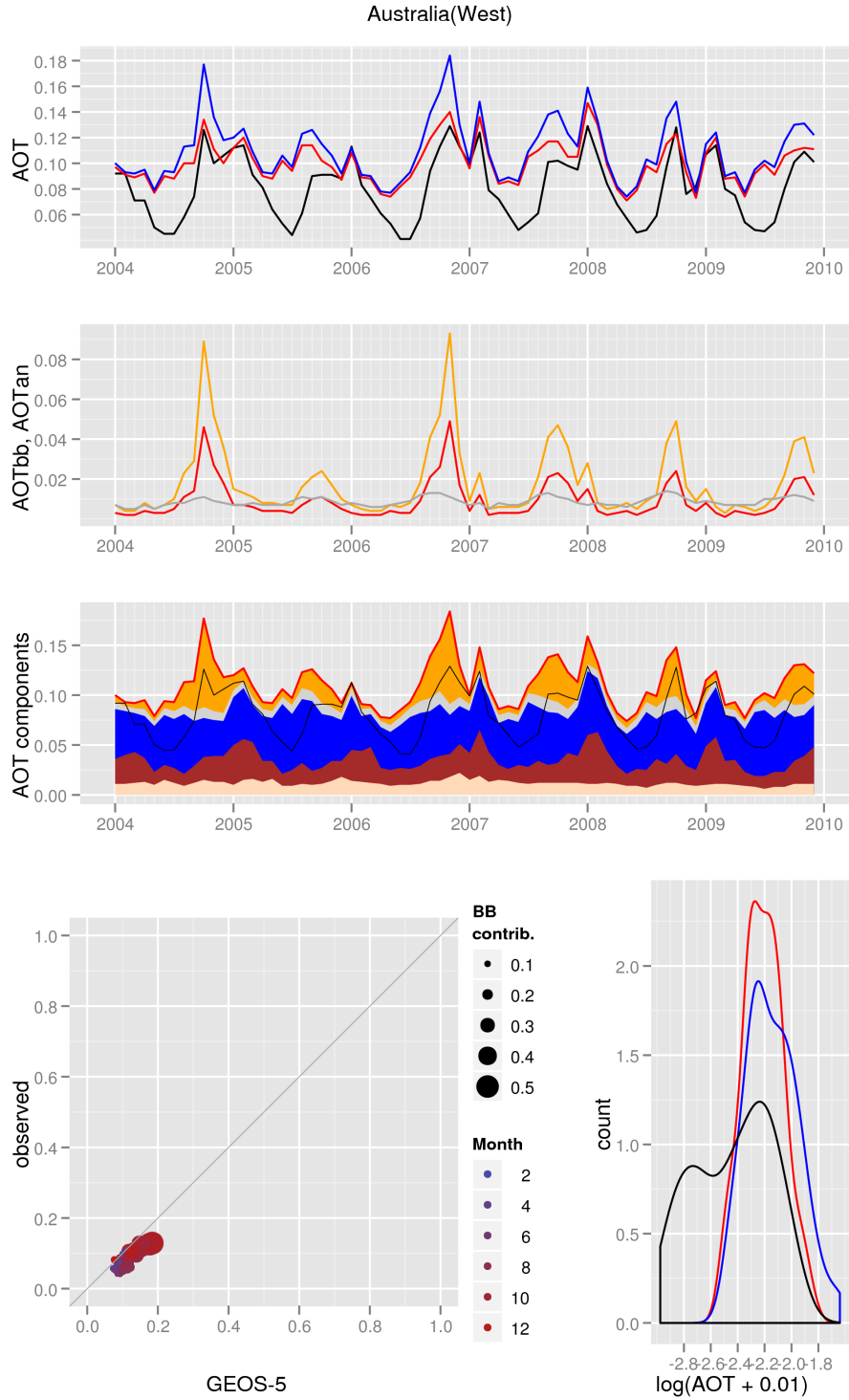
Africa - Zambia

(b) GEOS-5 and NNR-AOT/Terra

69
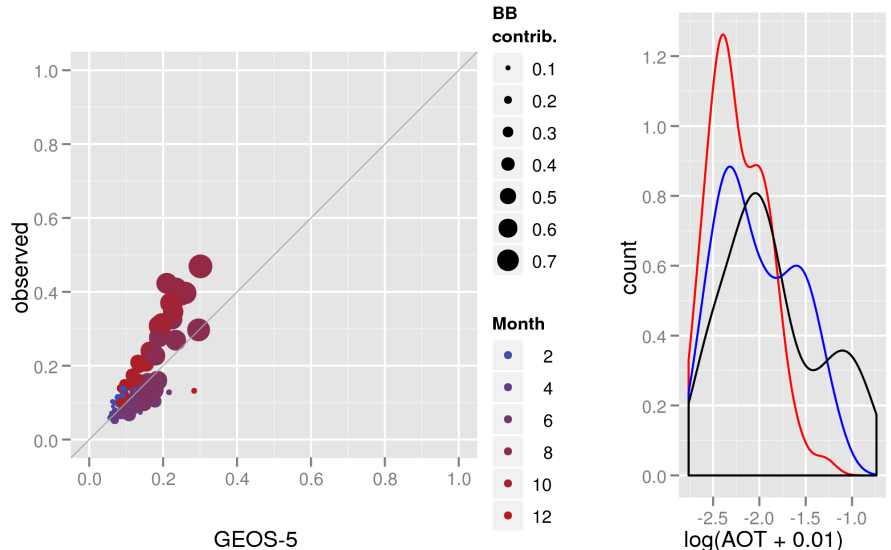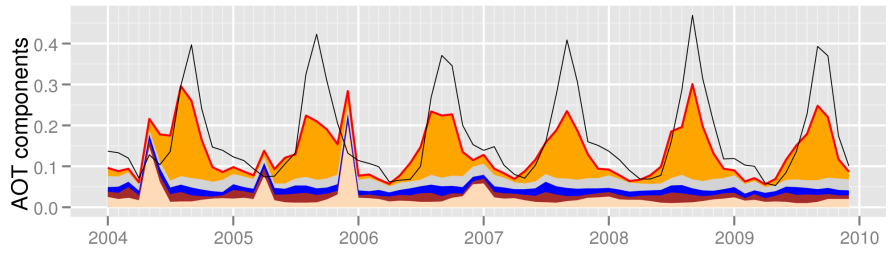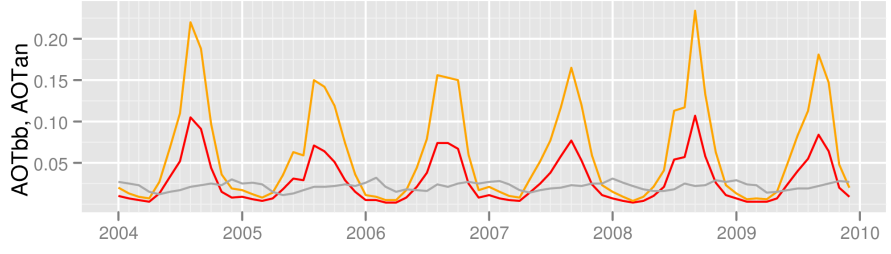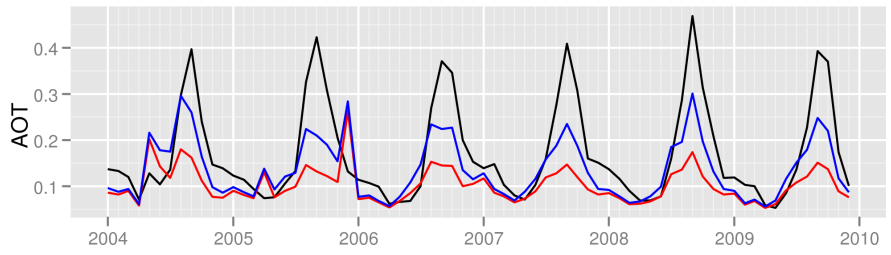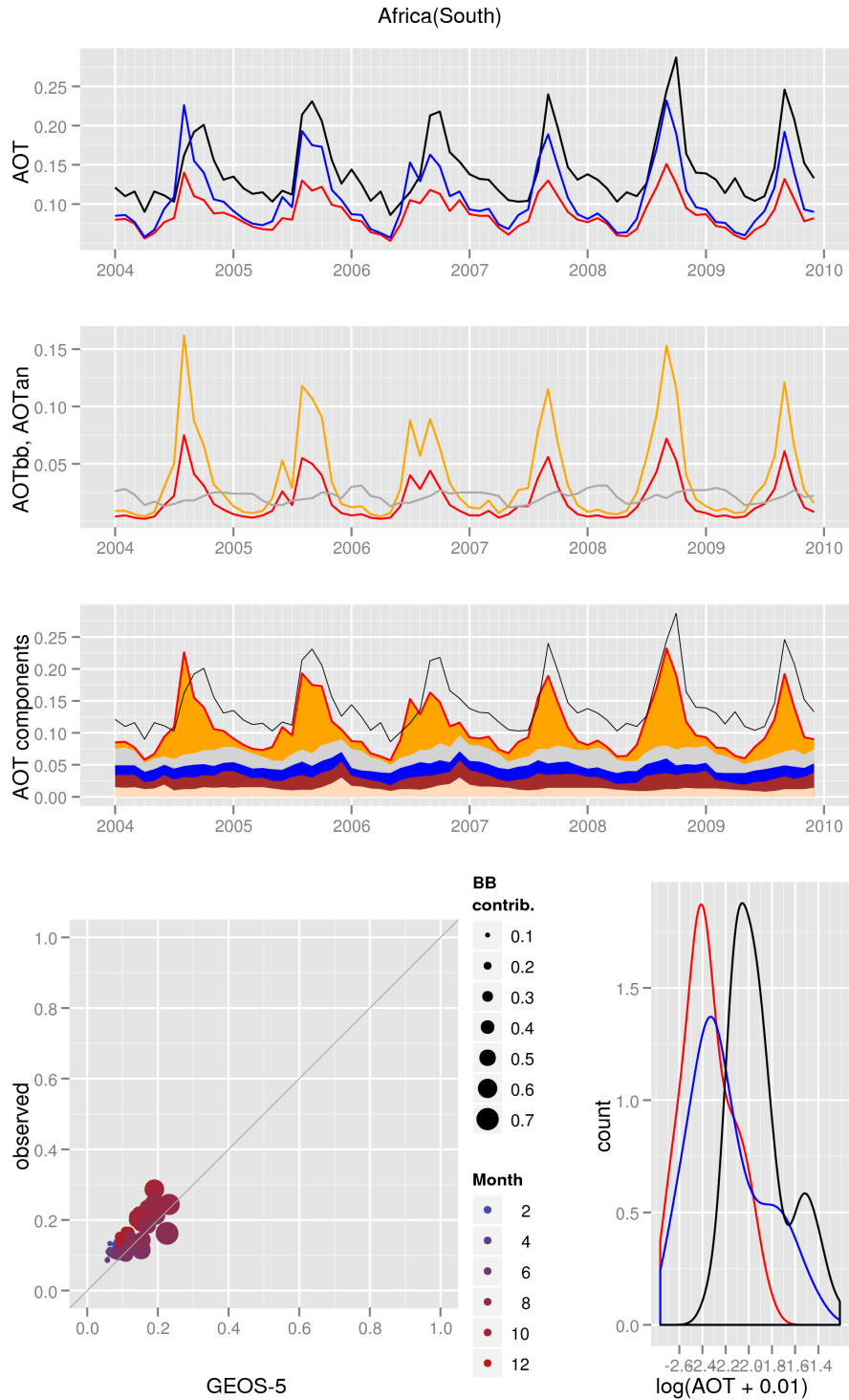
(a) GEOS-5 and NNR-AOT/Aqua

Figure B27: AOT diagnostics for the South Africa region.

(b) GEOS-5 and NNR-AOT/Terra
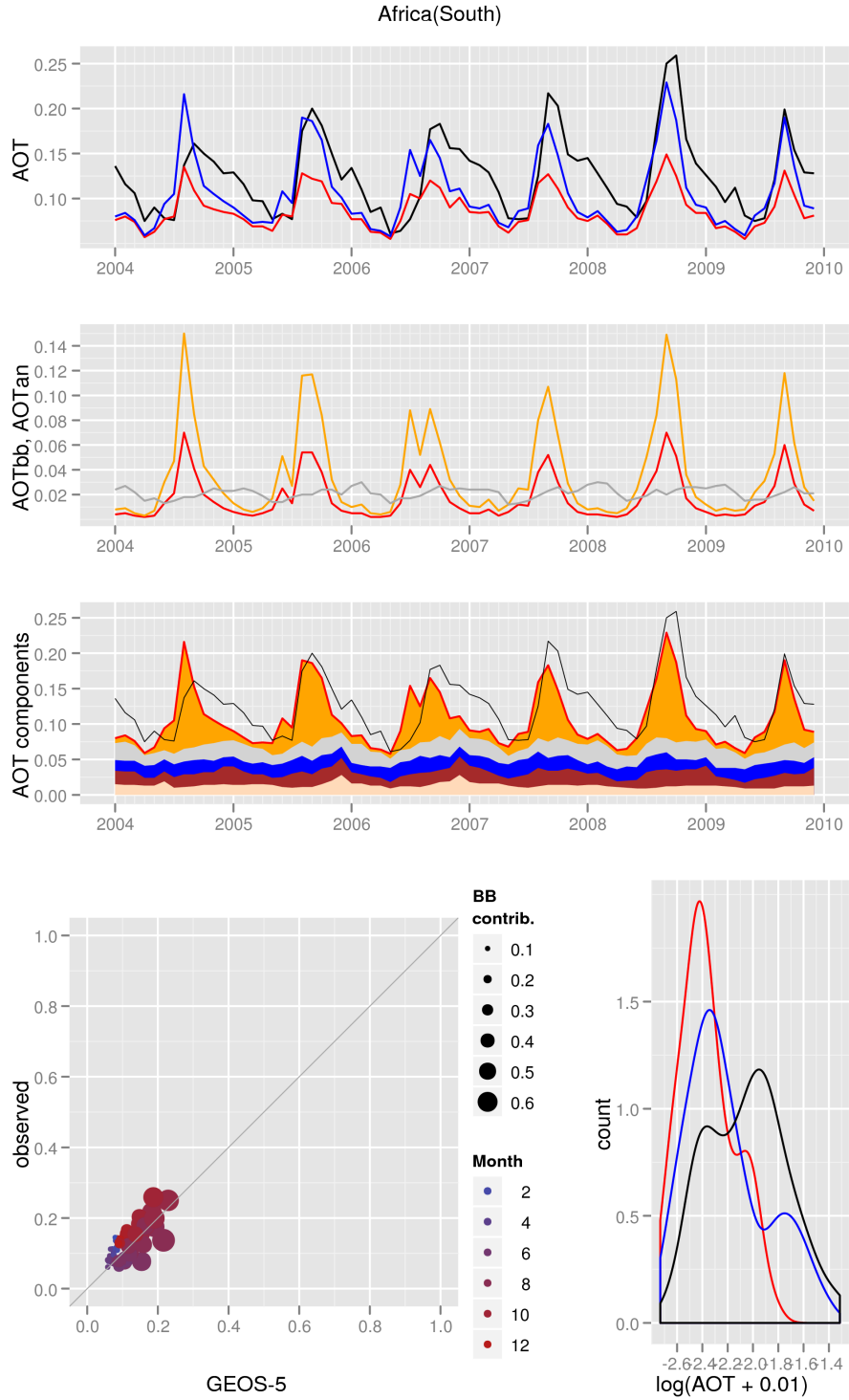
Africa - Madagascar

(a) GEOS-5 and NNR-AOT/Aqua
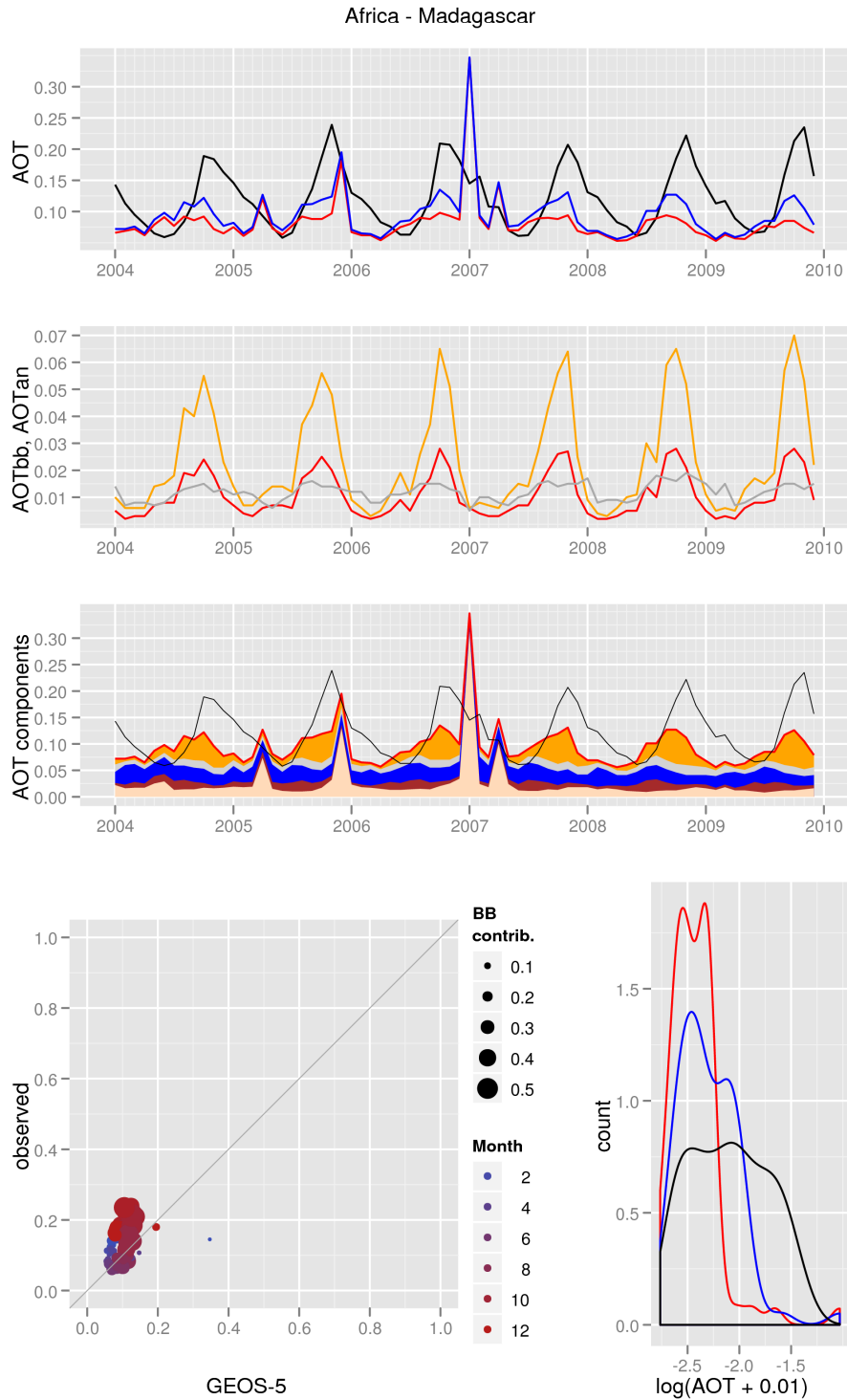
Figure B28: AOT diagnostics for the Madagascar region.

Africa - Madagascar

(b) GEOS-5 and NNR-AOT/Terra

73
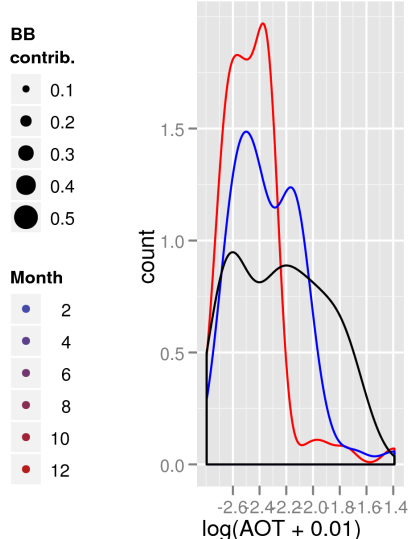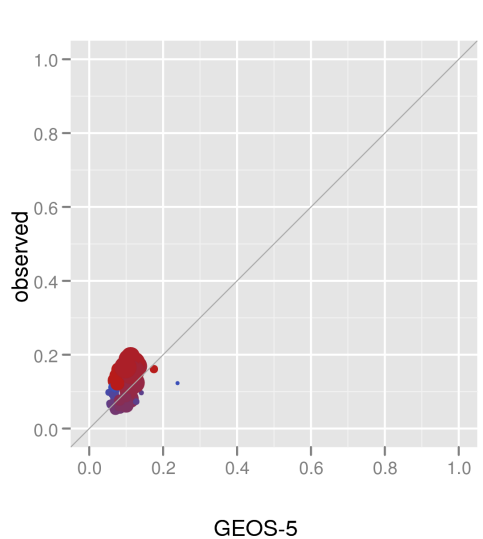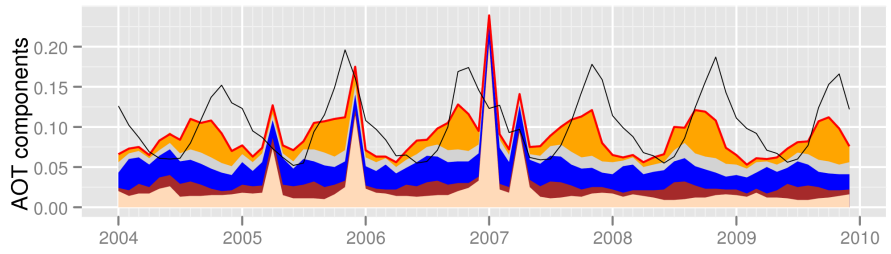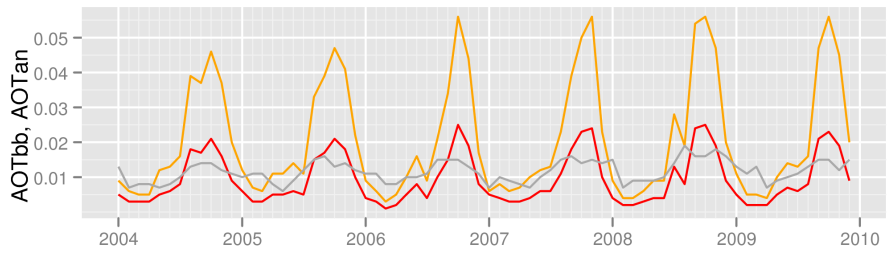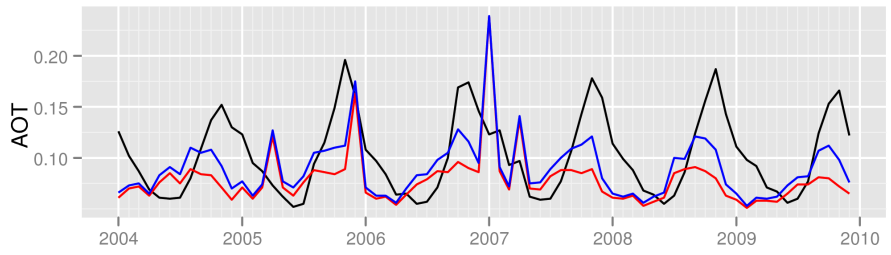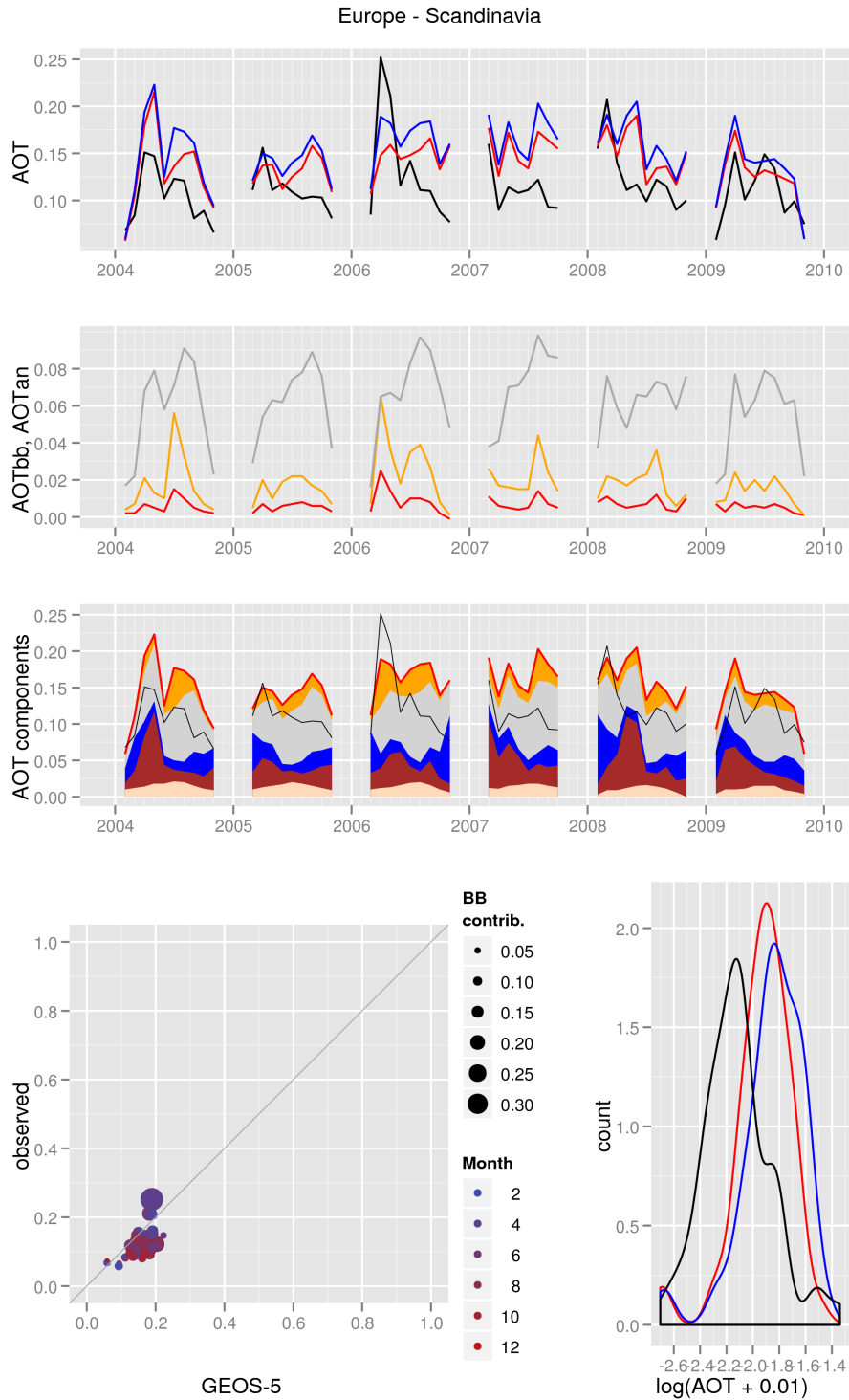
Figure B29: AOT diagnostics for the Scandinavia region.

Europe - Scandinavia

(b) GEOS-5 and NNR-AOT/Terra

75
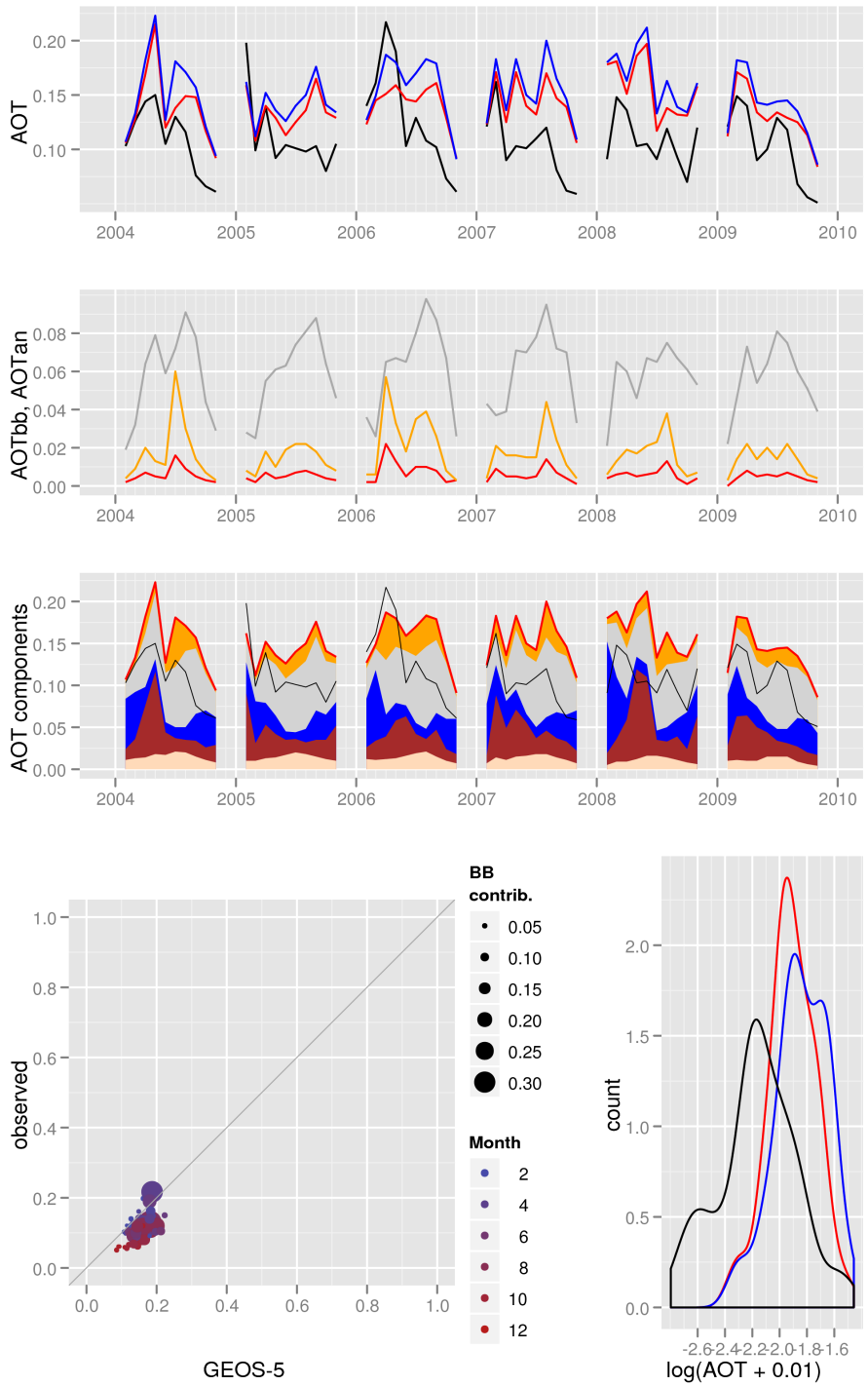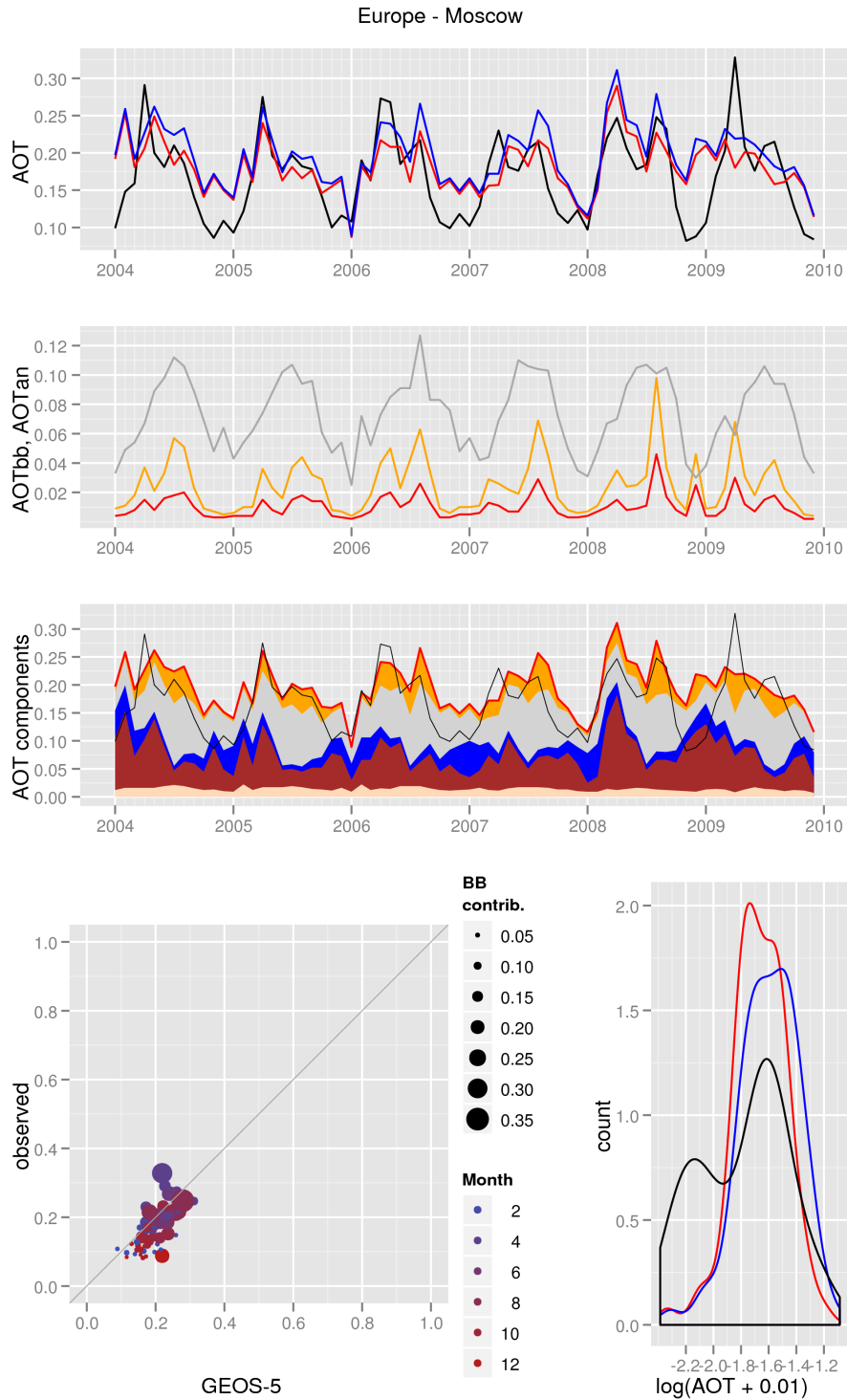
Europe - Moscow

(a) GEOS-5 and NNR-AOT/Aqua

Figure B30: AOT diagnostics for the Moscow region.

Europe - Moscow
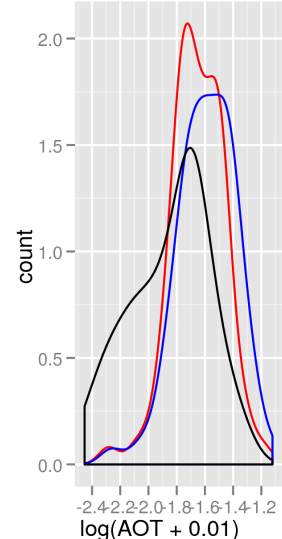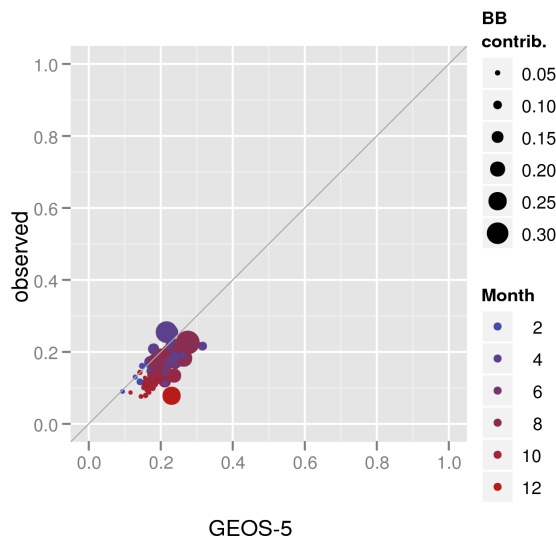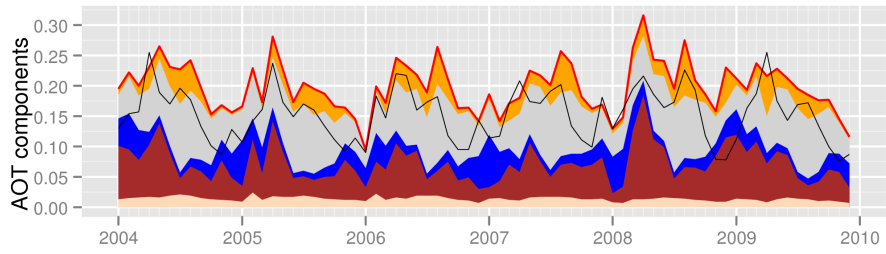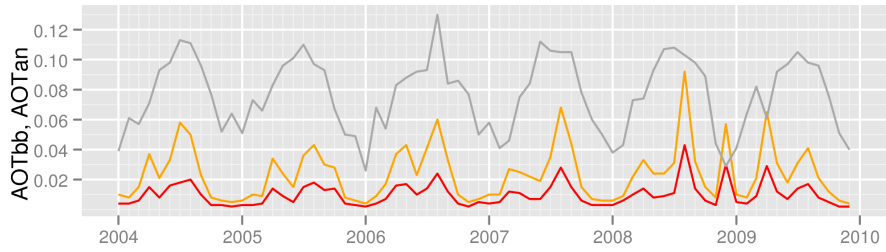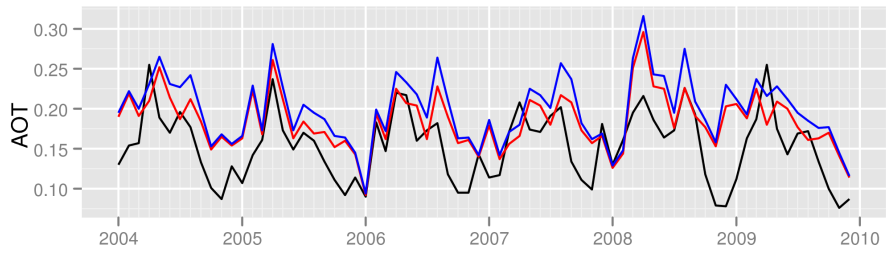
(b) GEOS-5 and NNR-AOT/Terra
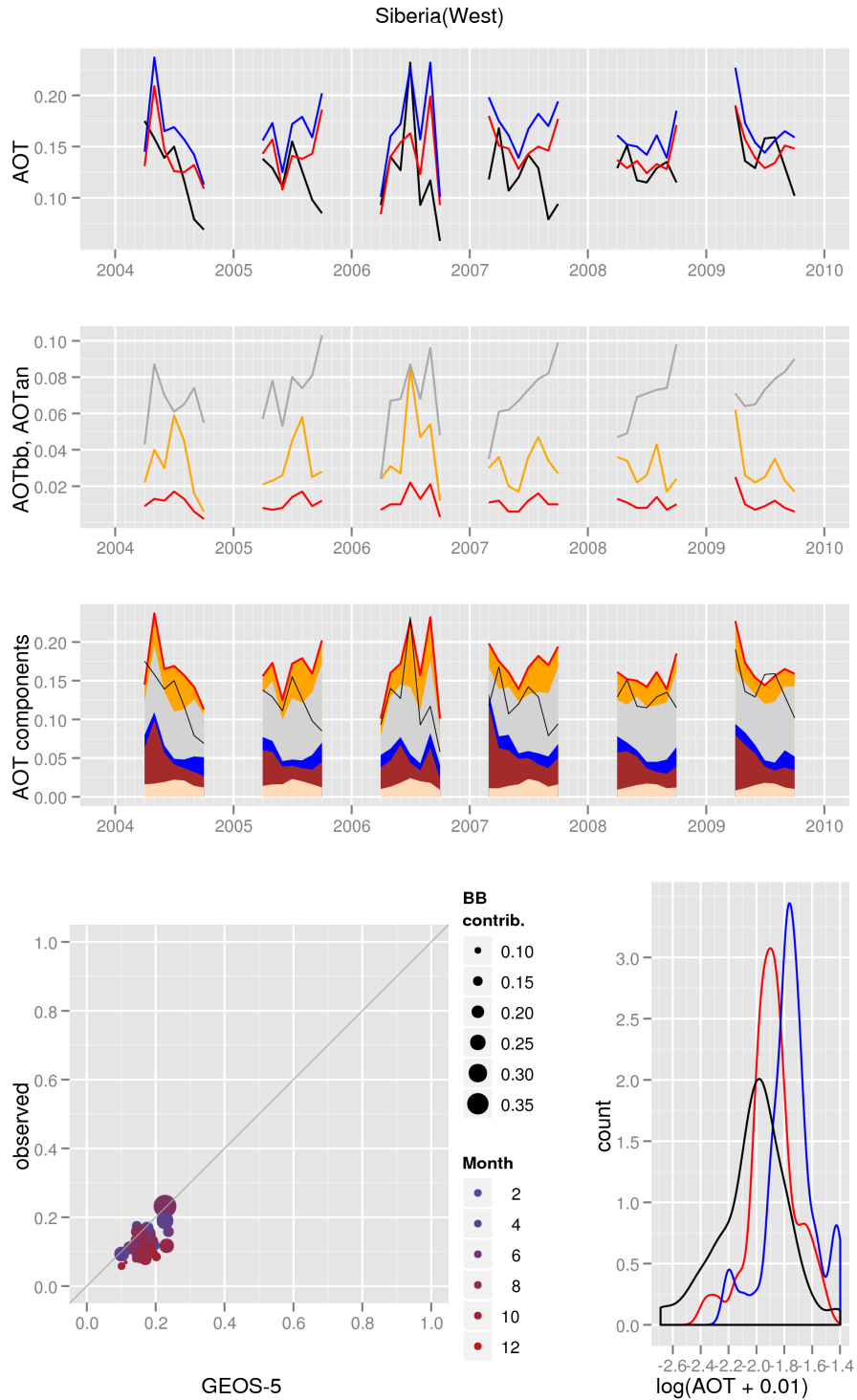
(a) GEOS-5 and NNR-AOT/Aqua

Figure B31: AOT diagnostics for the West Siberia region.
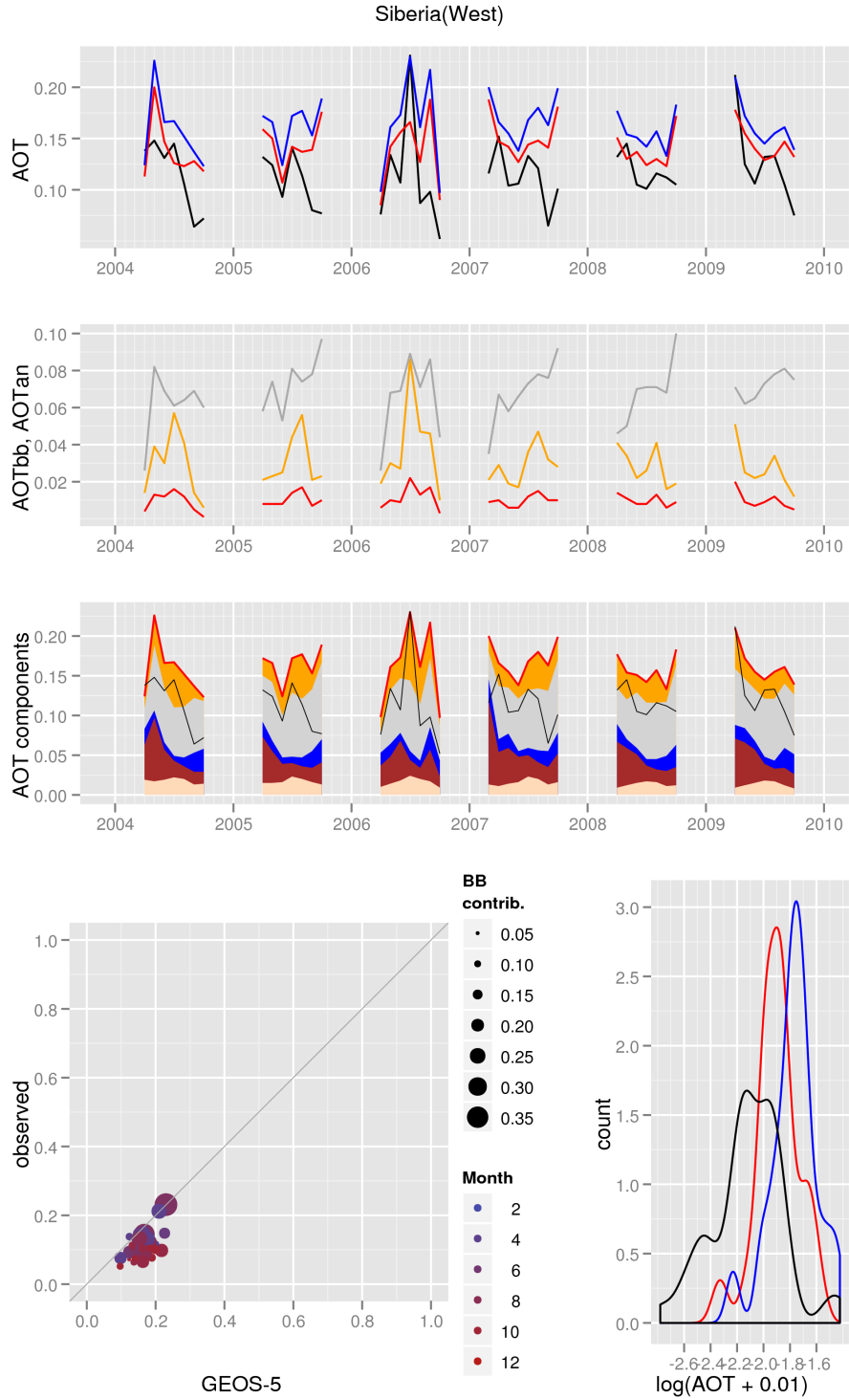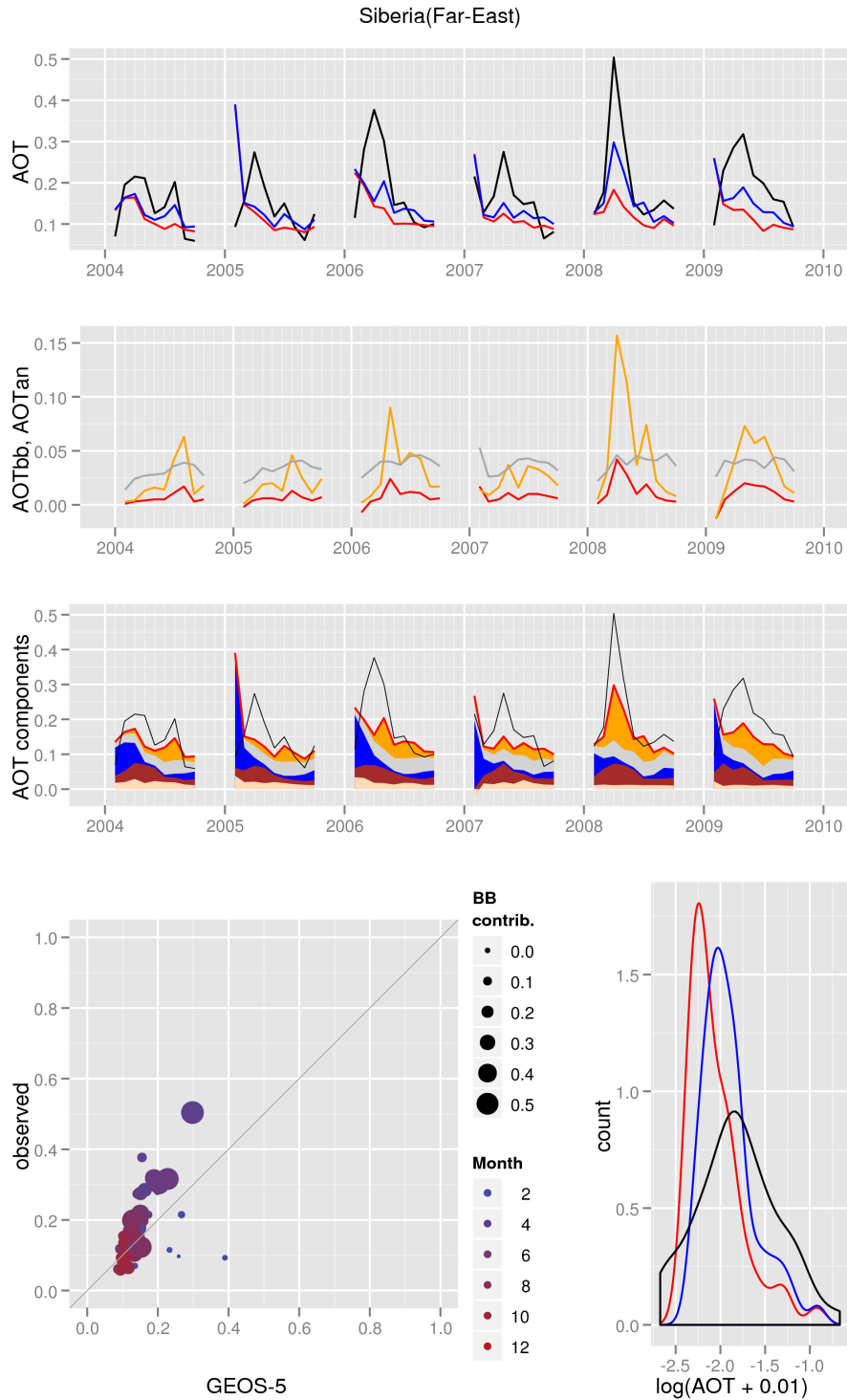
Siberia(West)

(b) GEOS-5 and NNR-AOT/Terra
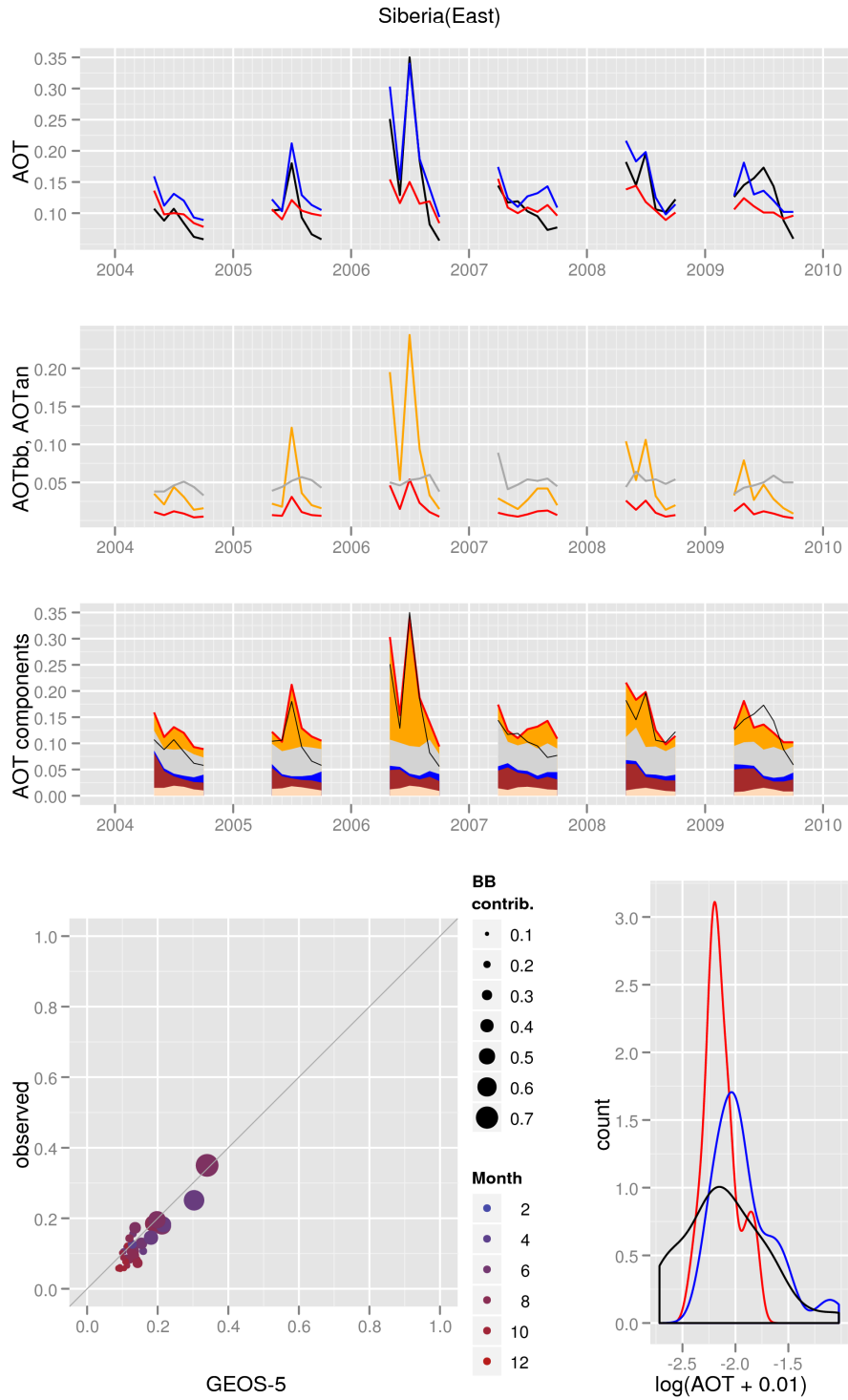
(a) GEOS-5 and NNR-AOT/Aqua

Figure B32: AOT diagnostics for the East Siberia region.
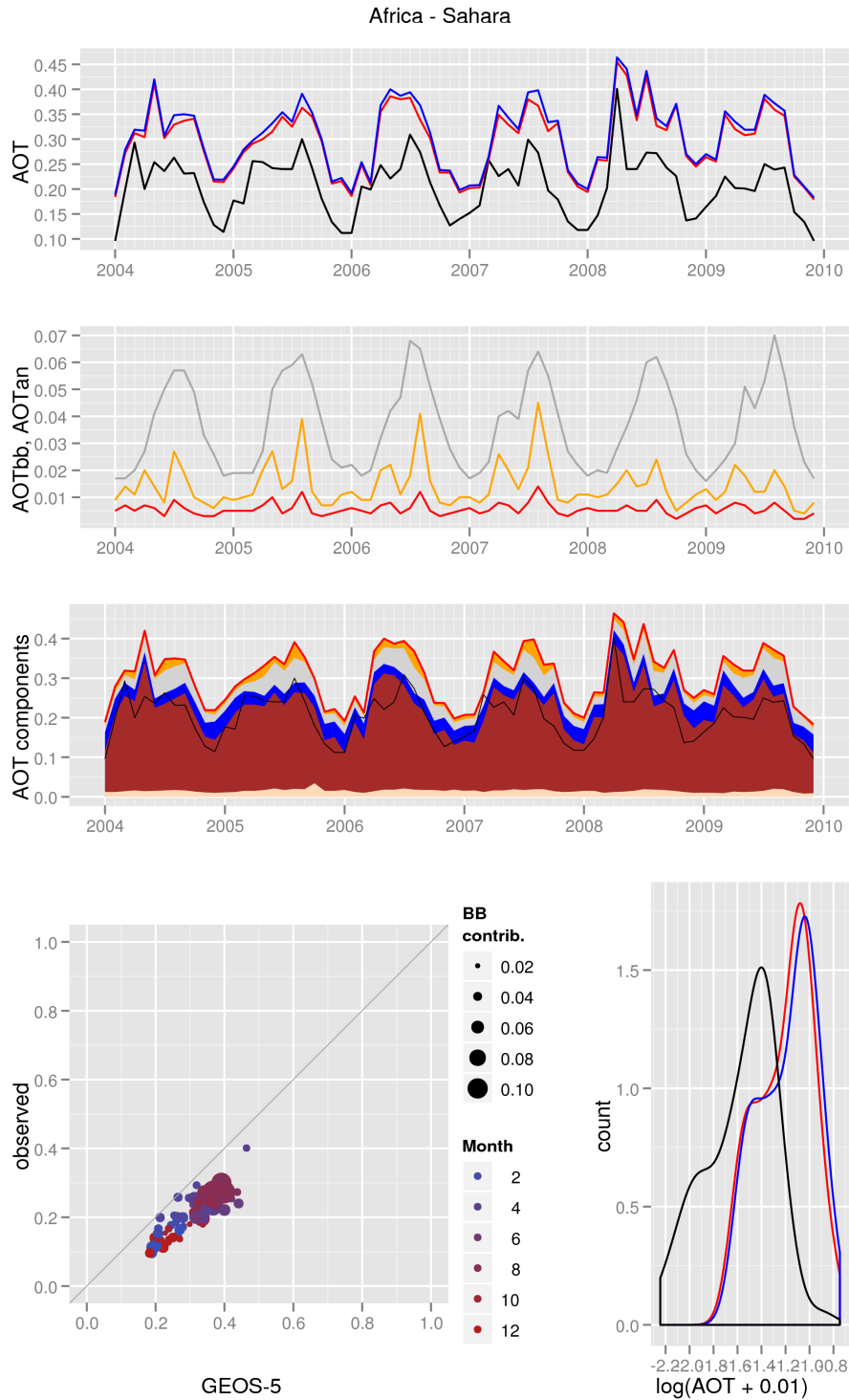
Siberia(East)
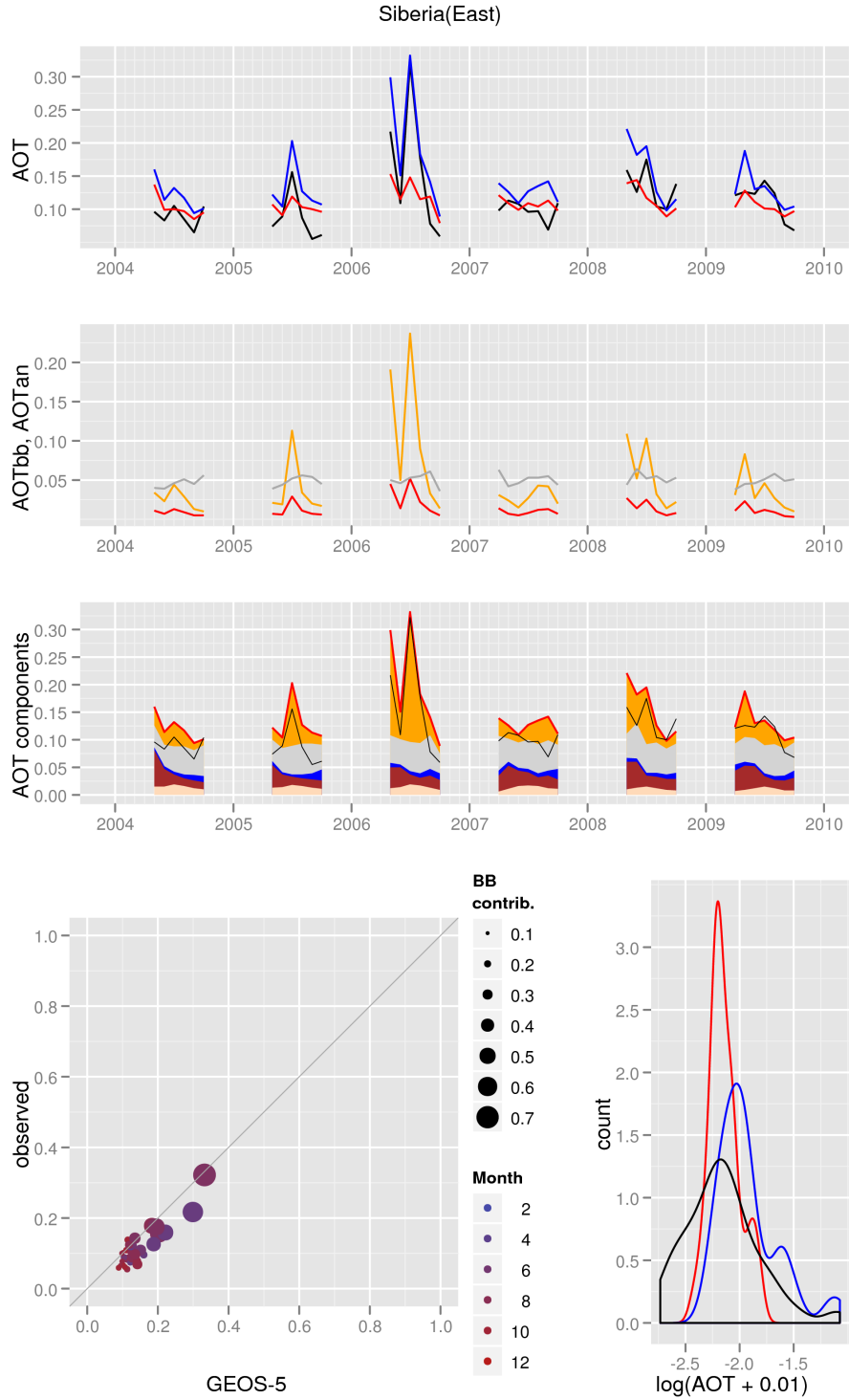
(b) GEOS-5 and NNR-AOT/Terra
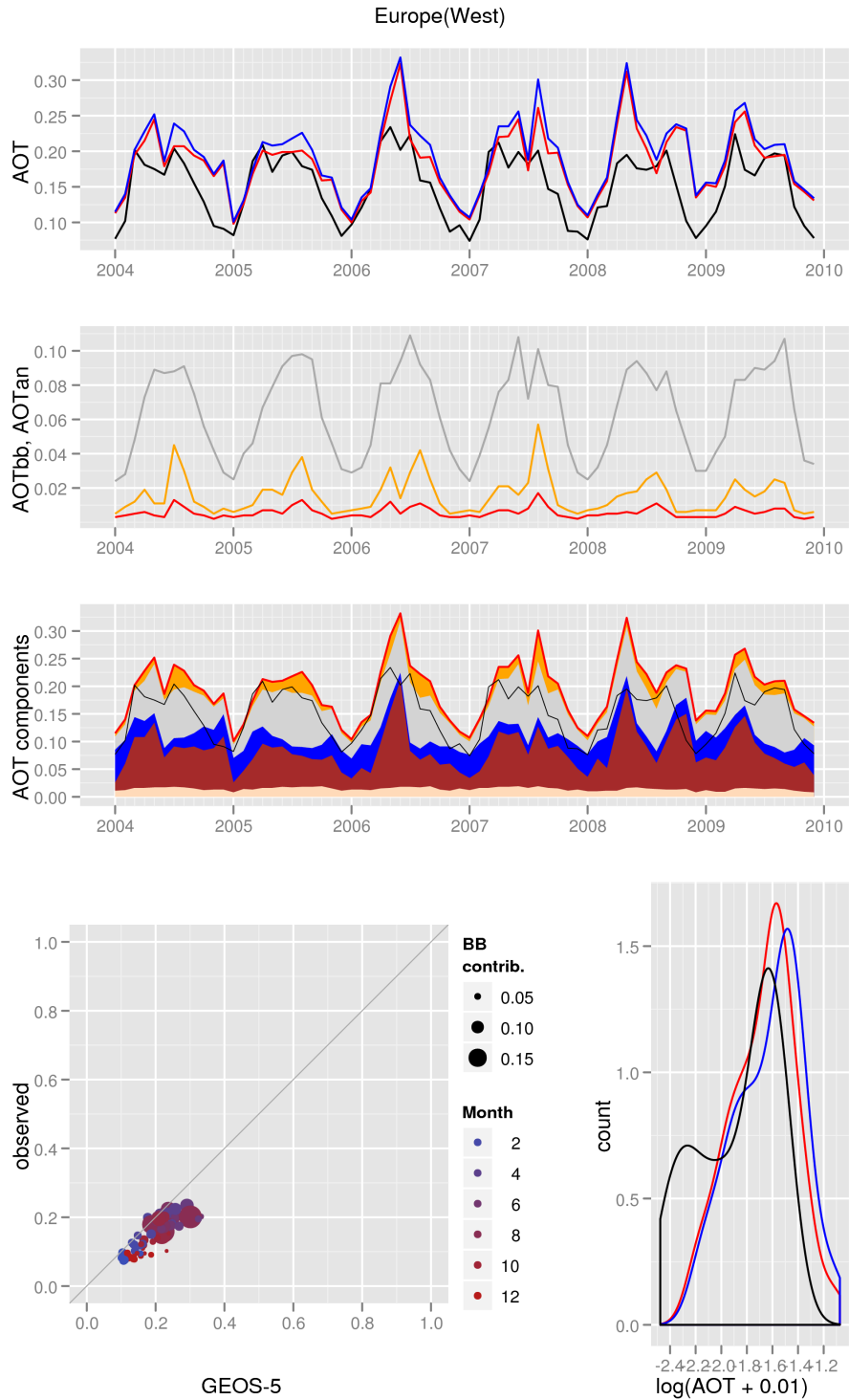
(a) GEOS-5 and NNR-AOT/Aqua

Figure B33: AOT diagnostics for the West Europe region.

Europe(West)

(b) GEOS-5 and NNR-AOT/Terra

83
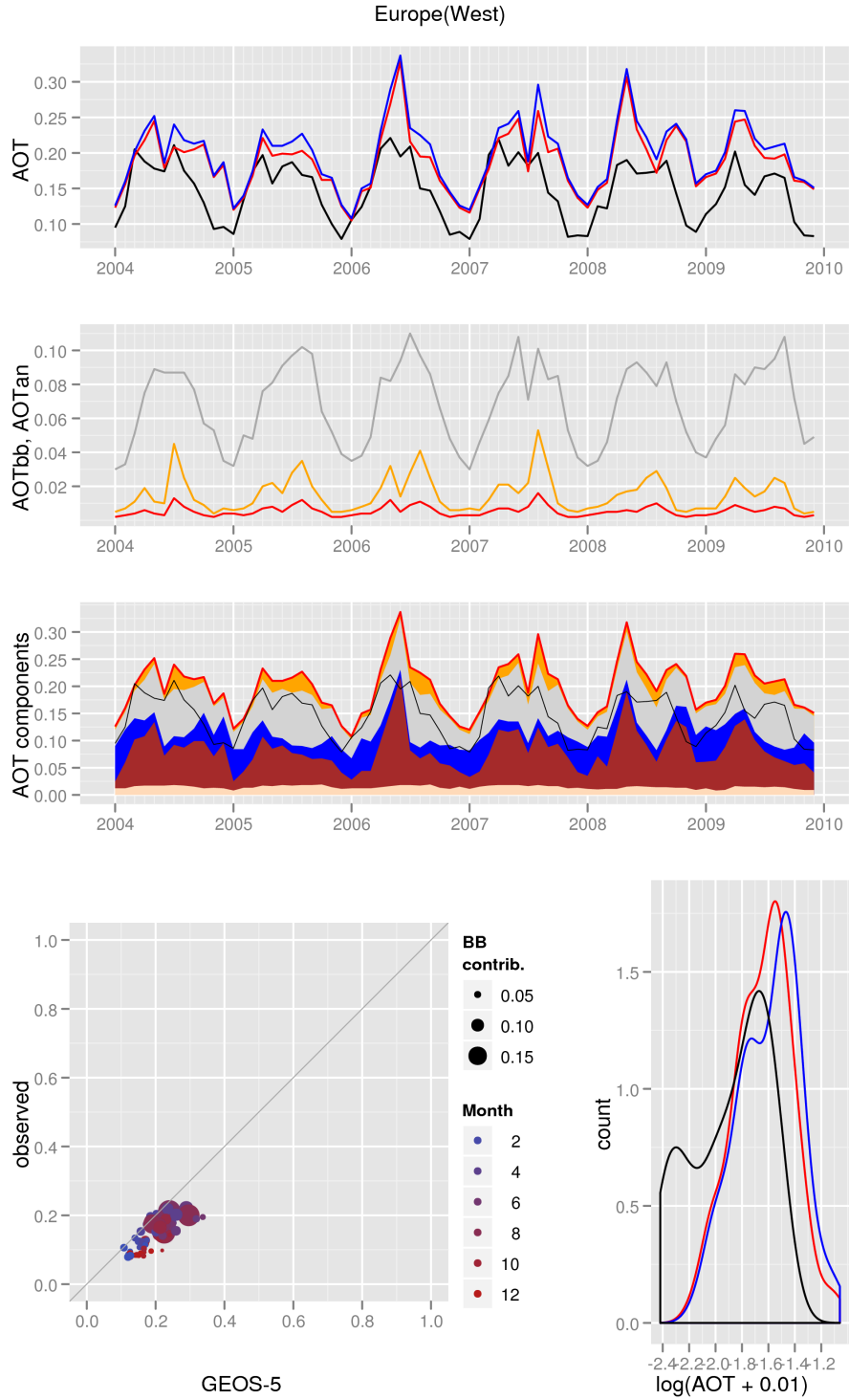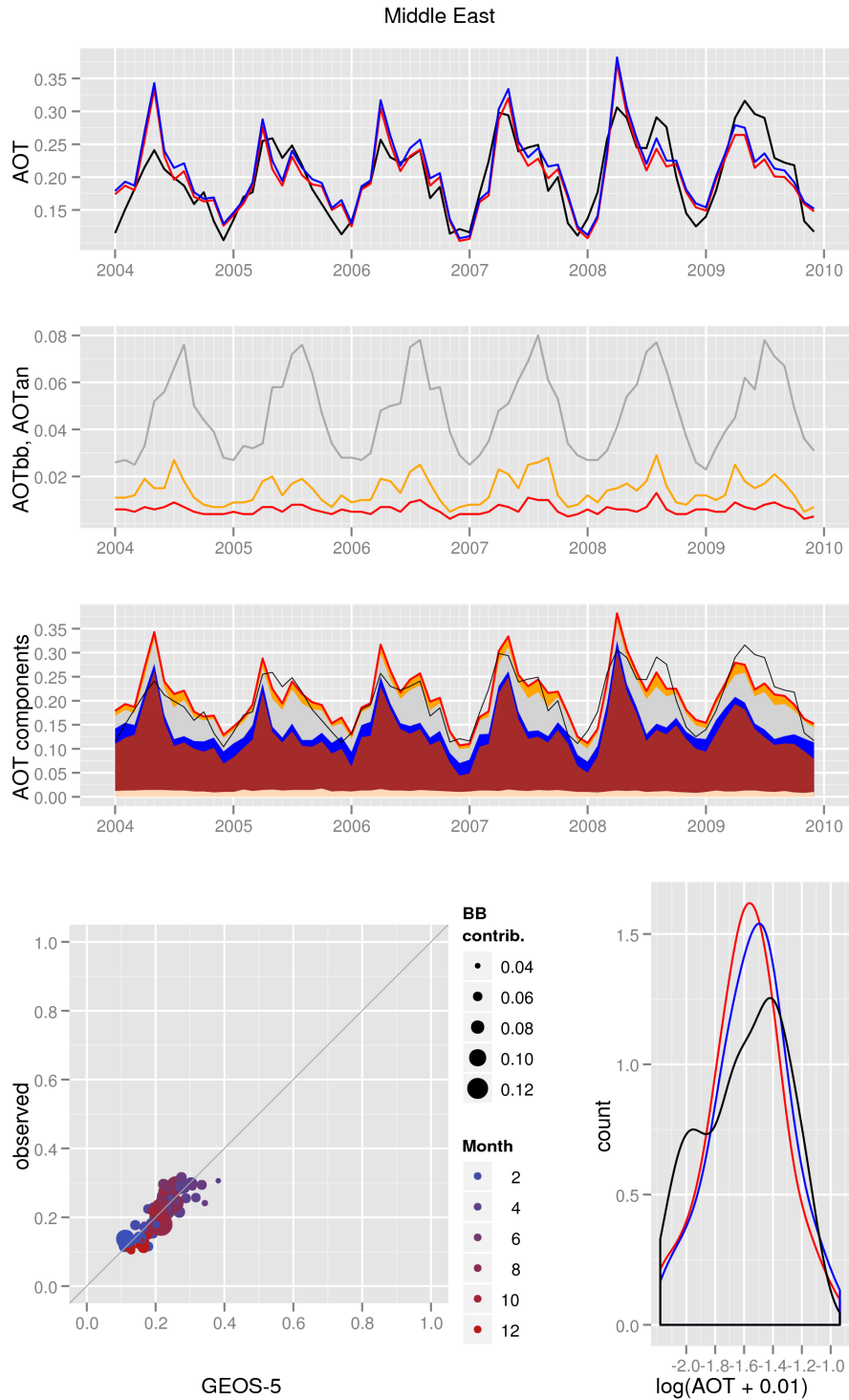
(a) GEOS-5 and NNR-AOT/Aqua

Figure B34: AOT diagnostics for the Middle East region.

Middle East
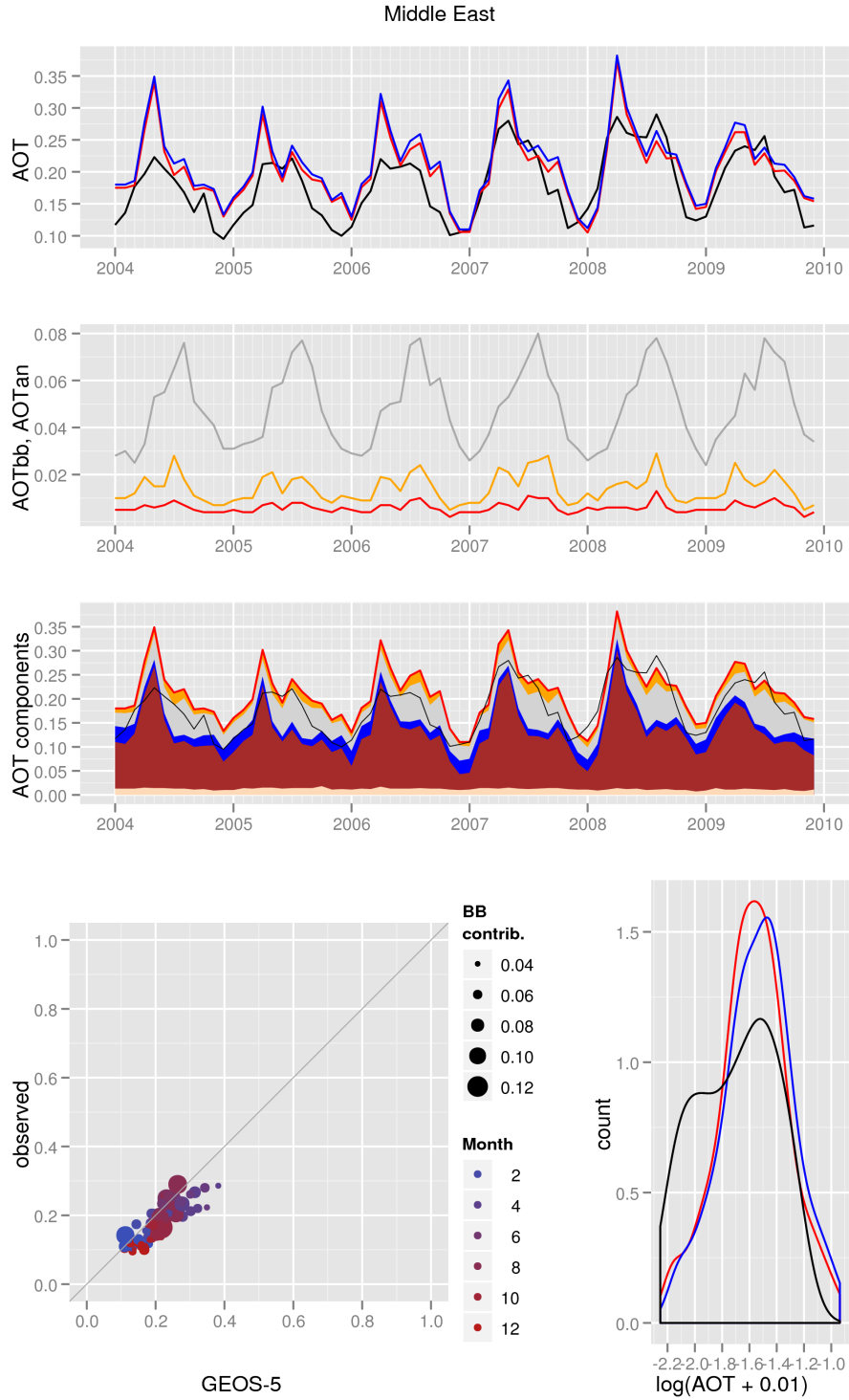
(b) GEOS-5 and NNR-AOT/Terra
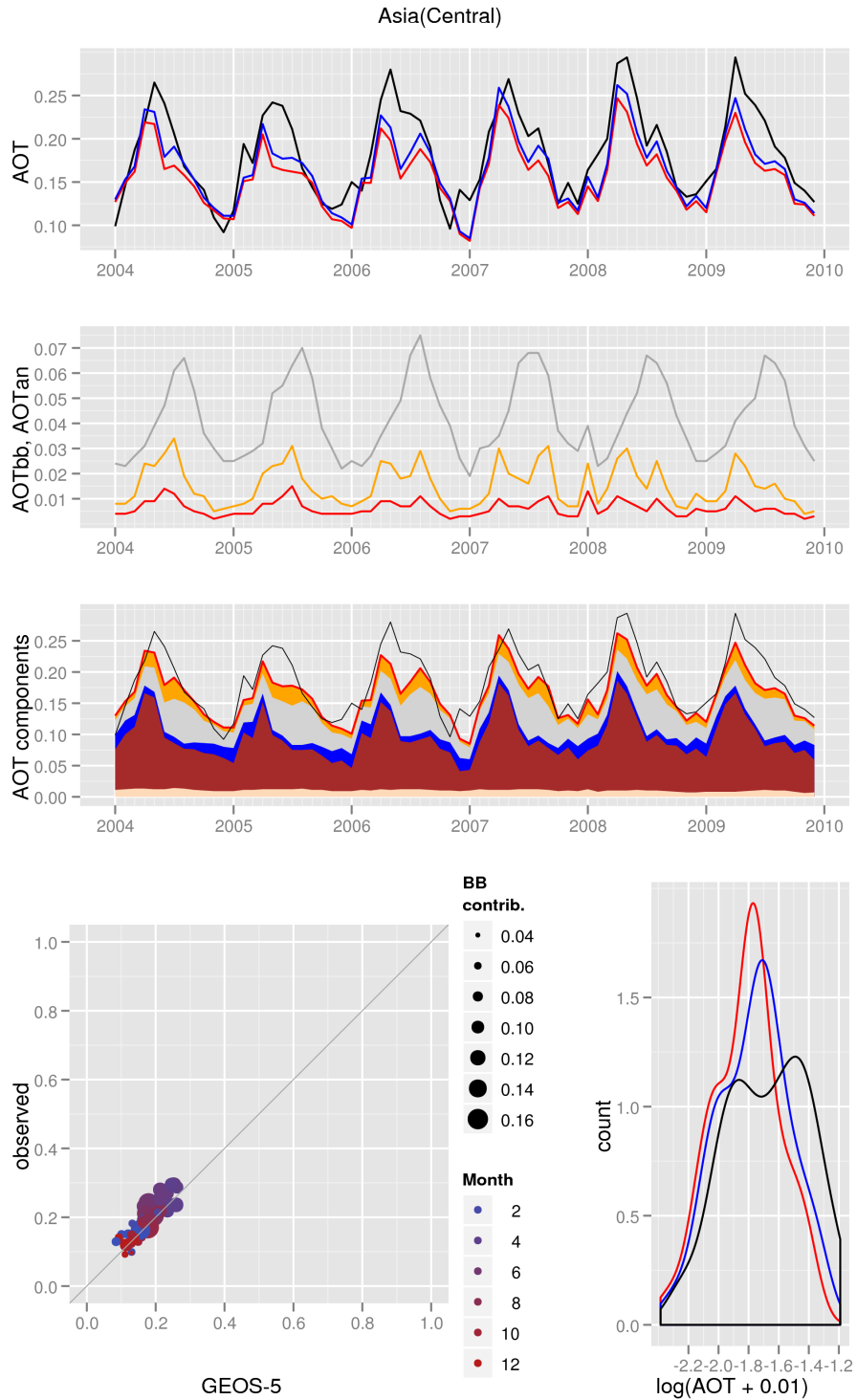
Asia(Central)

(a) GEOS-5 and NNR-AOT/Aqua

Figure B35: AOT diagnostics for the Central Asia region.
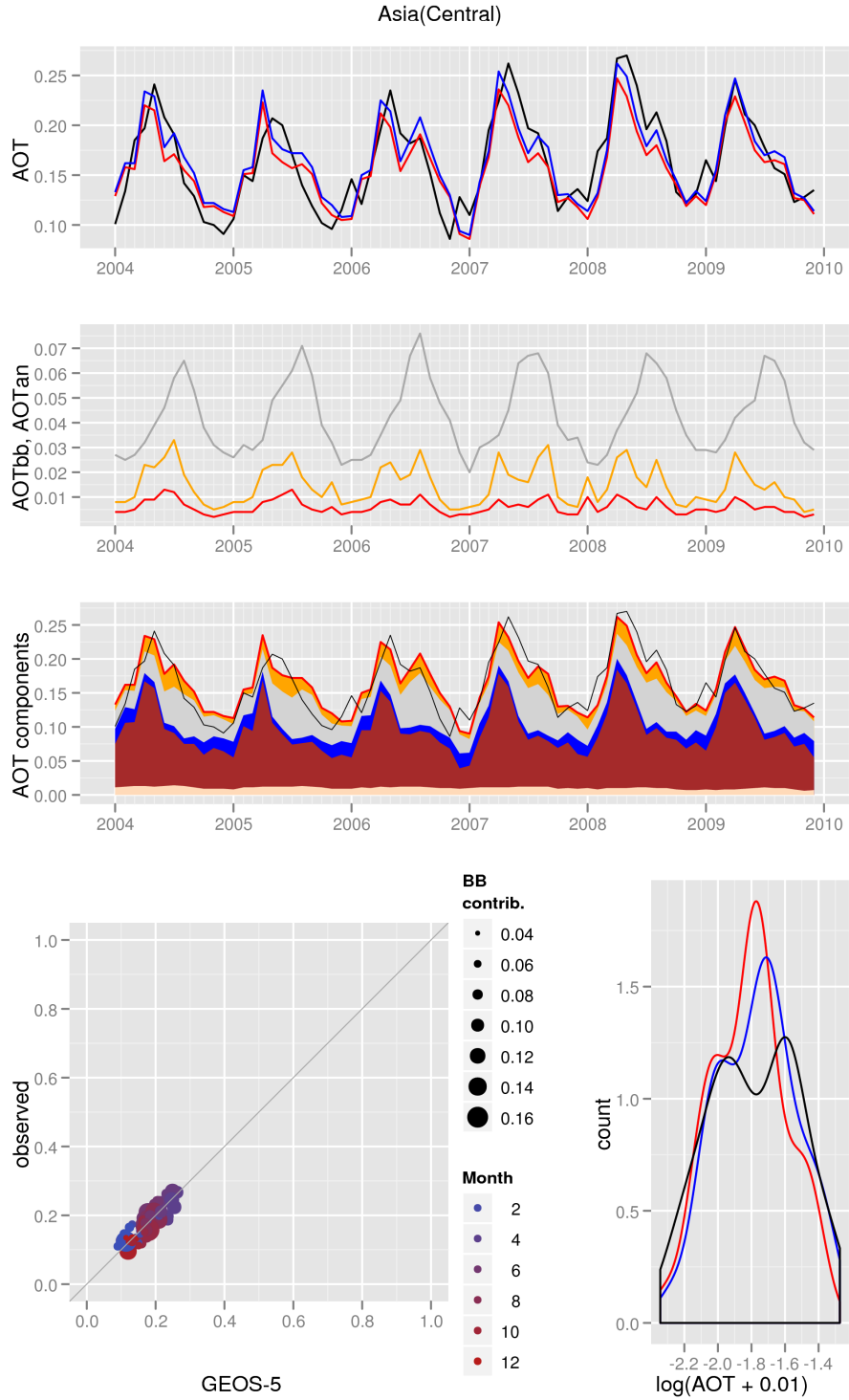
(b) GEOS-5 and NNR-AOT/Terra
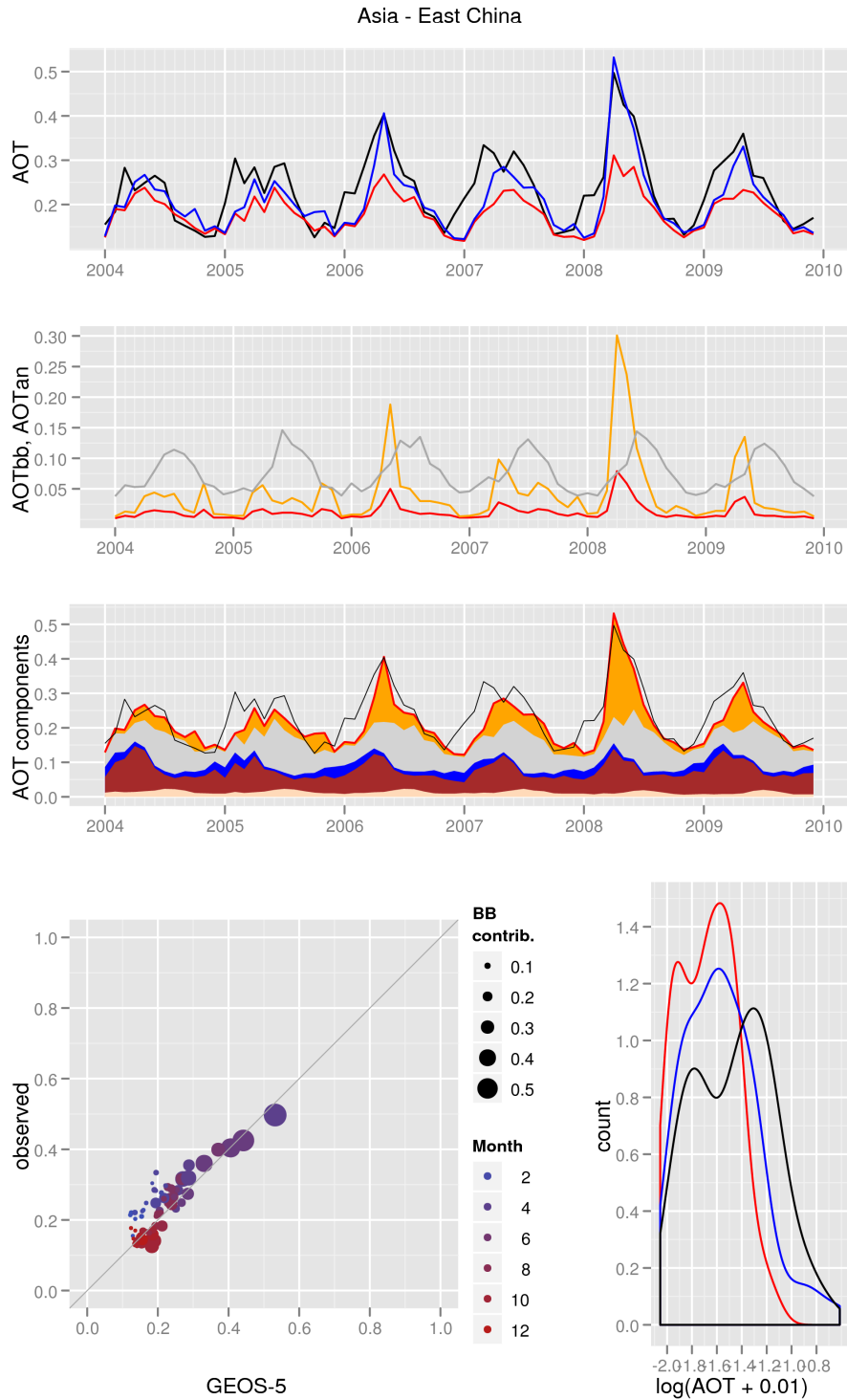
Asia - East China

(a) GEOS-5 and NNR-AOT/Aqua

Figure B36: AOT diagnostics for the East China region.

Asia - East China
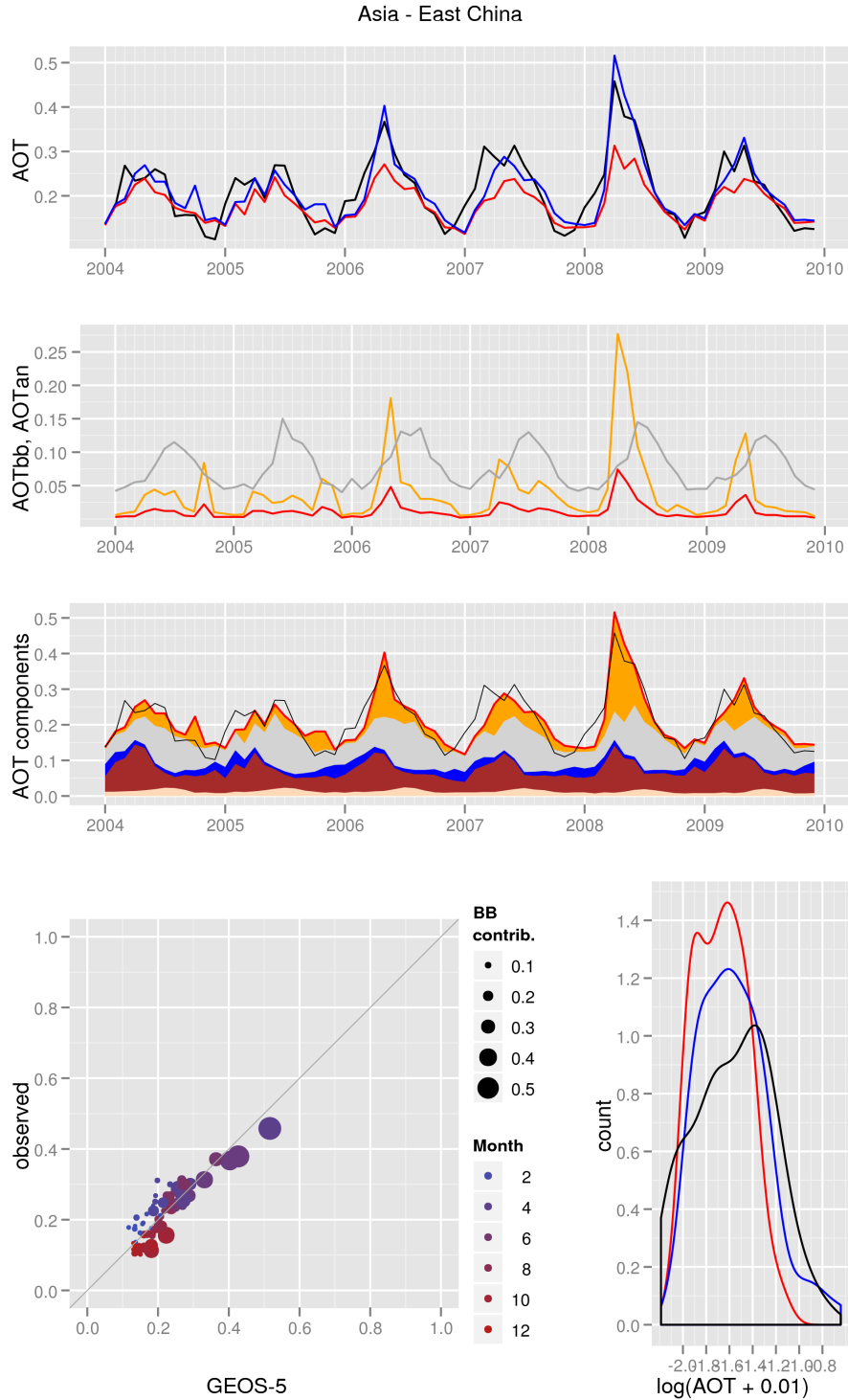
(b) GEOS-5 and NNR-AOT/Terra
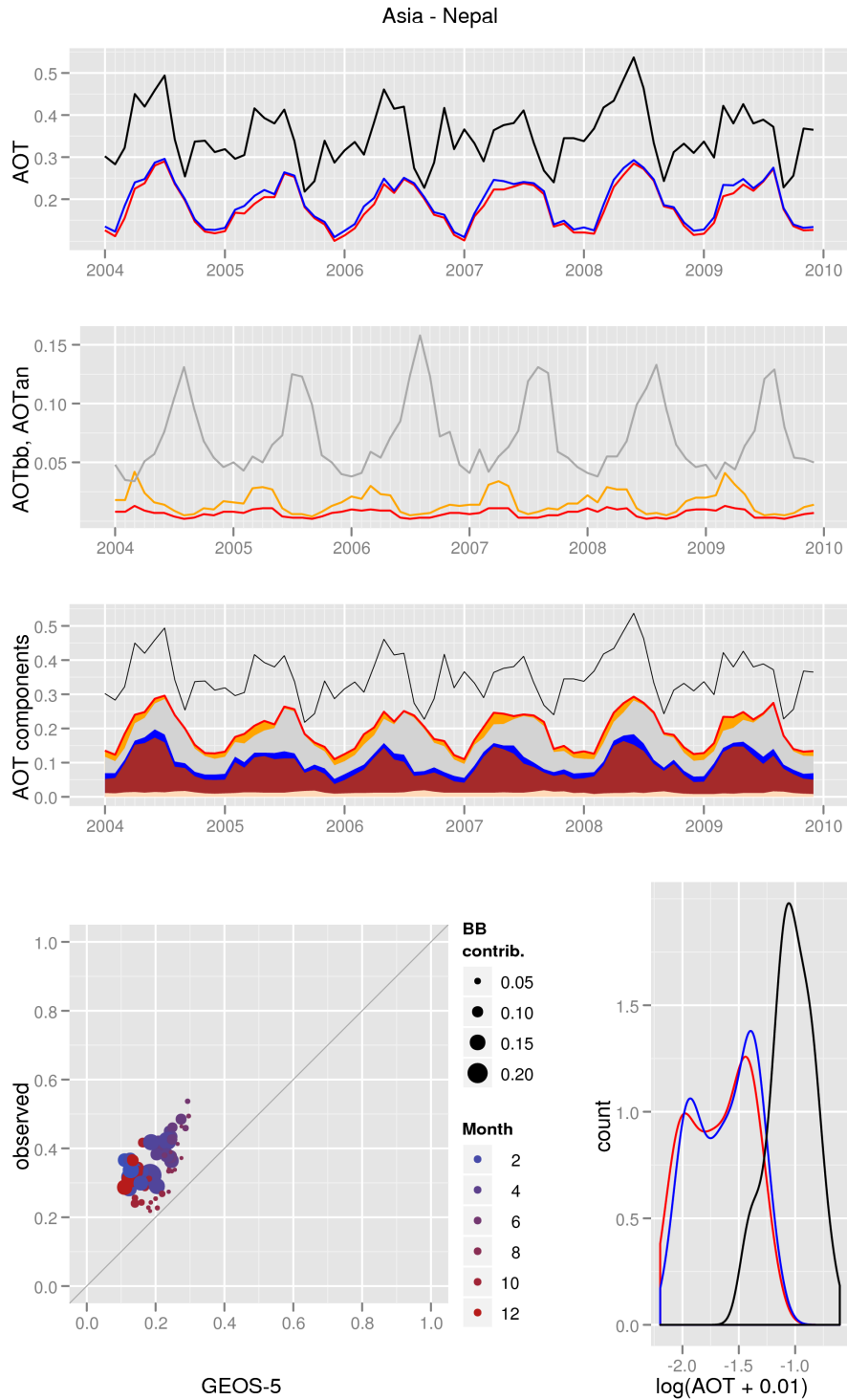
(a) GEOS-5 and NNR-AOT/Aqua

Figure B37: AOT diagnostics for the Nepal region.

Asia - Nepal

(b) GEOS-5 and NNR-AOT/Terra

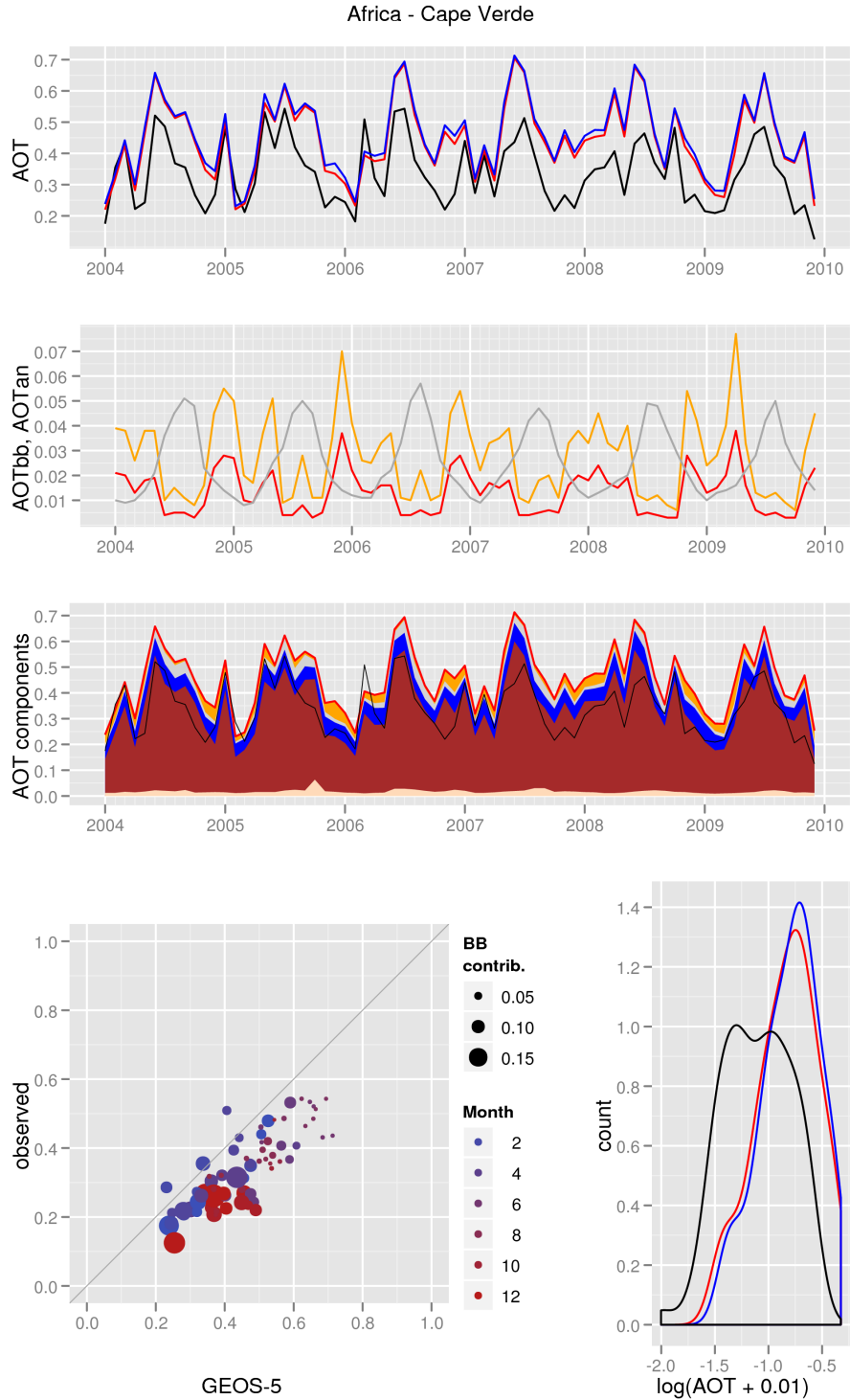91
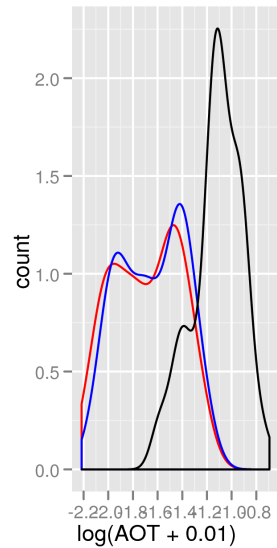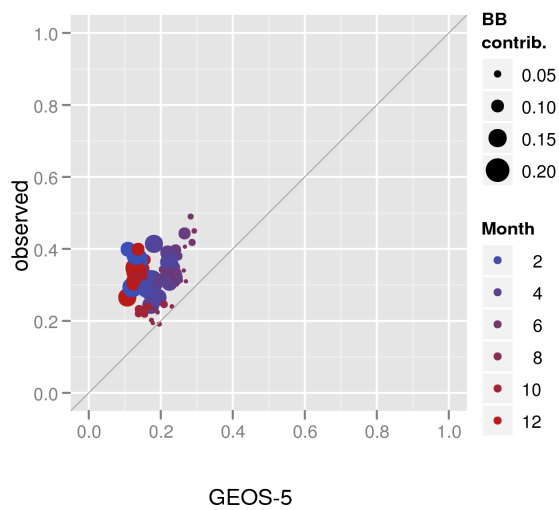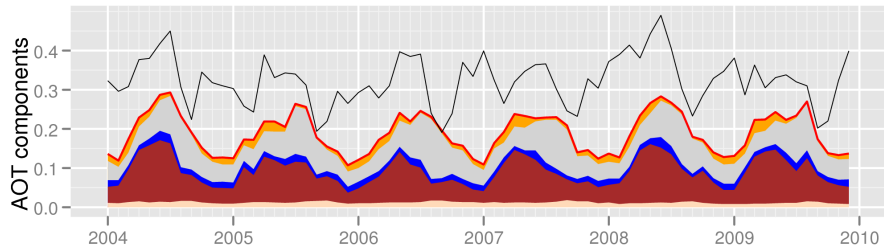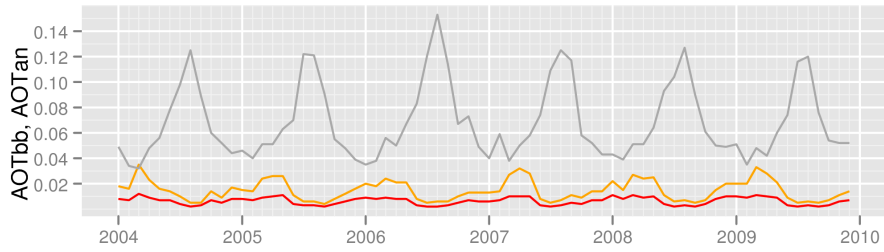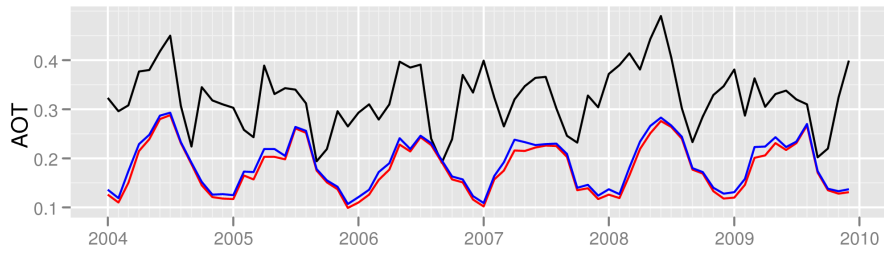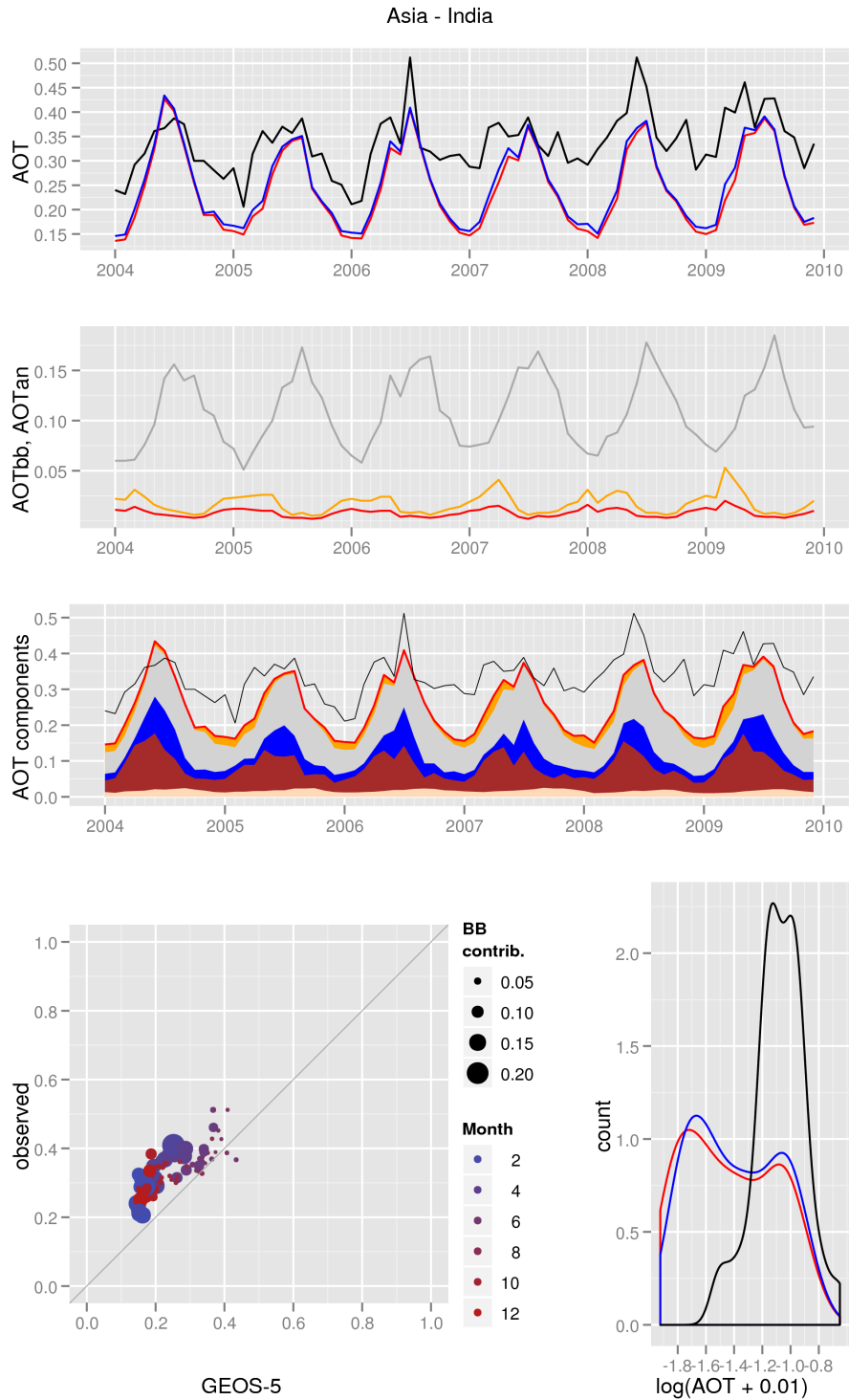
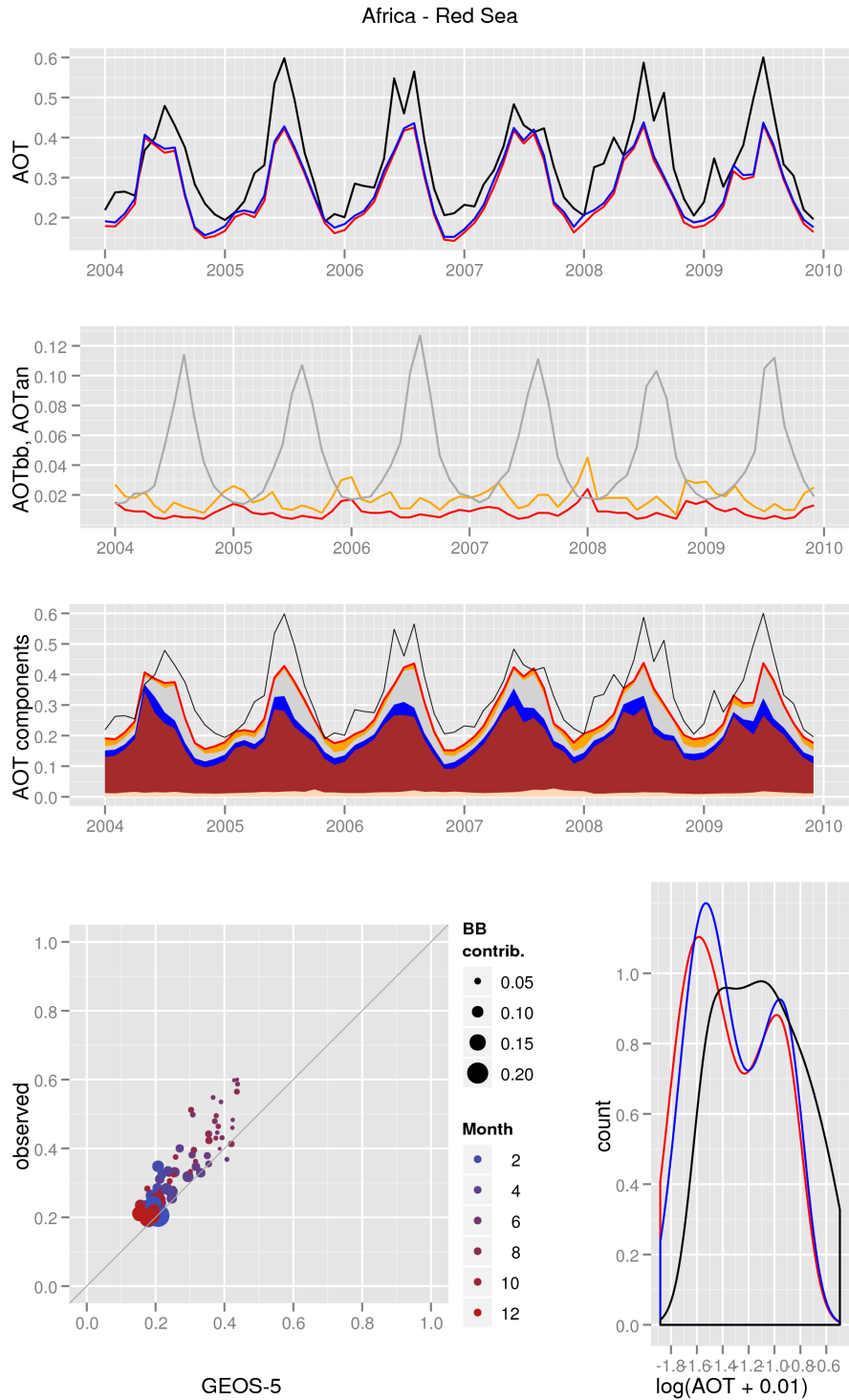Figure B38: AOT diagnostics for the India region.

Asia - India

(b) GEOS-5 and NNR-AOT/Terra

93
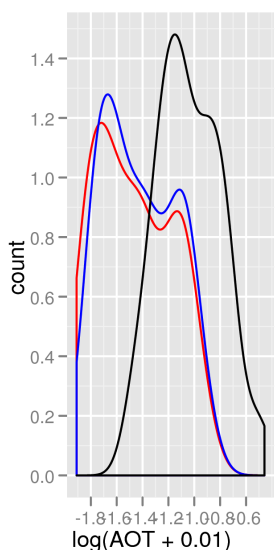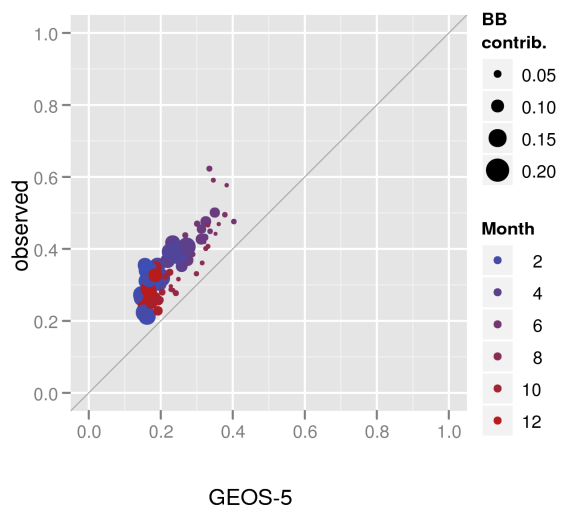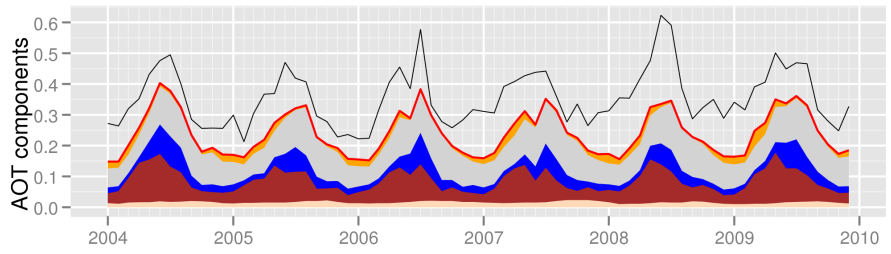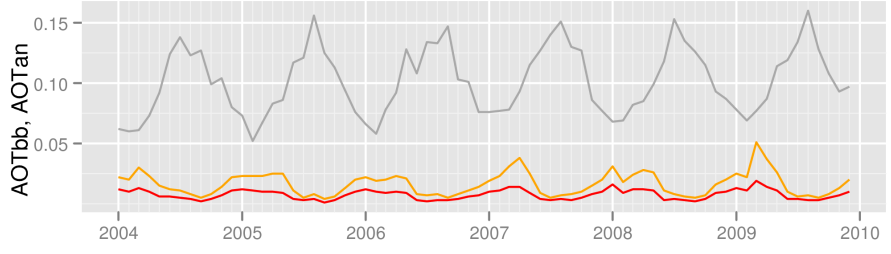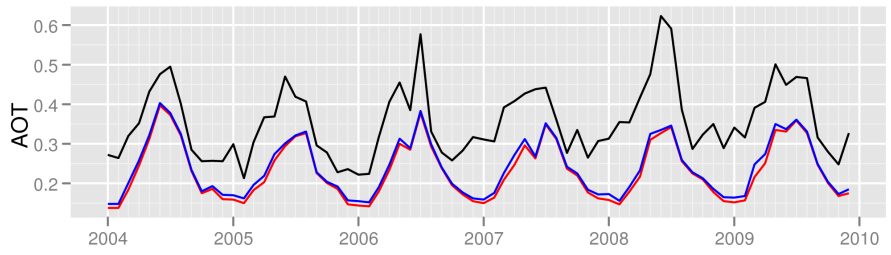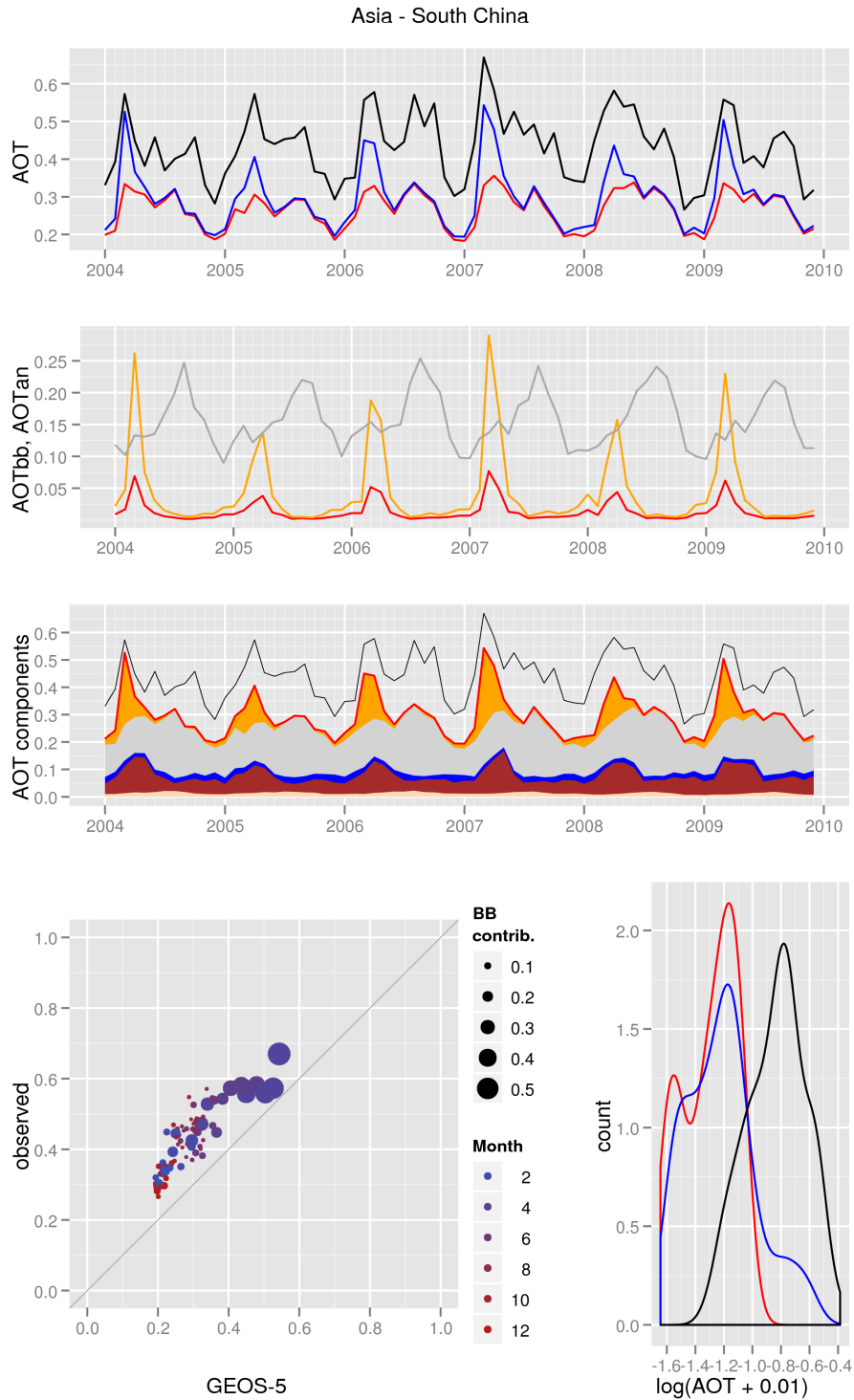
(a) GEOS-5 and NNR-AOT/Aqua

Figure B39: AOT diagnostics for the South China region.
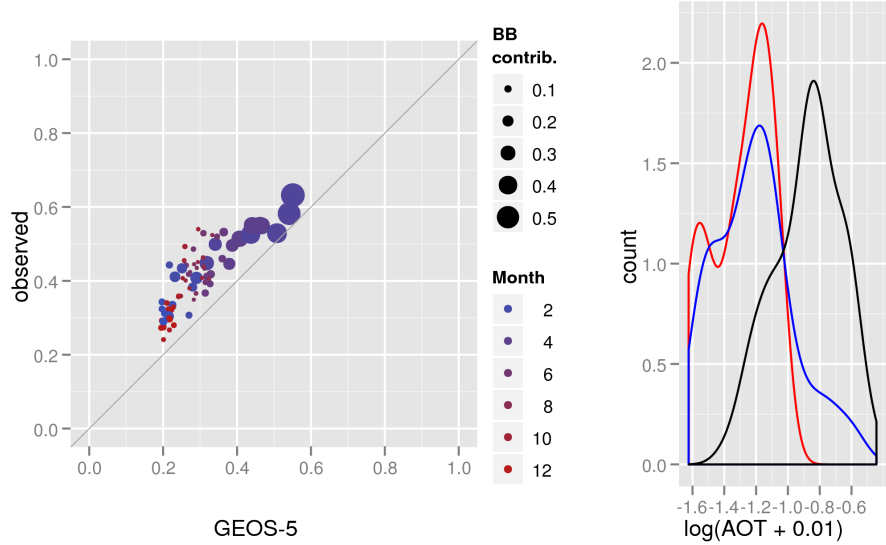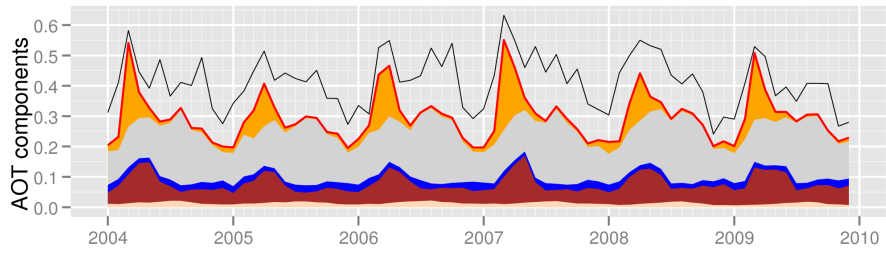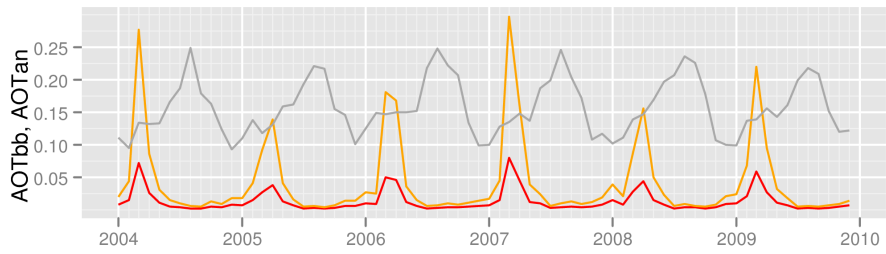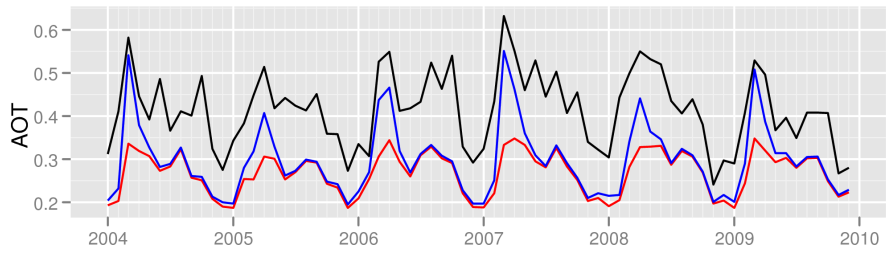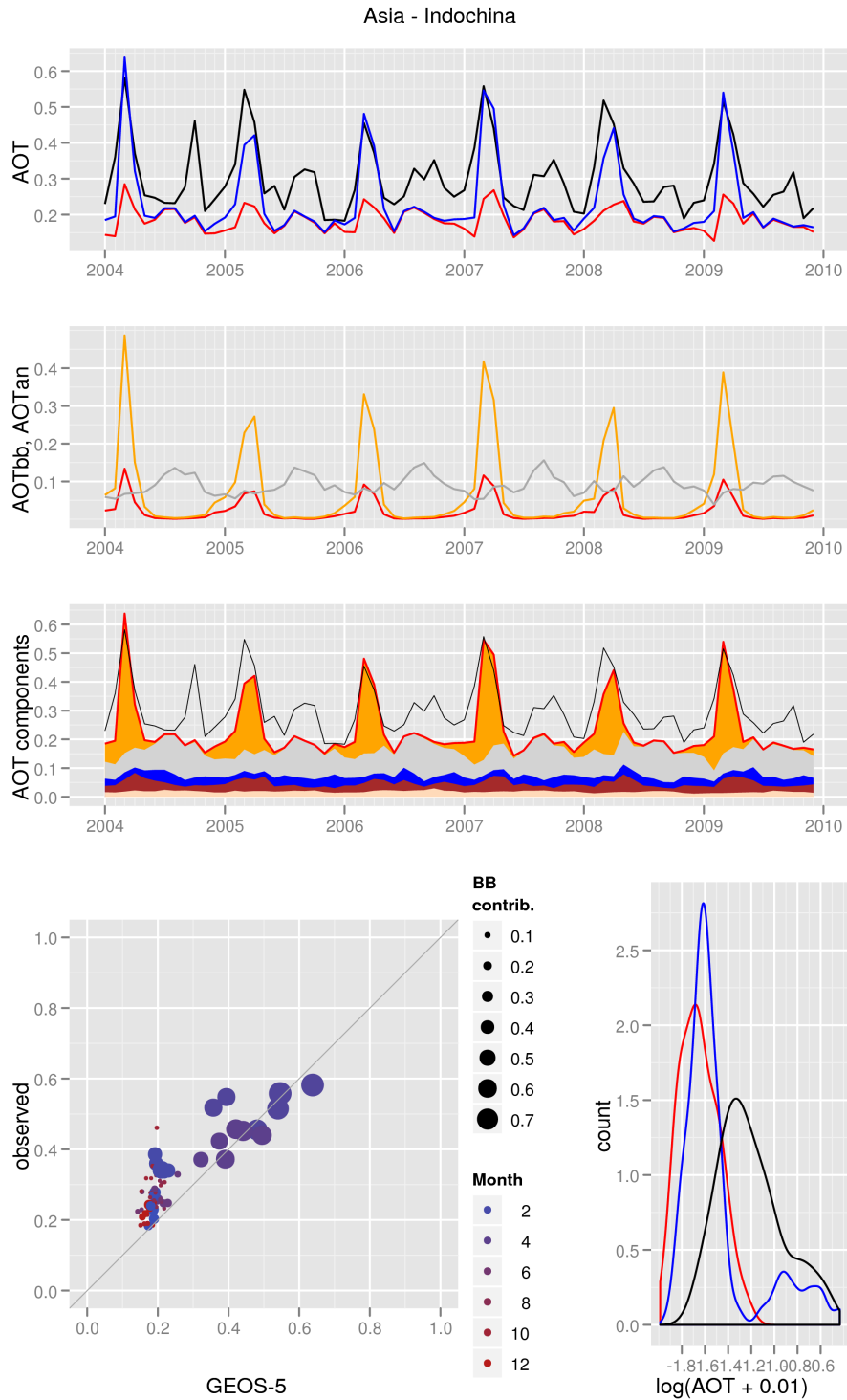
(b) GEOS-5 and NNR-AOT/Terra

Figure B40: AOT diagnostics for the Indochina region.

Asia - Indochina
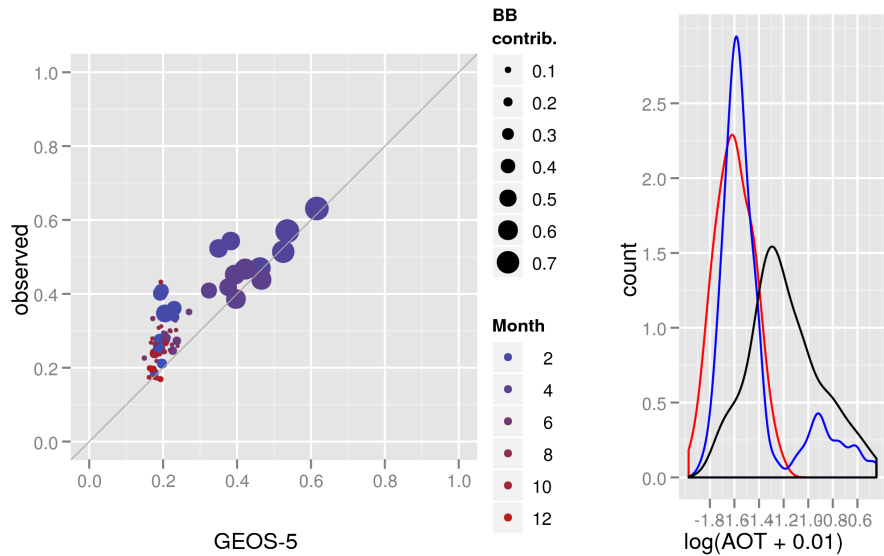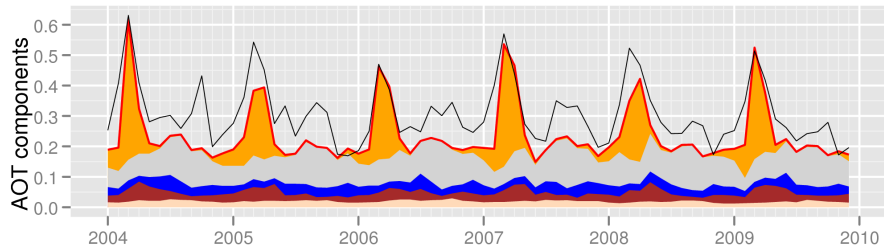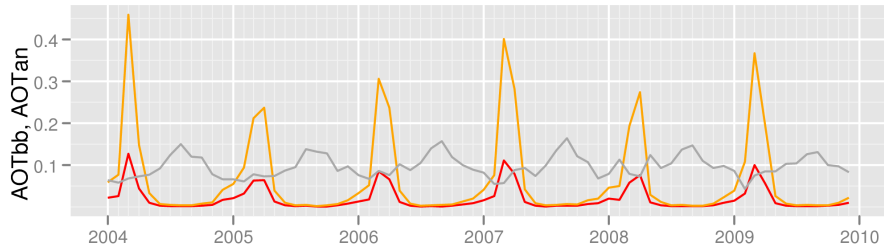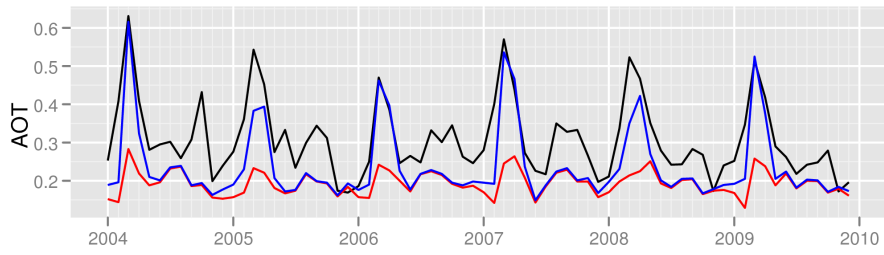
(b) GEOS-5 and NNR-AOT/Terra
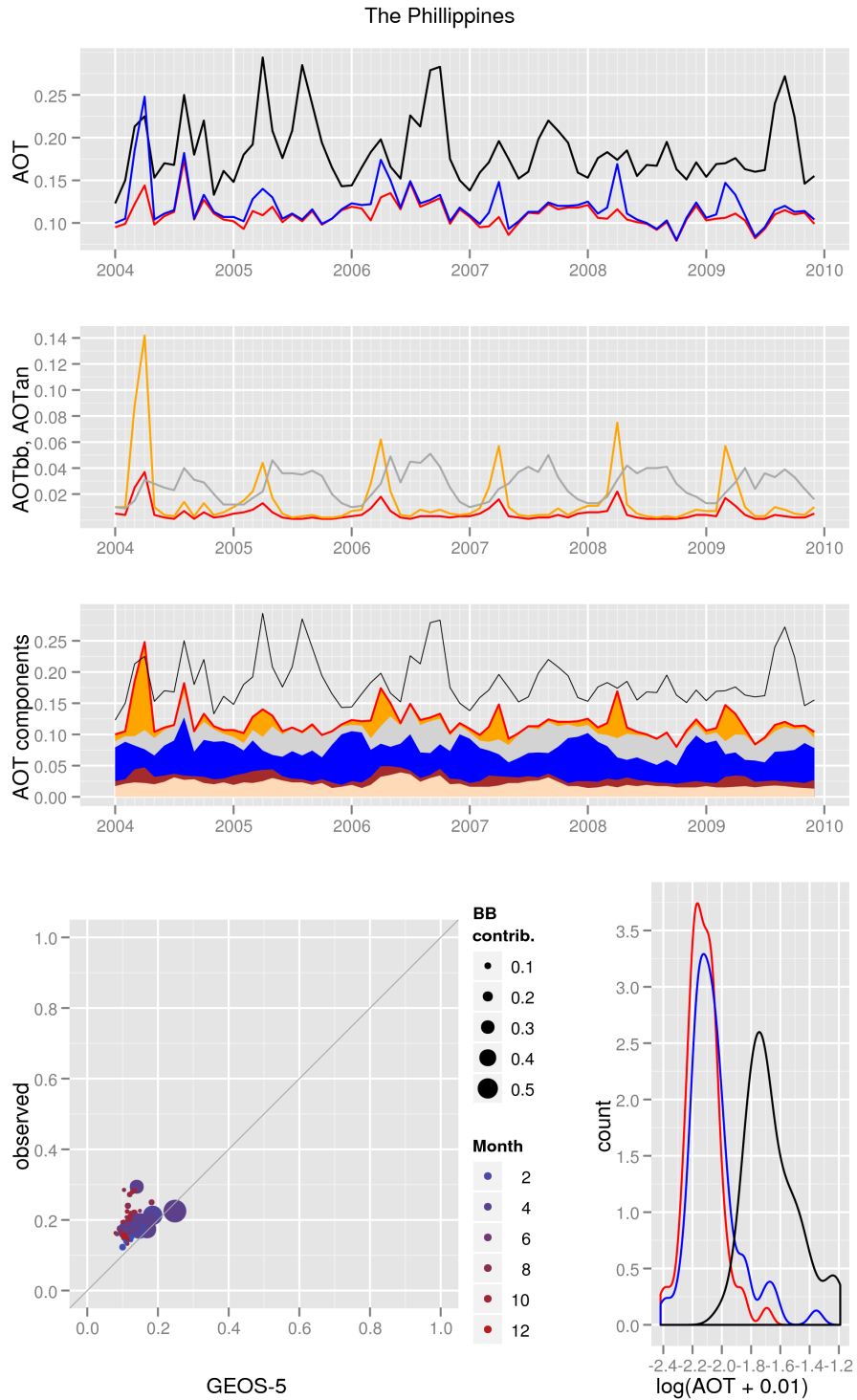
(a) GEOS-5 and NNR-AOT/Aqua

Figure B41: AOT diagnostics for the The Philippines region.

The Phillippines
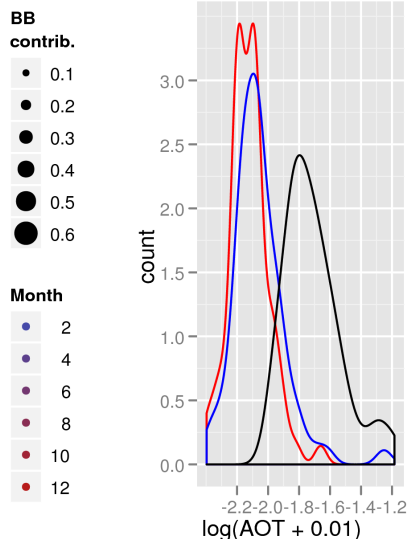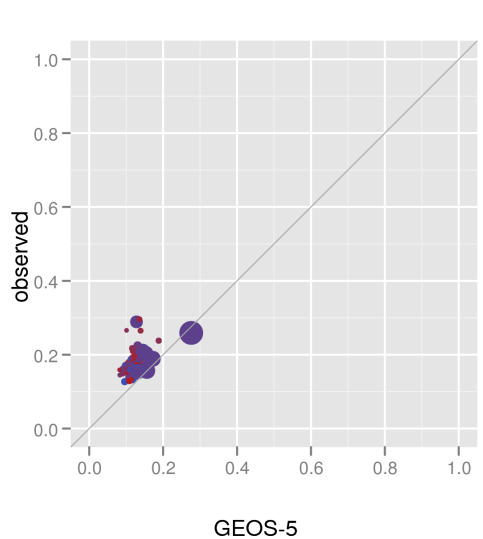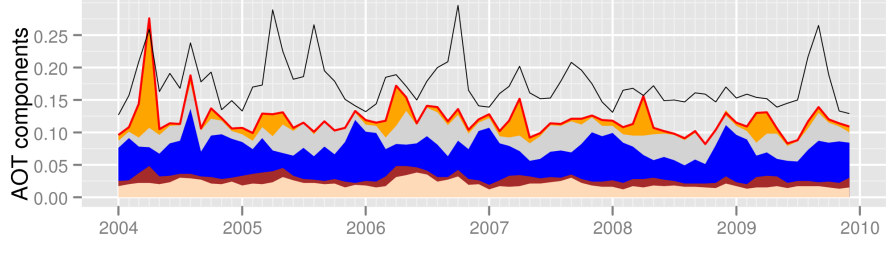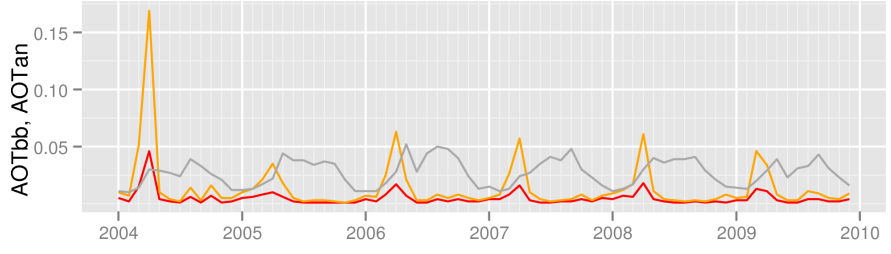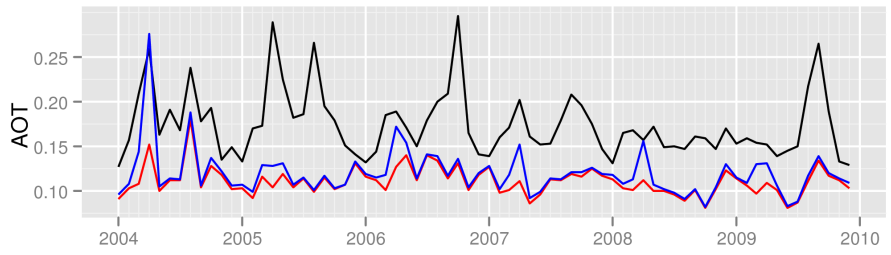
(b) GEOS-5 and NNR-AOT/Terra
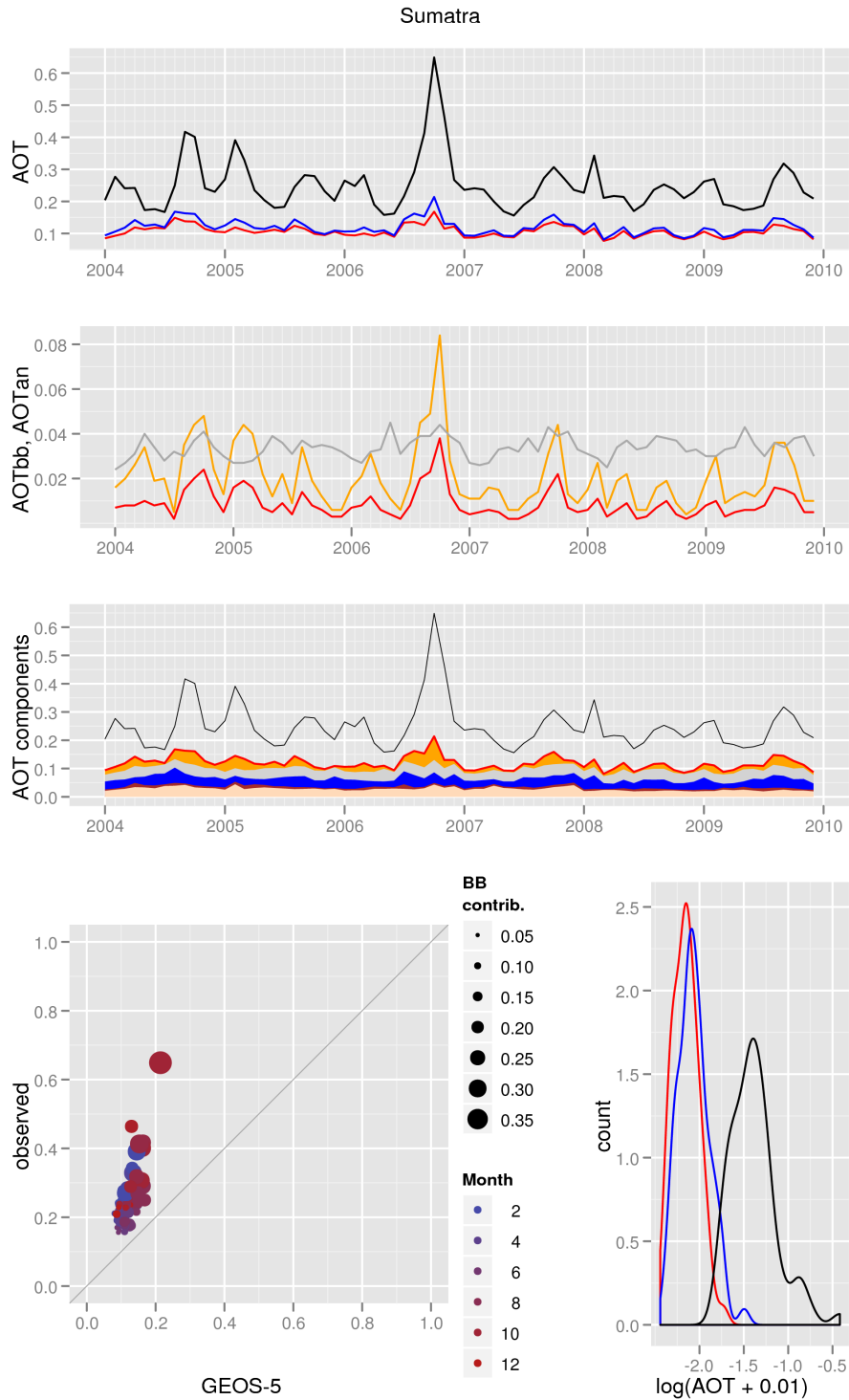
(a) GEOS-5 and NNR-AOT/Aqua

Figure B42: AOT diagnostics for the Sumatra region.
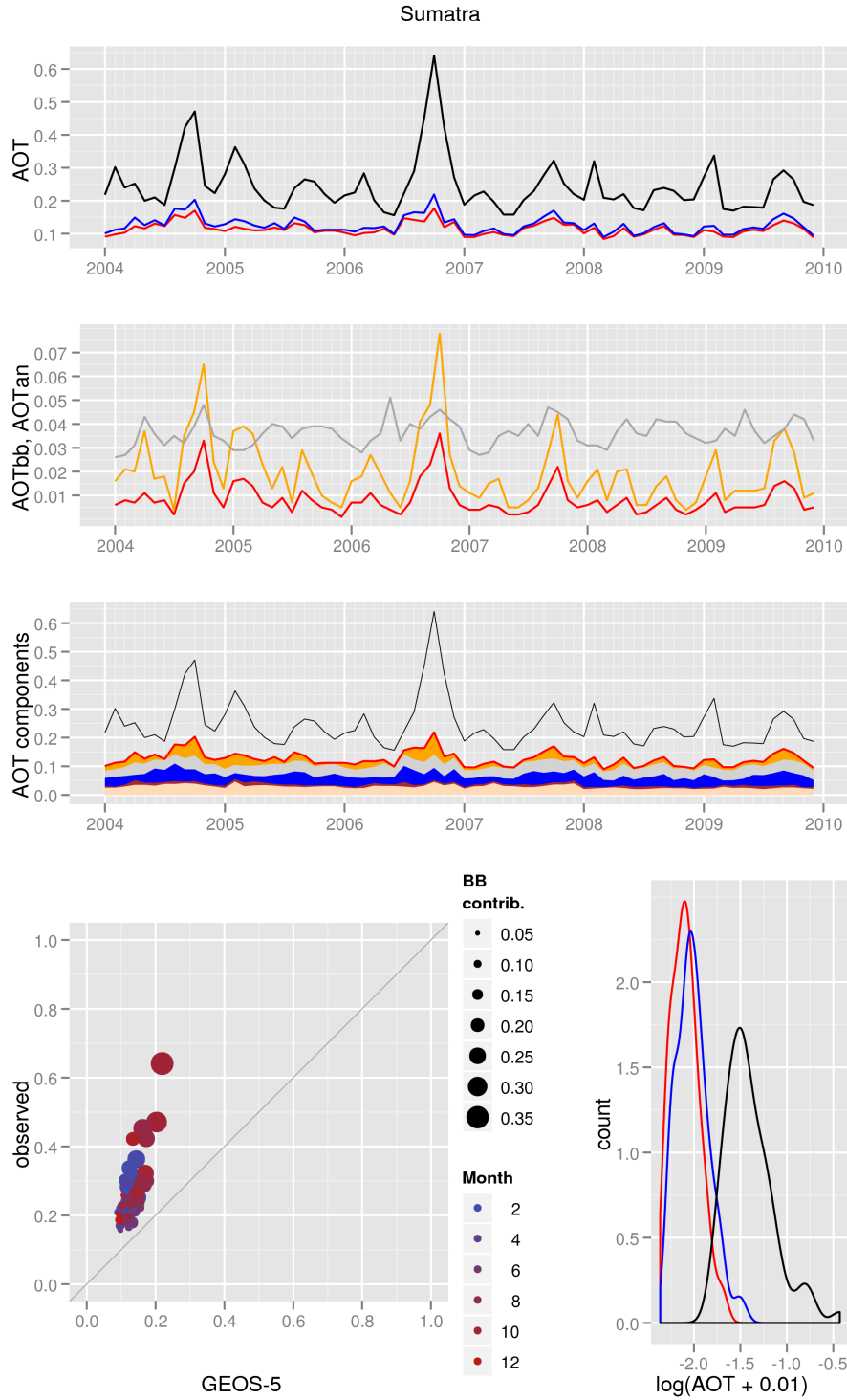
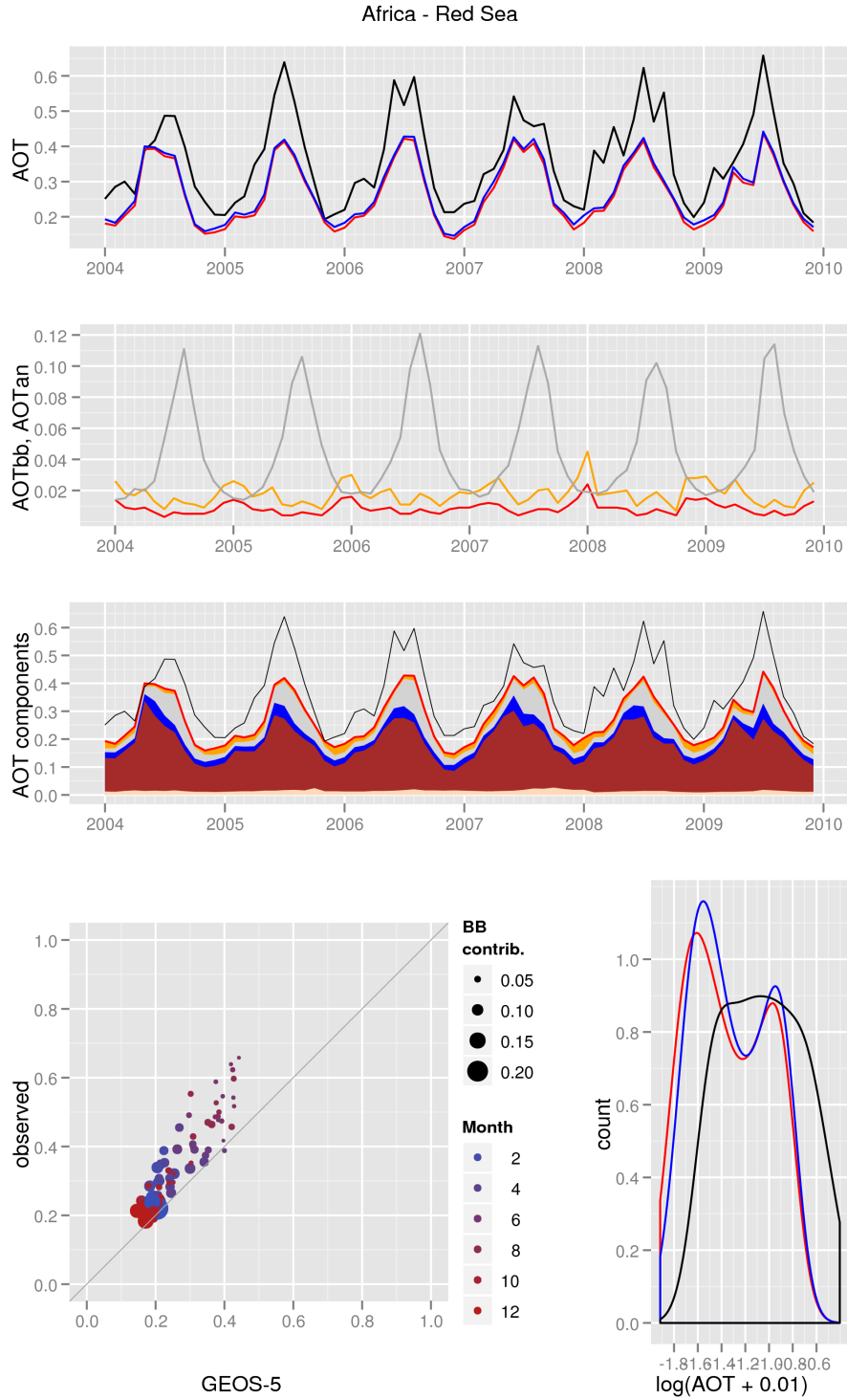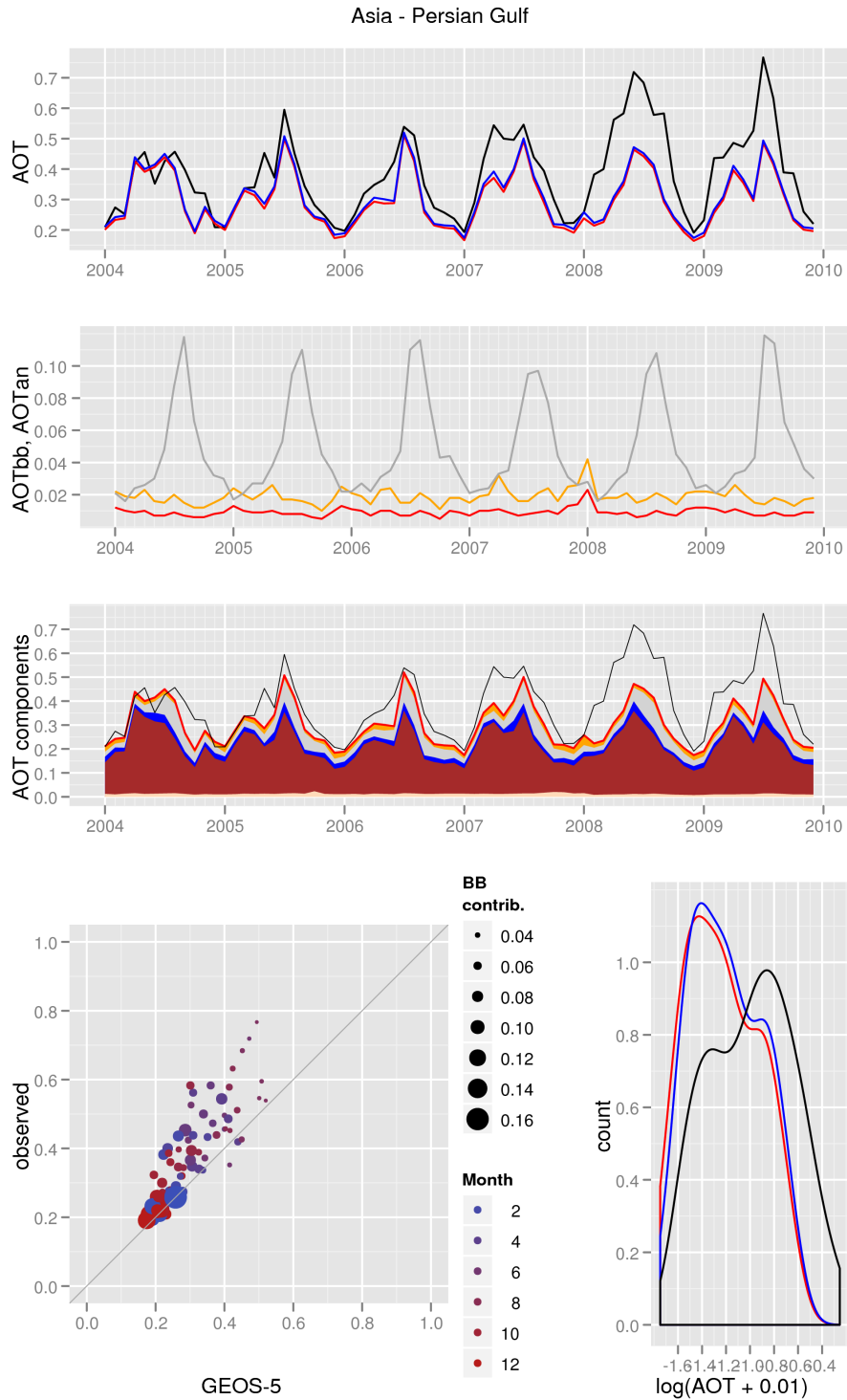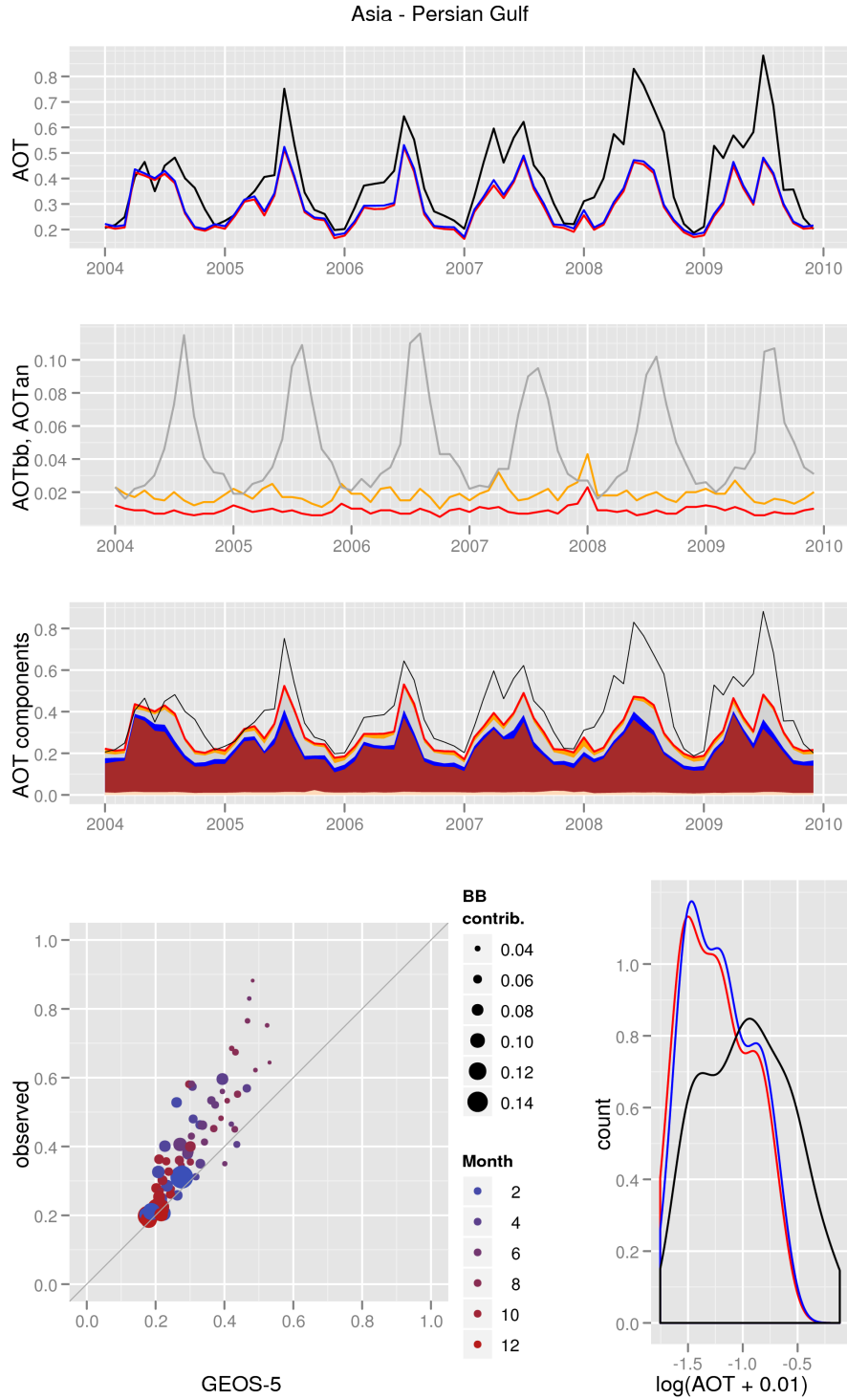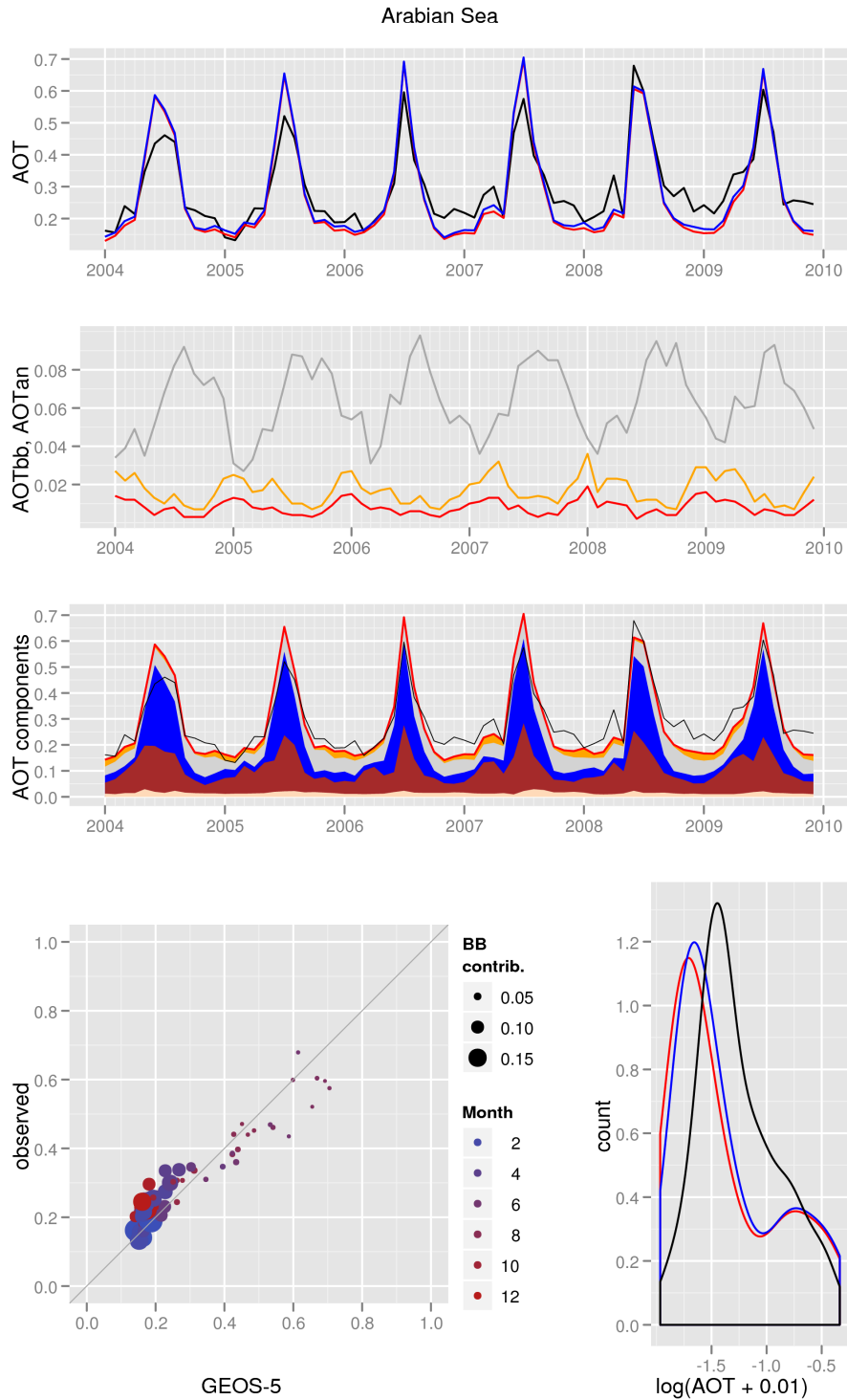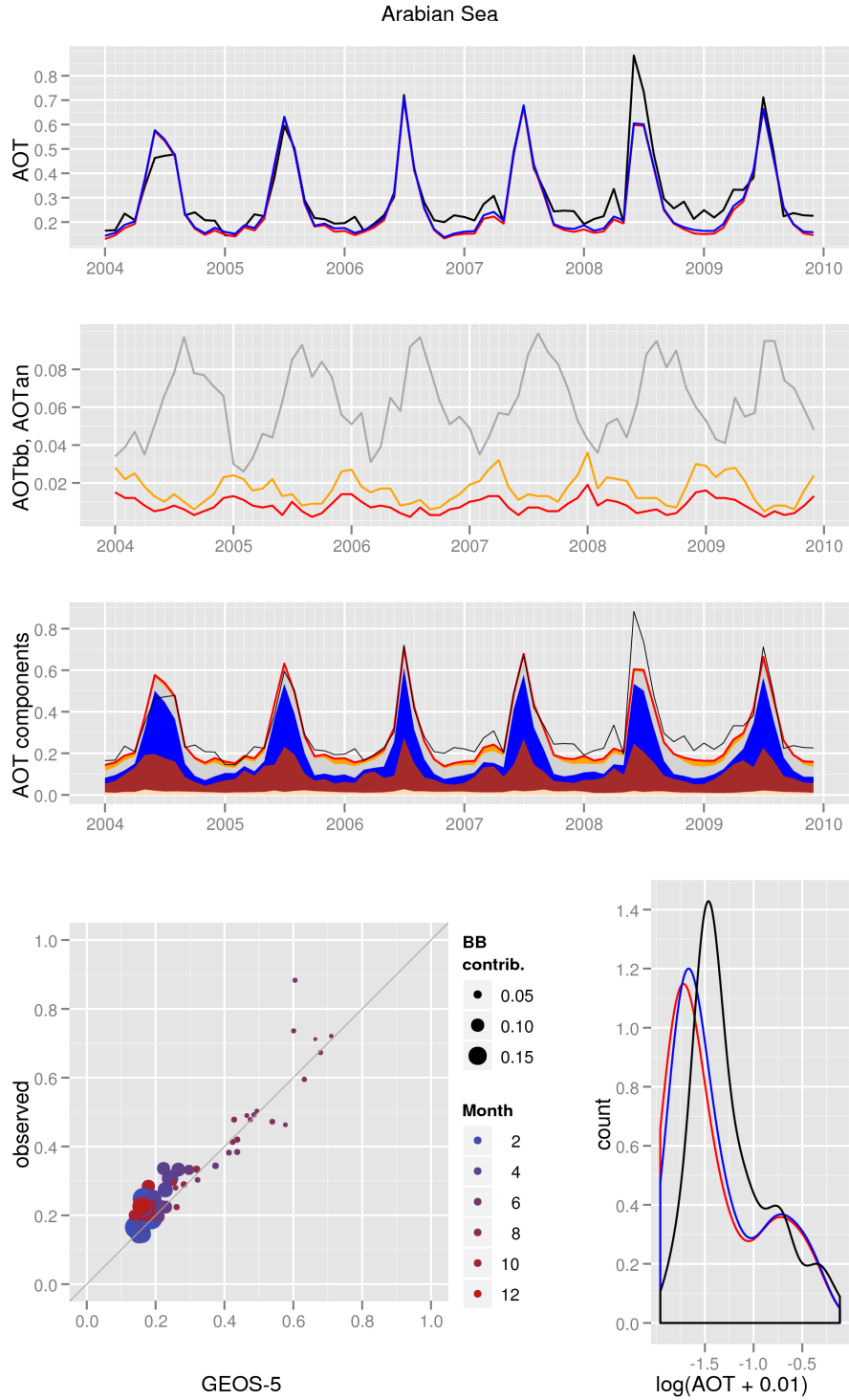(b) GEOS-5 and NNR-AOT/Terra

Borneo

(a) GEOS-5 and NNR-AOT/Aqua

Figure B43: AOT diagnostics for the Borneo region.

(b) GEOS-5 and NNR-AOT/Terra

103
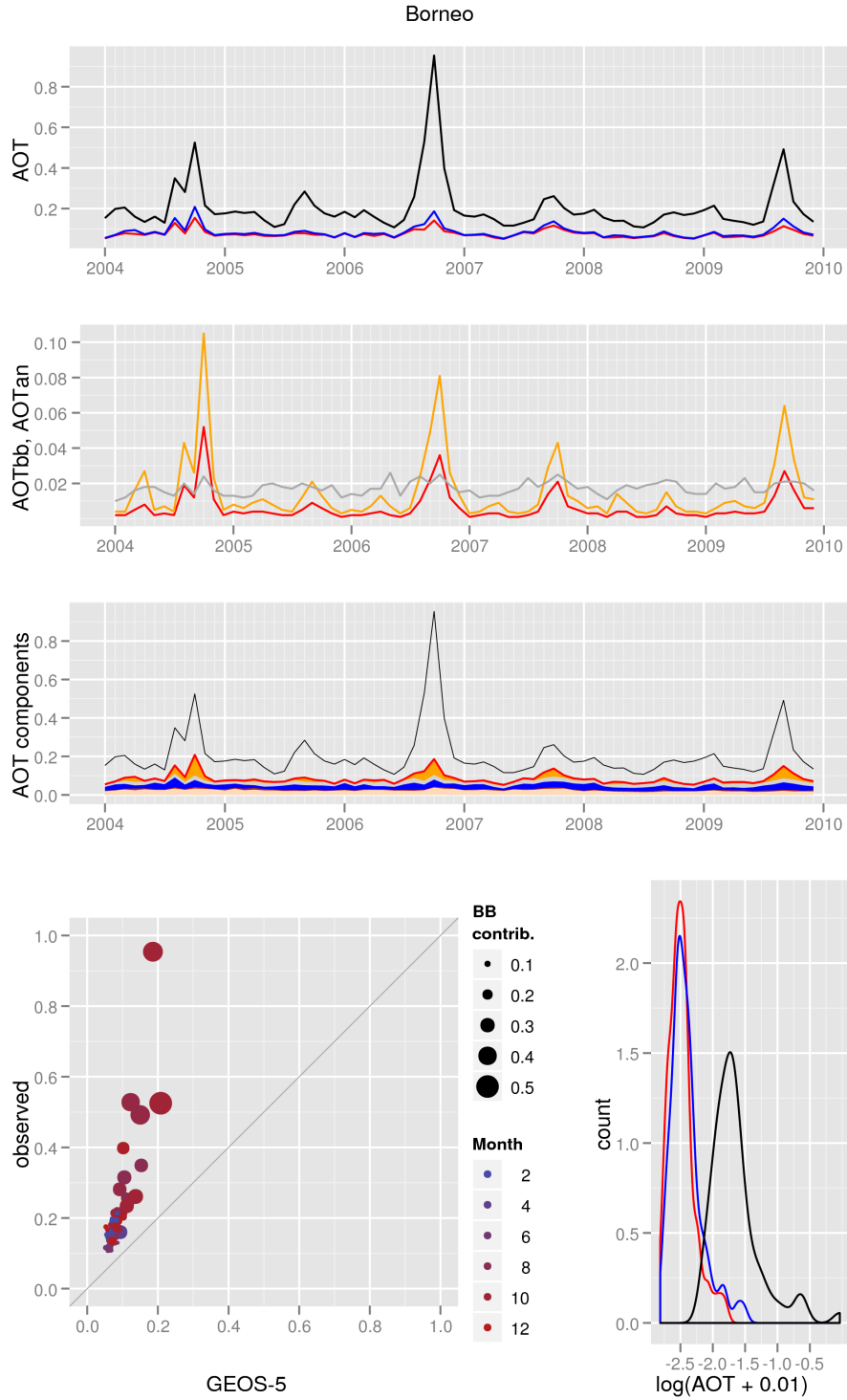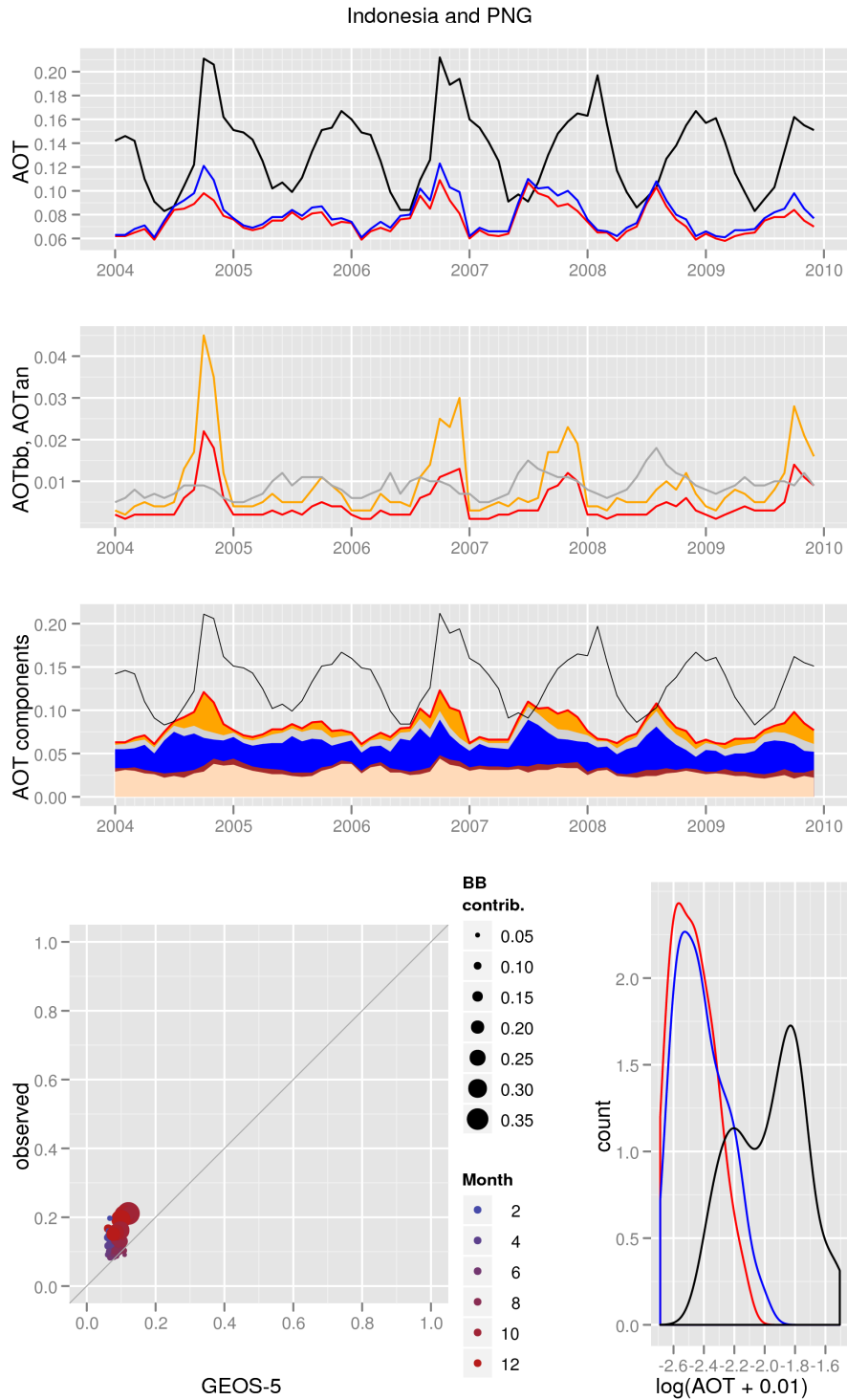
Figure B44: AOT diagnostics for the Indonesia and PNG region.
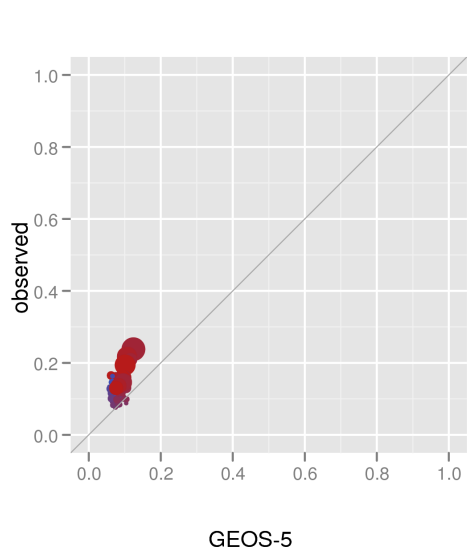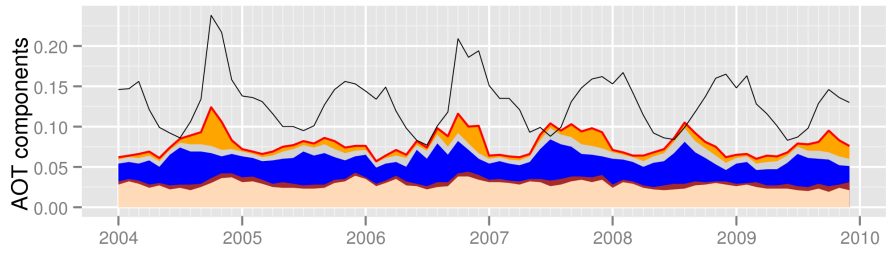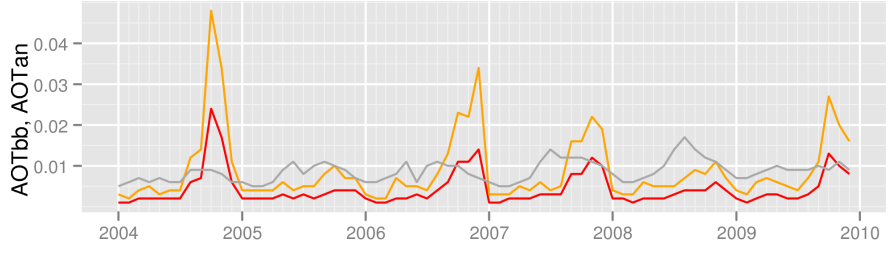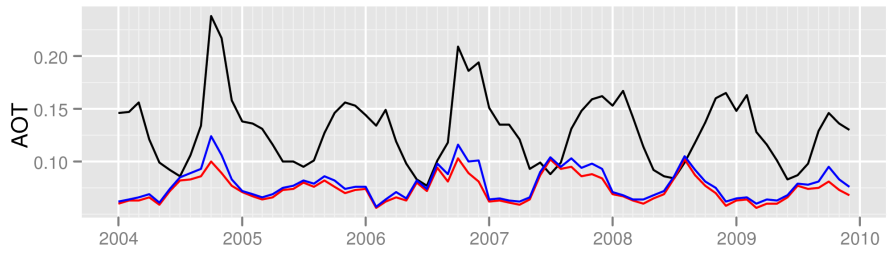
Indonesia and PNG

(b) GEOS-5 and NNR-AOT/Terra

105
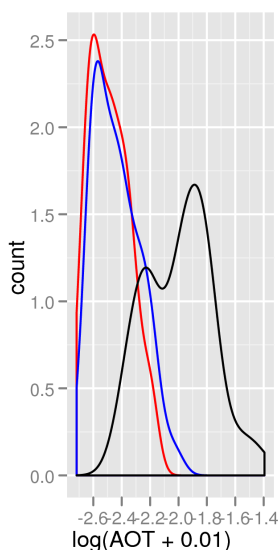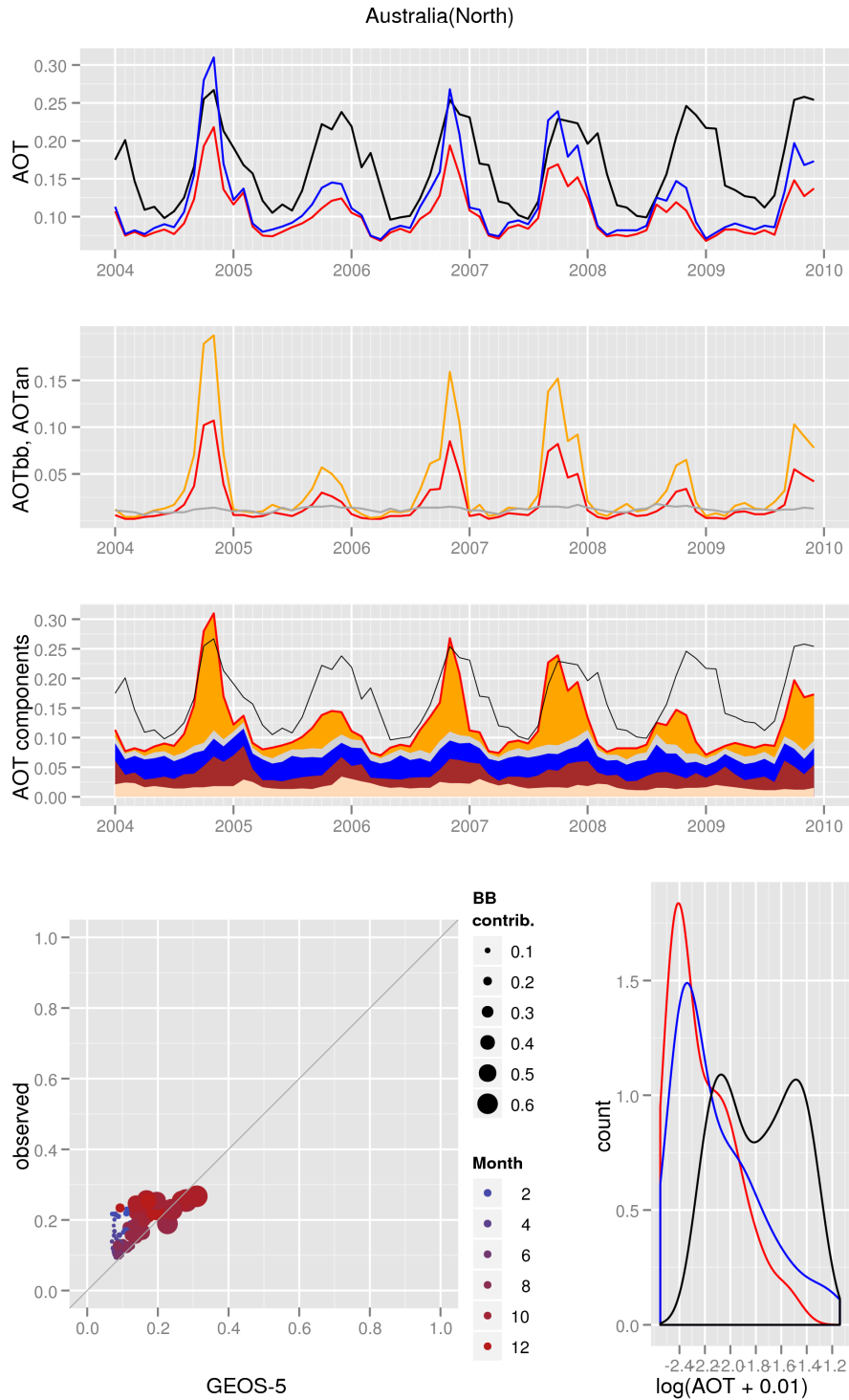
(a) GEOS-5 and NNR-AOT/Aqua

Figure B45: AOT diagnostics for the North Australia region.
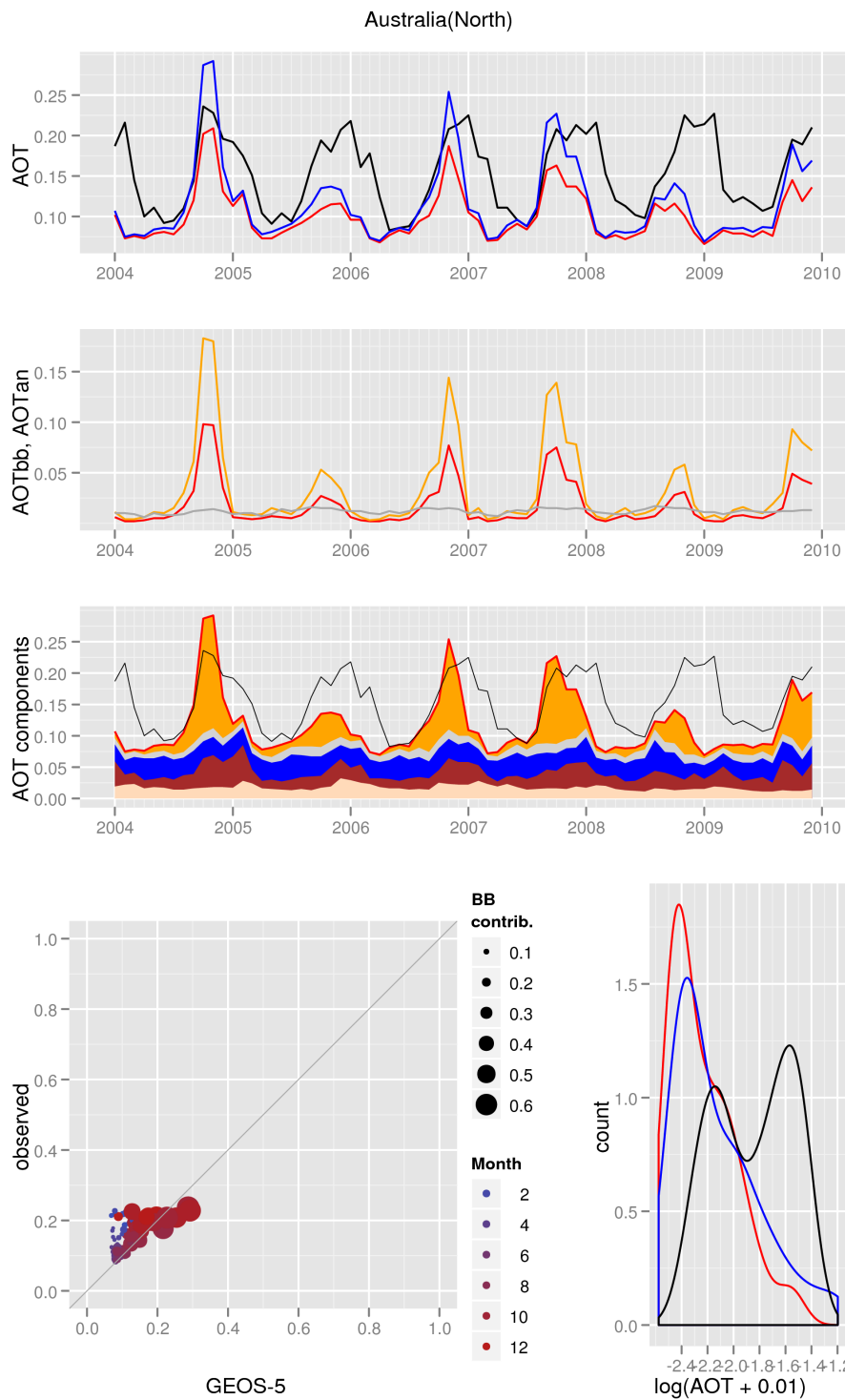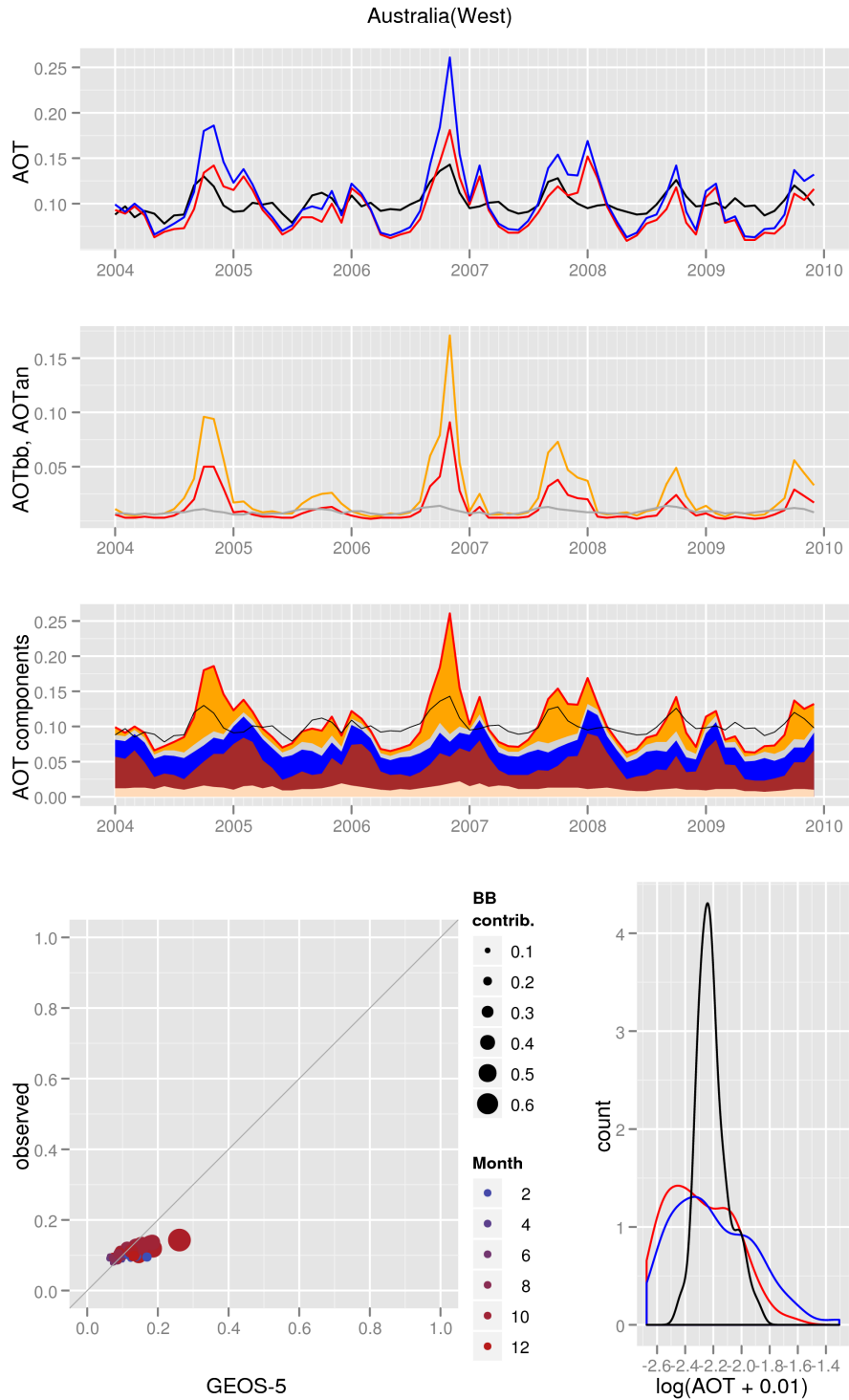
Australia(North)

(b) GEOS-5 and NNR-AOT/Terra

Figure B46: AOT diagnostics for the West Australia region.
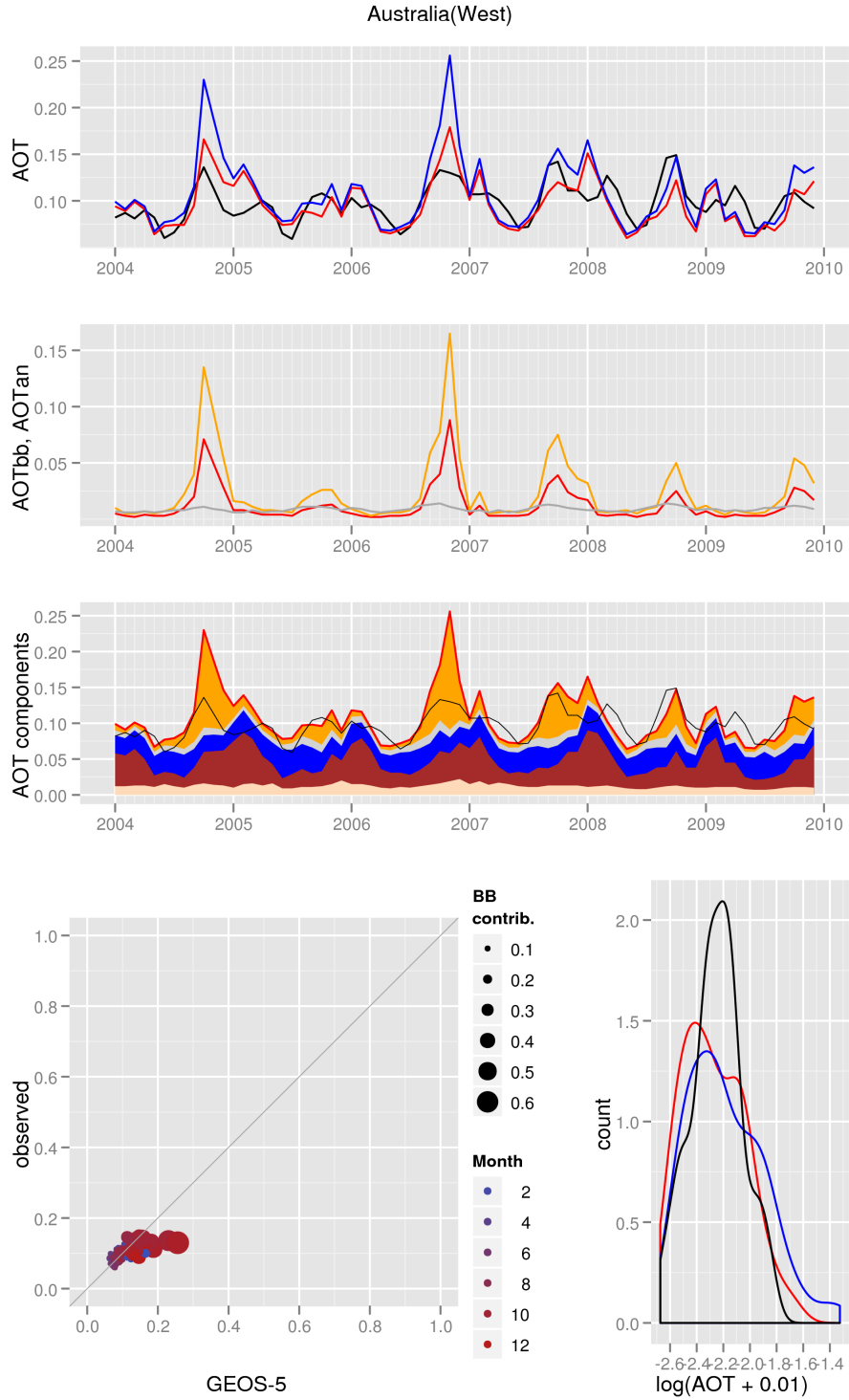
Australia(West)

(b) GEOS-5 and NNR-AOT/Terra
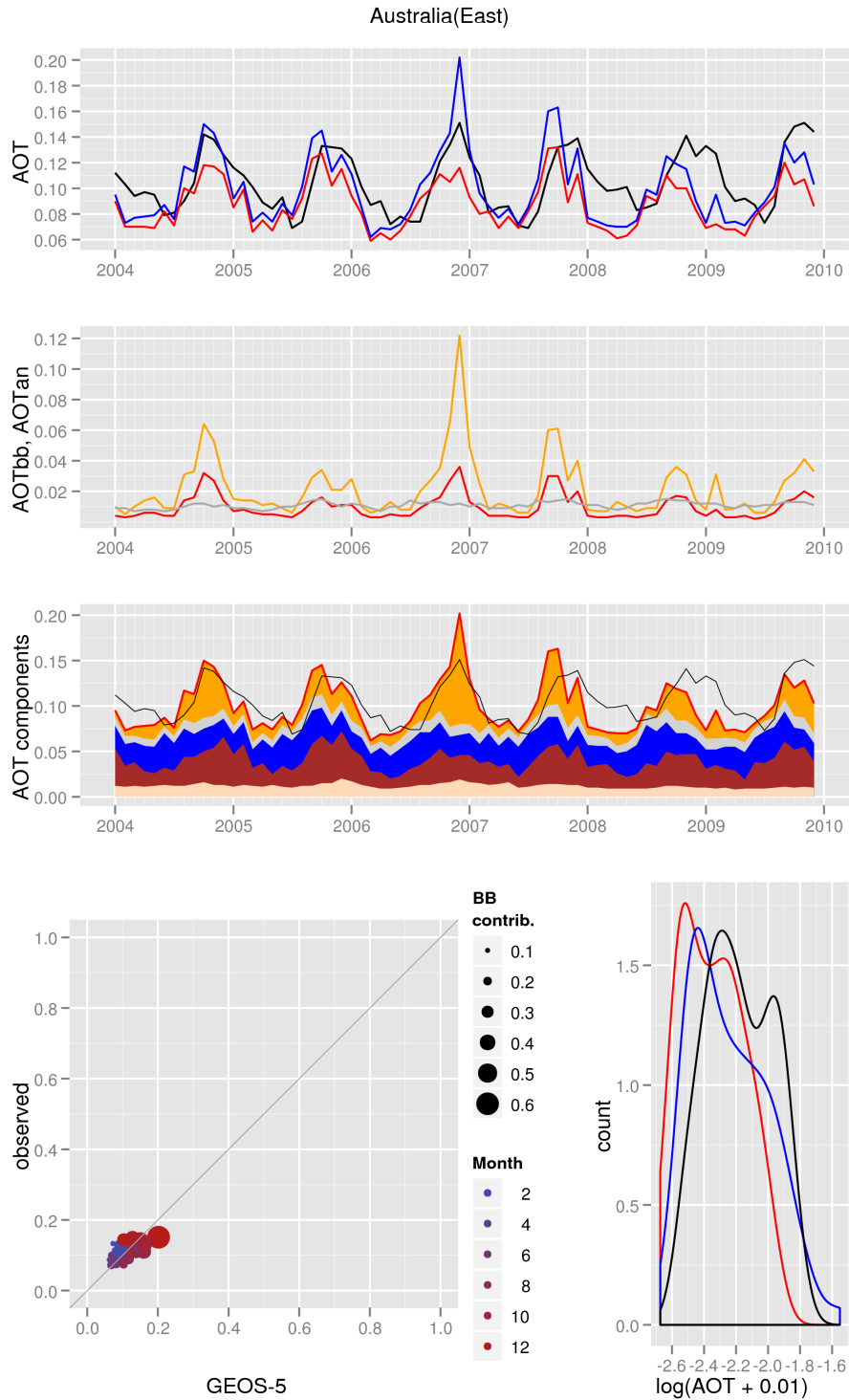
(a) GEOS-5 and NNR-AOT/Aqua

Figure B47: AOT diagnostics for the East Australia region.

Australia(East)

(b) GEOS-5 and NNR-AOT/Terra

111
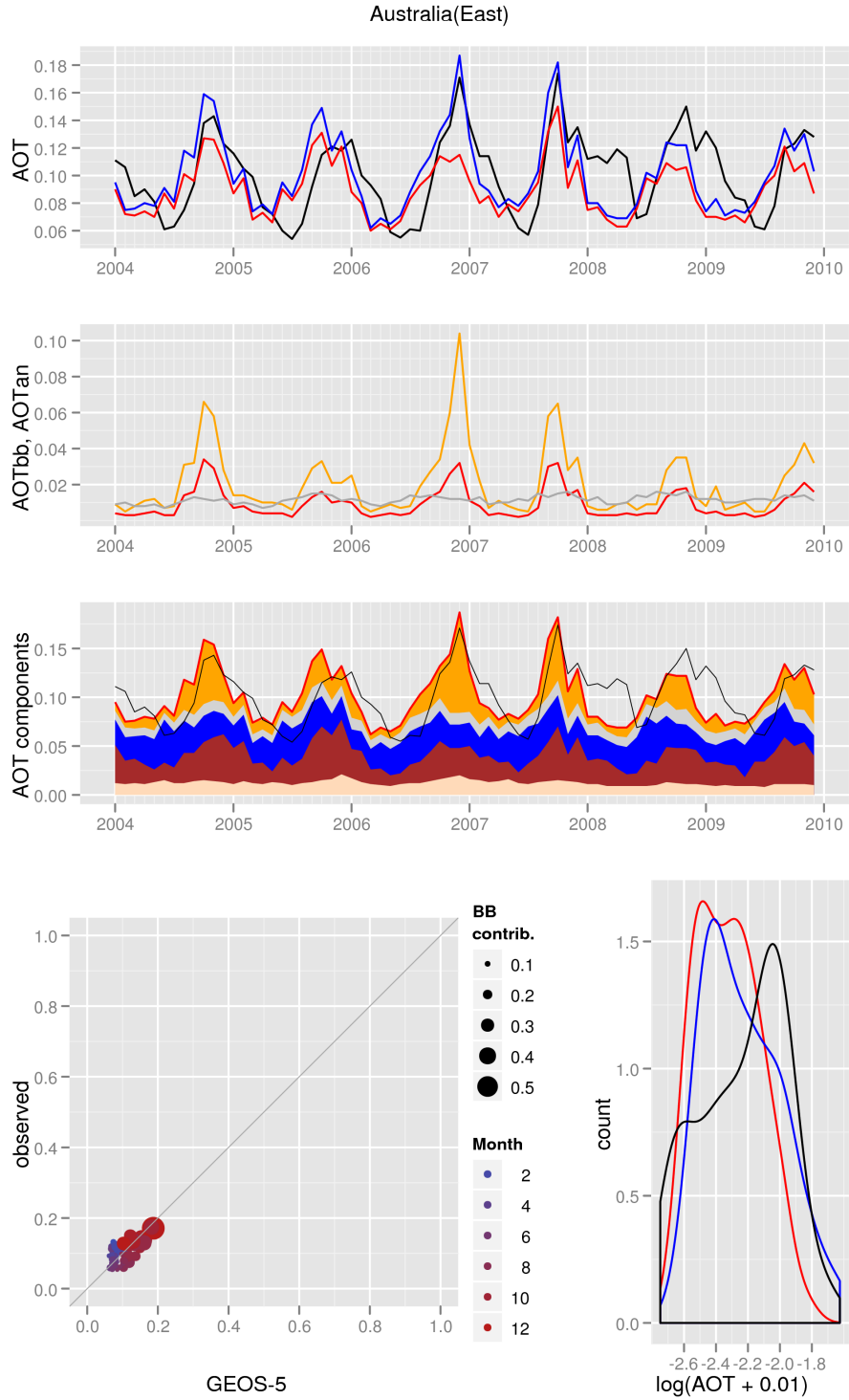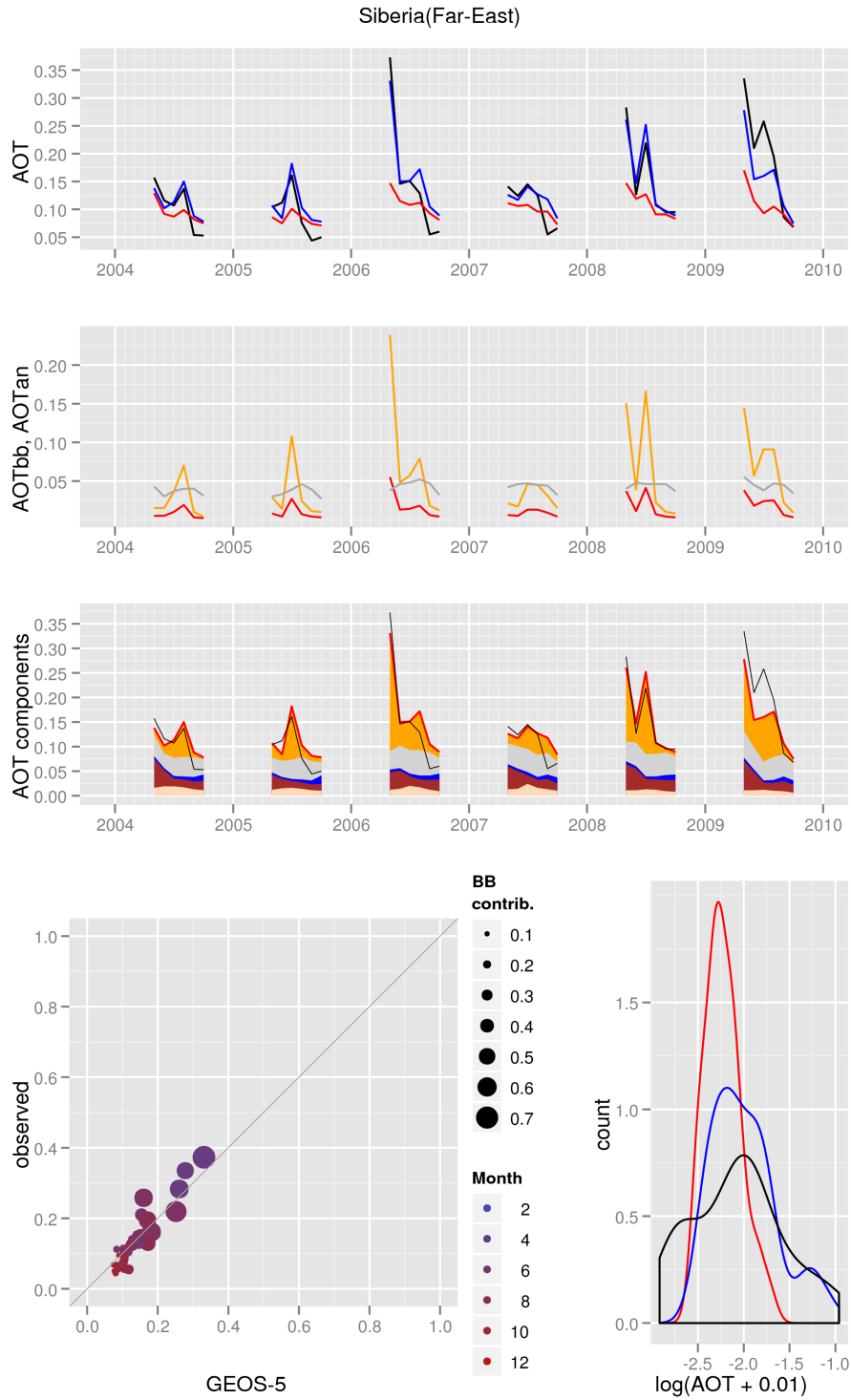
Figure B48: AOT diagnostics for the Siberia (Far East) region.

(a) GEOS-5 and NNR-AOT/Aqua

Siberia(Far-East)

(b) GEOS-5 and NNR-AOT/Terra

113

Africa - Sahara
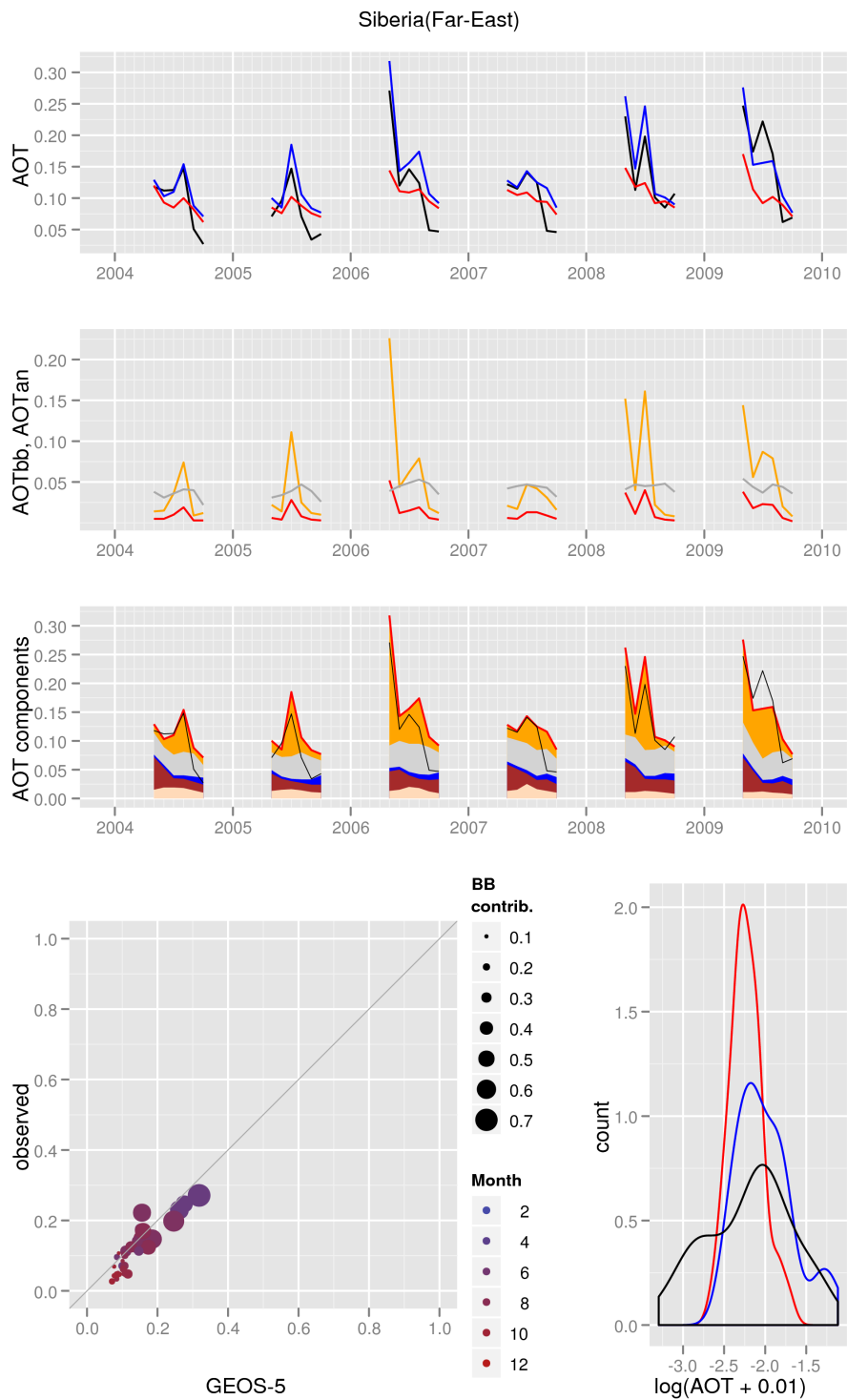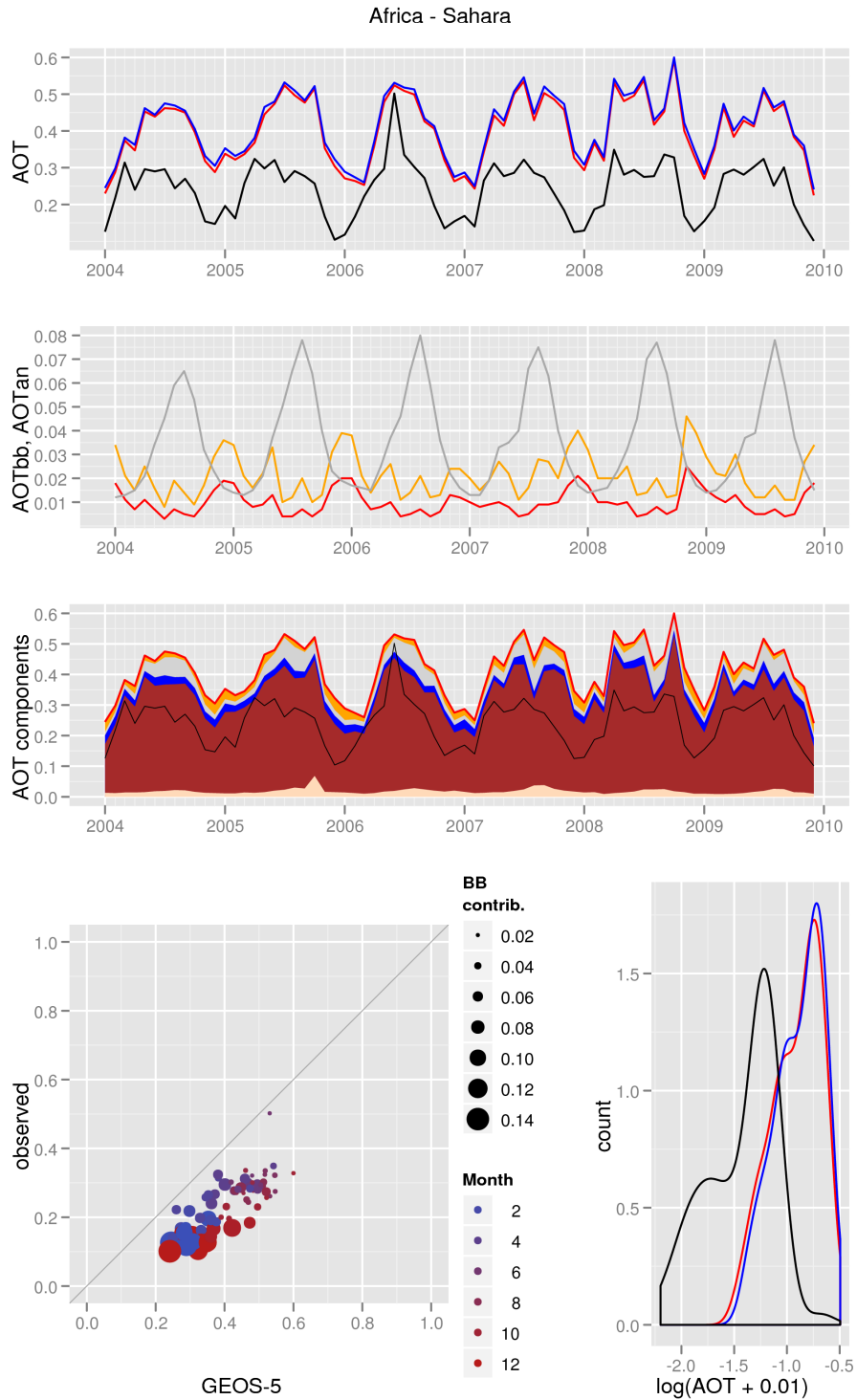
(a) GEOS-5 and NNR-AOT/Aqua

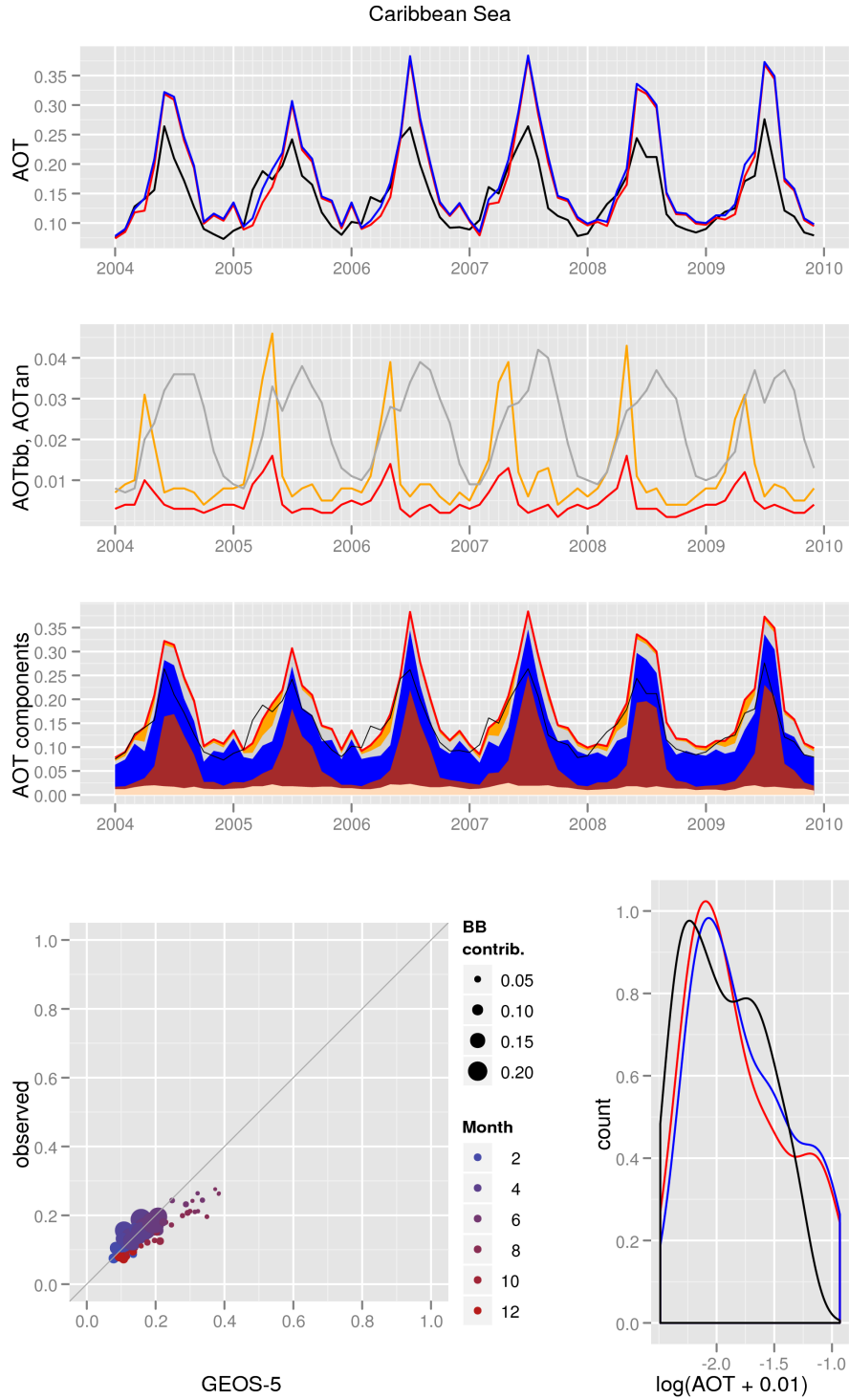Figure B49: AOT diagnostics for the Sahara region.

Africa - Sahara
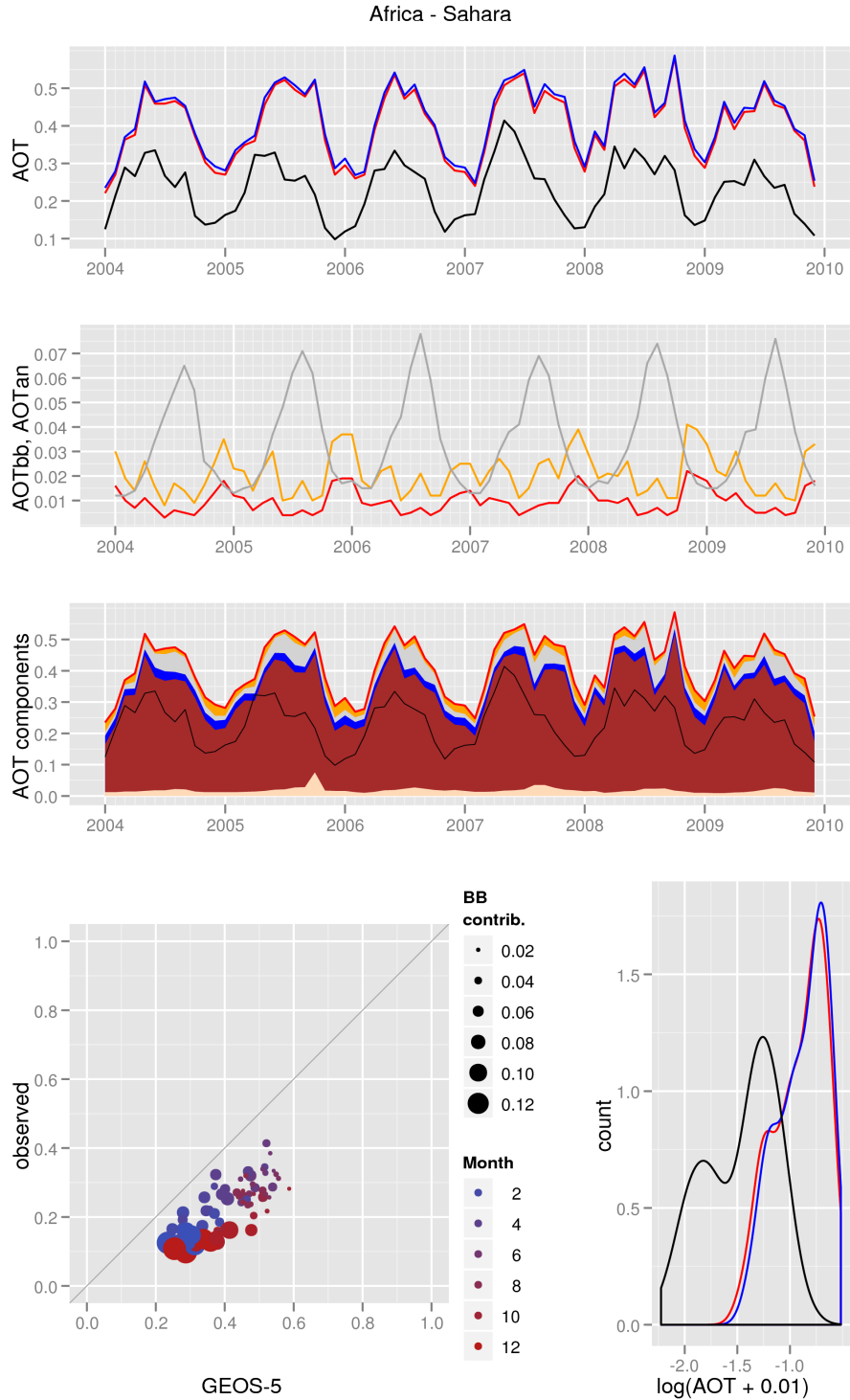
(b) GEOS-5 and NNR-AOT/Terra
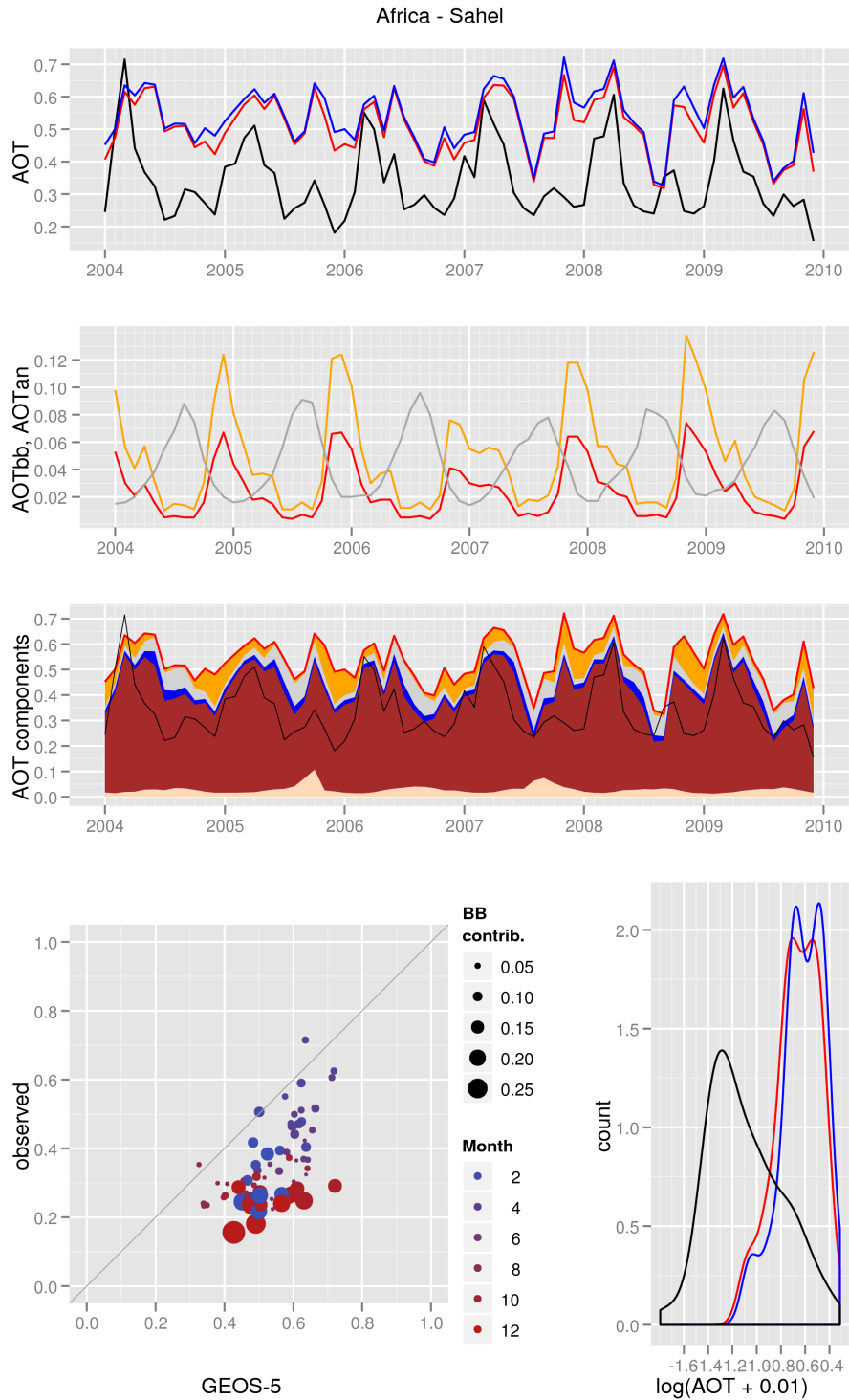
(a) GEOS-5 and NNR-AOT/Aqua

Figure B50: AOT diagnostics for the Sahel region.

Africa - Sahel
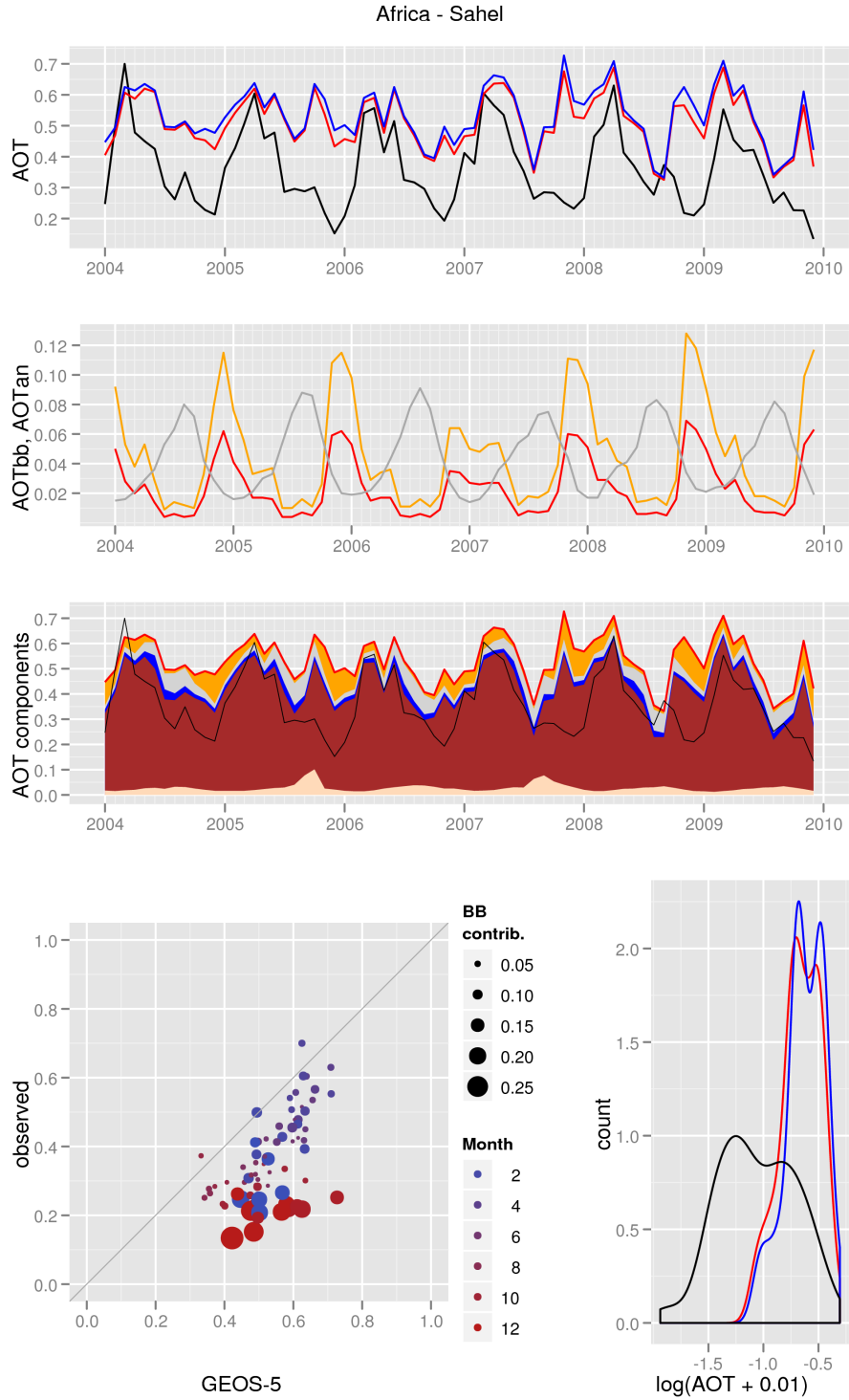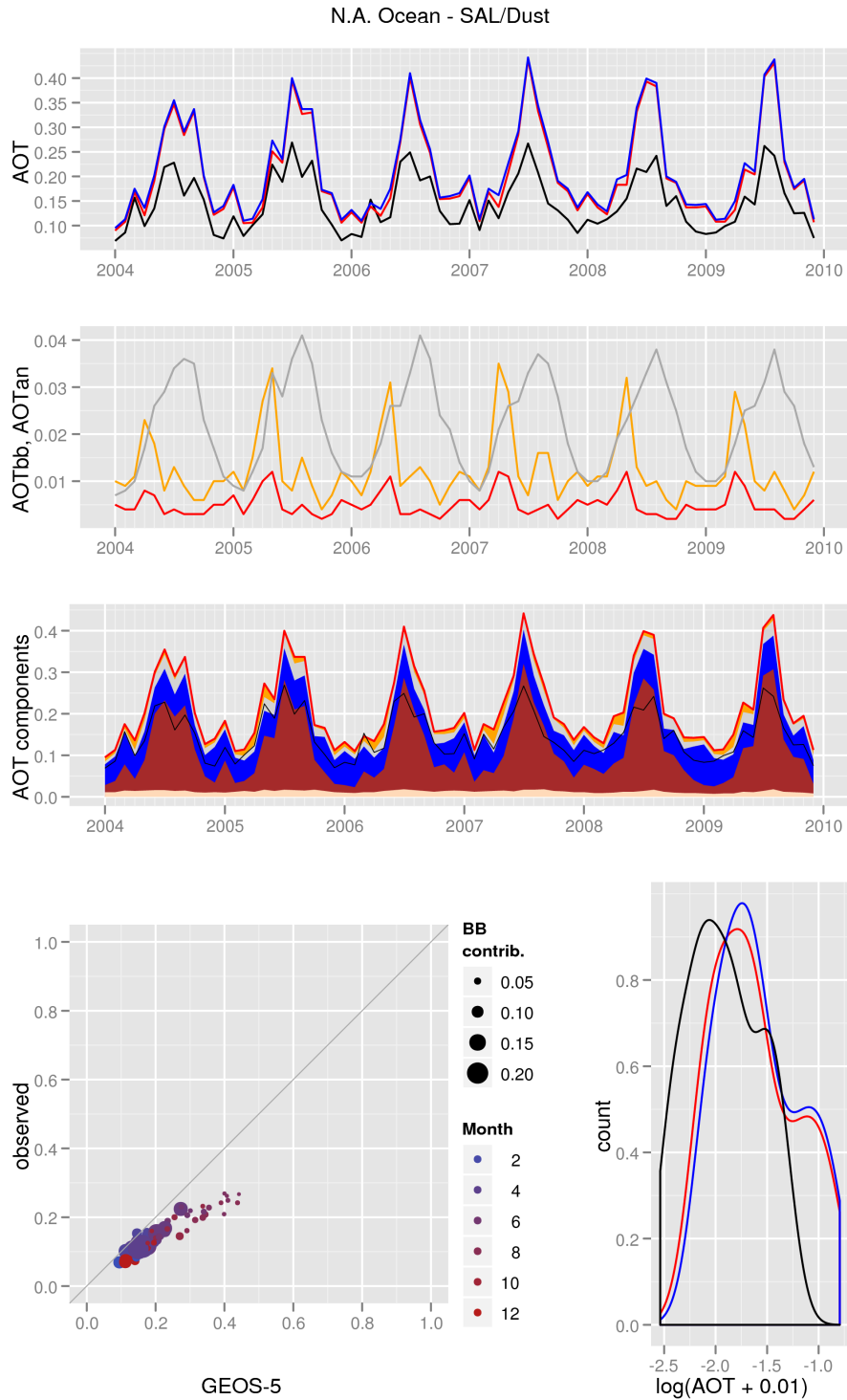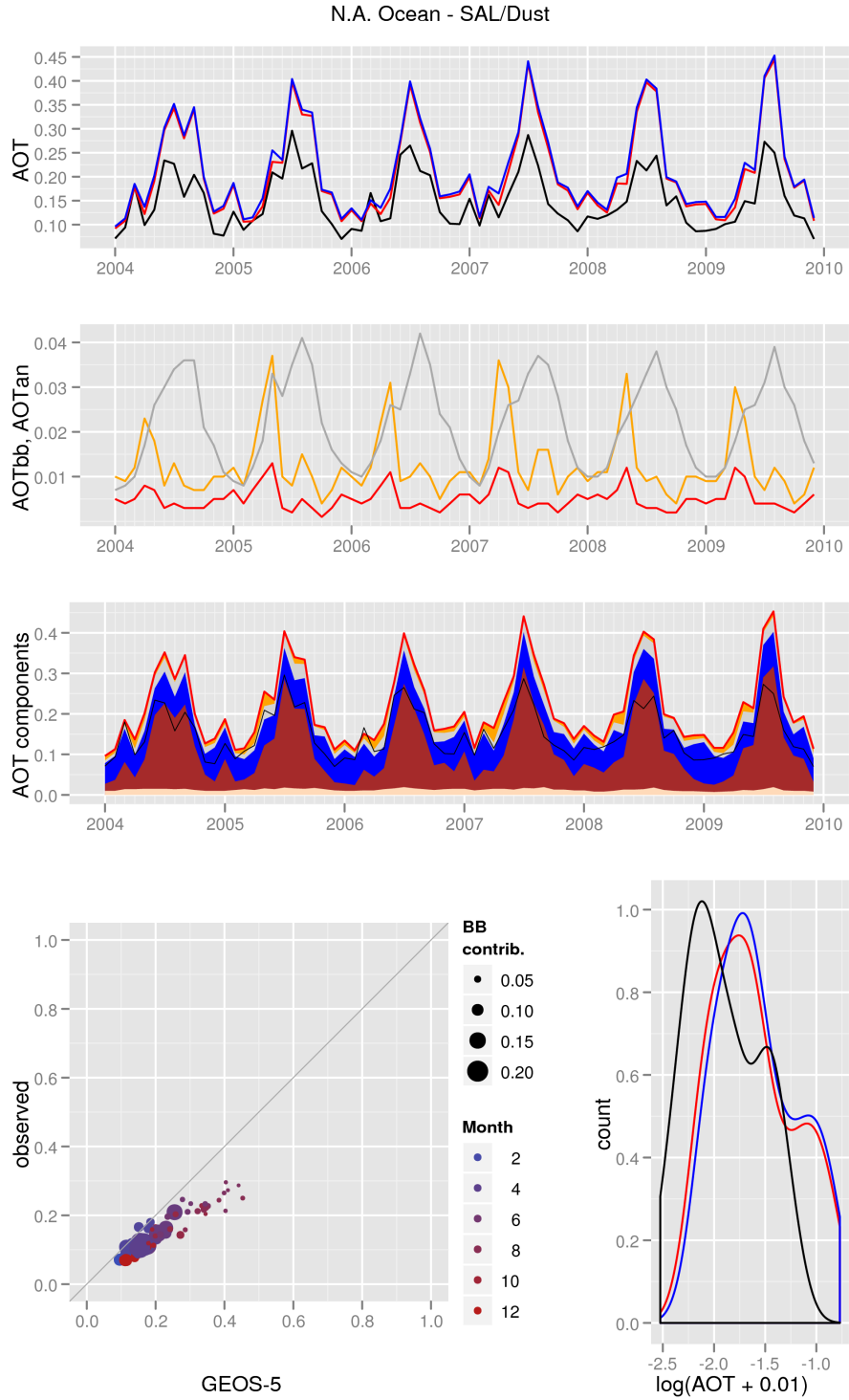
(b) GEOS-5 and NNR-AOT/Terra

# Appendix C. Regional diagnostics of GEOS-5 AOT over water

North America - Alaska
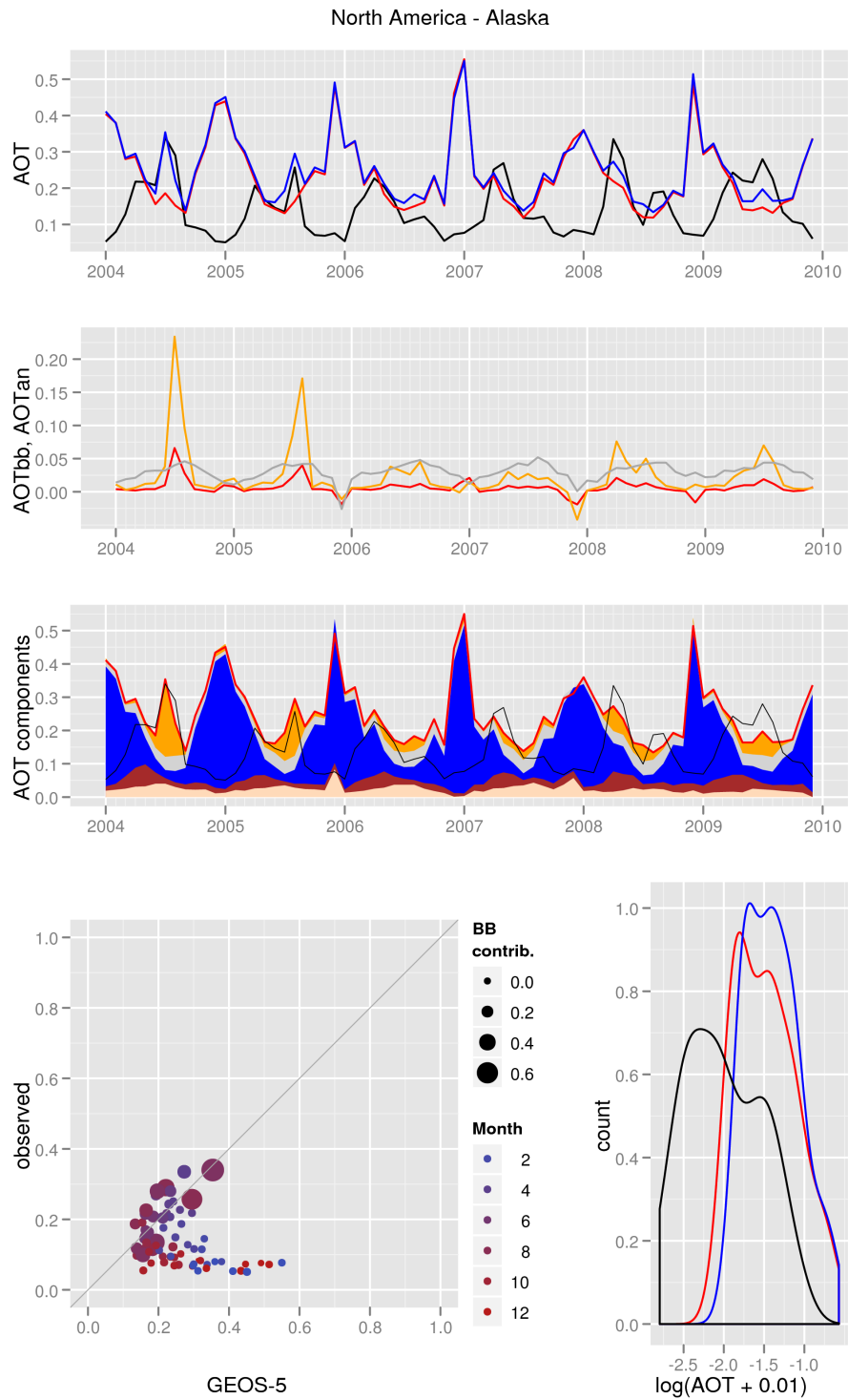
(a) GEOS-5 and NNR-AOT/Aqua

Figure C51: AOT diagnostics for the Alaska region. See the discussion surrounding Figure 5 for explanation.

North America - Alaska

(b) GEOS-5 and NNR-AOT/Terra

119

North America - USA(West)
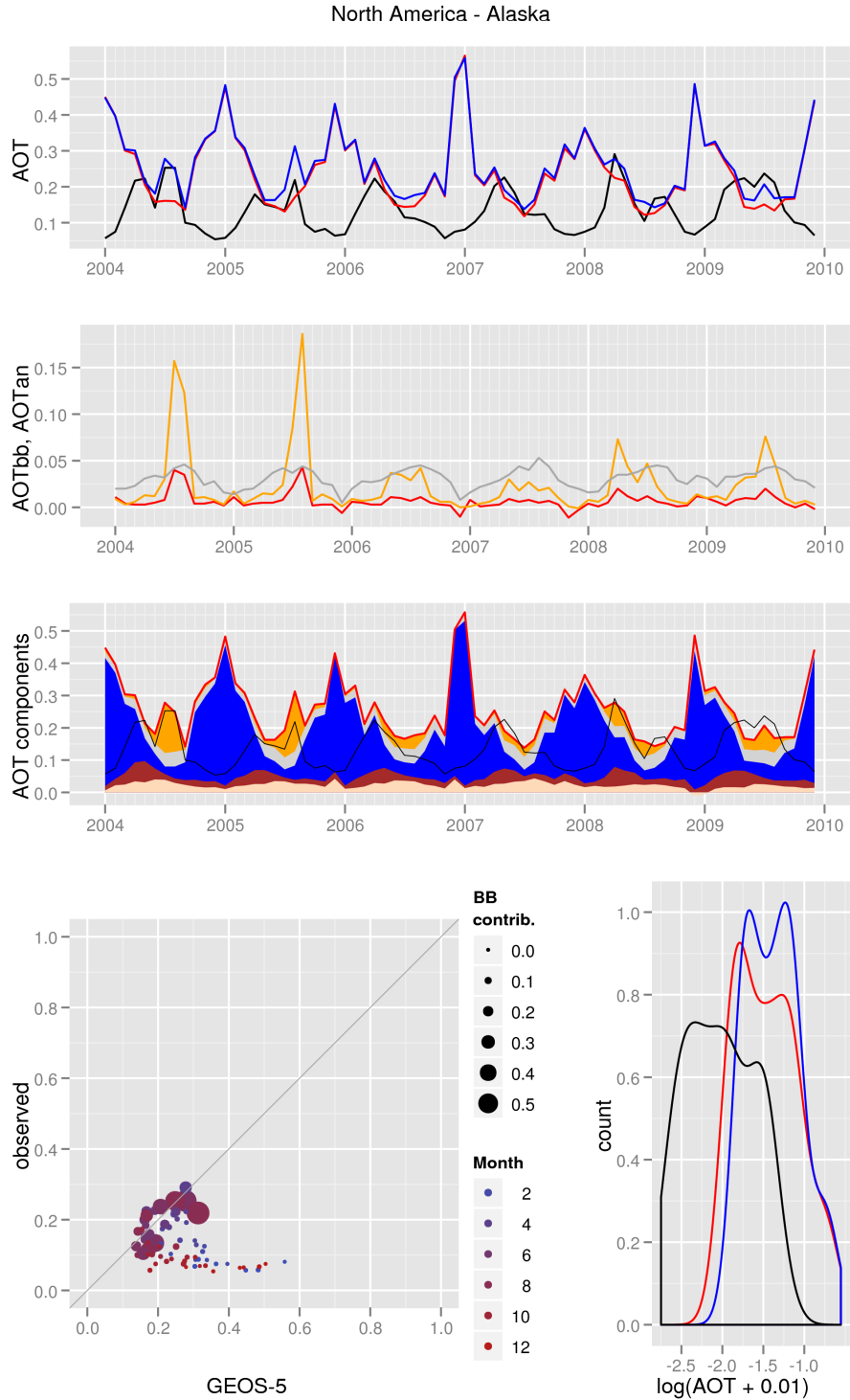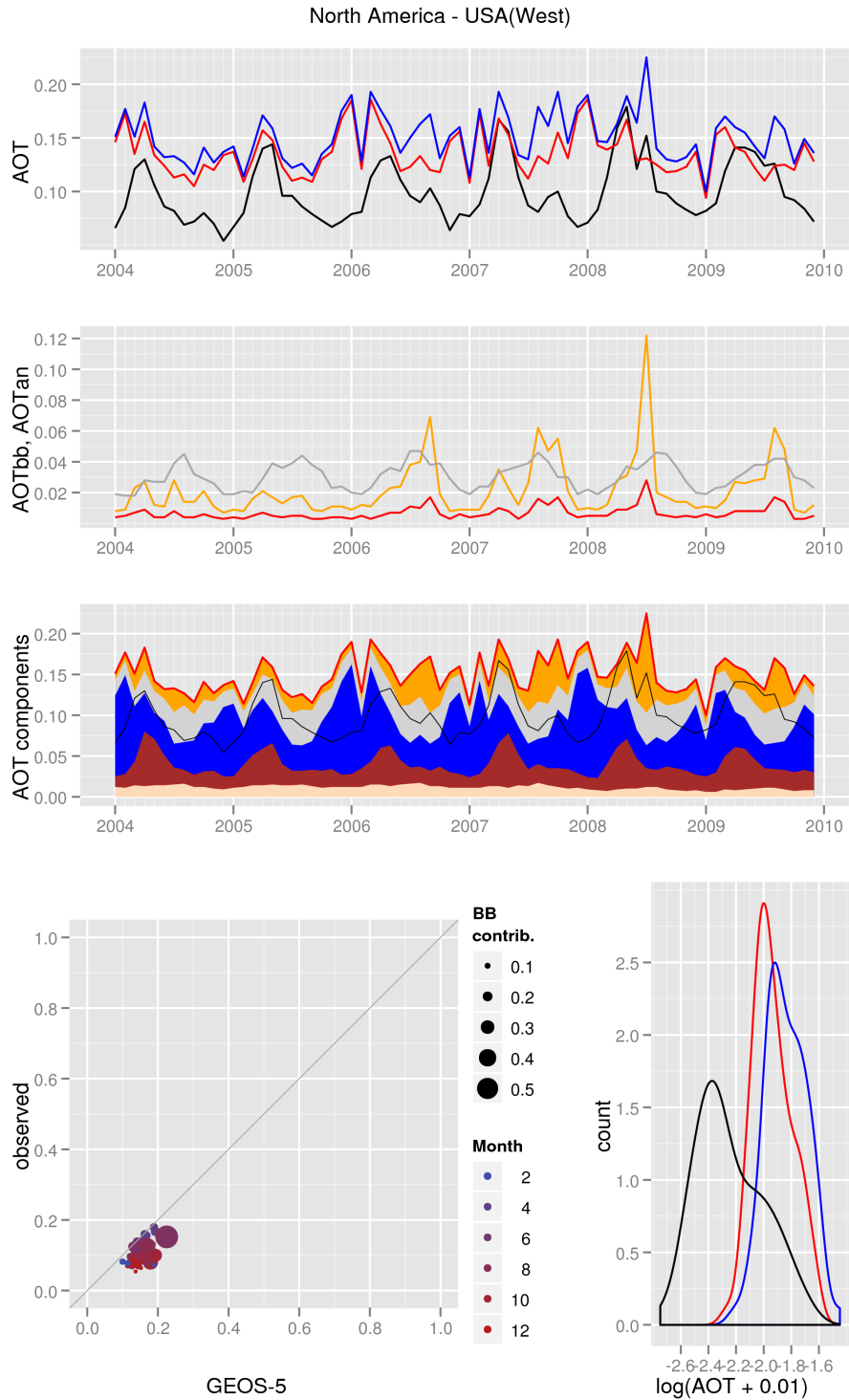
(a) GEOS-5 and NNR-AOT/Aqua

Figure C52: AOT diagnostics for the US West region.

North America - USA(West)

(b) GEOS-5 and NNR-AOT/Terra

North America - USA(East)
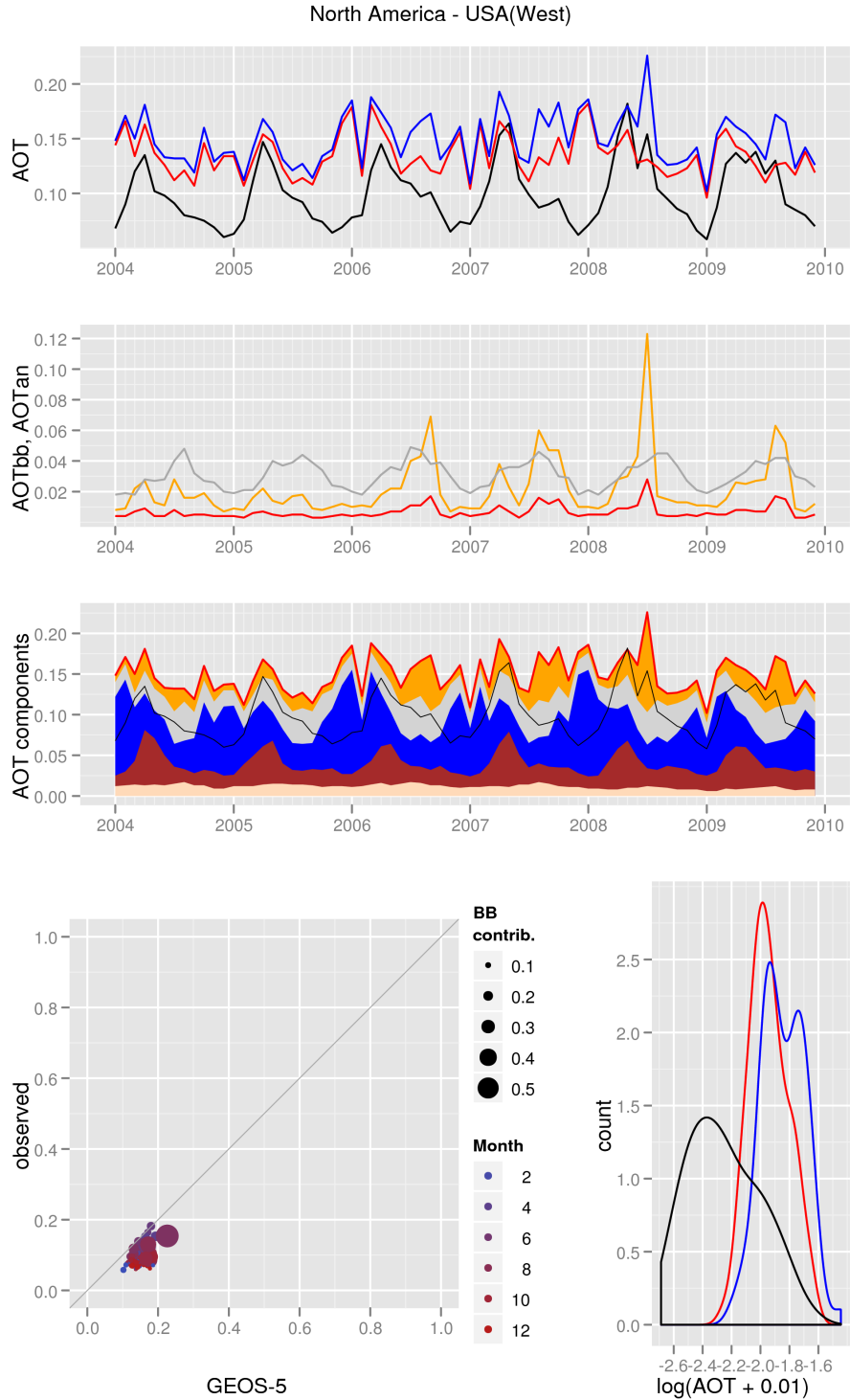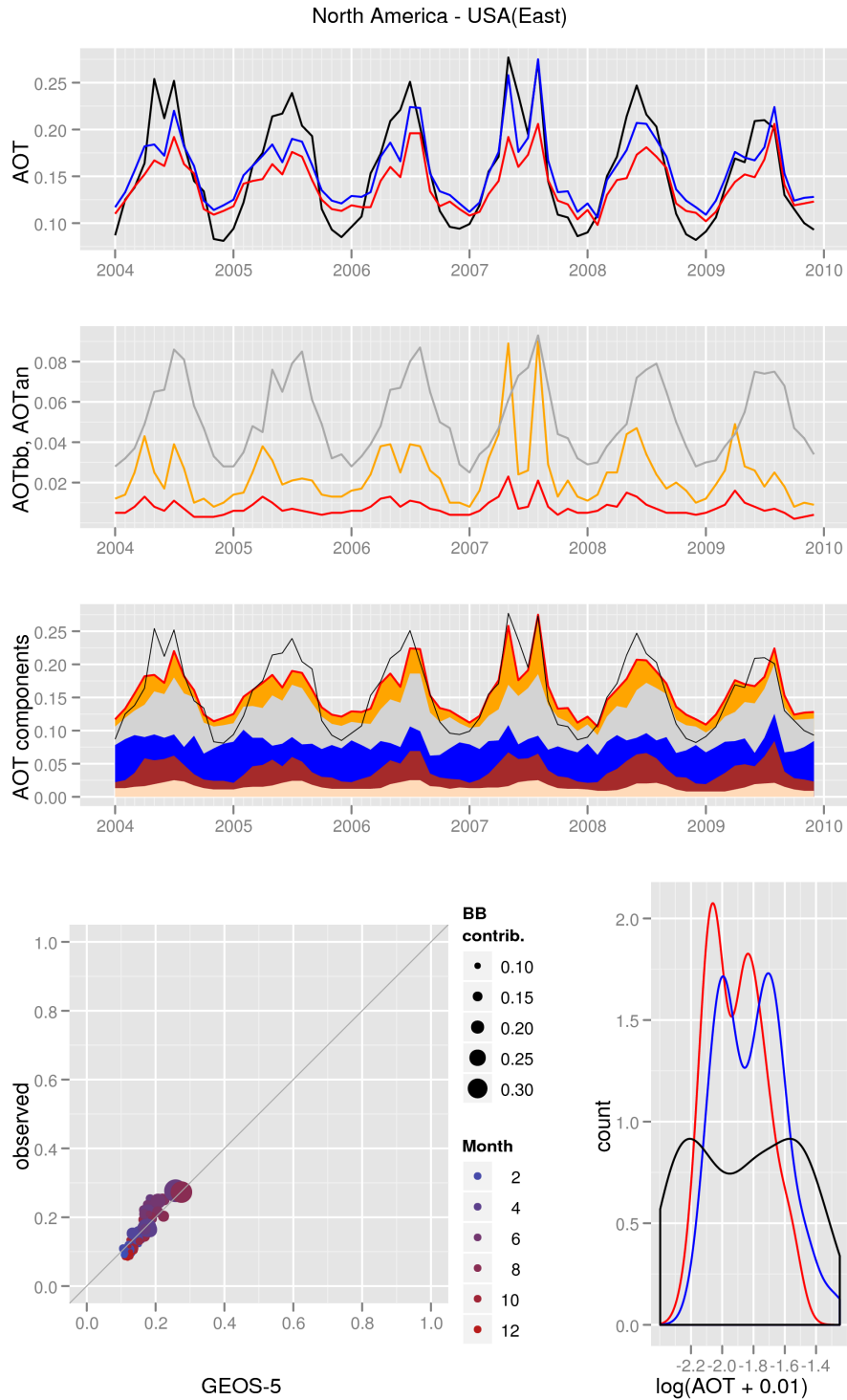
(a) GEOS-5 and NNR-AOT/Aqua

Figure C53: AOT diagnostics for the US East region.

North America - USA(East)

(b) GEOS-5 and NNR-AOT/Terra
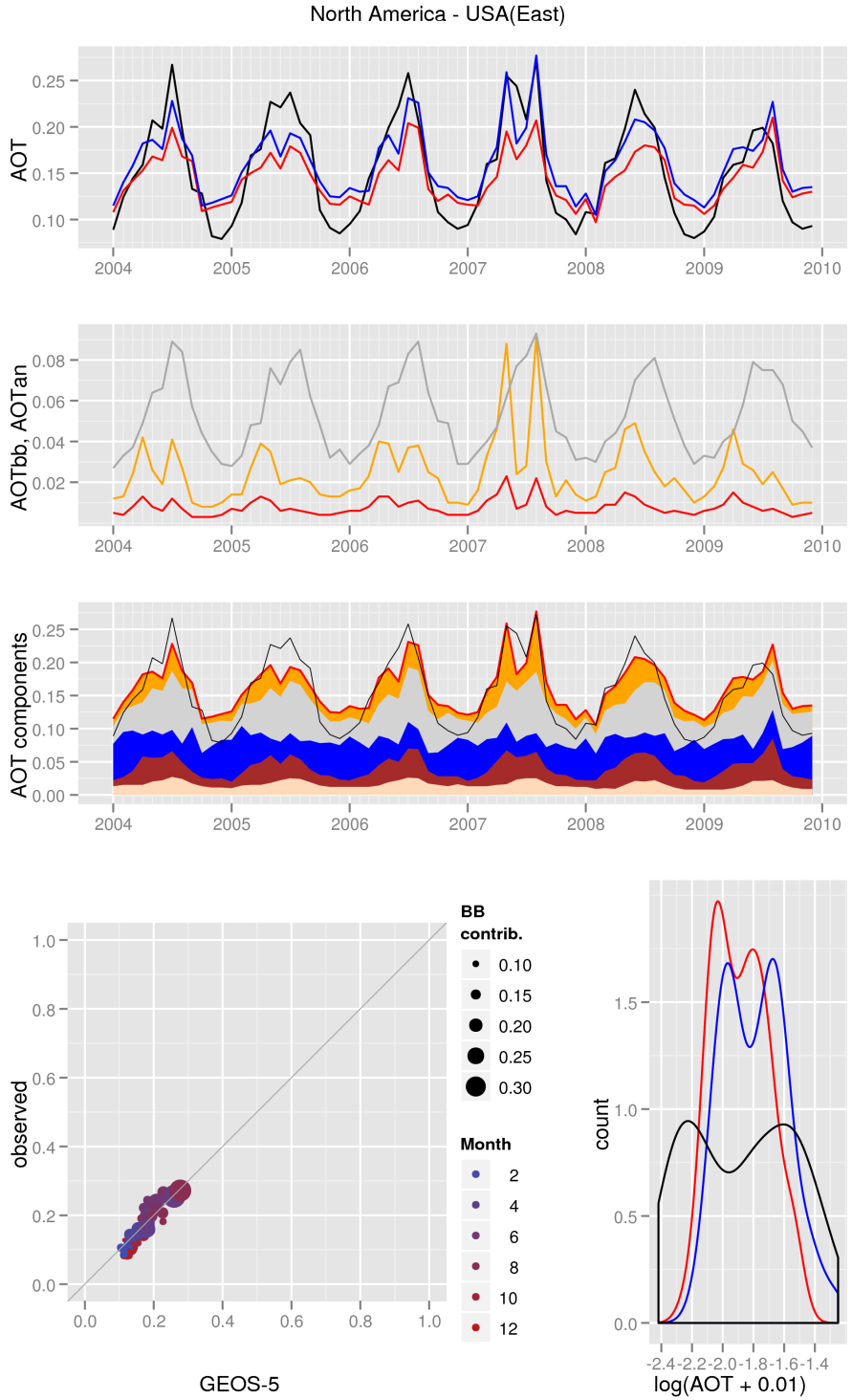
South America - Mexico
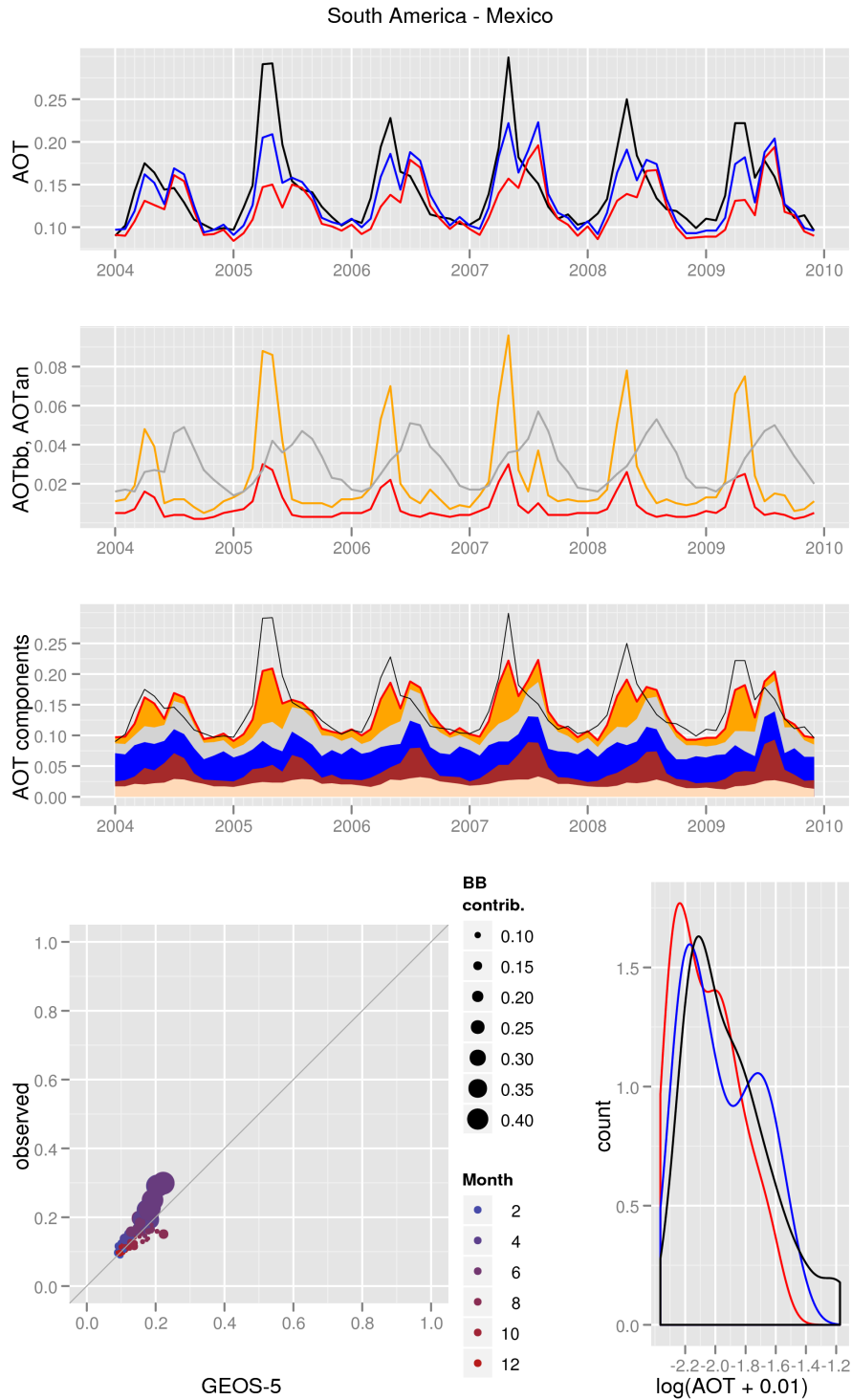
(a) GEOS-5 and NNR-AOT/Aqua

Figure C54: AOT diagnostics for the Mexico region.

South America - Mexico

(b) GEOS-5 and NNR-AOT/Terra
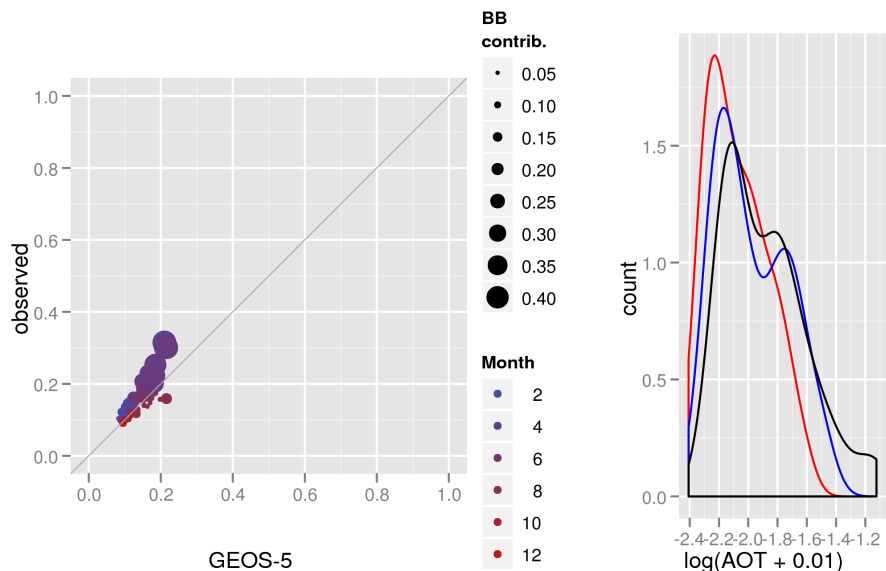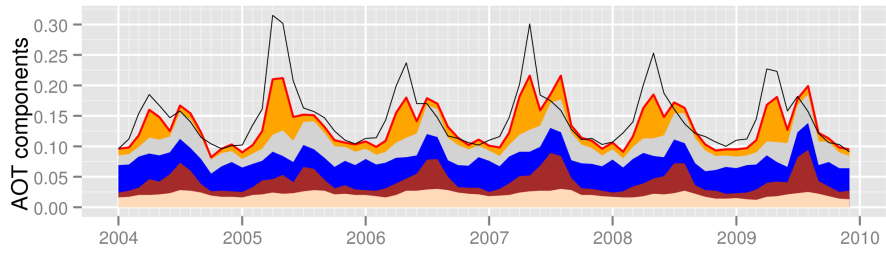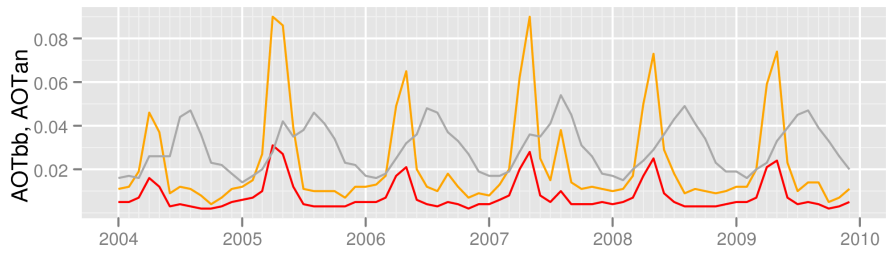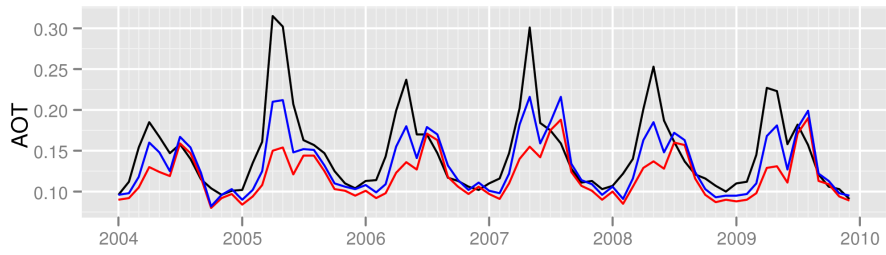
South America - Brazil(Forest)

(a) GEOS-5 and NNR-AOT/Aqua

Figure C55: AOT diagnostics for the Brazil-Forest region.

South America - Brazil(Forest)

(b) GEOS-5 and NNR-AOT/Terra

South America - Brazil(Cerrado)
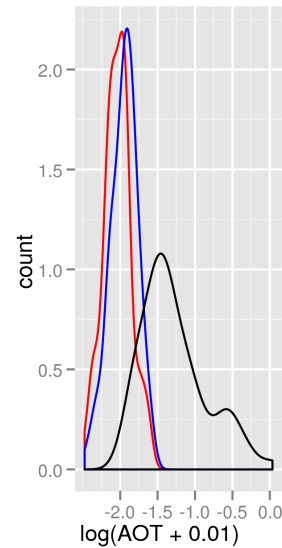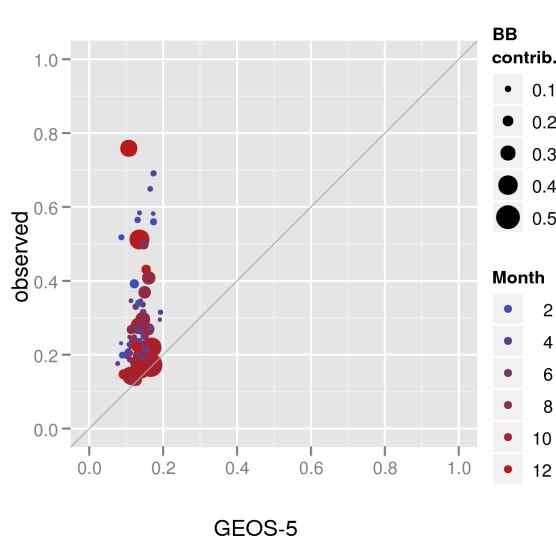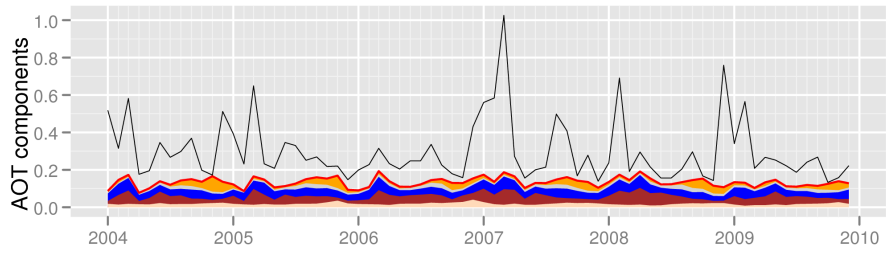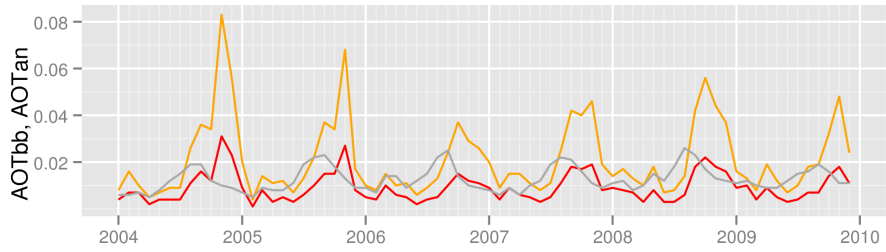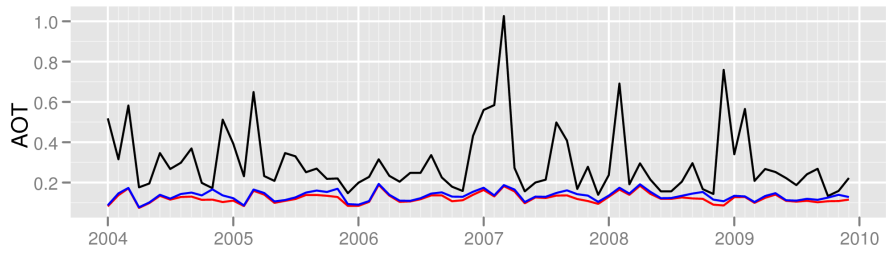
(a) GEOS-5 and NNR-AOT/Aqua
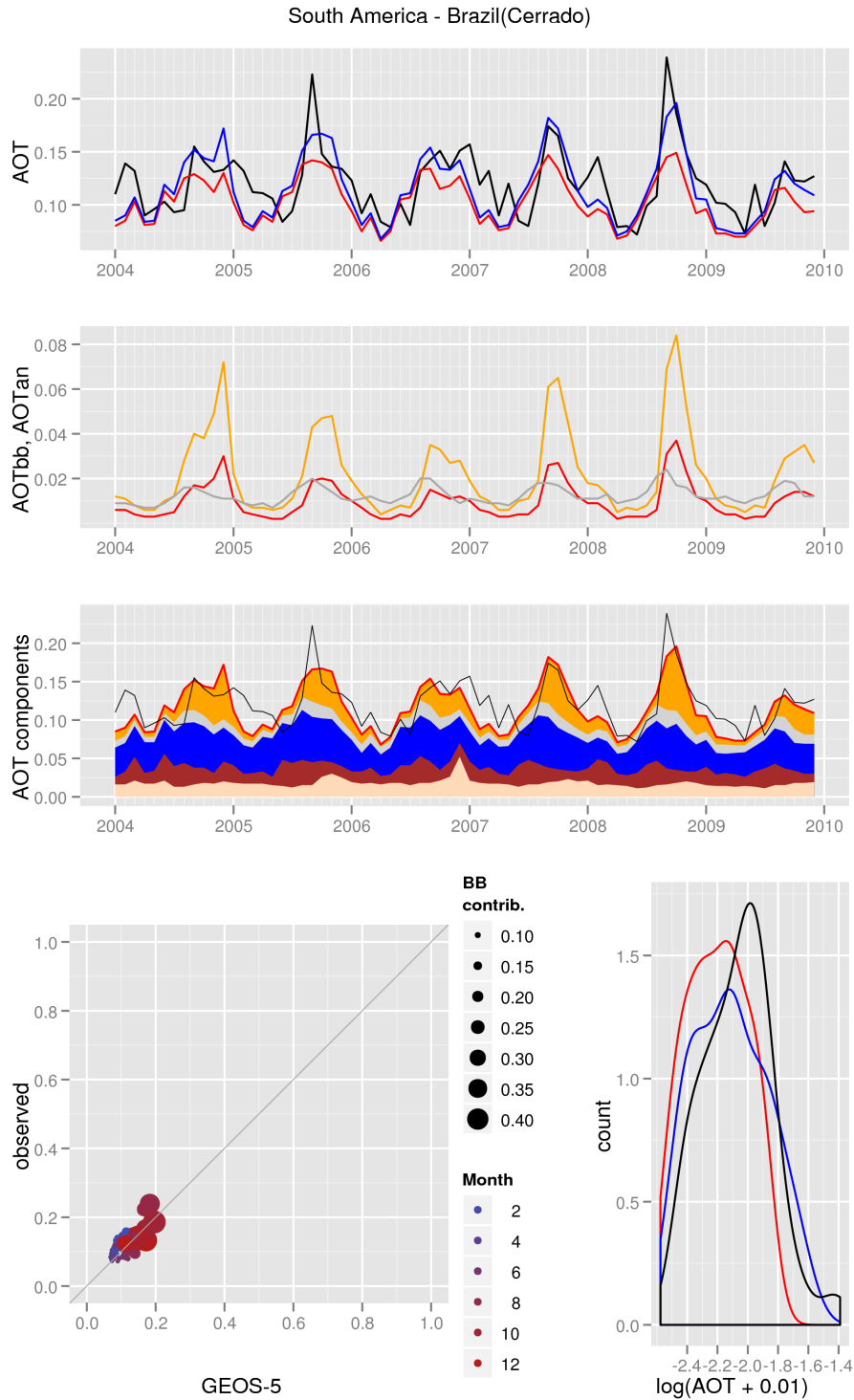
Figure C56: AOT diagnostics for the Brazil-Cerrado region.

South America - Brazil(Cerrado)
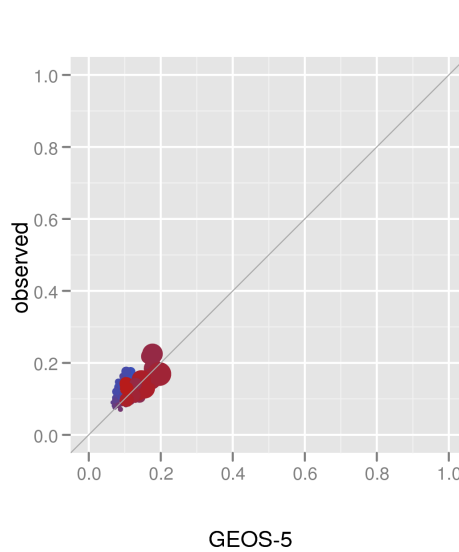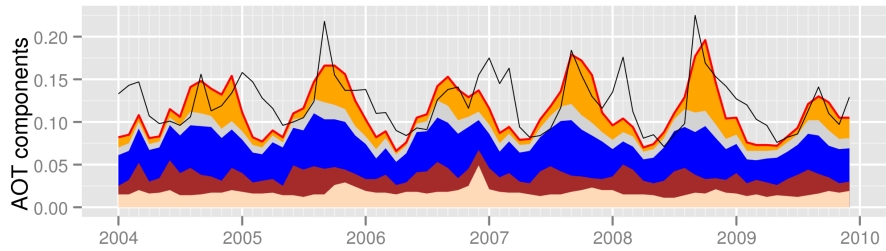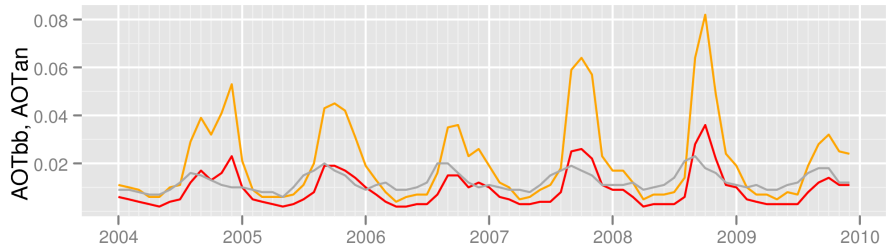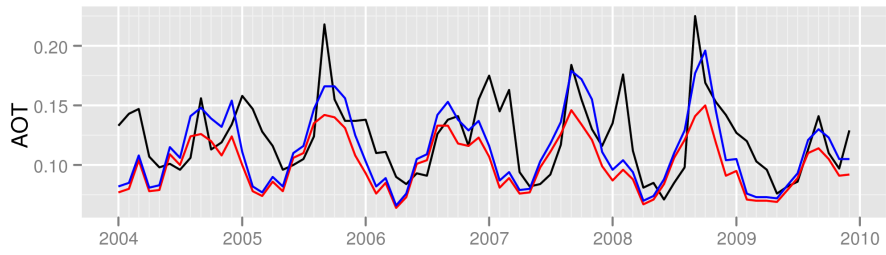
(b) GEOS-5 and NNR-AOT/Terra
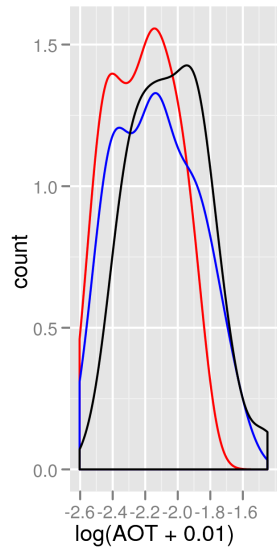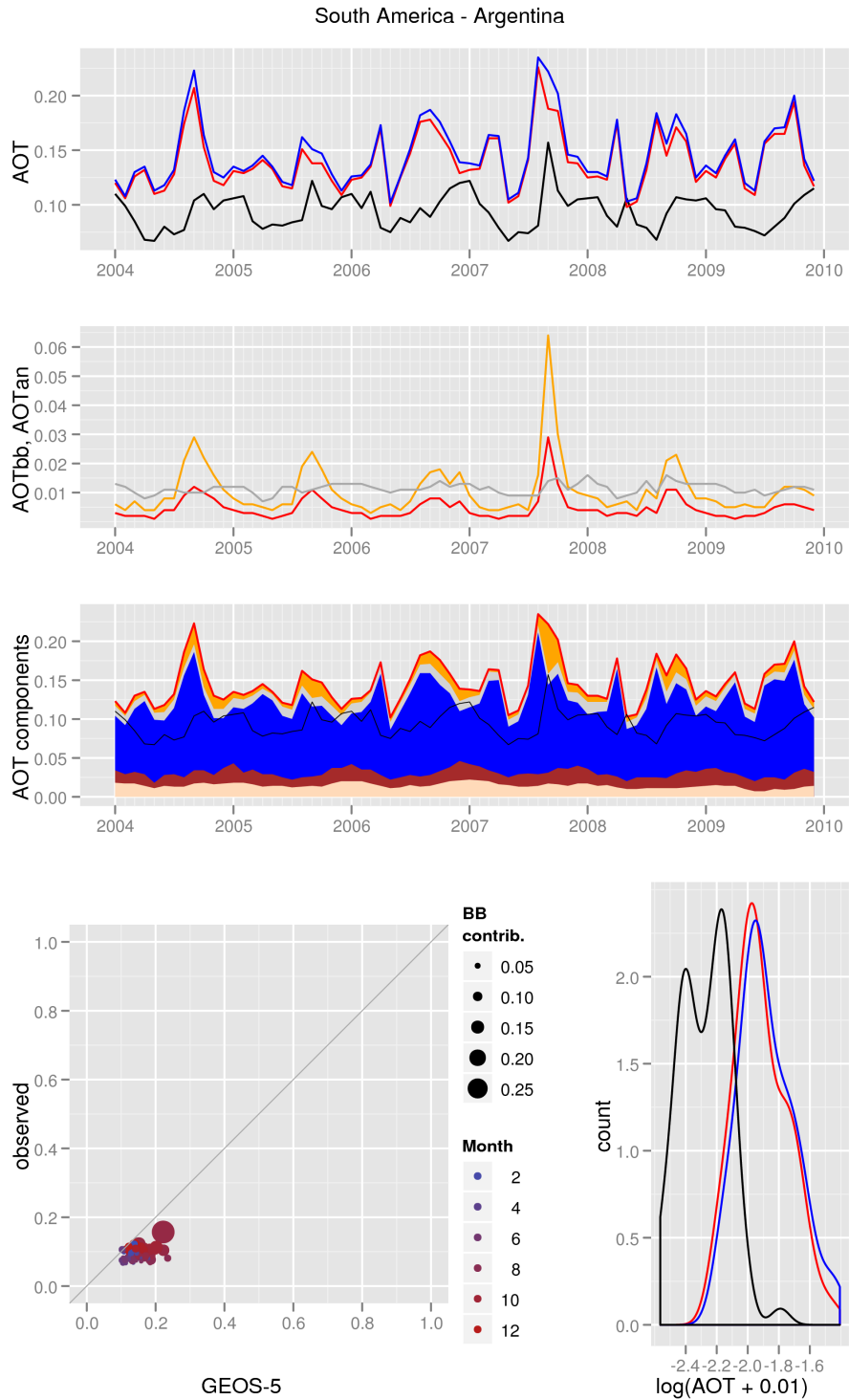
(a) GEOS-5 and NNR-AOT/Aqua

Figure C57: AOT diagnostics for the Argentina region.

South America - Argentina
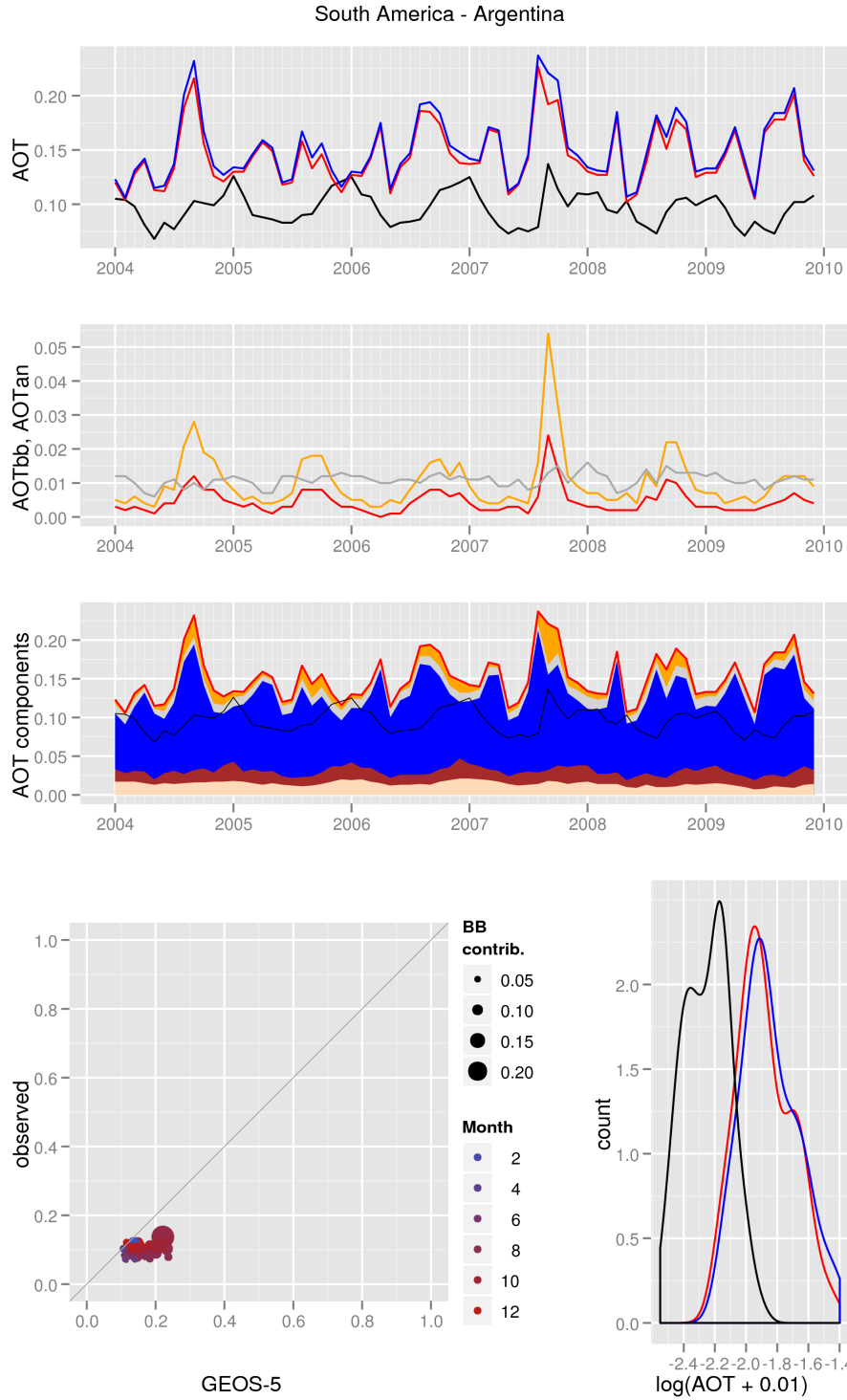
(b) GEOS-5 and NNR-AOT/Terra
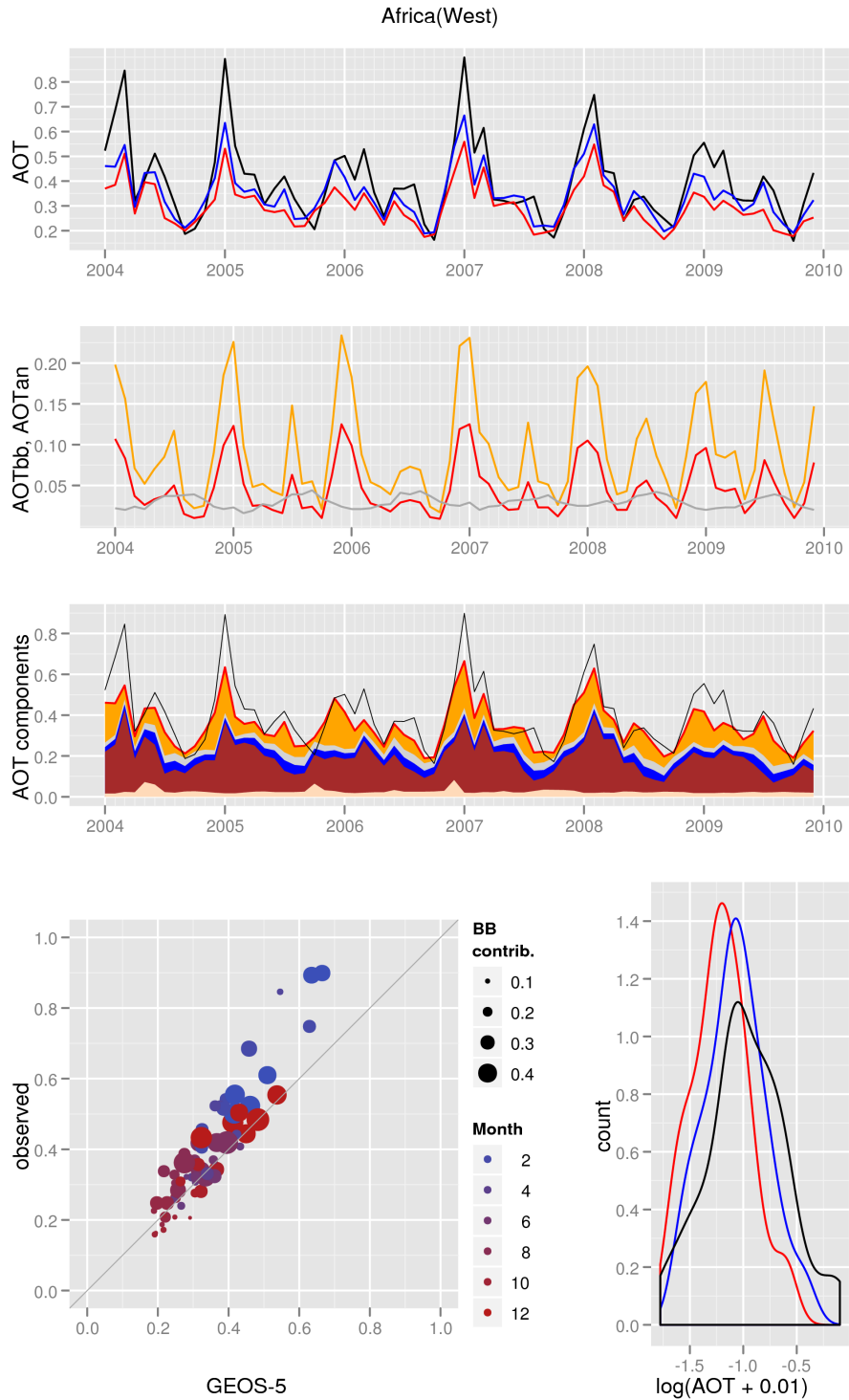
(a) GEOS-5 and NNR-AOT/Aqua

Figure C58: AOT diagnostics for the West Africa region.
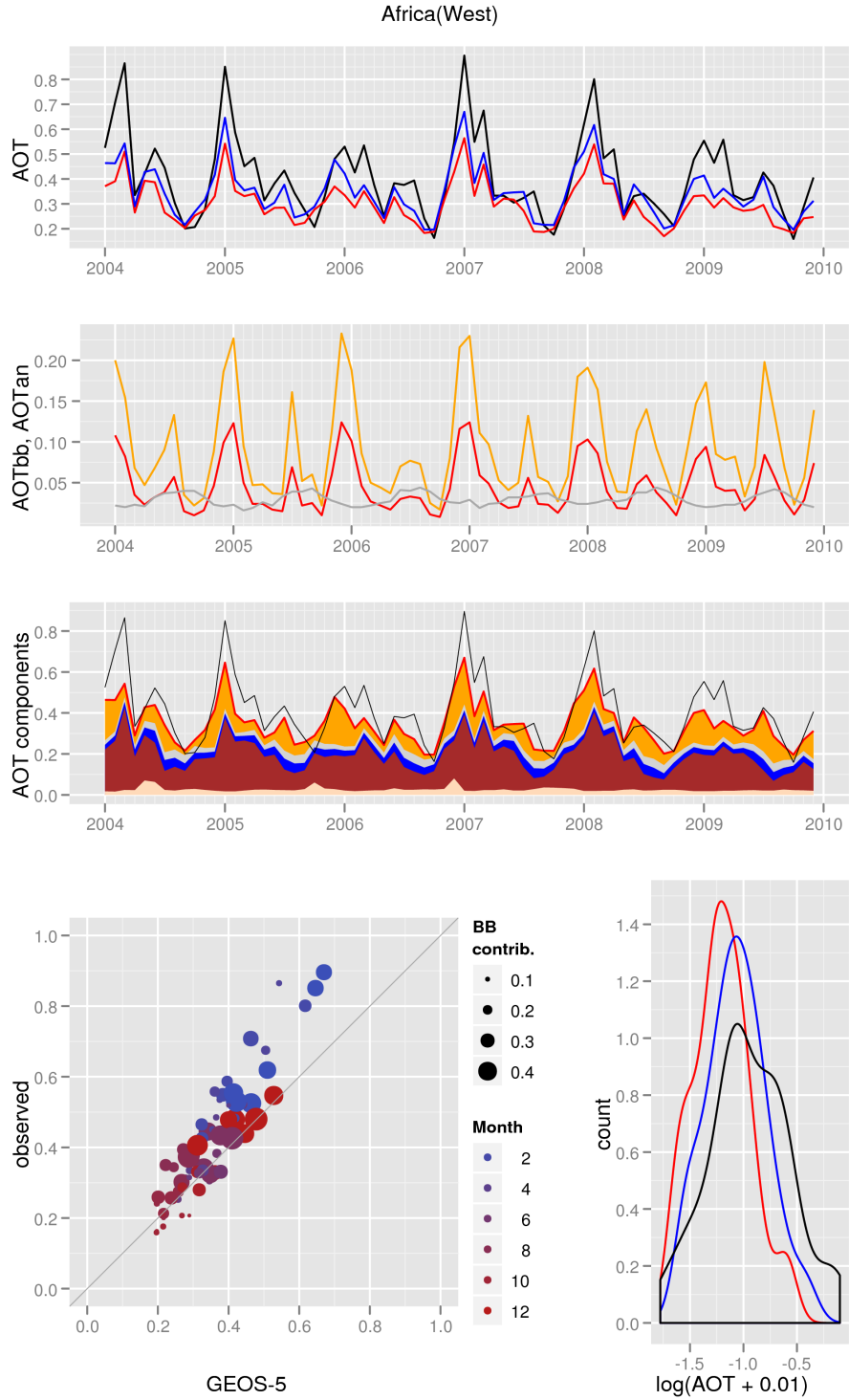
(b) GEOS-5 and NNR-AOT/Terra
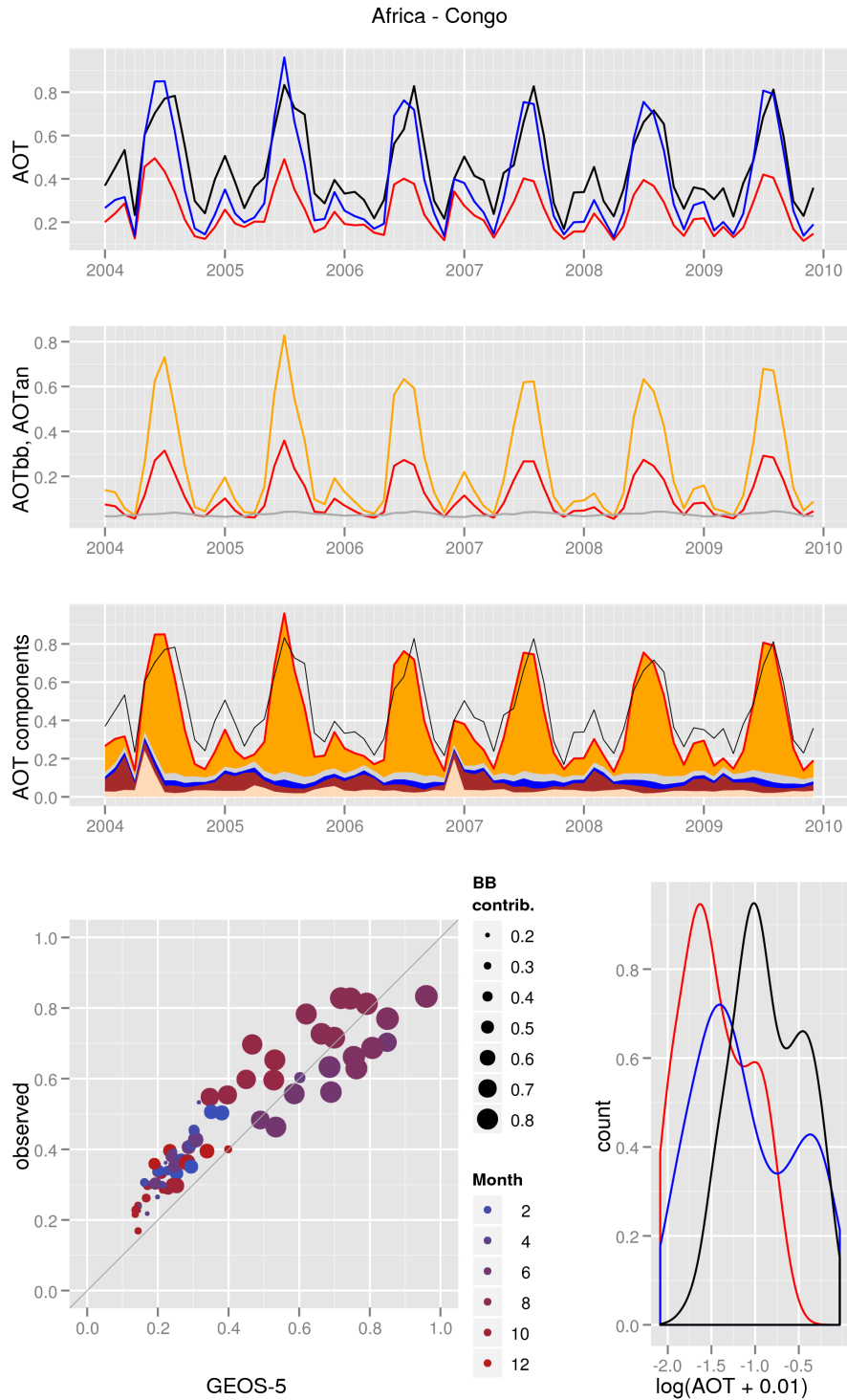
Africa - Congo

(a) GEOS-5 and NNR-AOT/Aqua

Figure C59: AOT diagnostics for the Congo region.

Africa - Congo

(b) GEOS-5 and NNR-AOT/Terra

135
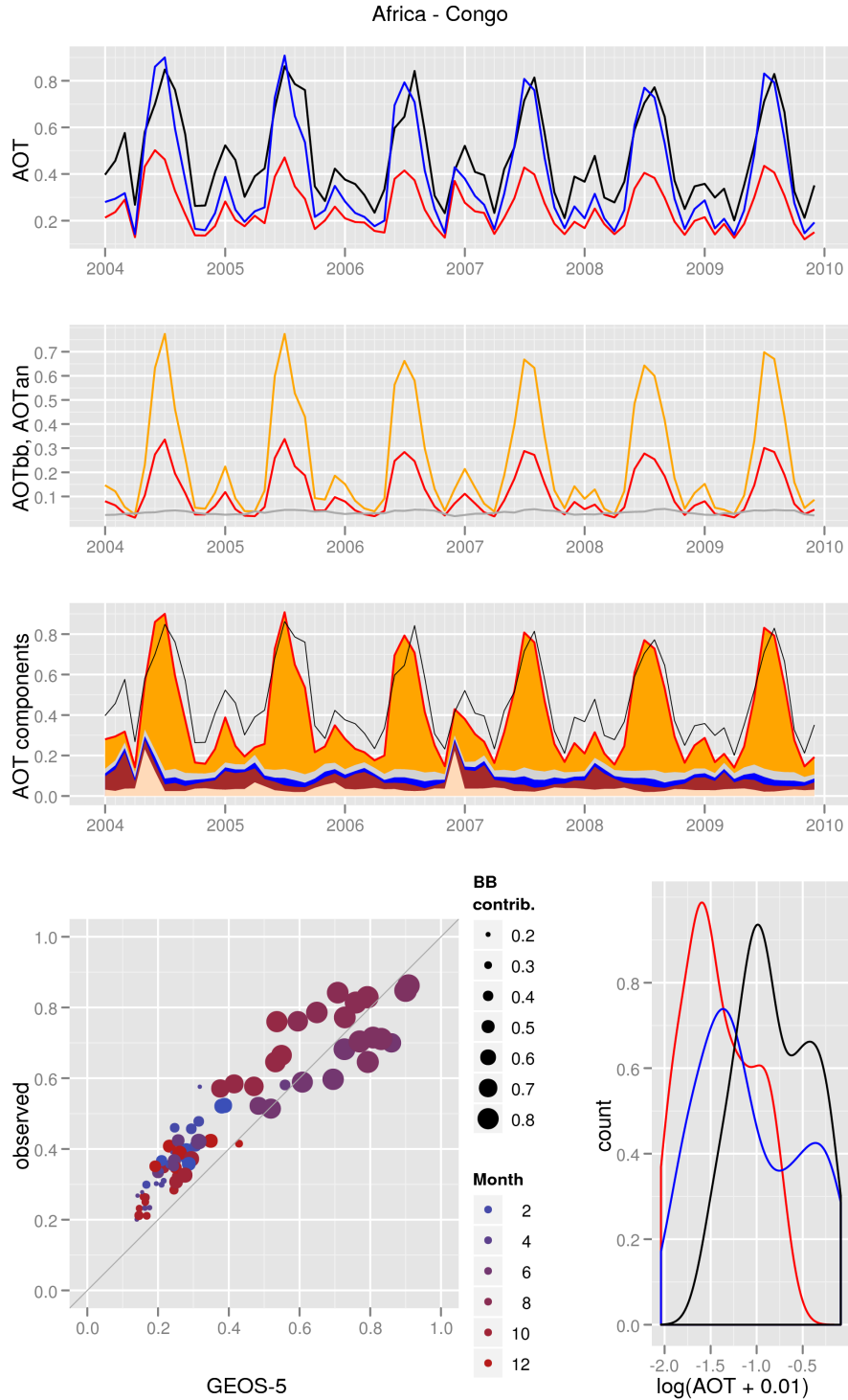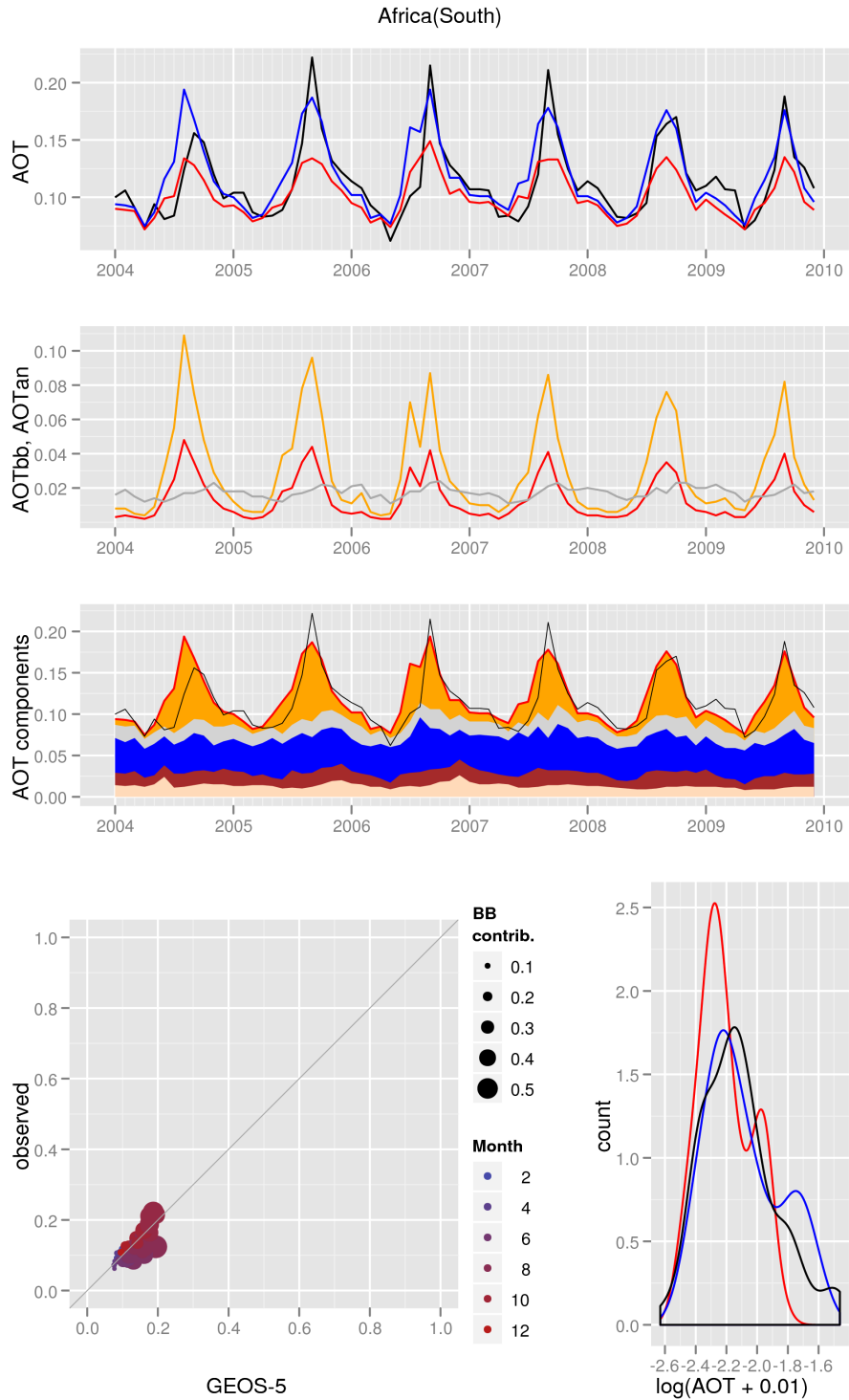
(a) GEOS-5 and NNR-AOT/Aqua

Figure C60: AOT diagnostics for the South Africa region.
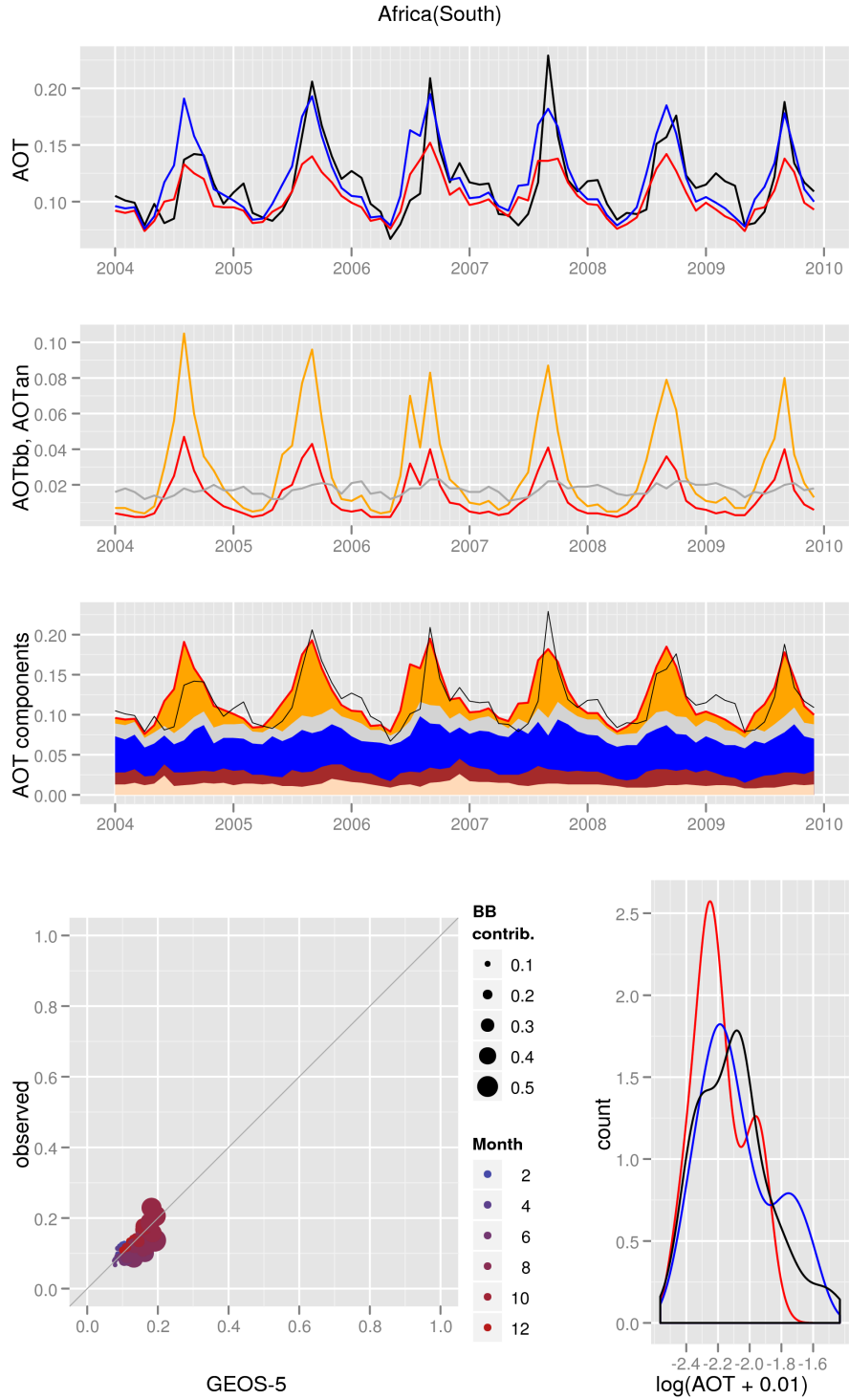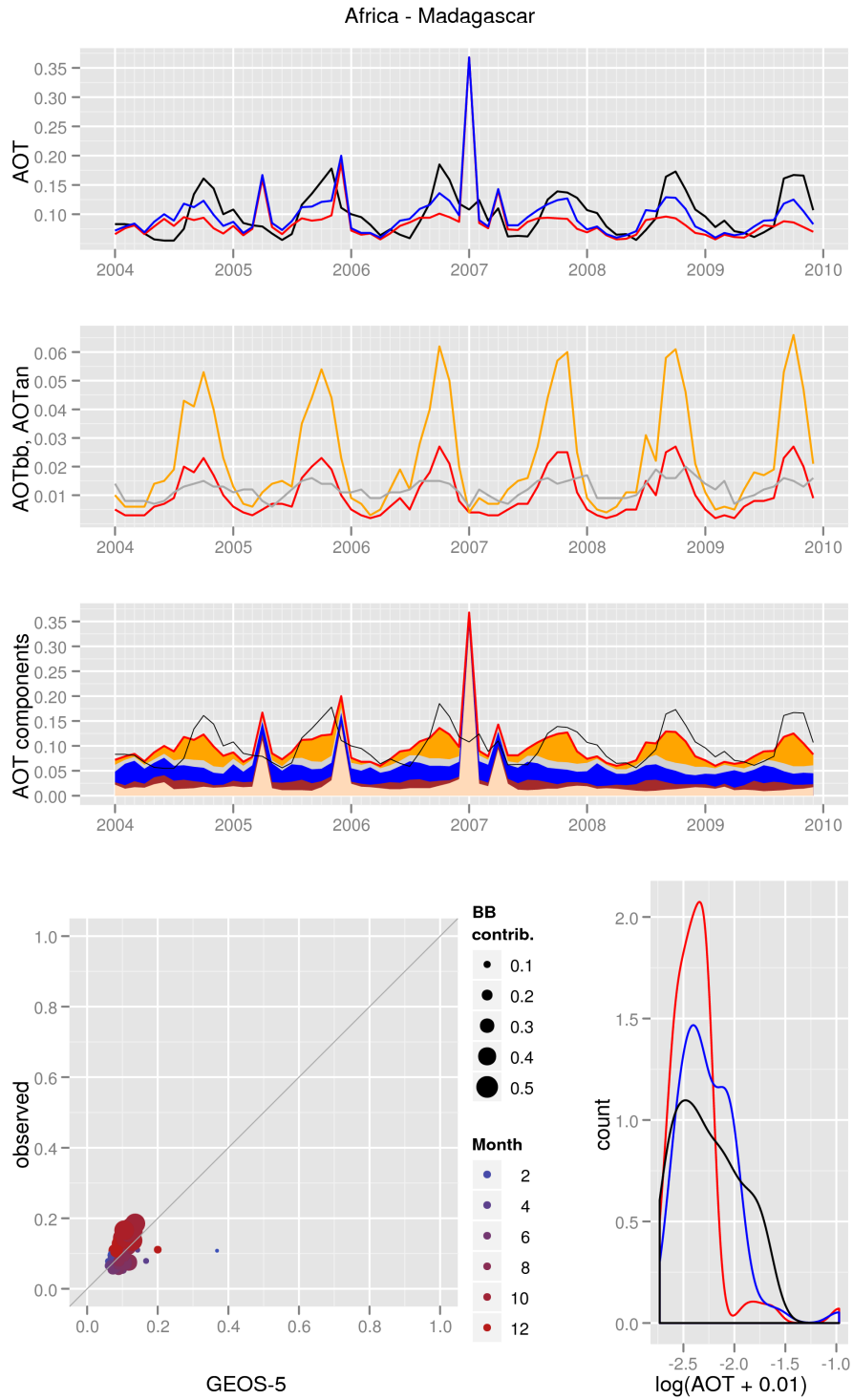
(b) GEOS-5 and NNR-AOT/Terra

Figure C61: AOT diagnostics for the Madagascar region.

(b) GEOS-5 and NNR-AOT/Terra

139
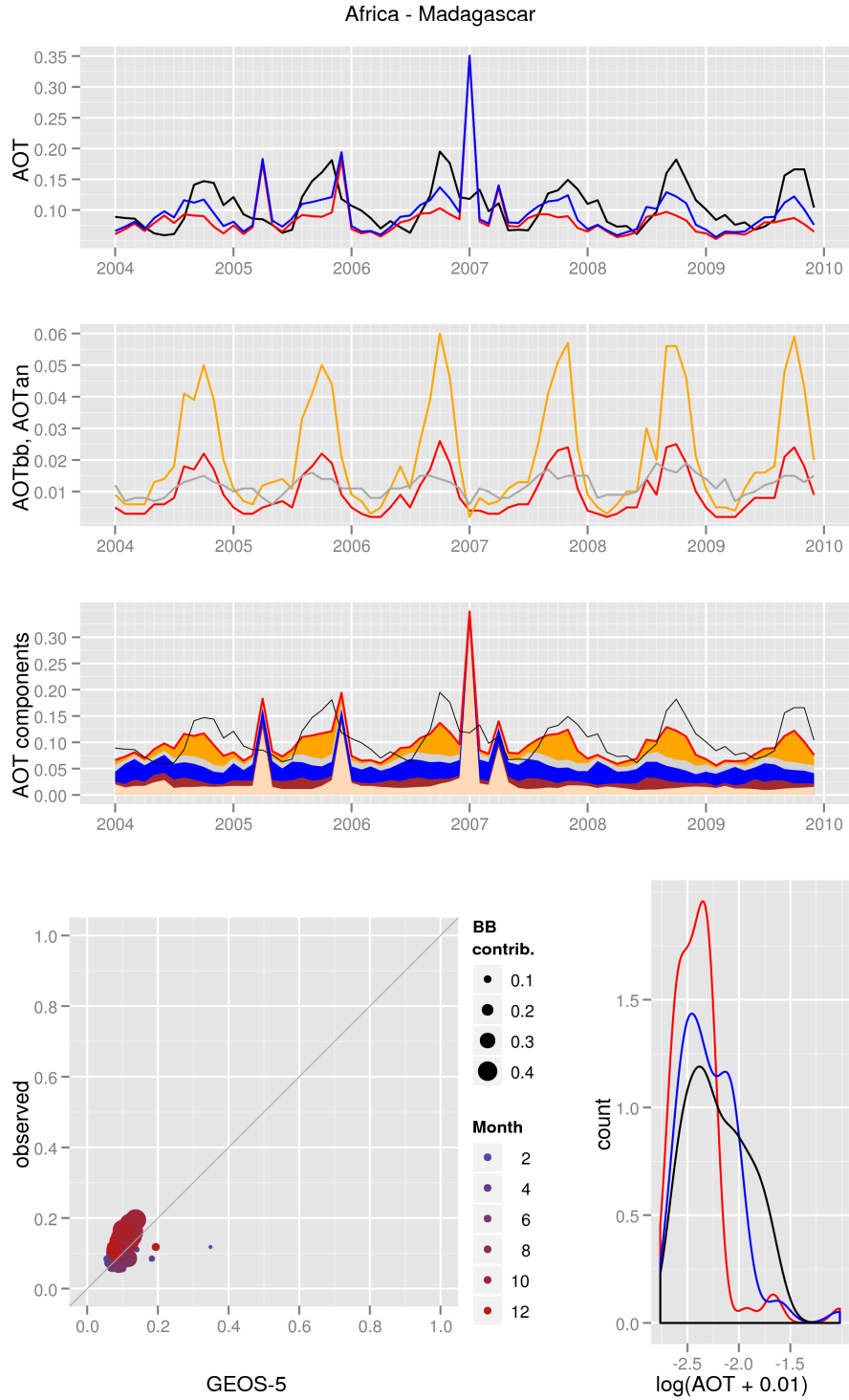
Europe - Scandinavia
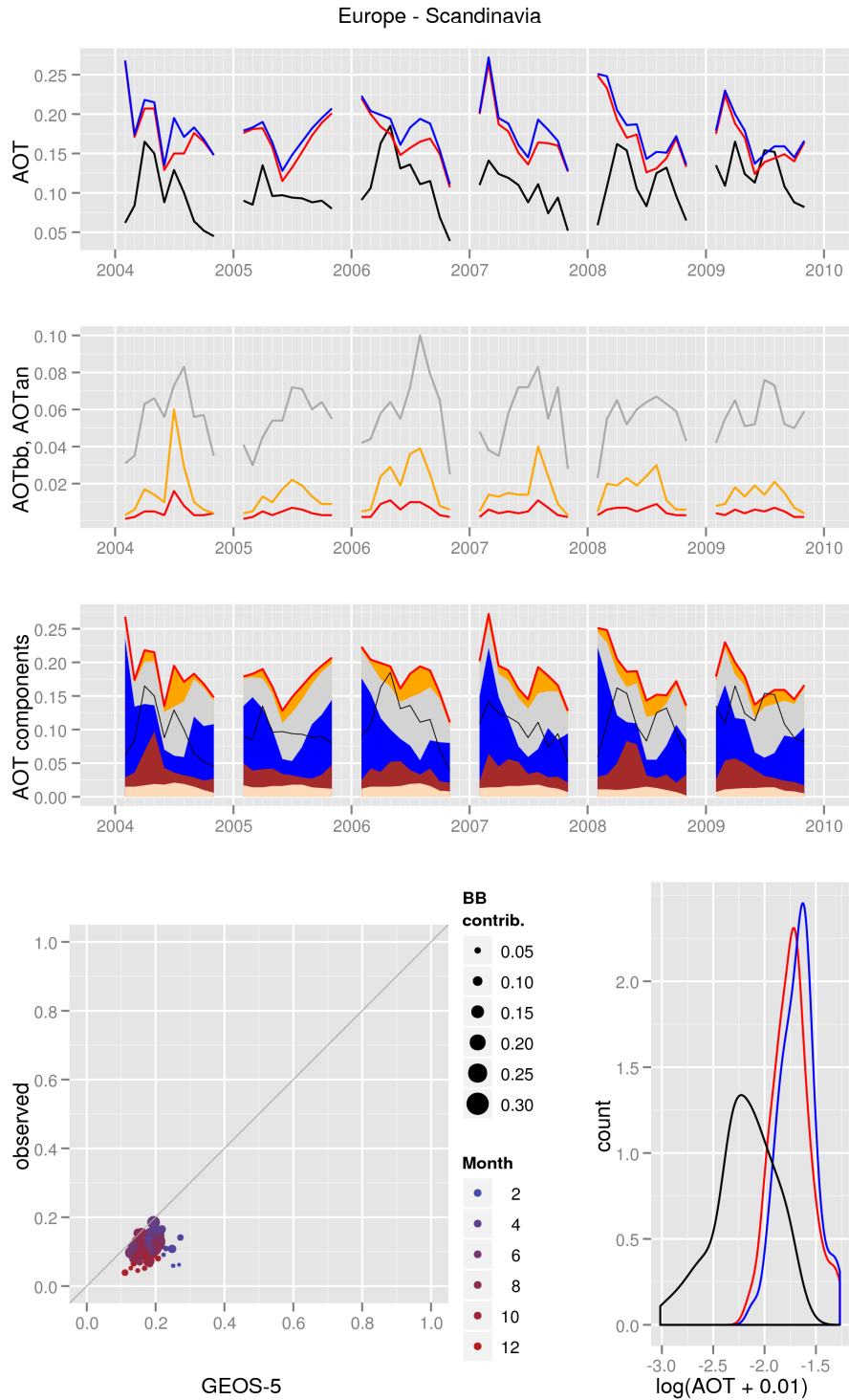
(a) GEOS-5 and NNR-AOT/Aqua

Figure C62: AOT diagnostics for the Scandinavia region.

Europe - Scandinavia

(b) GEOS-5 and NNR-AOT/Terra

141
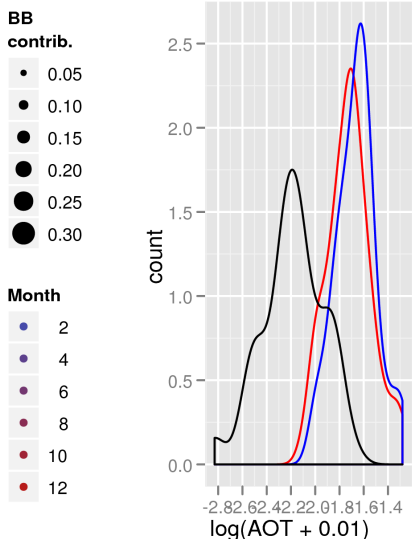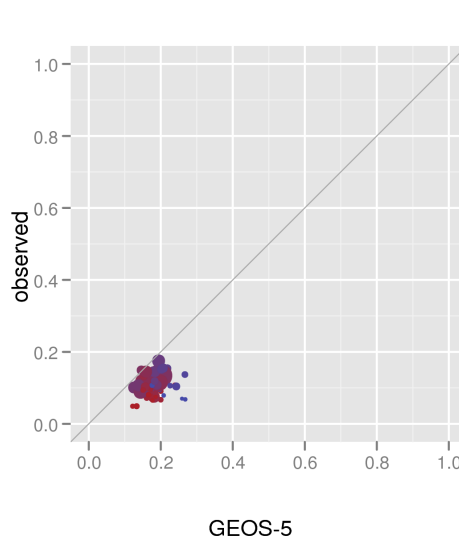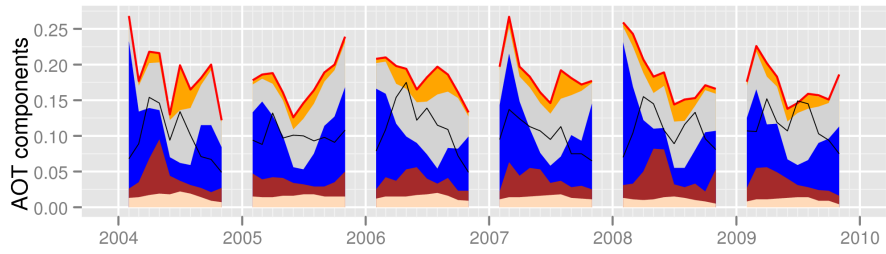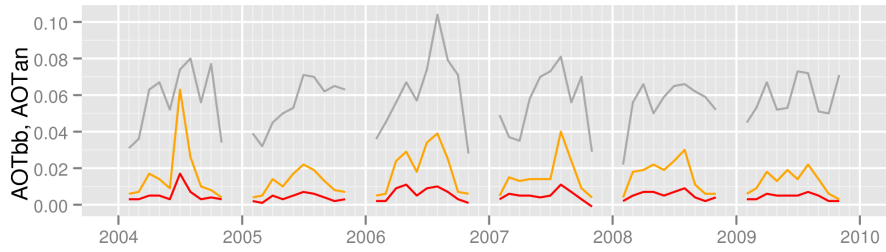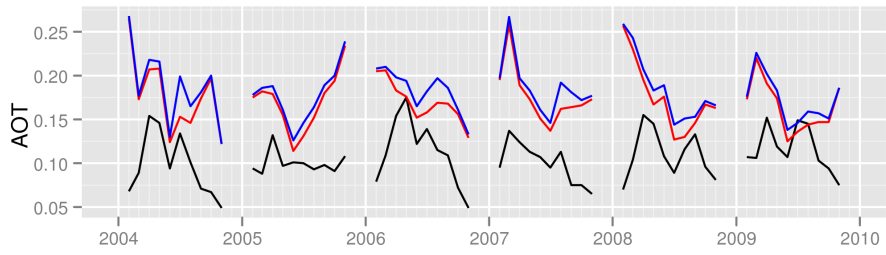
(a) GEOS-5 and NNR-AOT/Aqua
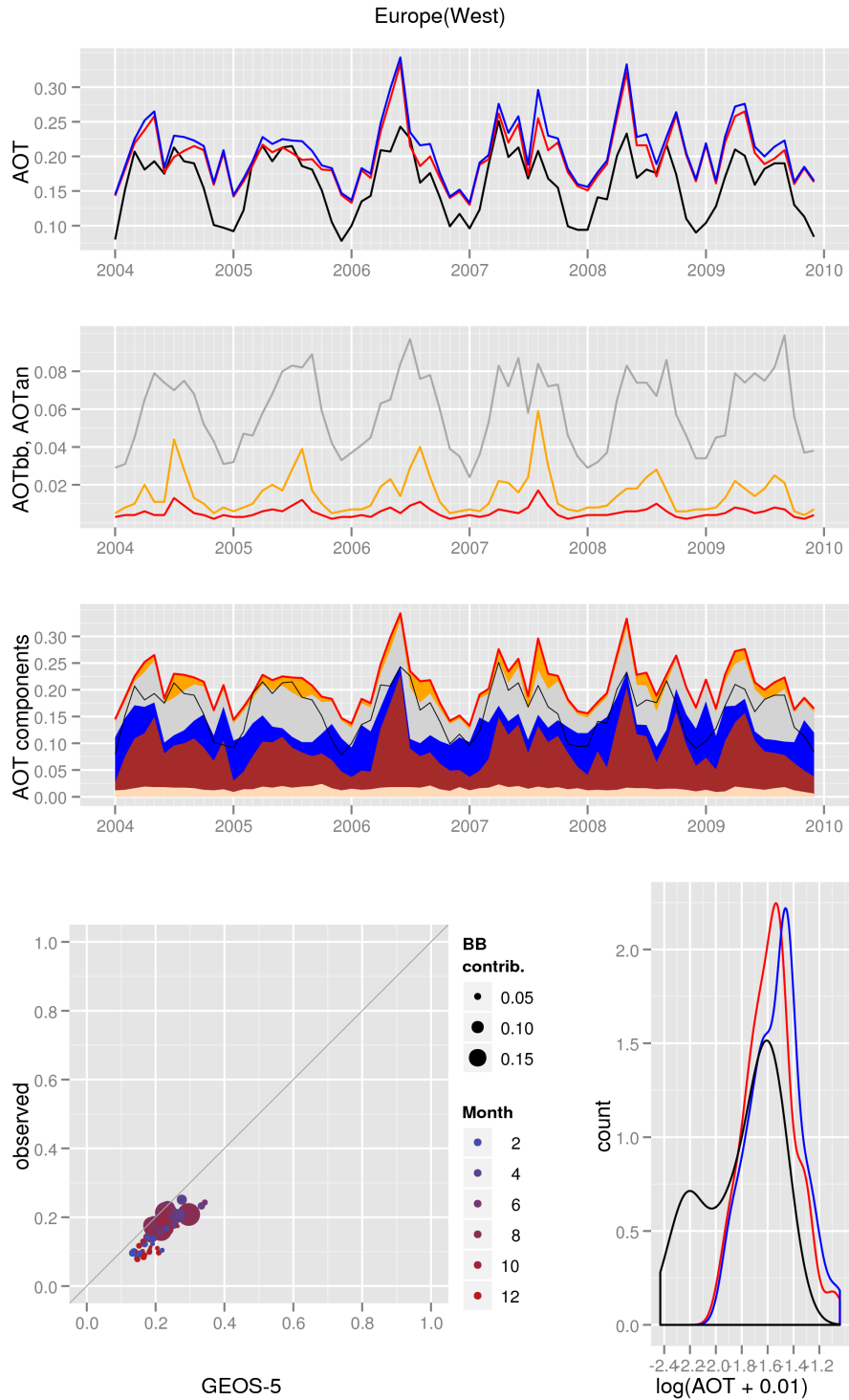
Figure C63: AOT diagnostics for the West Europe region.

Europe(West)
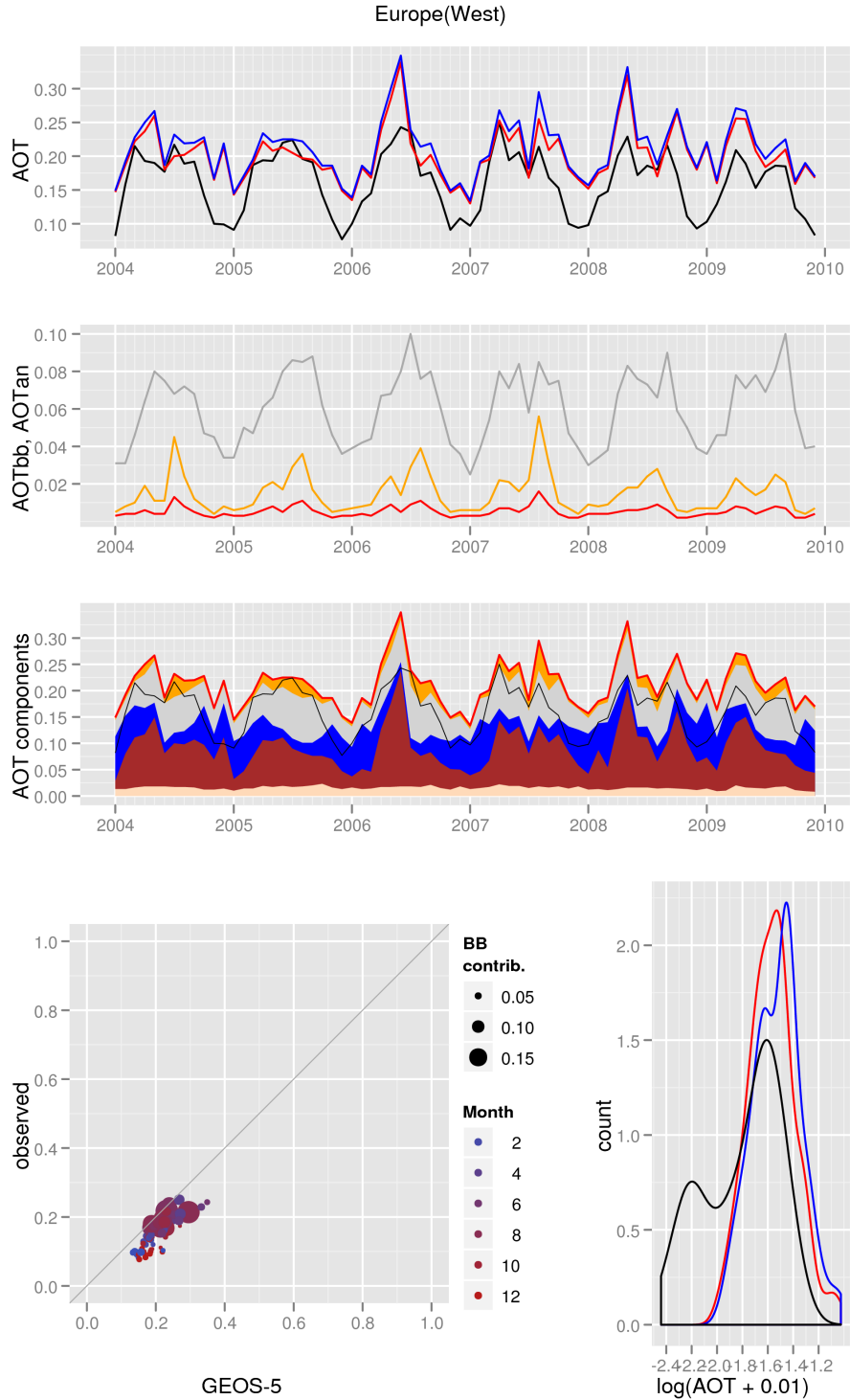
(b) GEOS-5 and NNR-AOT/Terra
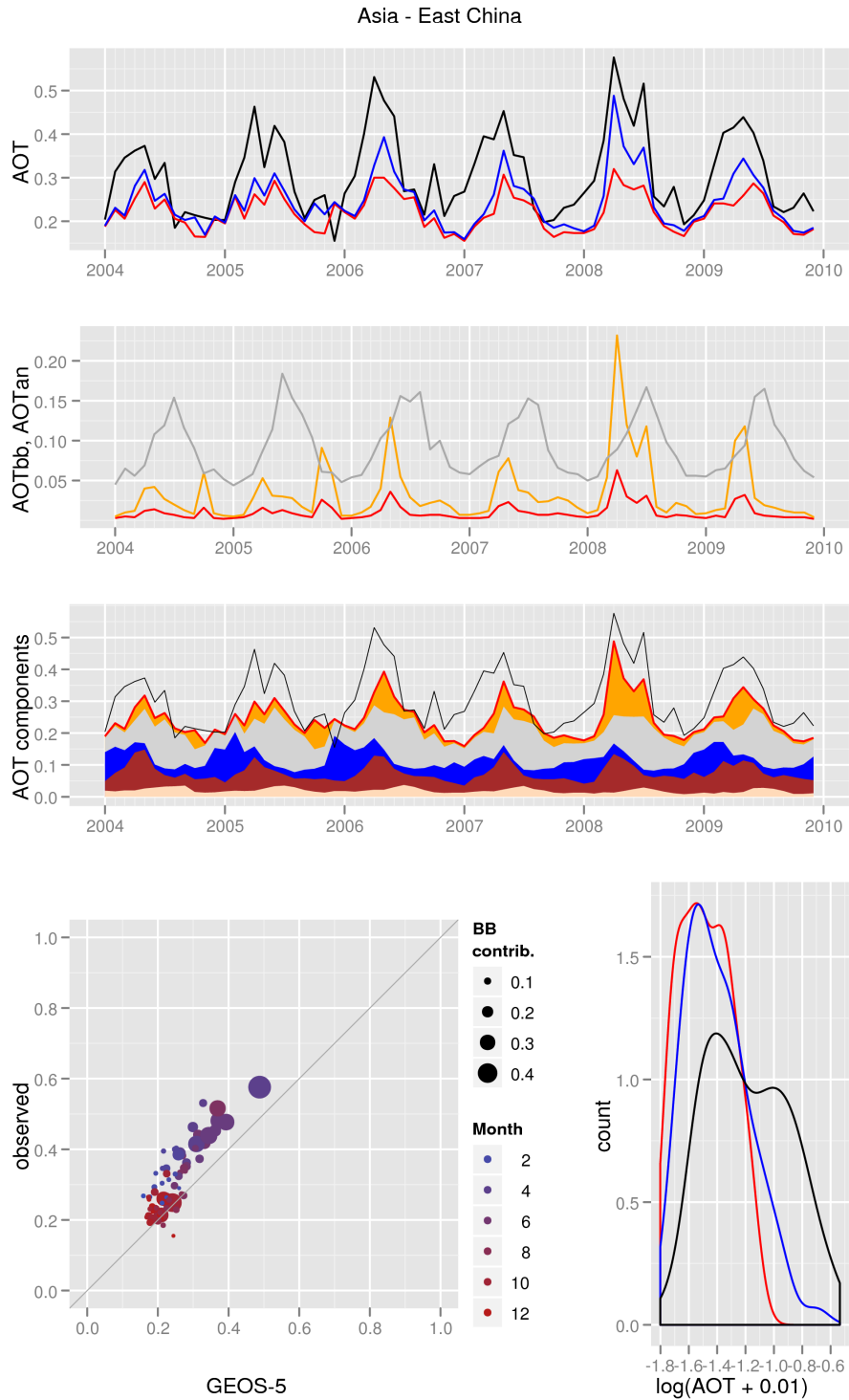
Asia - East China

(a) GEOS-5 and NNR-AOT/Aqua

Figure C64: AOT diagnostics for the East China region.

Asia - East China

(b) GEOS-5 and NNR-AOT/Terra

145
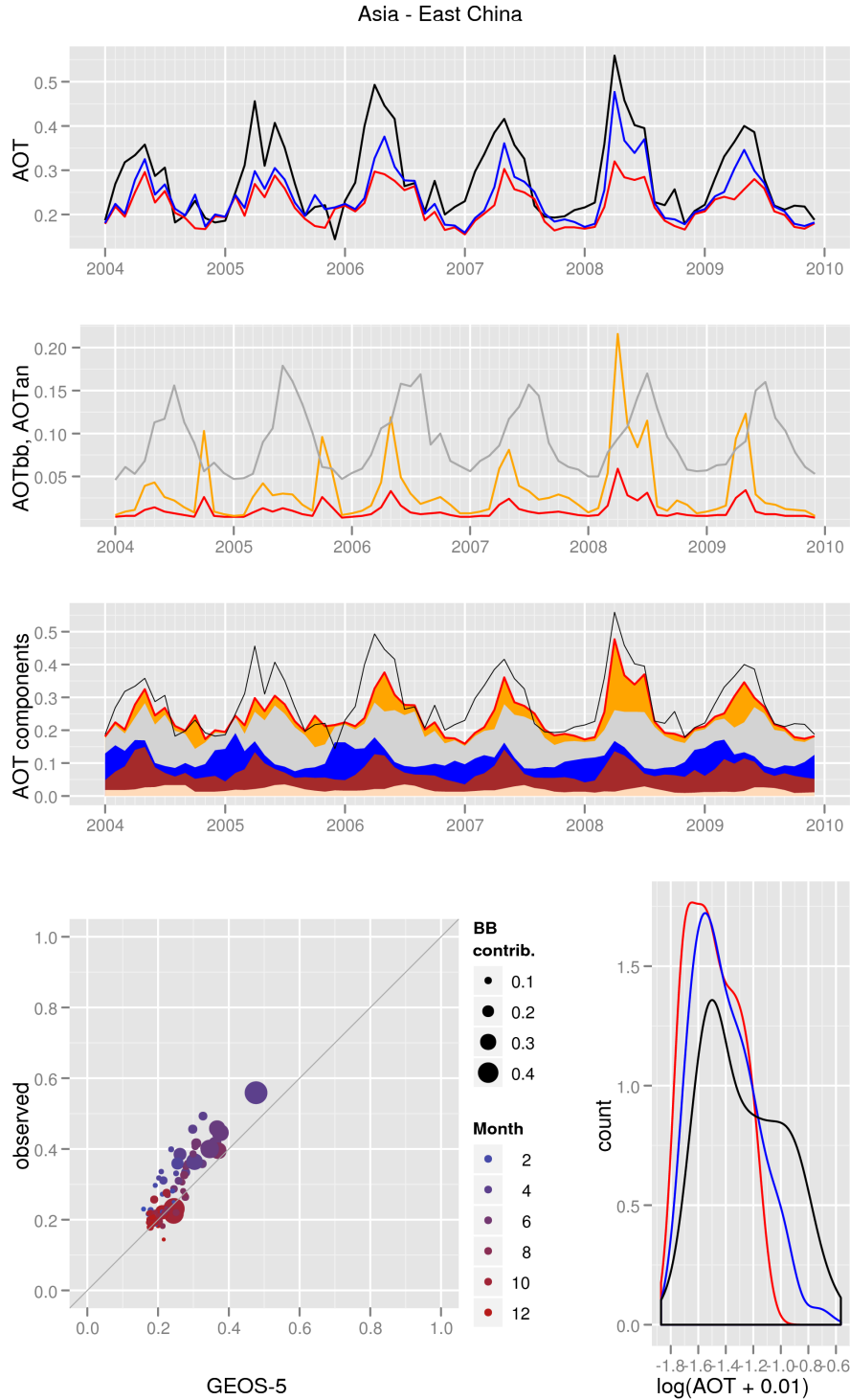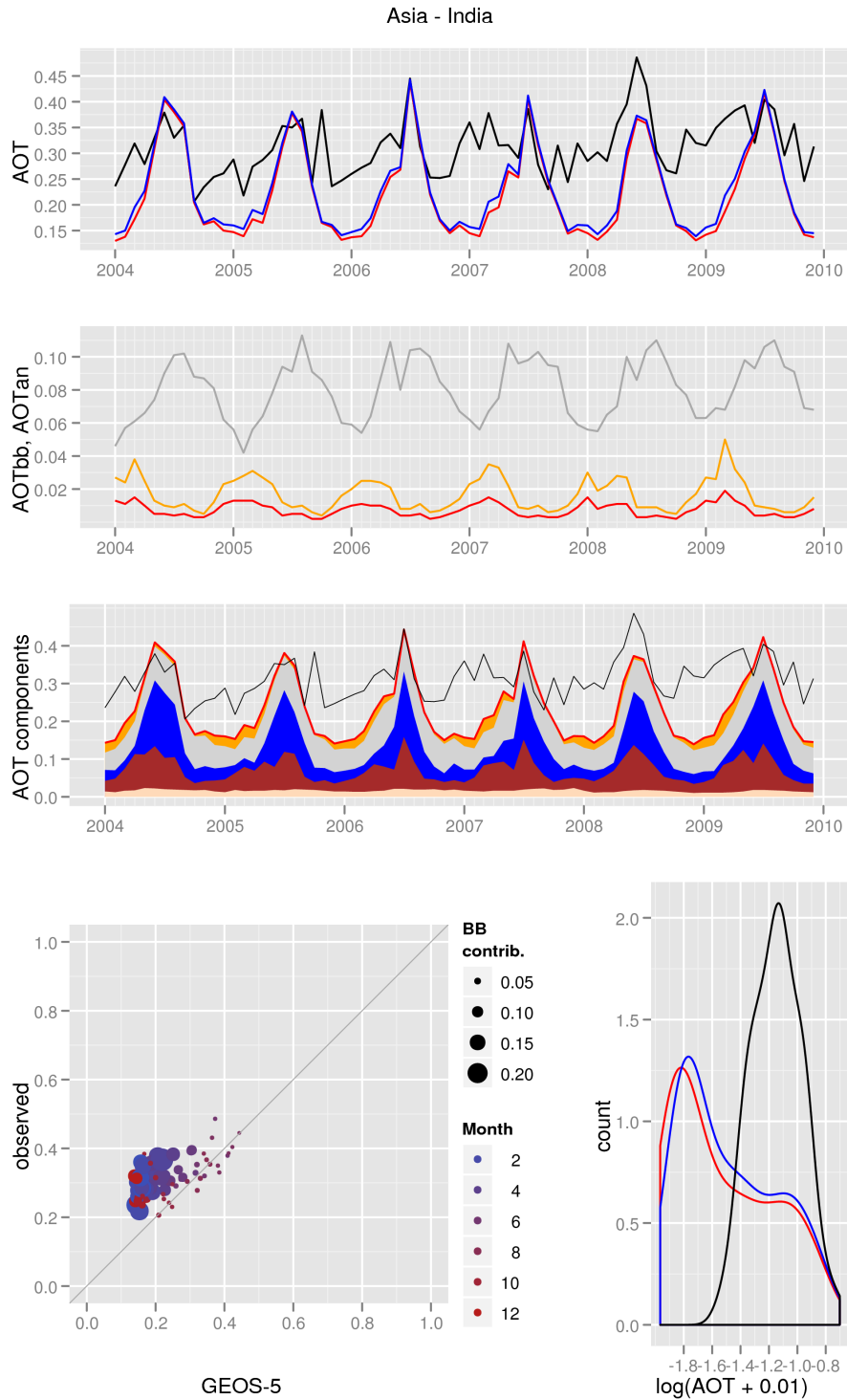
(a) GEOS-5 and NNR-AOT/Aqua

Figure C65: AOT diagnostics for the India region.

Asia - India
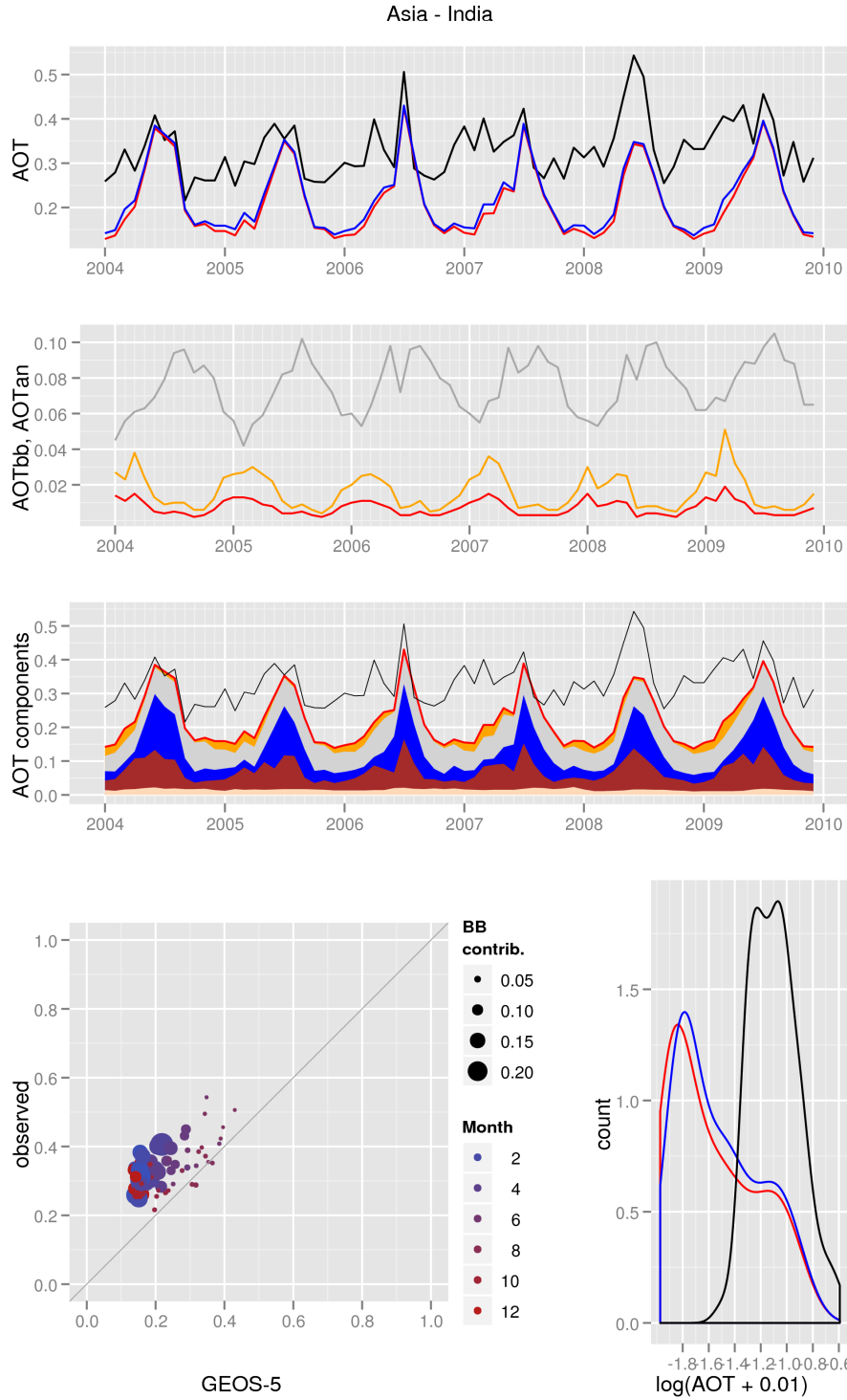
(b) GEOS-5 and NNR-AOT/Terra
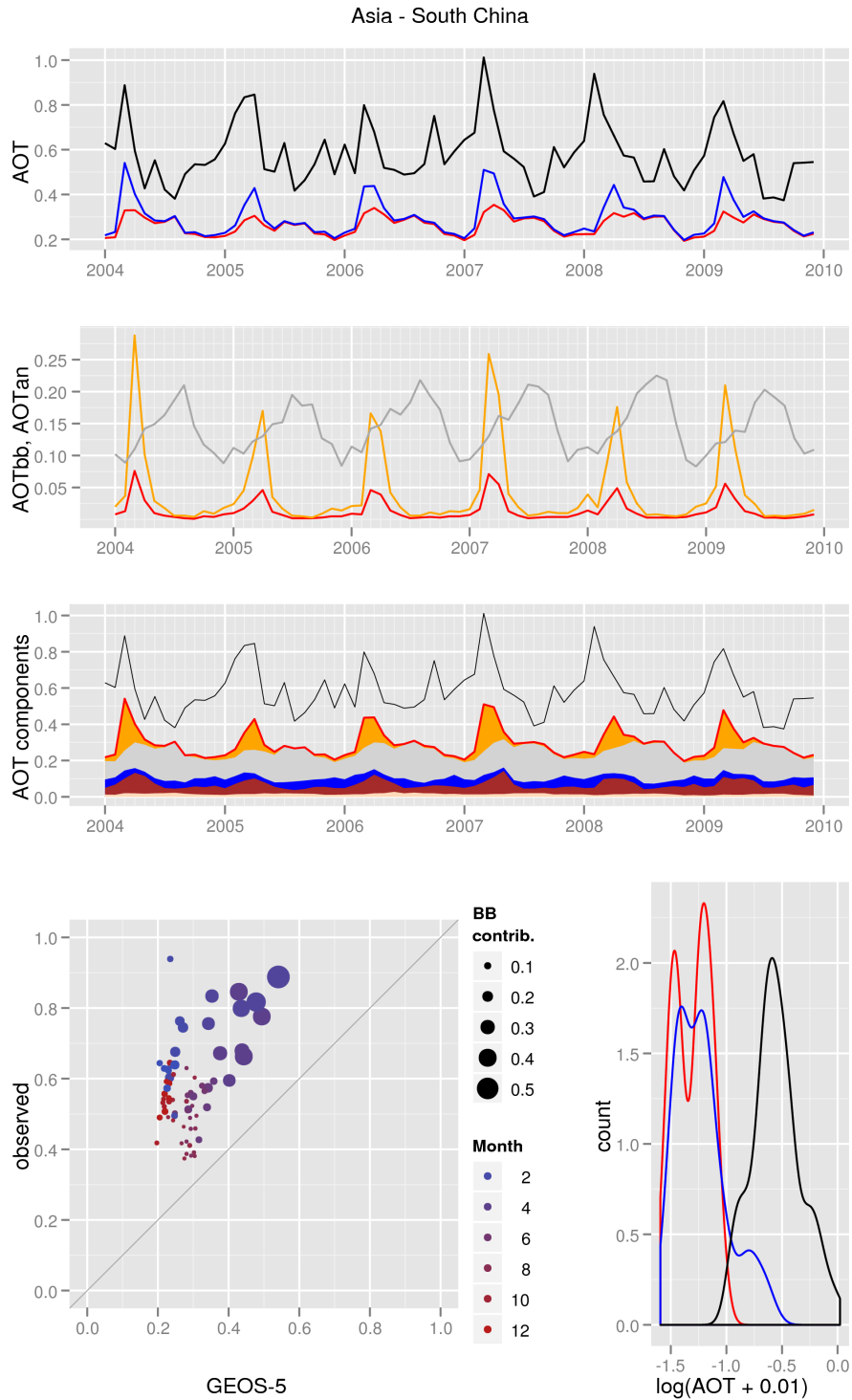
Asia - South China

(a) GEOS-5 and NNR-AOT/Aqua

Figure C66: AOT diagnostics for the South China region.

Asia - South China

(b) GEOS-5 and NNR-AOT/Terra

149
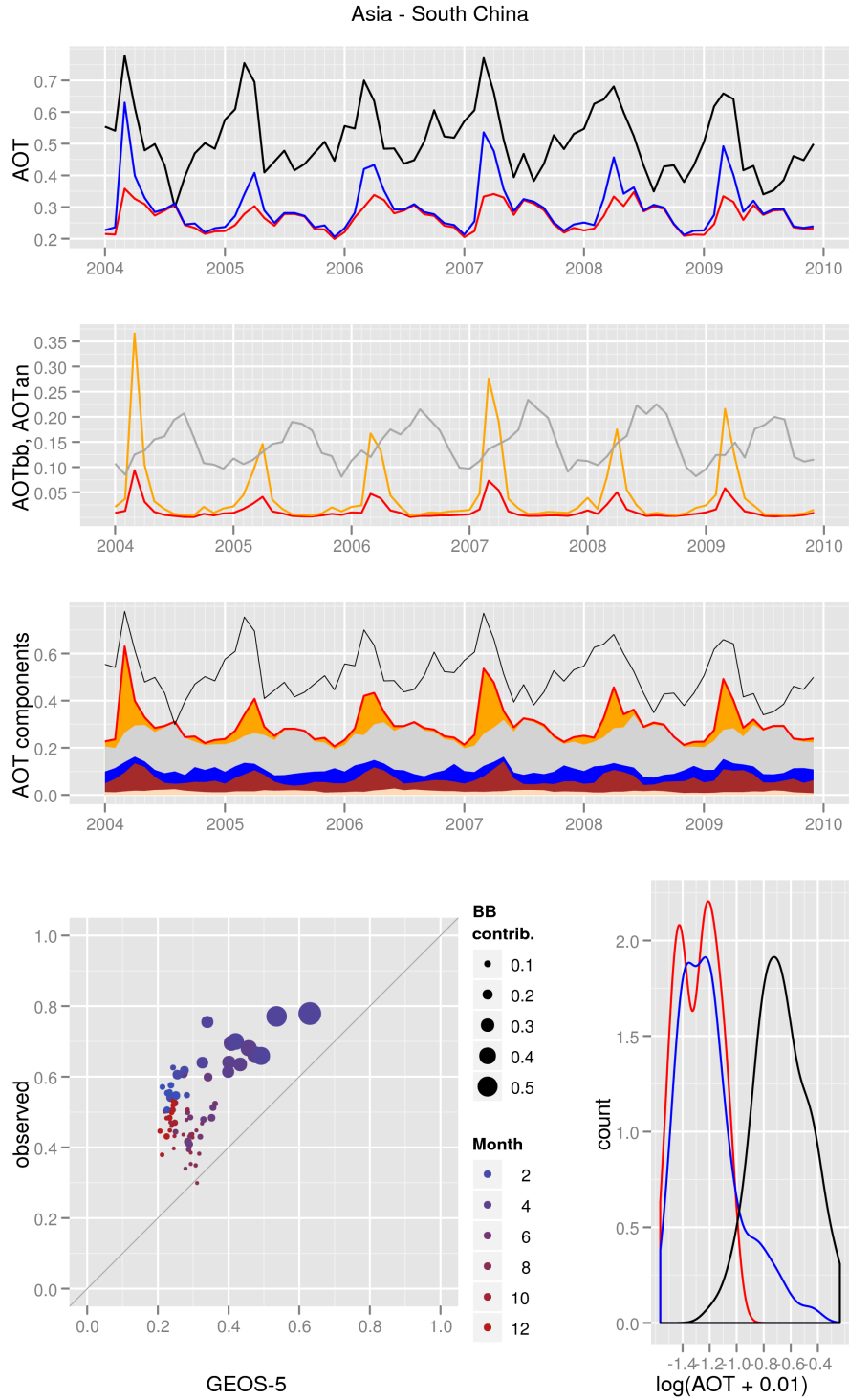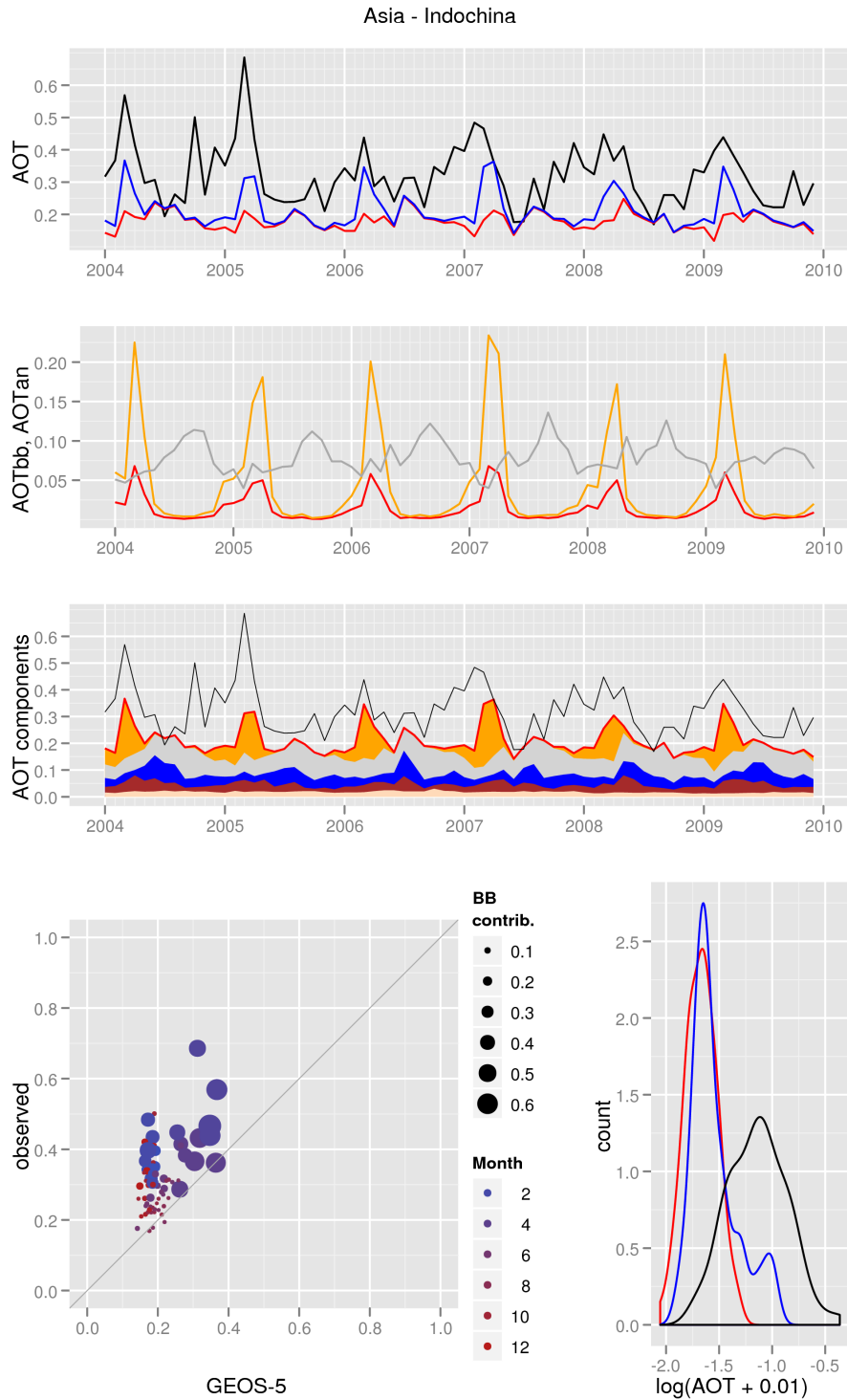
Asia - Indochina

(a) GEOS-5 and NNR-AOT/Aqua

Figure C67: AOT diagnostics for the Indochina region.
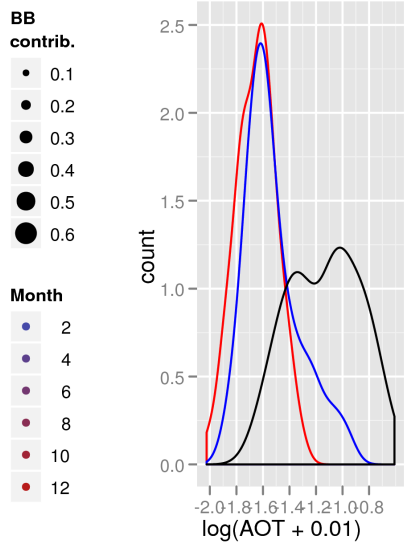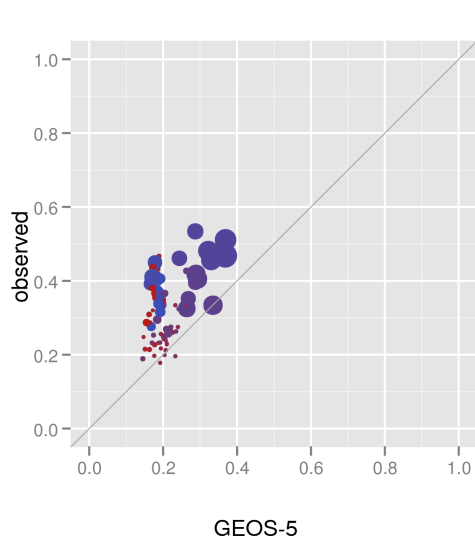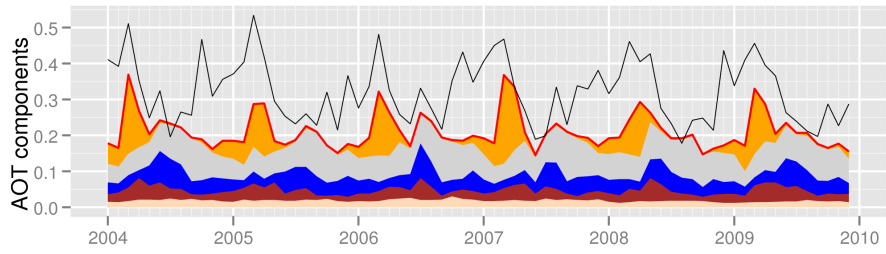
(b) GEOS-5 and NNR-AOT/Terra
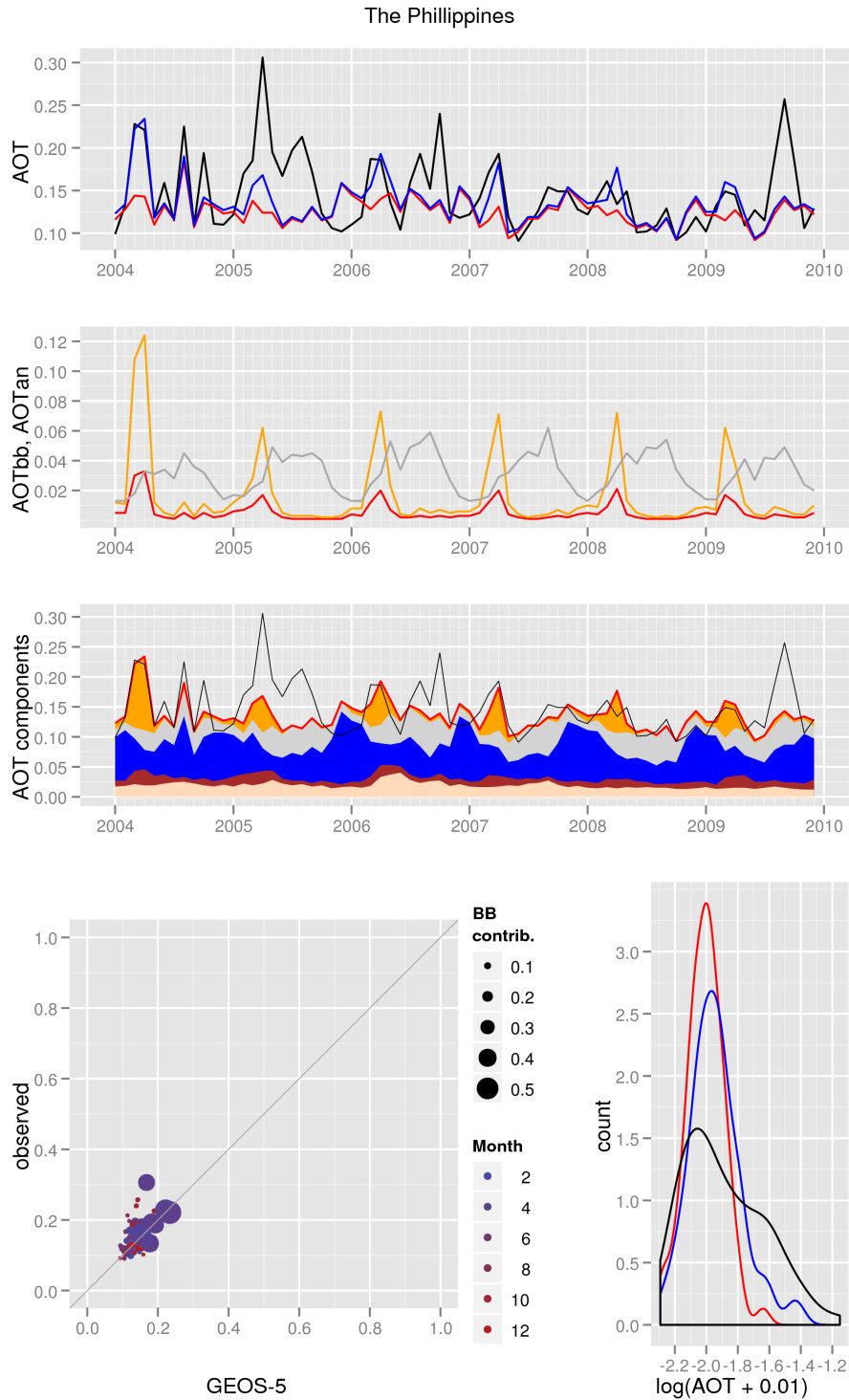
The Phillippines

(a) GEOS-5 and NNR-AOT/Aqua

Figure C68: AOT diagnostics for the The Philippines region.

The Phillippines
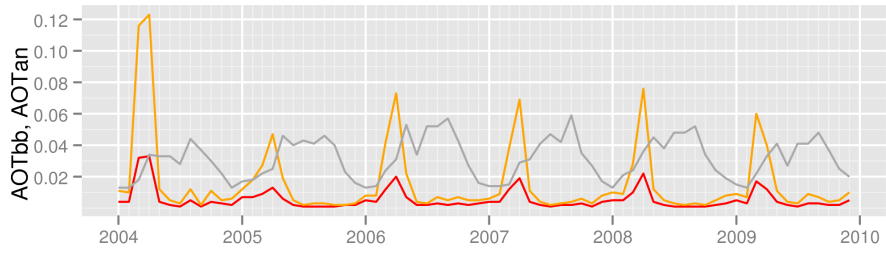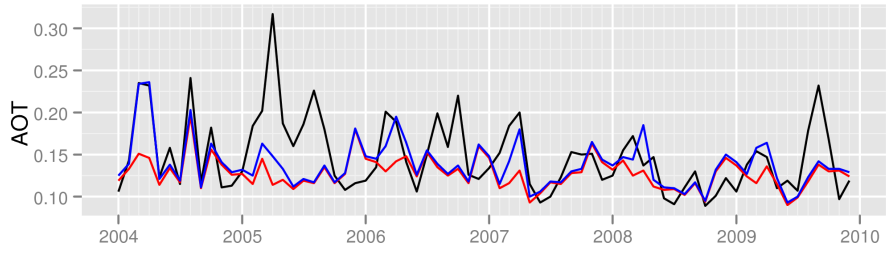
(b) GEOS-5 and NNR-AOT/Terra
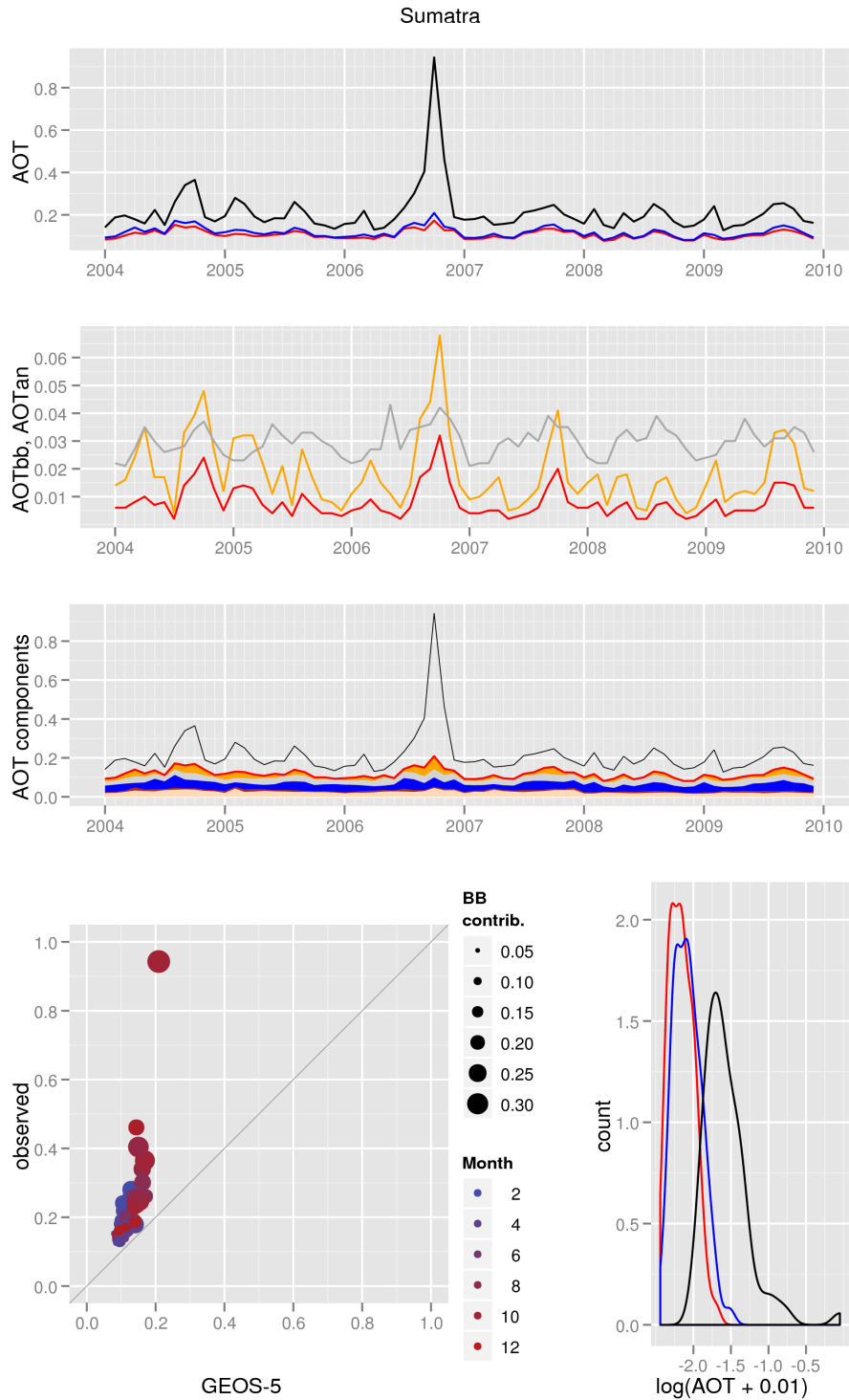
(a) GEOS-5 and NNR-AOT/Aqua

Figure C69: AOT diagnostics for the Sumatra region.

Sumatra

(b) GEOS-5 and NNR-AOT/Terra

155
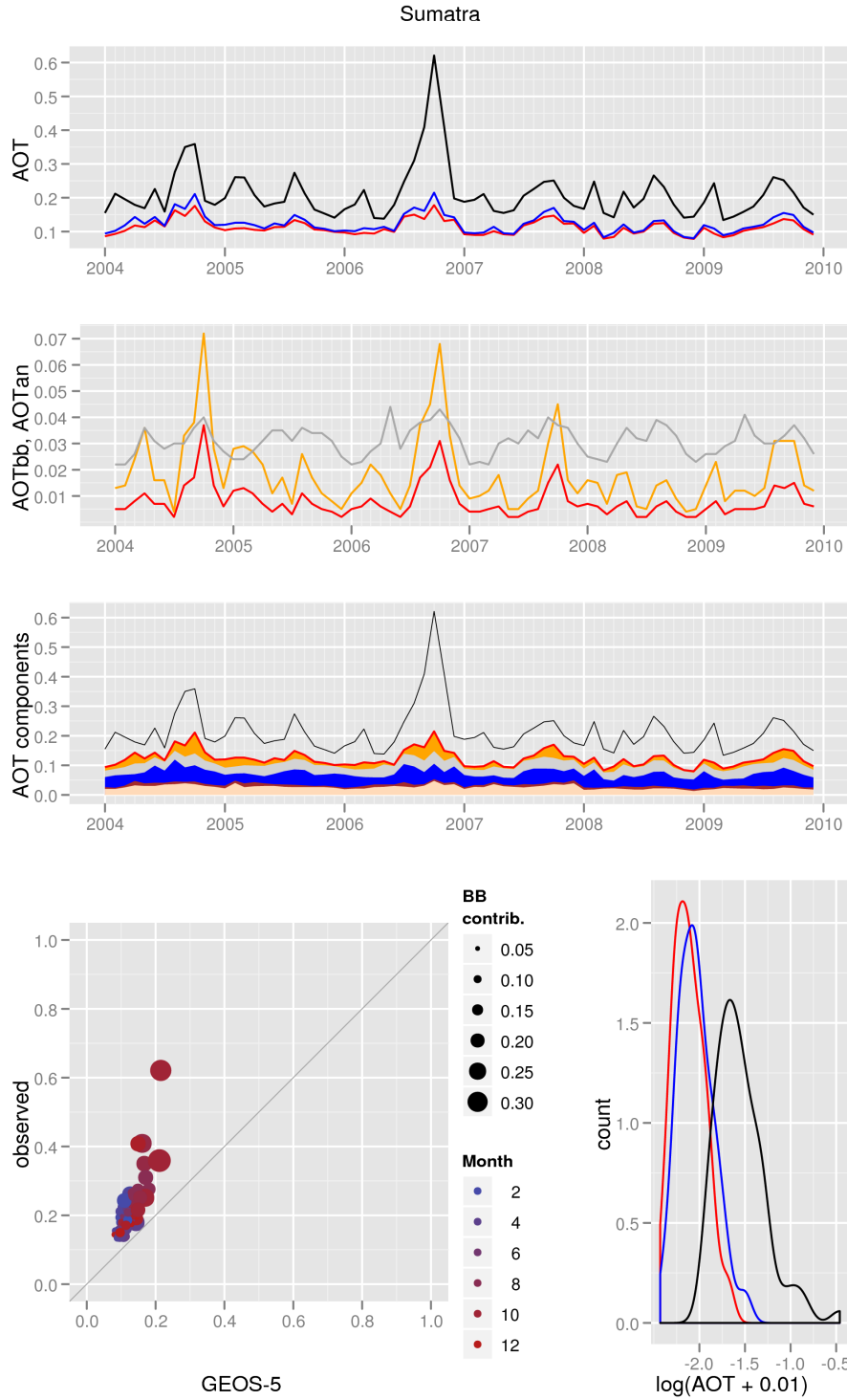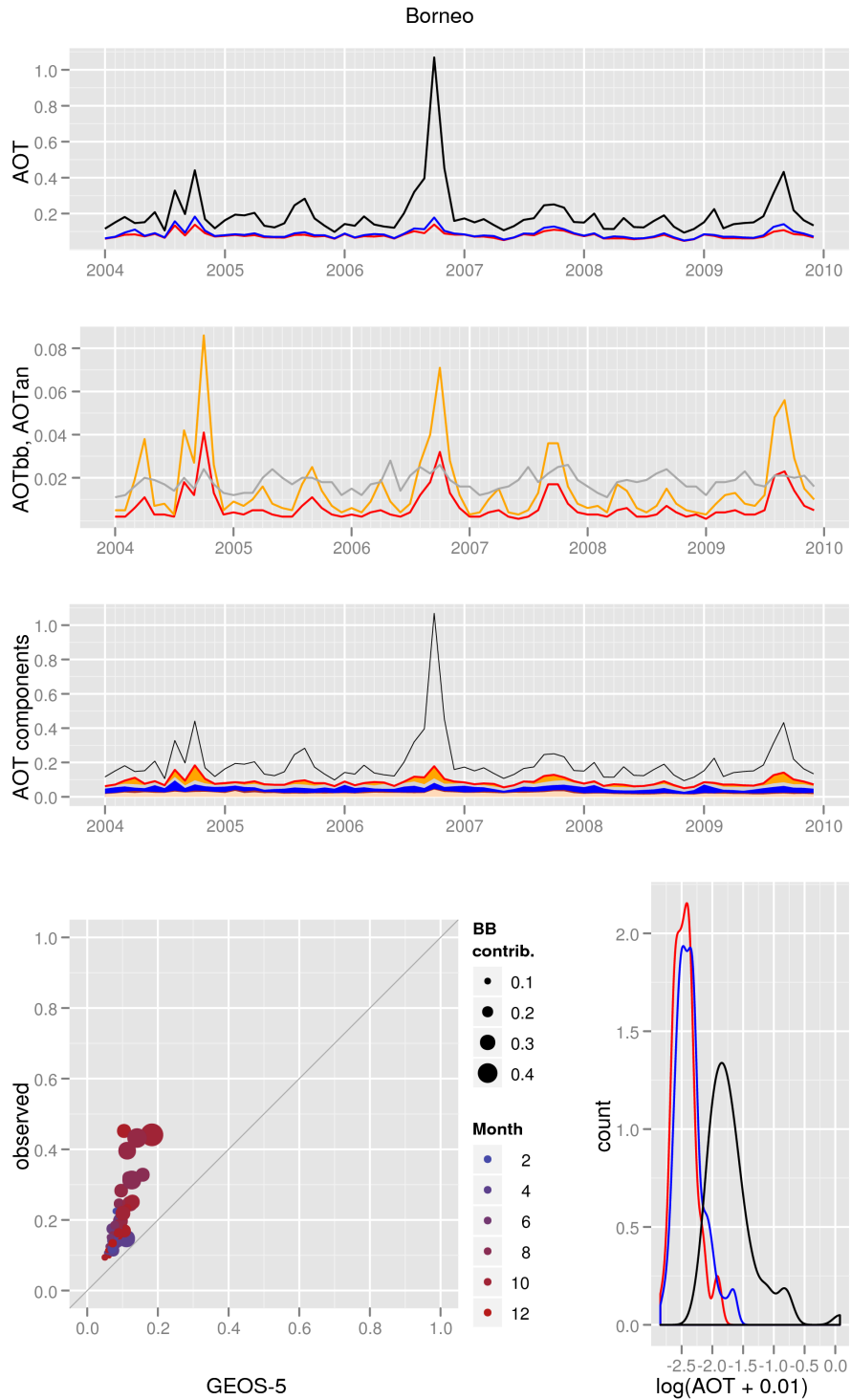
(a) GEOS-5 and NNR-AOT/Aqua

Figure C70: AOT diagnostics for the Borneo region.

156

Borneo

(b) GEOS-5 and NNR-AOT/Terra

157
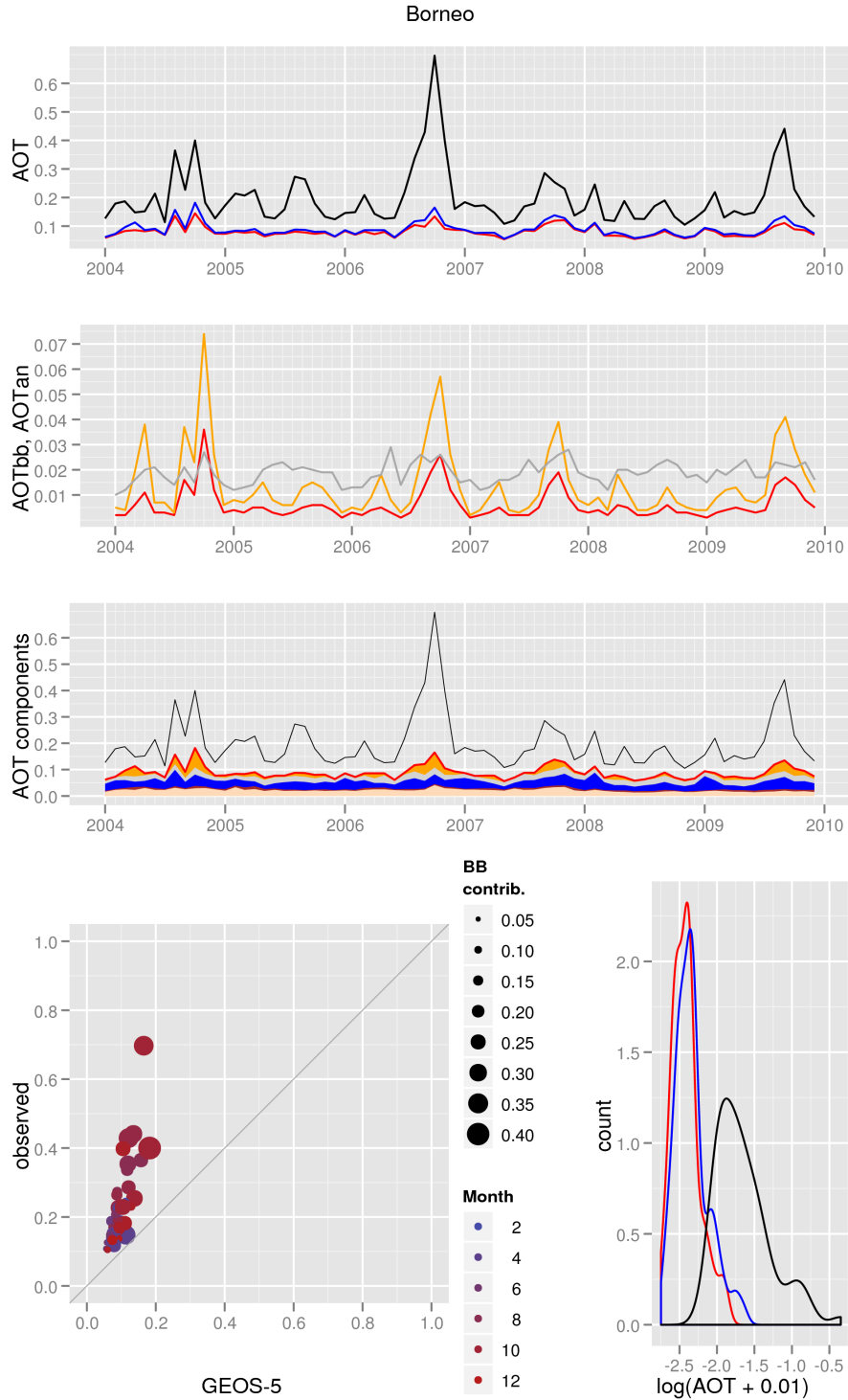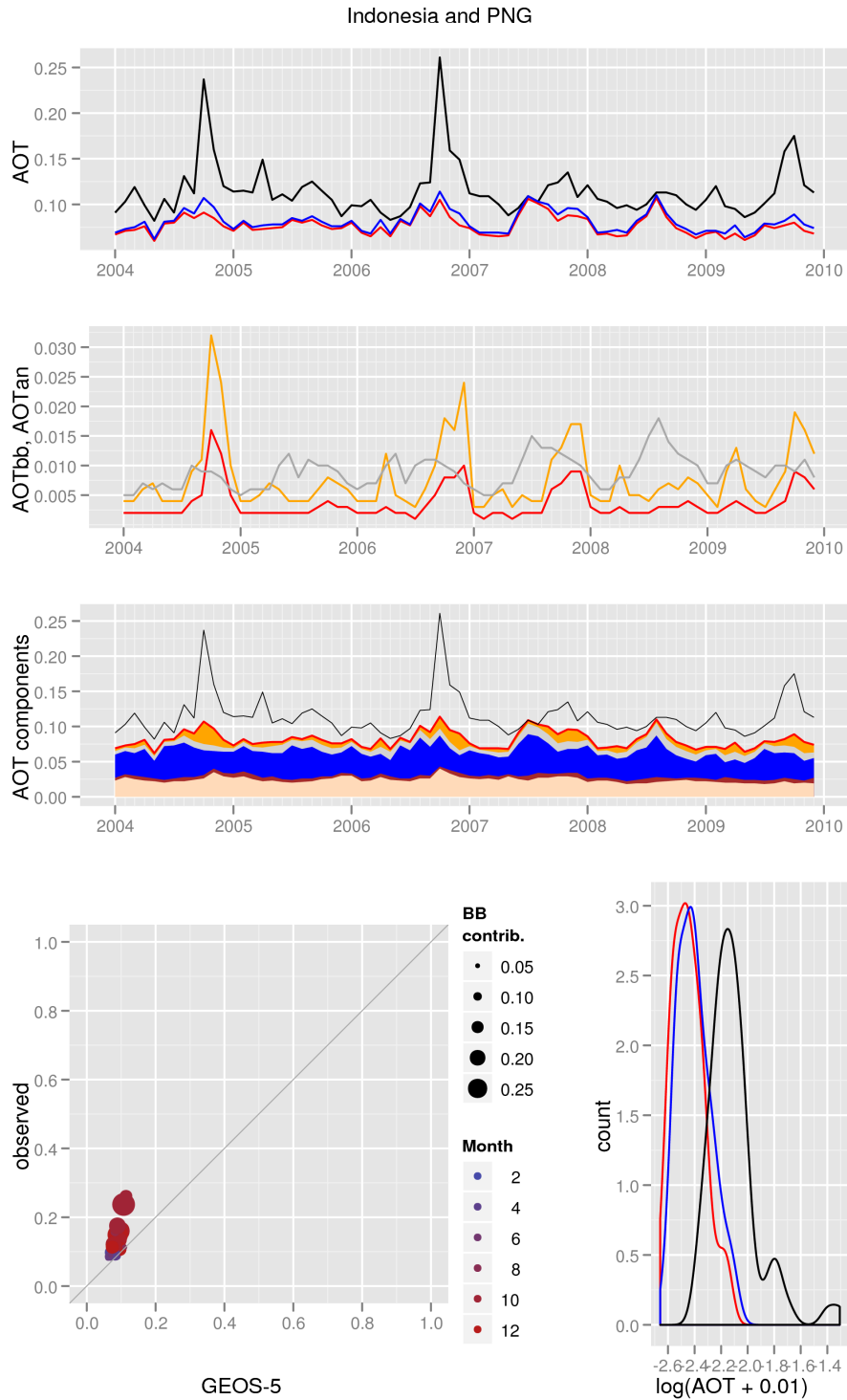
Figure C71: AOT diagnostics for the Indonesia and PNG region.
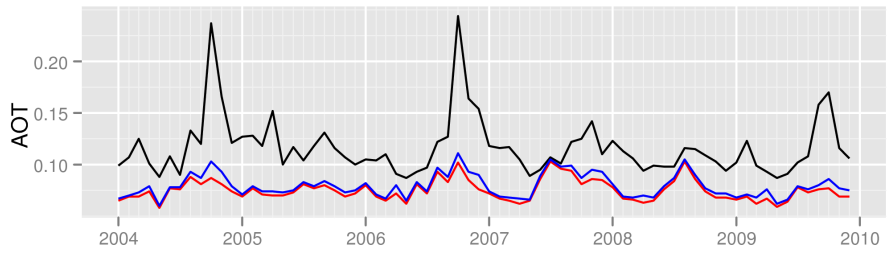
Indonesia and PNG

(b) GEOS-5 and NNR-AOT/Terra

159

Australia(North)

(a) GEOS-5 and NNR-AOT/Aqua

Figure C72: AOT diagnostics for the North Australia region.

Australia(North)
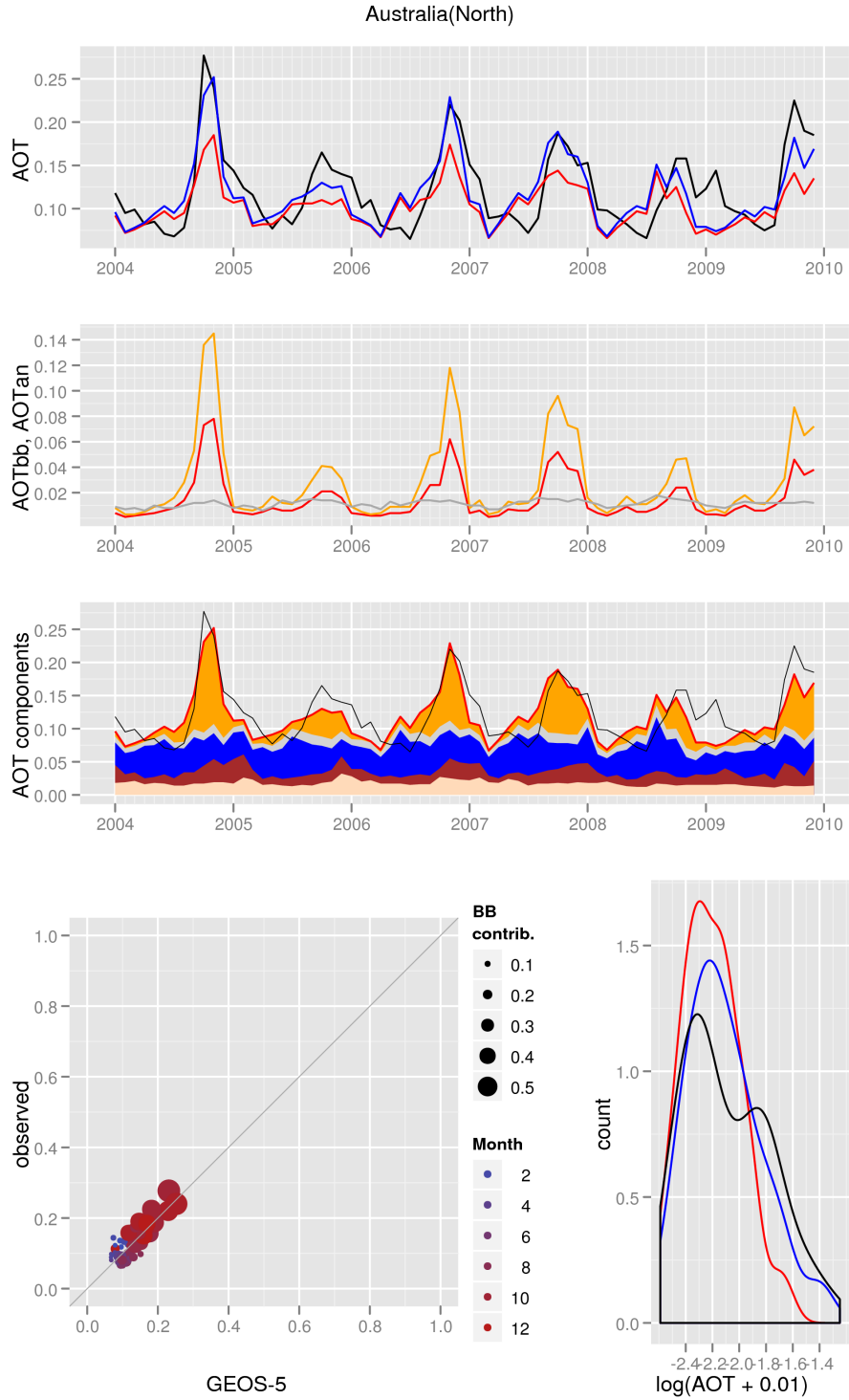
(b) GEOS-5 and NNR-AOT/Terra

Australia(West)

(a) GEOS-5 and NNR-AOT/Aqua

Figure C73: AOT diagnostics for the West Australia region.

(b) GEOS-5 and NNR-AOT/Terra

163
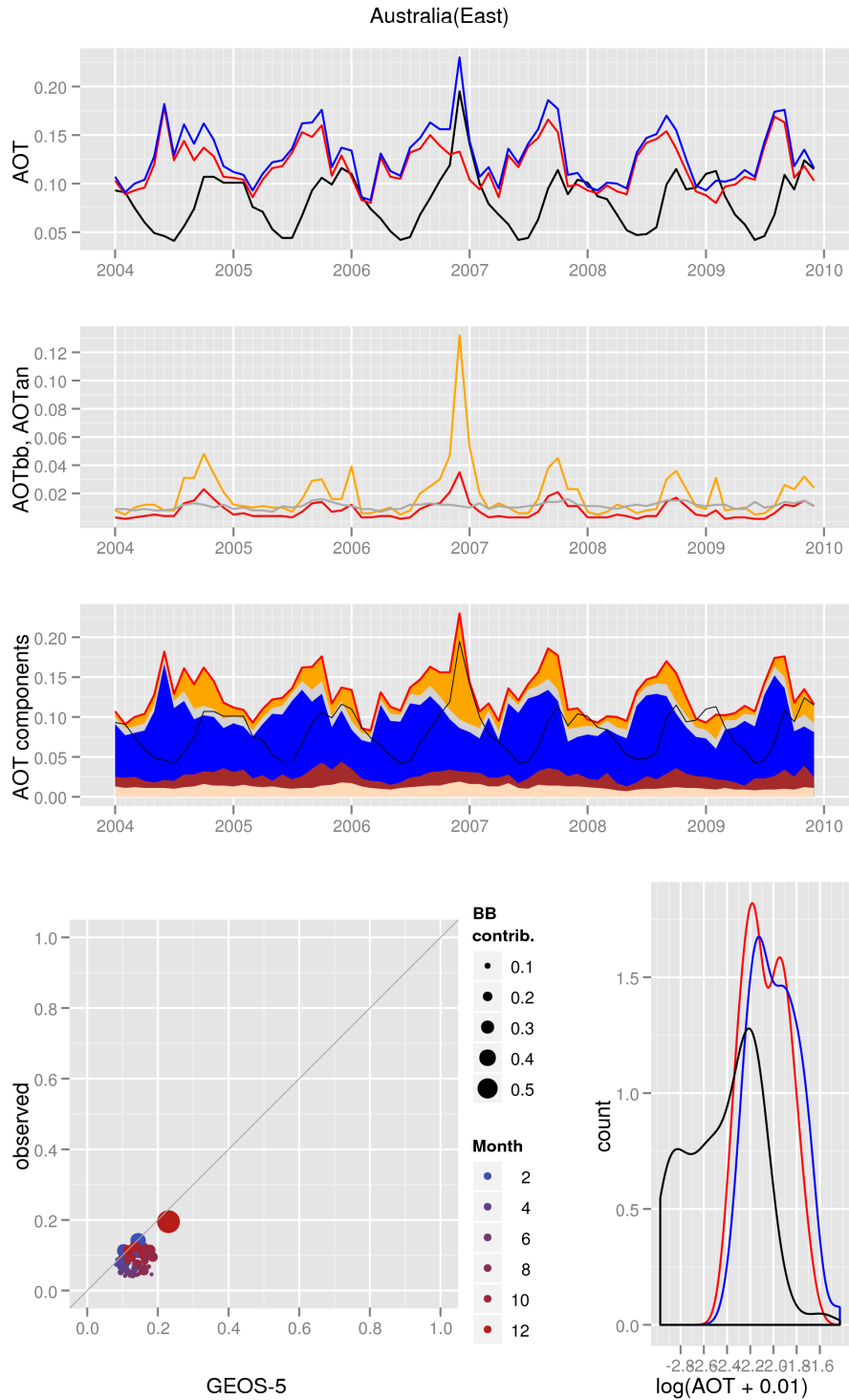
Australia(East)

(a) GEOS-5 and NNR-AOT/Aqua

Figure C74: AOT diagnostics for the East Australia region.
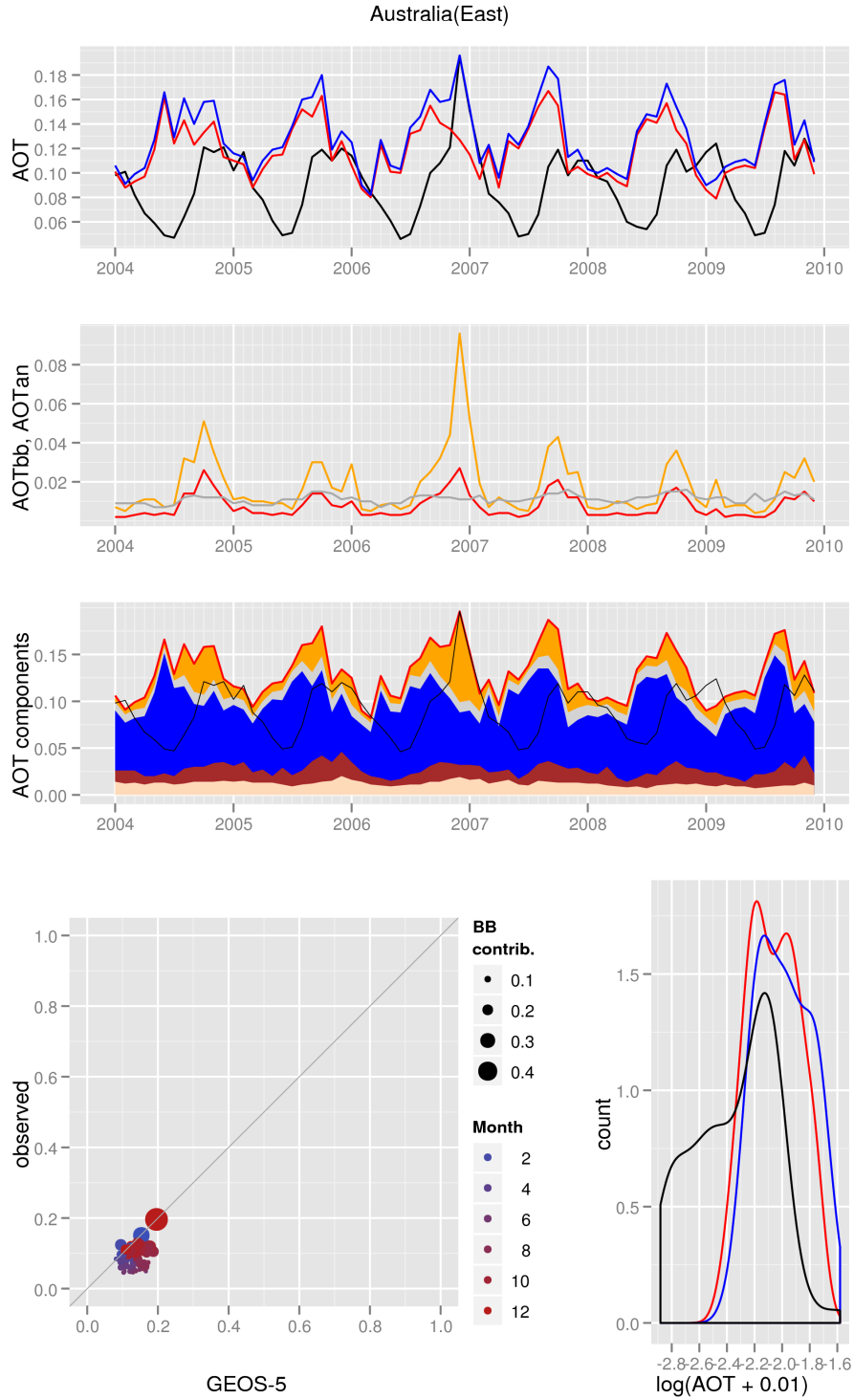
(b) GEOS-5 and NNR-AOT/Terra

(a) GEOS-5 and NNR-AOT/Aqua

Figure C75: AOT diagnostics for the Siberia (Far East) region.

Siberia(Far-East)

(b) GEOS-5 and NNR-AOT/Terra

167
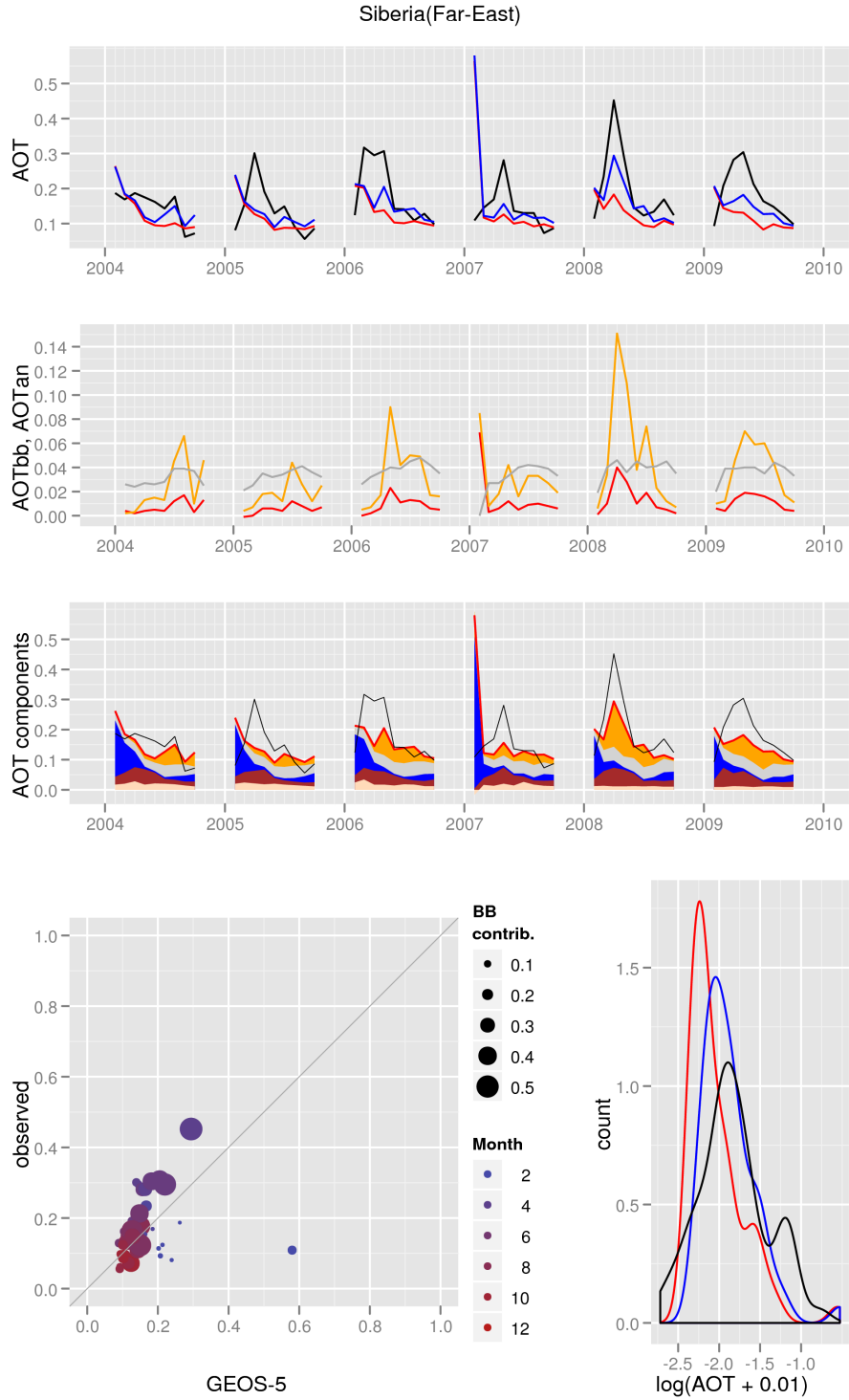
Figure C76: AOT diagnostics for the Sahara region.

(a) GEOS-5 and NNR-AOT/Aqua

Africa - Sahara

(b) GEOS-5 and NNR-AOT/Terra

169
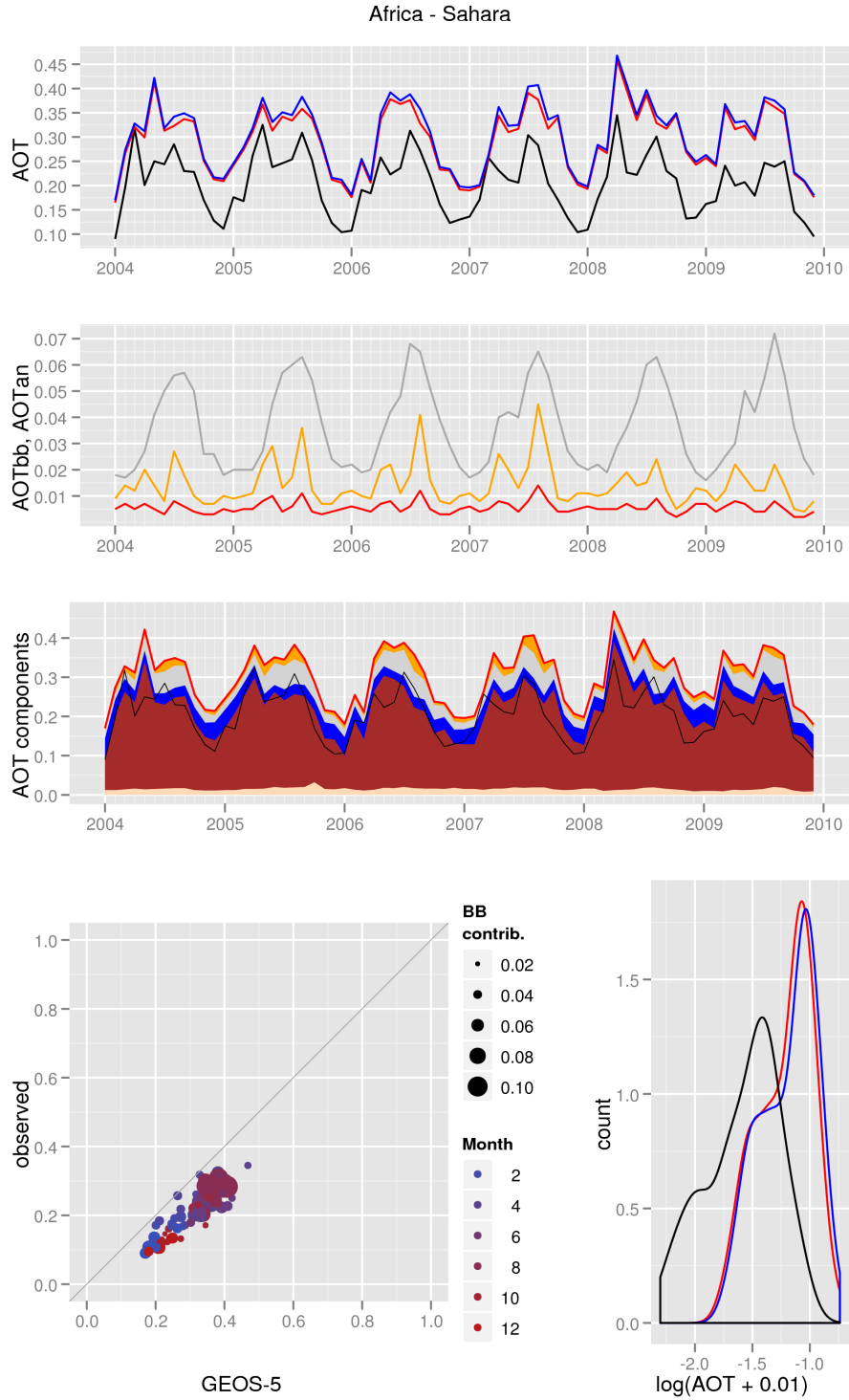
(a) GEOS-5 and NNR-AOT/Aqua

Figure C77: AOT diagnostics for the Sahel region.

(b) GEOS-5 and NNR-AOT/Terra

Africa - Cape Verde
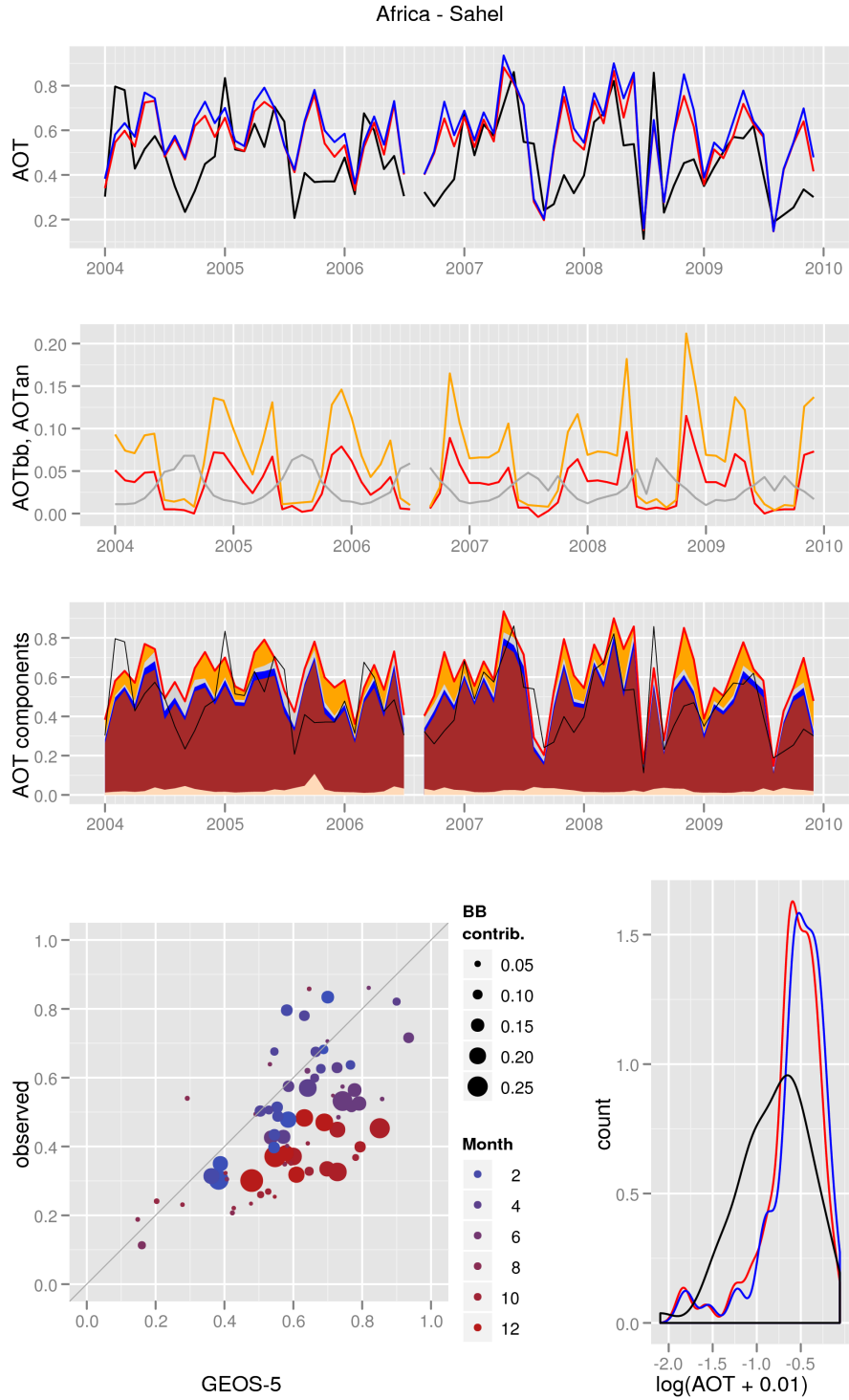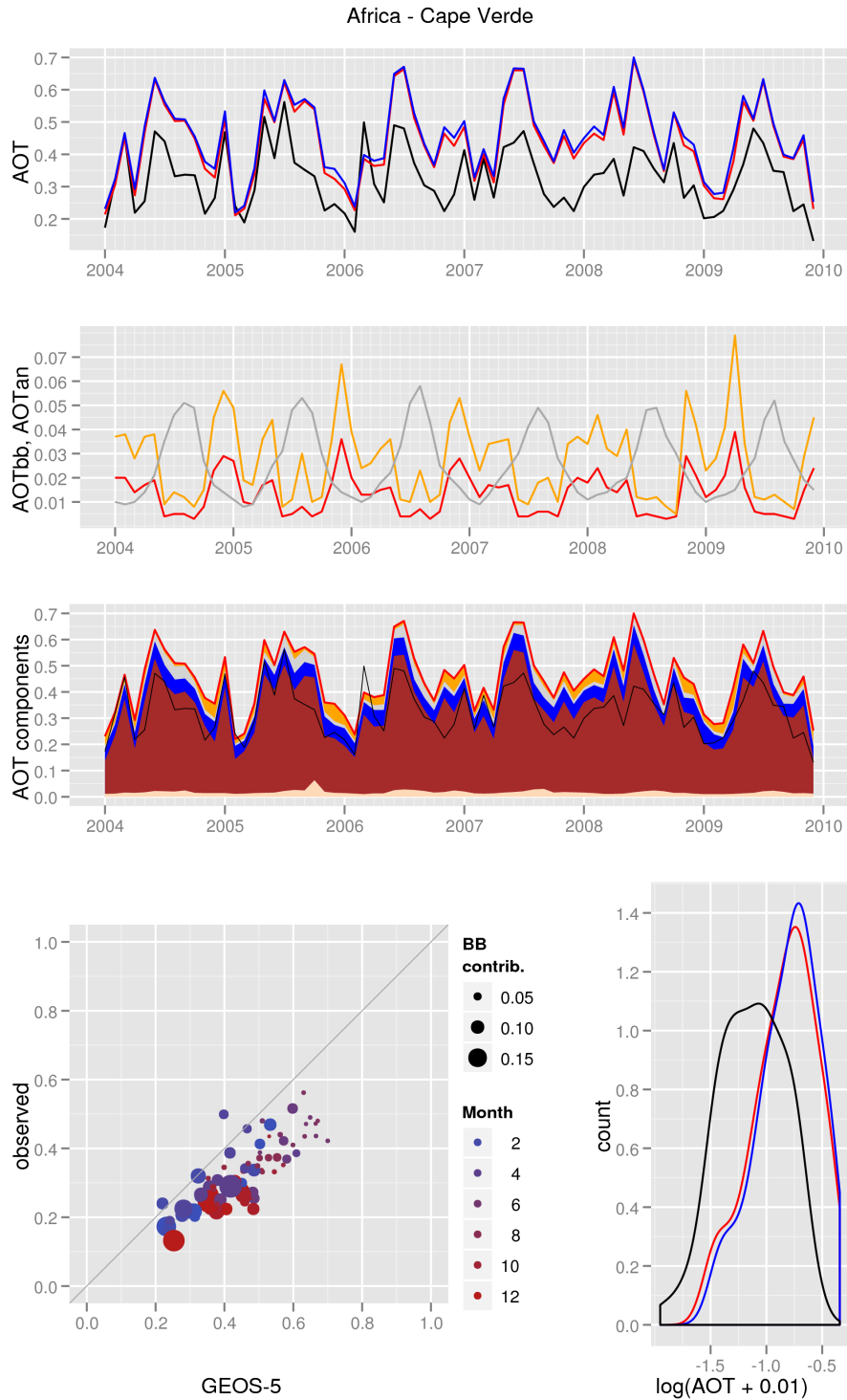
(a) GEOS-5 and NNR-AOT/Aqua

Figure C78: AOT diagnostics for the Cape Verde region.

Africa - Cape Verde

(b) GEOS-5 and NNR-AOT/Terra

173

Africa - Red Sea

(a) GEOS-5 and NNR-AOT/Aqua

Figure C79: AOT diagnostics for the Red Sea region.

Africa - Red Sea

(b) GEOS-5 and NNR-AOT/Terra

175

Asia - Persian Gulf

(a) GEOS-5 and NNR-AOT/Aqua

Figure C80: AOT diagnostics for the Persian Gulf region.

(b) GEOS-5 and NNR-AOT/Terra

Arabian Sea

(a) GEOS-5 and NNR-AOT/Aqua

Figure C81: AOT diagnostics for the Arabian Sea region.

Arabian Sea

(b) GEOS-5 and NNR-AOT/Terra

179
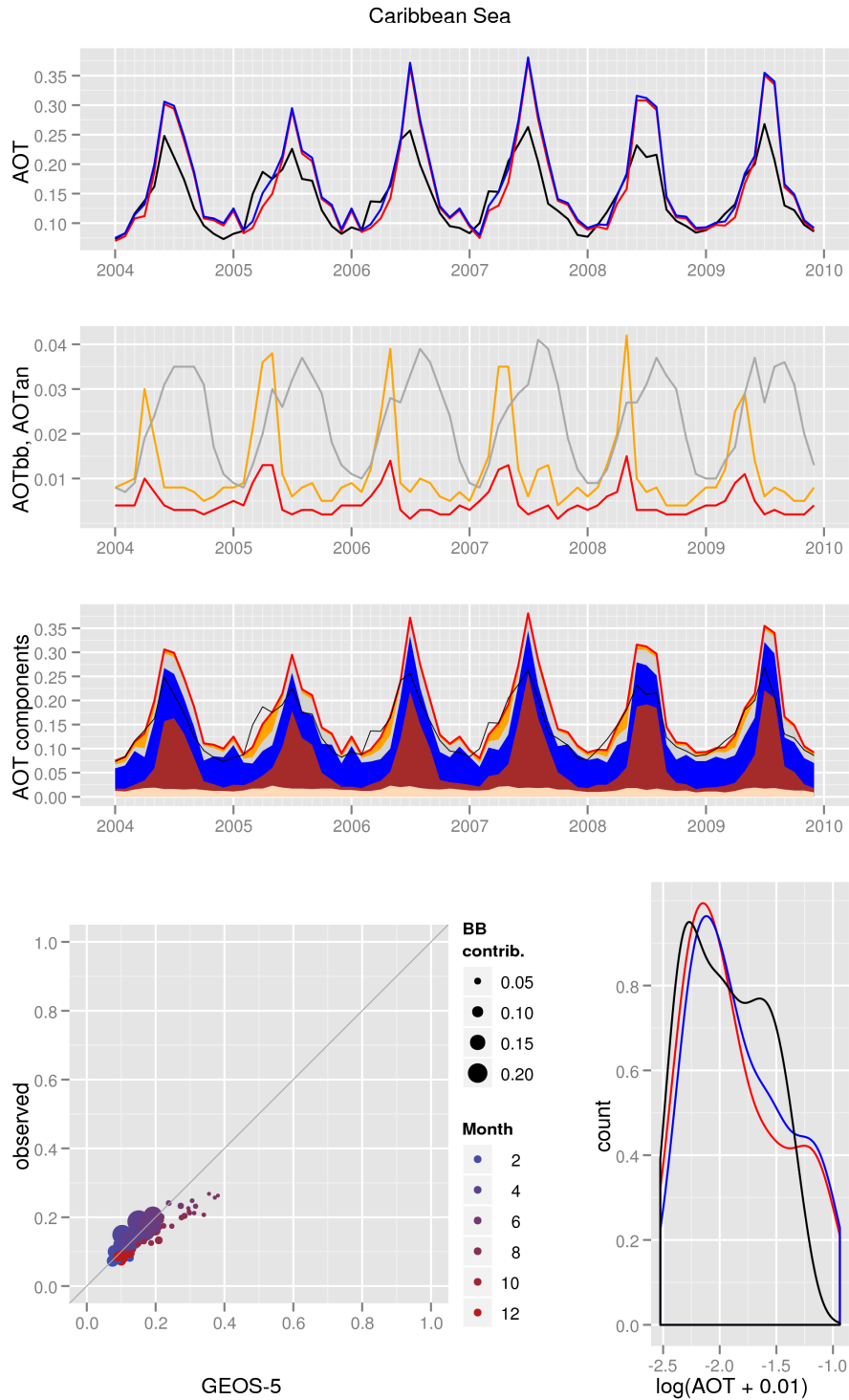
Caribbean Sea

(a) GEOS-5 and NNR-AOT/Aqua

Figure C82: AOT diagnostics for the Caribbean Sea region.

Caribbean Sea

(b) GEOS-5 and NNR-AOT/Terra

181

N.A. Ocean - SAL/Dust

(a) GEOS-5 and NNR-AOT/Aqua

Figure C83: AOT diagnostics for the SAL/Dust region.

N.A. Ocean - SAL/Dust

(b) GEOS-5 and NNR-AOT/Terra

183

S.A. Ocean - BB Corridor
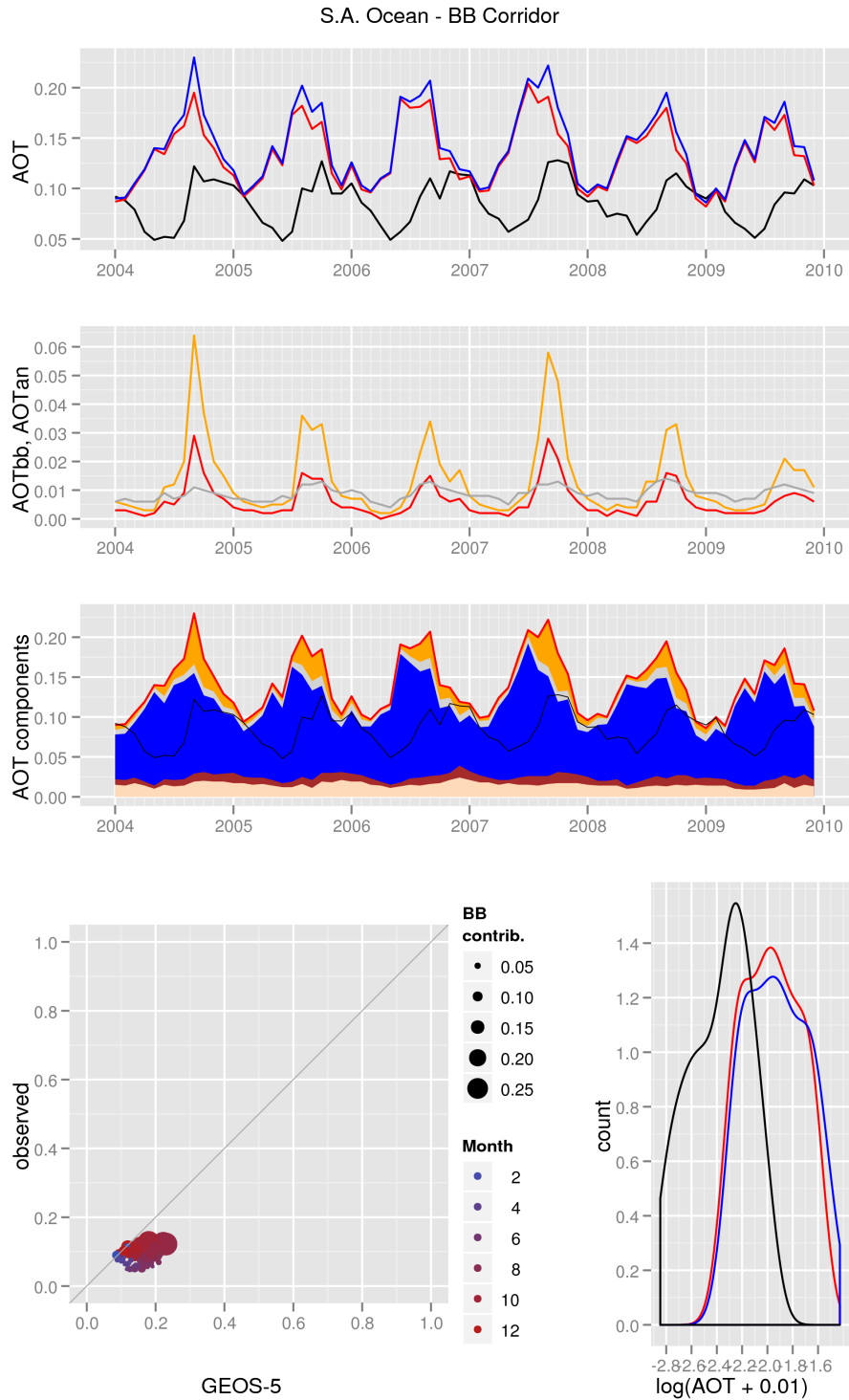
(a) GEOS-5 and NNR-AOT/Aqua

Figure C84: AOT diagnostics for the South America BB region.

S.A. Ocean - BB Corridor
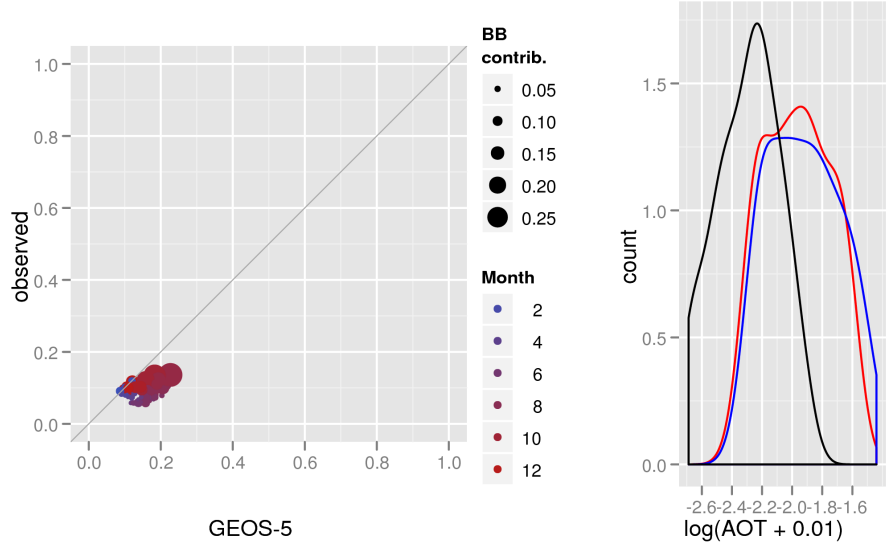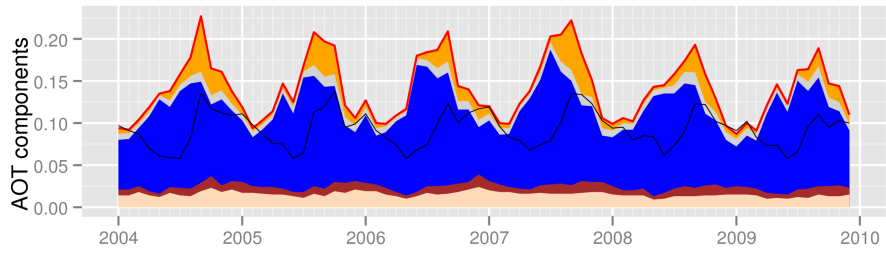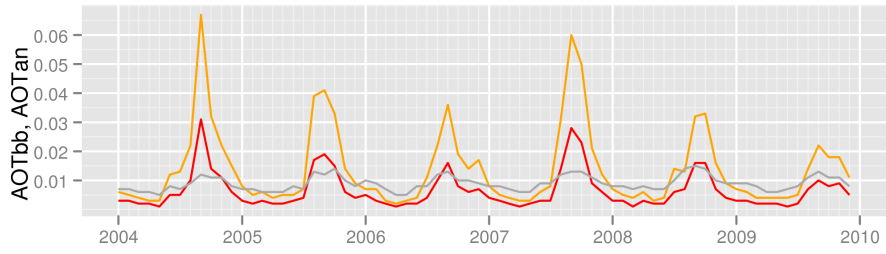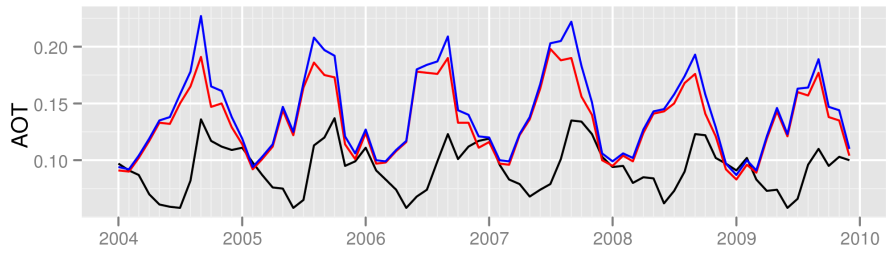
(b) GEOS-5 and NNR-AOT/Terra

Appendix D. Regional comparison of QFED with the GFED, GFAS and FLAMBE datasets in the GFED basis regions
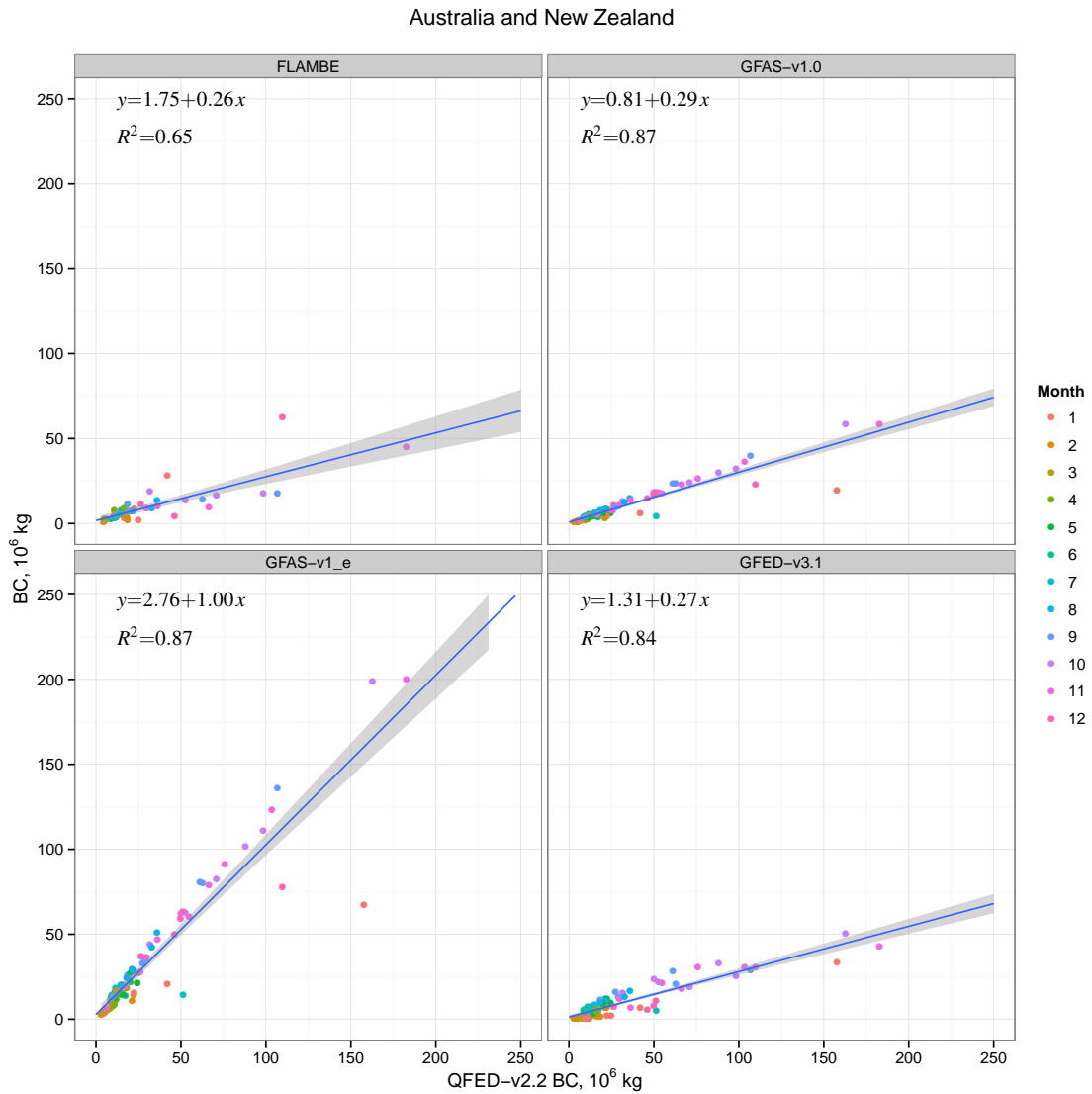
Figure D85: Scatter plots of monthly black carbon (BC) emissions from the FLAMBE, GFAS, GFED and QFED datasets for the Australia and New Zealand region.
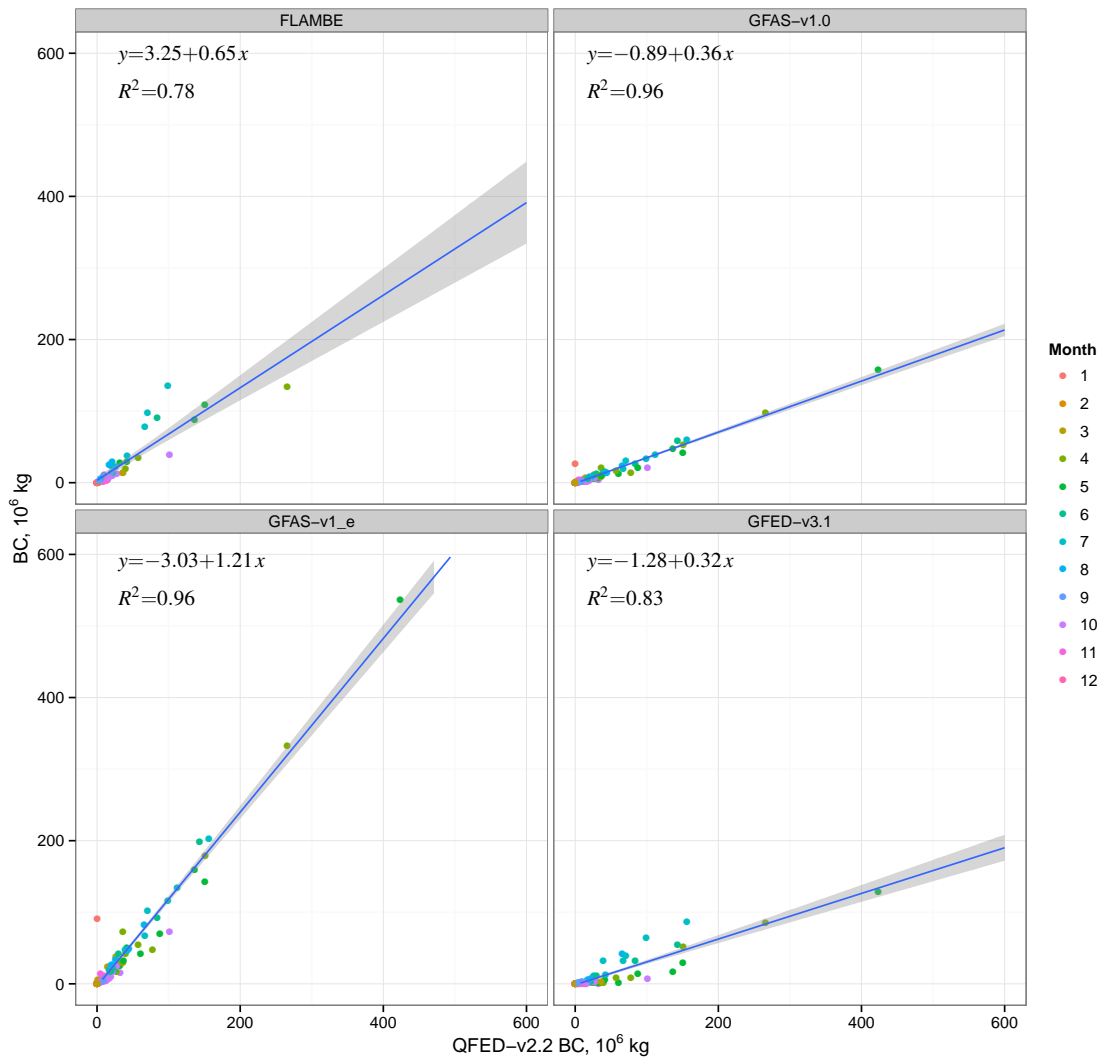
Figure D86: Scatter plots of monthly black carbon (BC) emissions from the FLAMBE, GFAS, GFED and QFED datasets for the Boreal Asia region.

Boreal North America

$y=-1.73+0.56x$
$R^2=0.81$

$y=-0.86+0.39x$
$R^2=0.93$

$y=-2.94+1.32x$
$R^2=0.93$

$y=-2.62+0.48x$
$R^2=0.83$
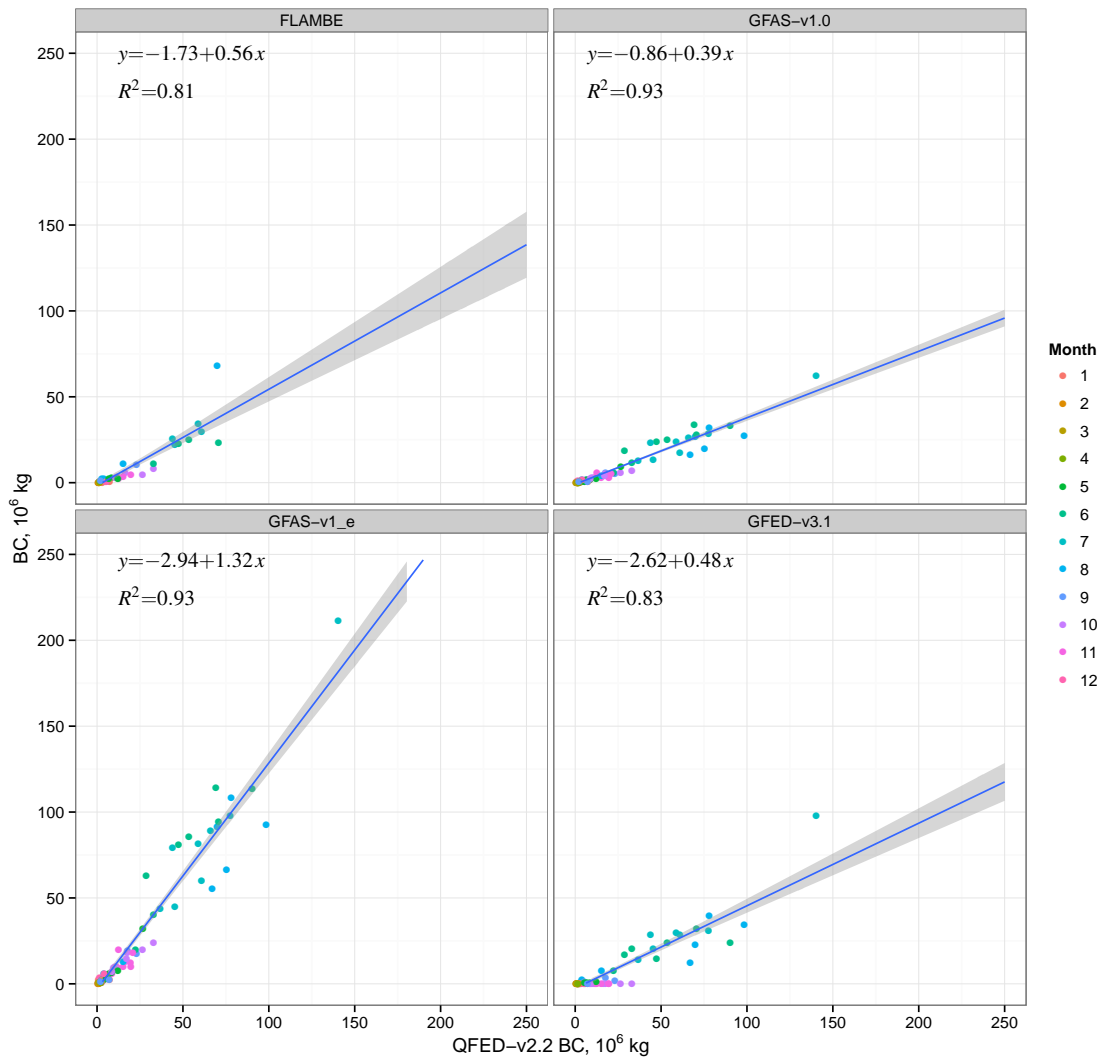
Figure D87: Scatter plots of monthly black carbon (BC) emissions from the FLAMBE, GFAS, GFED and QFED datasets for the Boreal North America region.

Central America

FLAMBE
$y=0.59+0.29x$
$R^2=0.85$

GFAS−v1.0
$y=-0.18+0.29x$
$R^2=0.98$

GFAS−v1_e
$y=-0.61+0.98x$
$R^2=0.98$

GFED−v3.1
$y=-0.42+0.19x$
$R^2=0.88$

BC, 10^6 kg

QFED−v2.2 BC, 10^6 kg

Month
1
2
3
4
5
6
7
8
9
10
11
12
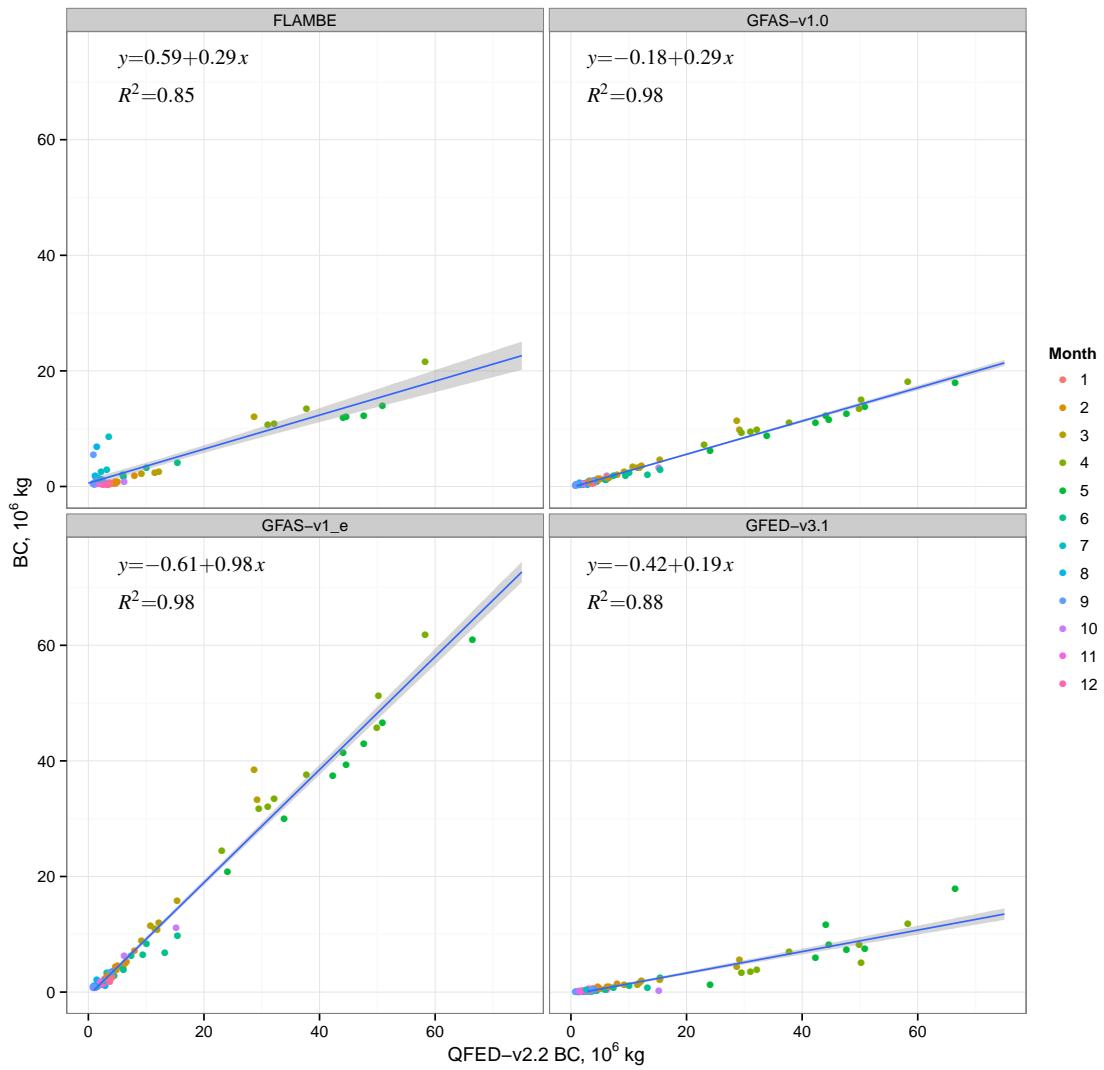
Figure D88: Scatter plots of monthly black carbon (BC) emissions from the FLAMBE, GFAS, GFED and QFED datasets for the Central America region.

Central Asia
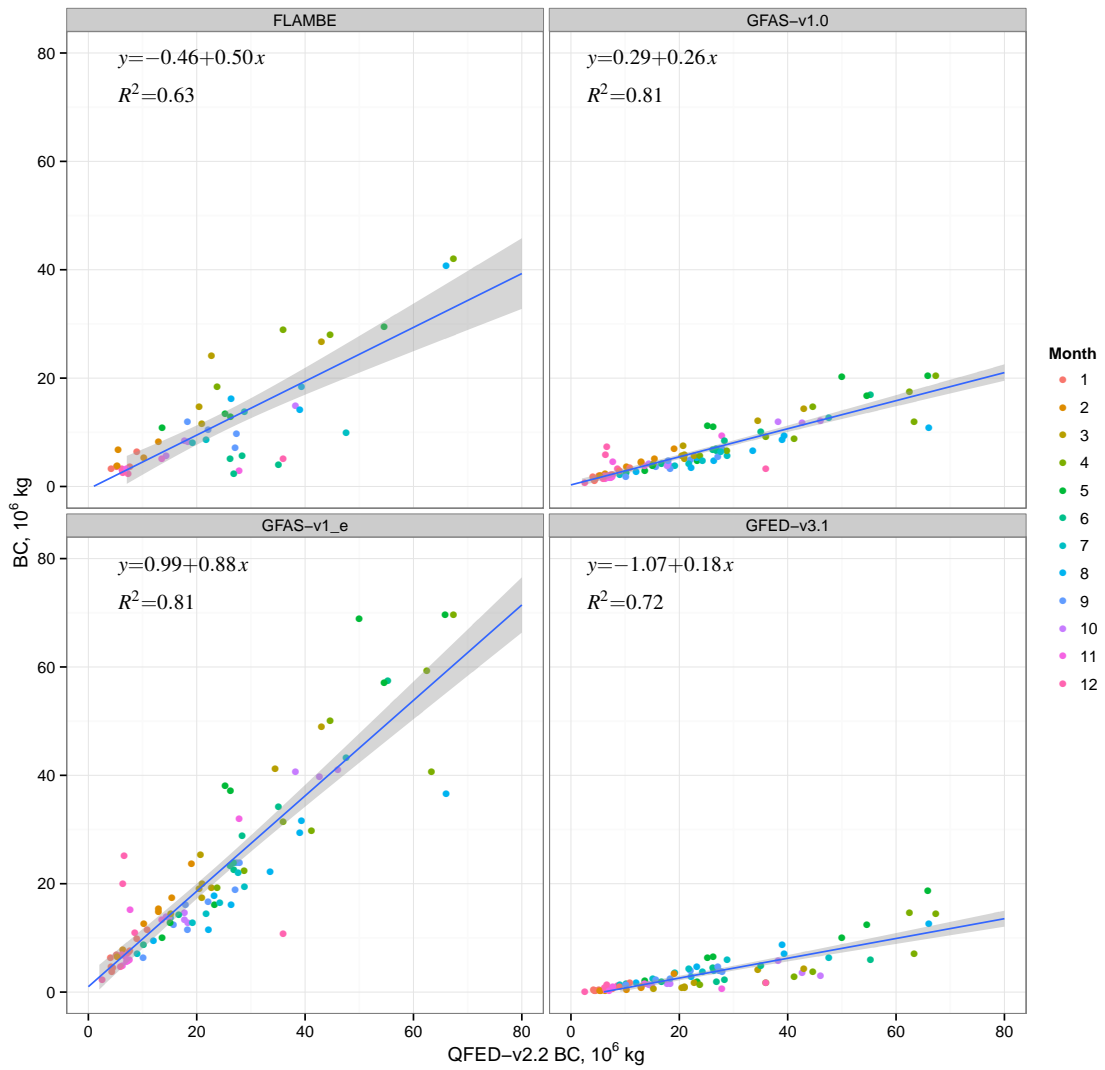
Figure D89: Scatter plots of monthly black carbon (BC) emissions from the FLAMBE, GFAS, GFED and QFED datasets for the Central Asia region.
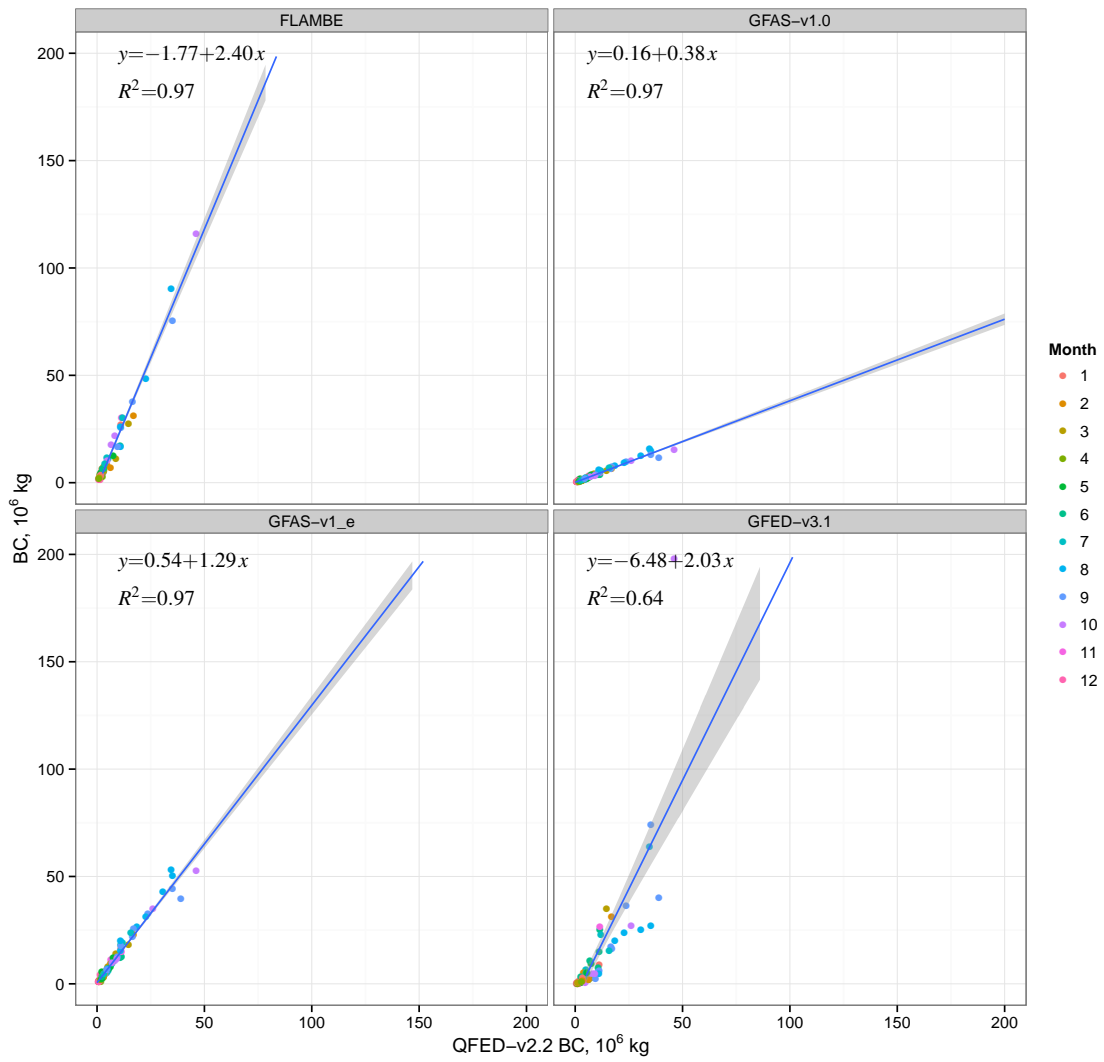
Figure D90: Scatter plots of monthly black carbon (BC) emissions from the FLAMBE, GFAS, GFED and QFED datasets for the Equatorial Asia region.
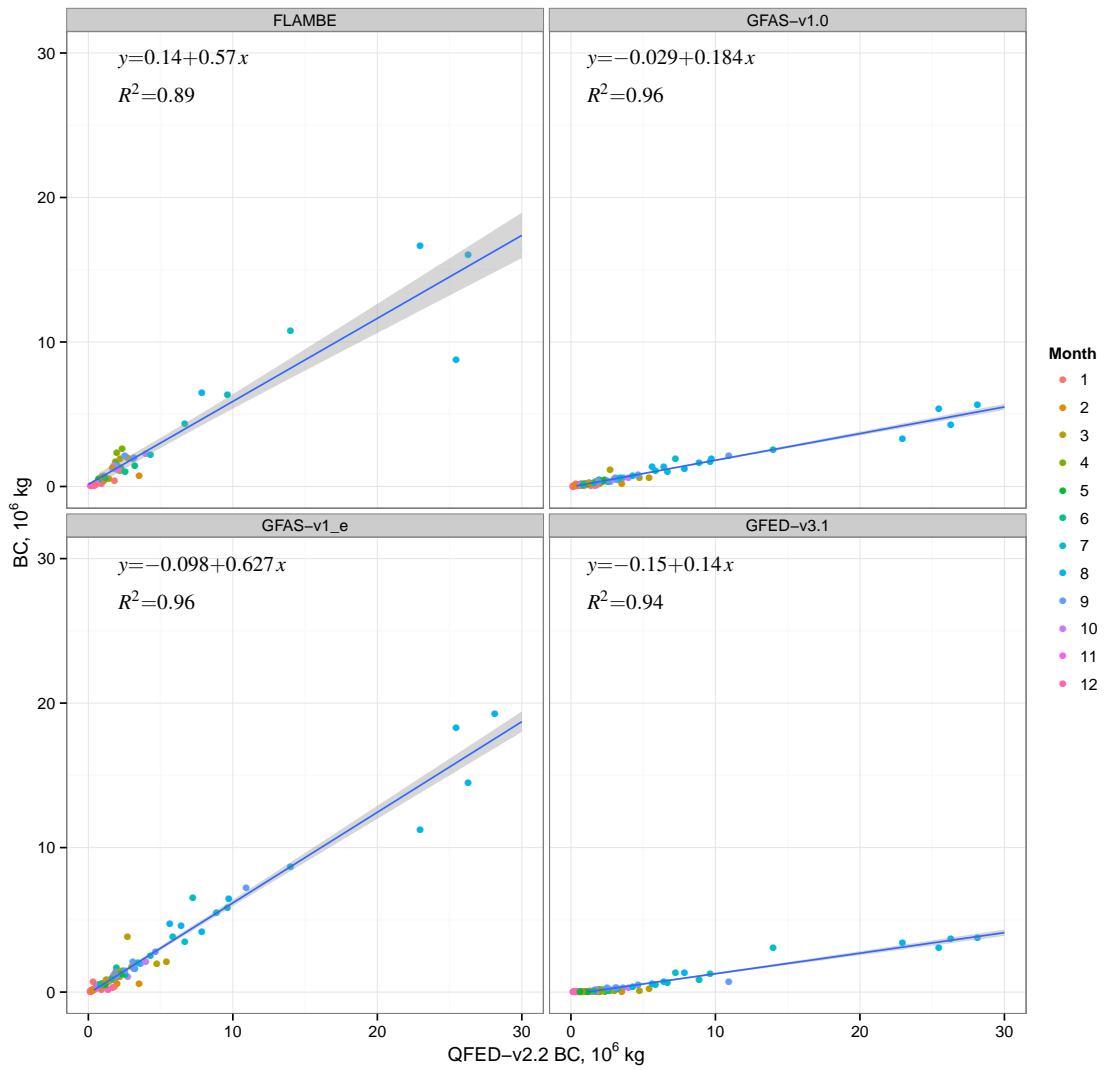
Figure D91: Scatter plots of monthly black carbon (BC) emissions from the FLAMBE, GFAS, GFED and QFED datasets for the Europe region.
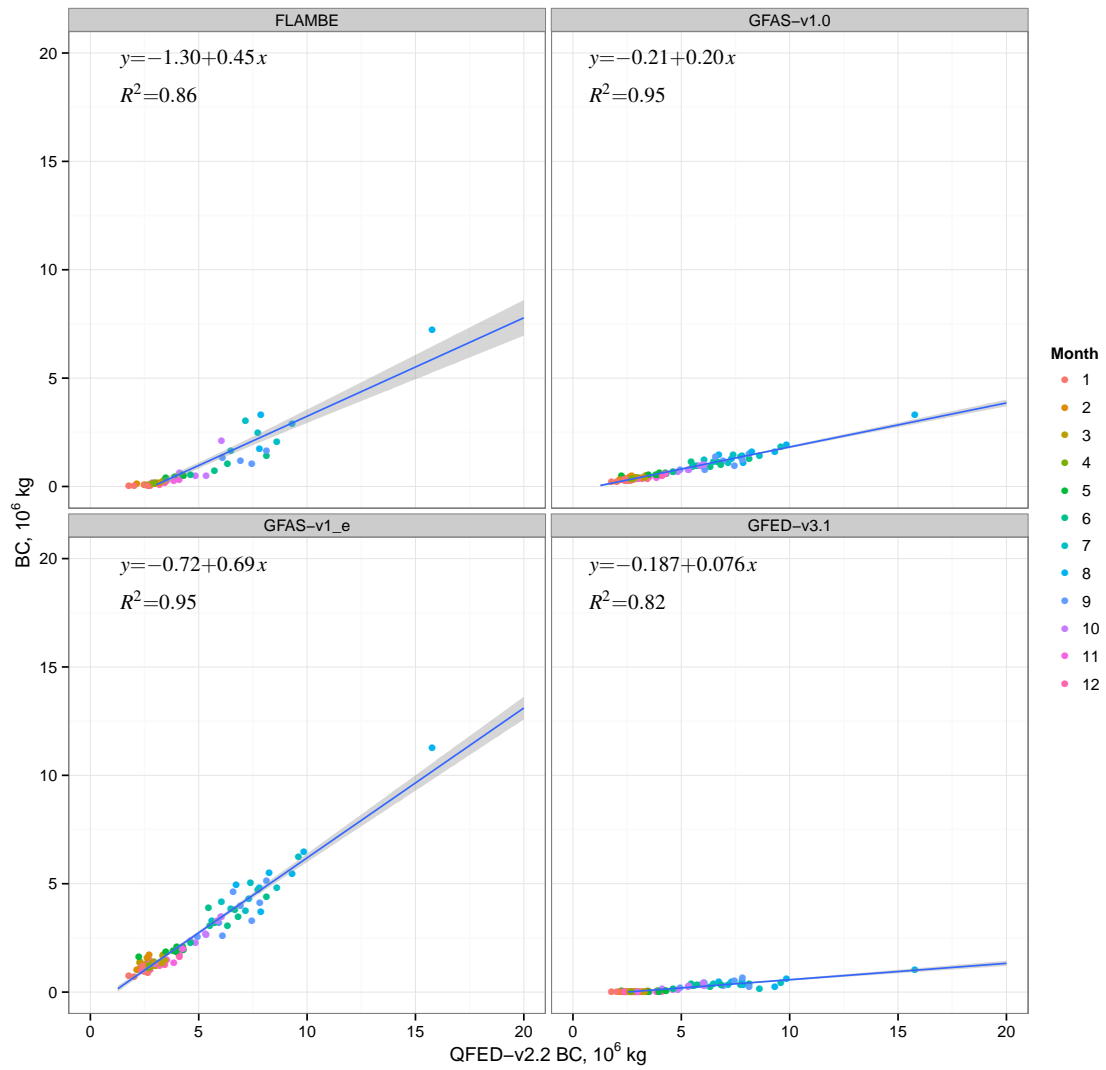
Figure D92: Scatter plots of monthly black carbon (BC) emissions from the FLAMBE, GFAS, GFED and QFED datasets for the Middle East region.
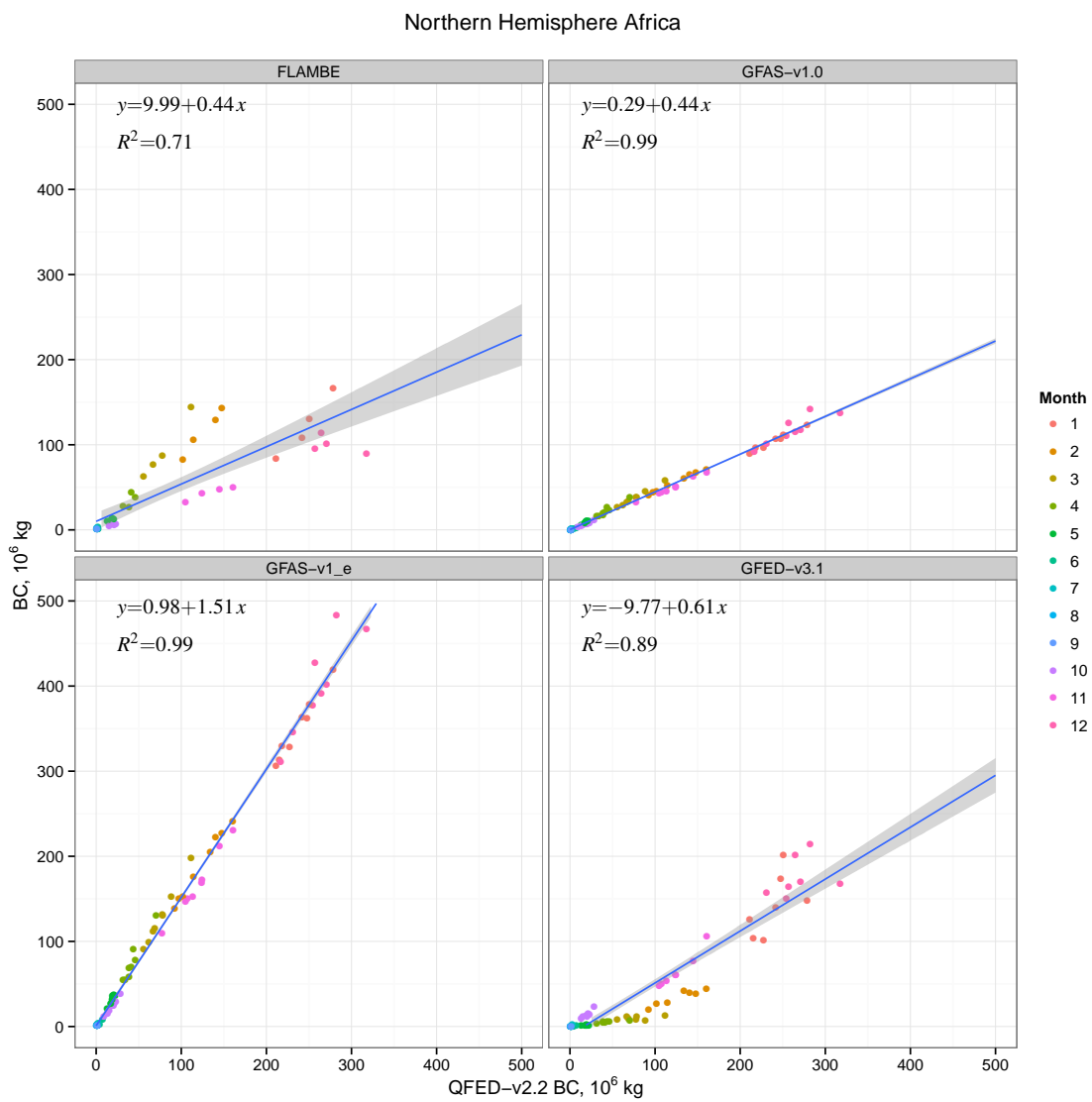
Figure D93: Scatter plots of monthly black carbon (BC) emissions from the FLAMBE, GFAS, GFED and QFED datasets for the N.H. Africa region.
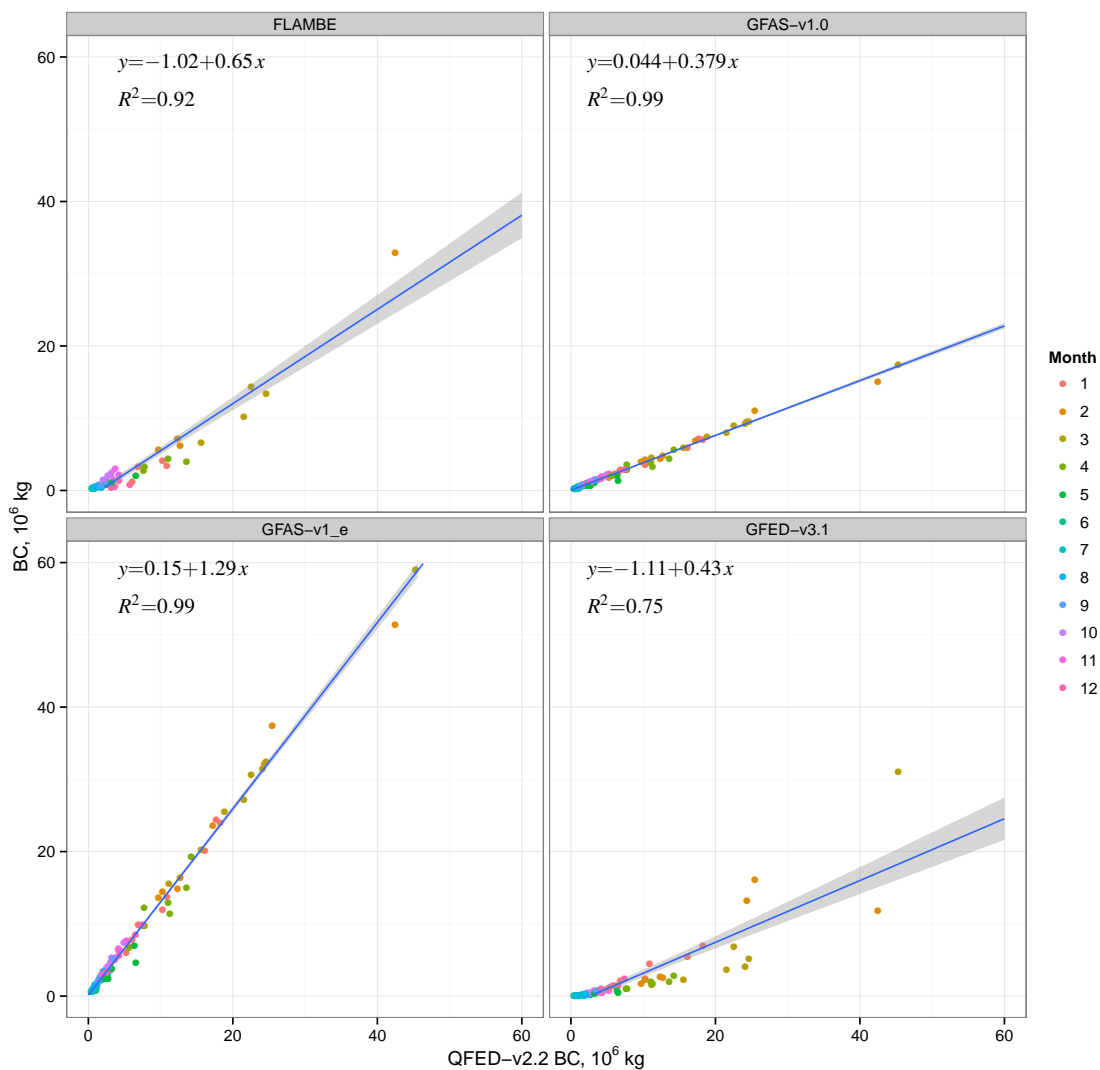
Figure D94: Scatter plots of monthly black carbon (BC) emissions from the FLAMBE, GFAS, GFED and QFED datasets for the N.H. South America region.
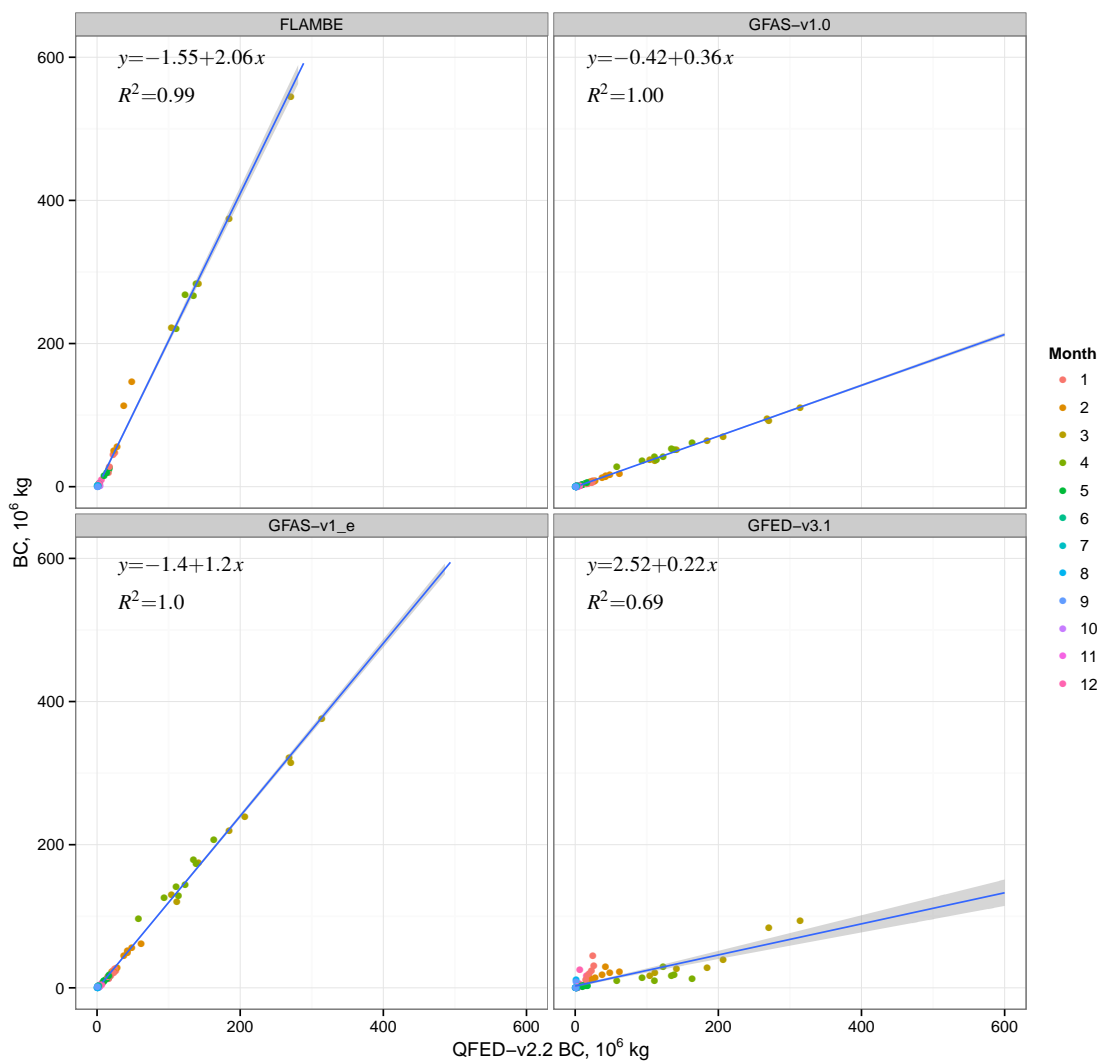
Figure D95: Scatter plots of monthly black carbon (BC) emissions from the FLAMBE, GFAS, GFED and QFED datasets for the Southeast Asia region.
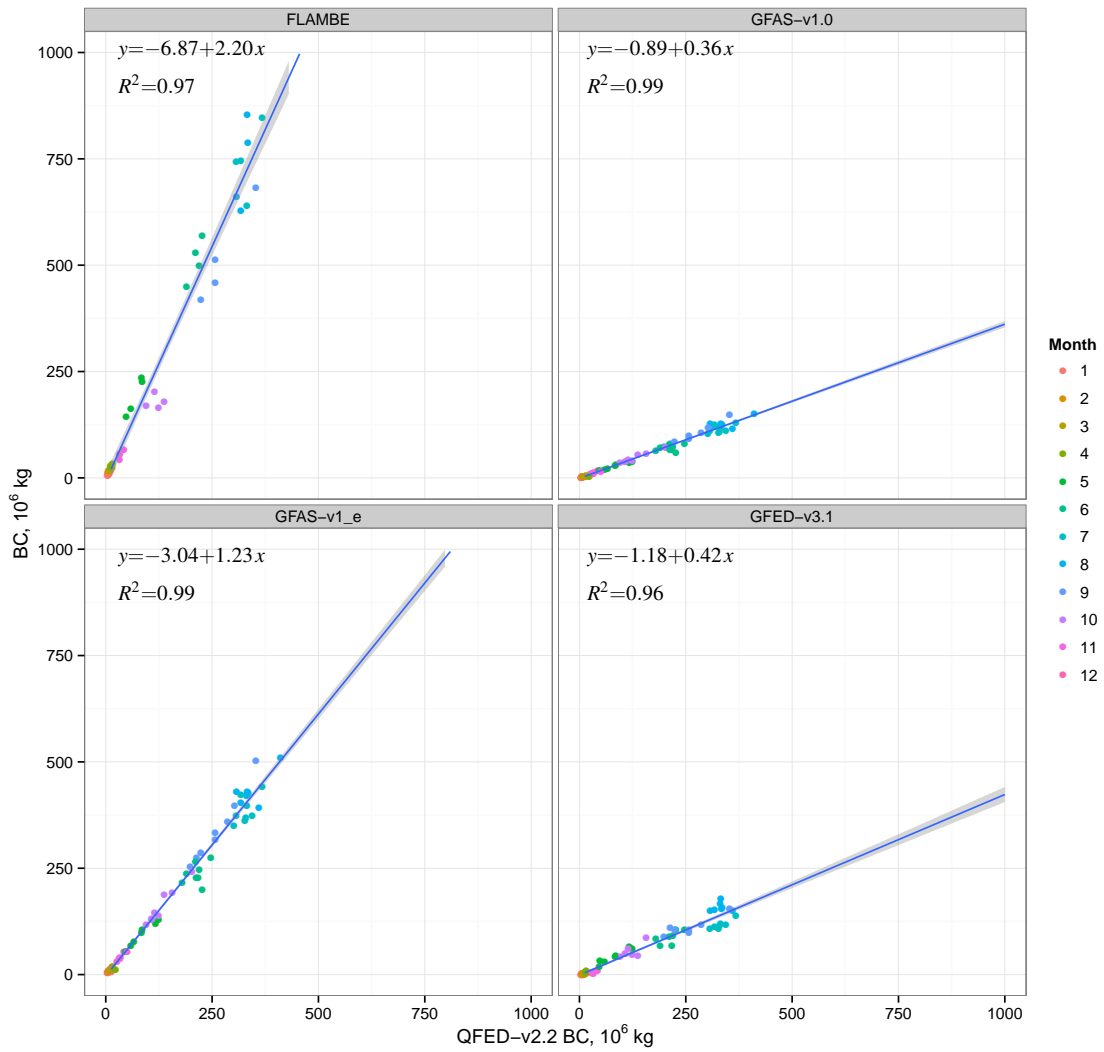
Figure D96: Scatter plots of monthly black carbon (BC) emissions from the FLAMBE, GFAS, GFED and QFED datasets for the S.H. Africa region.
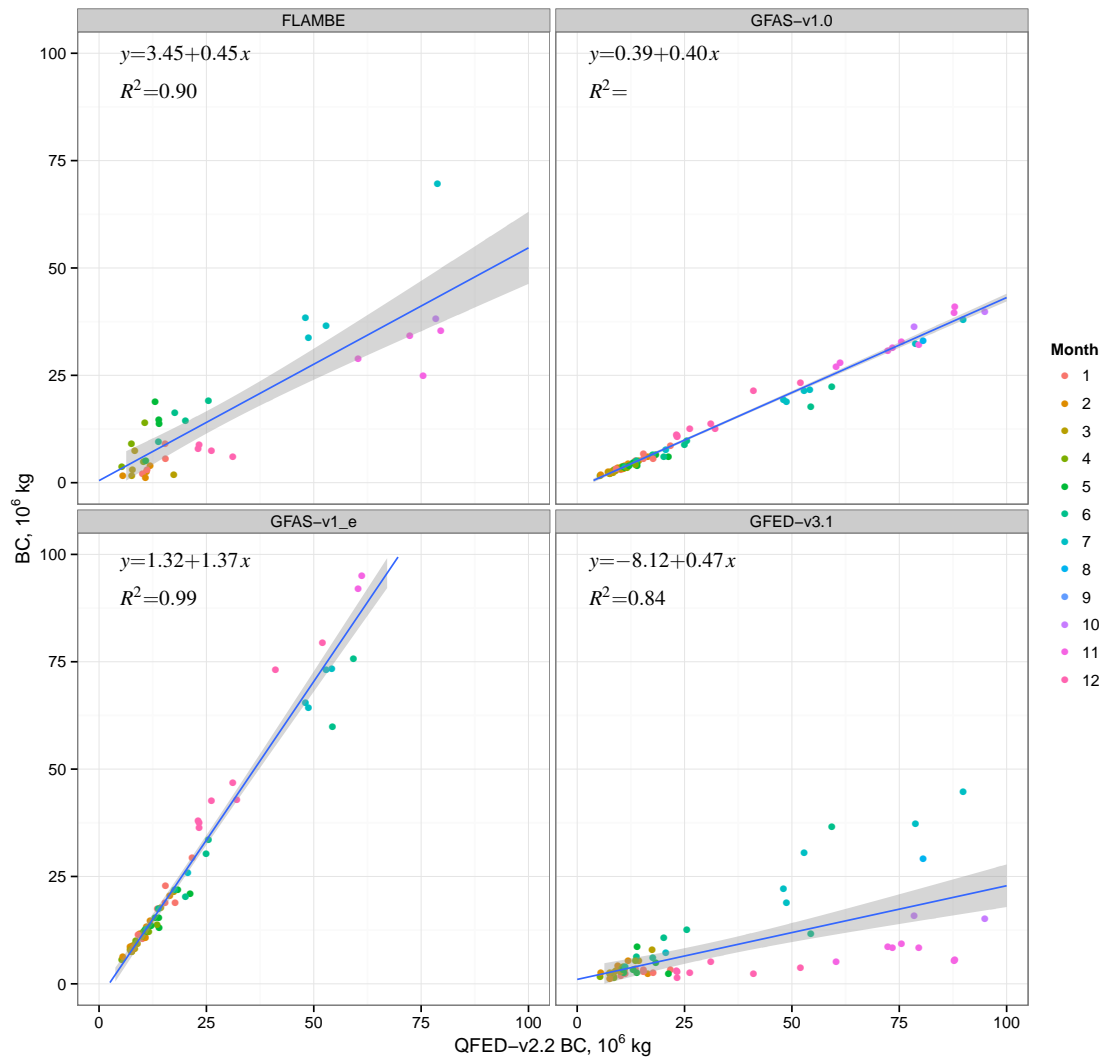
Figure D97: Scatter plots of monthly black carbon (BC) emissions from the FLAMBE, GFAS, GFED and QFED datasets for the S.H. South America region.
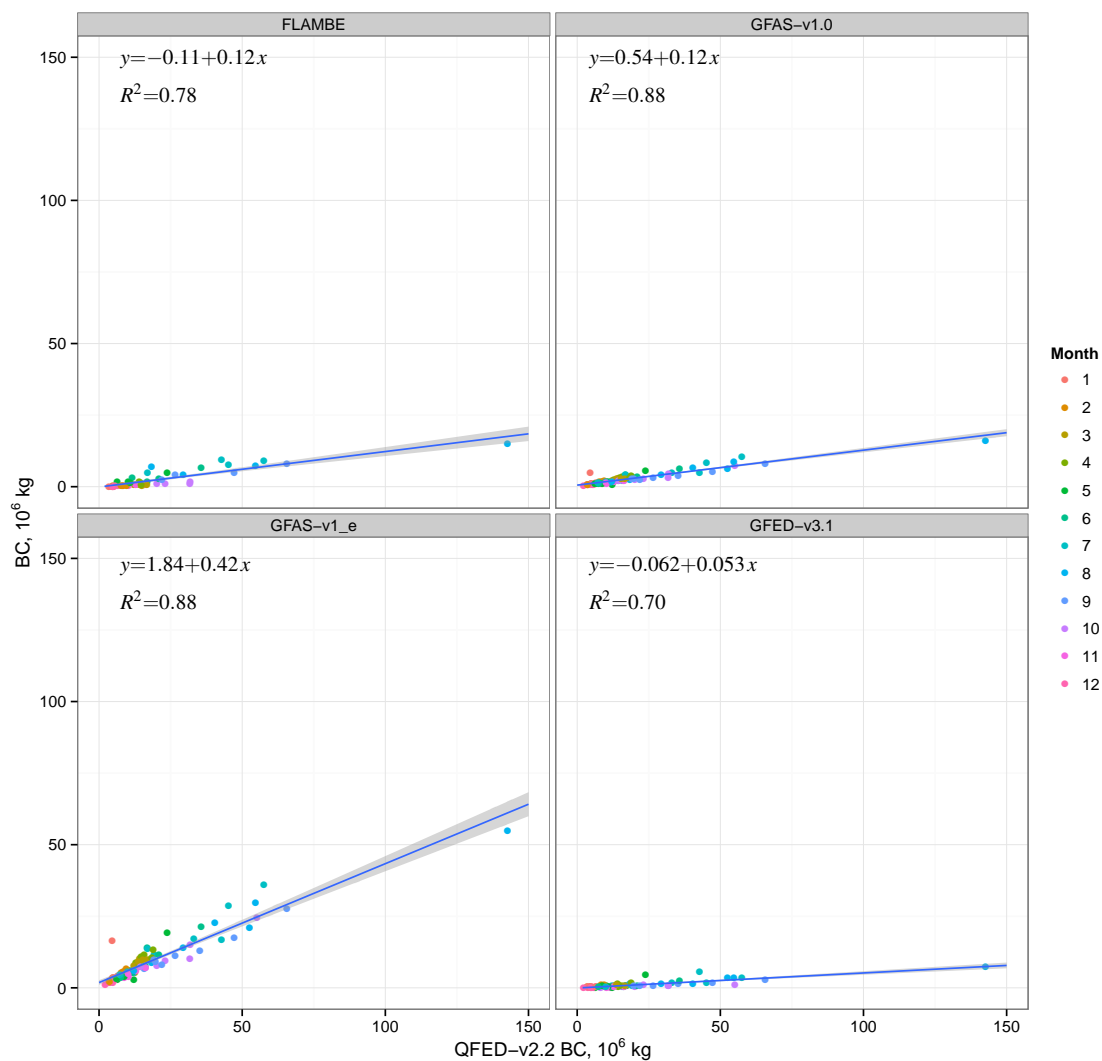
Figure D98: Scatter plots of monthly black carbon (BC) emissions from the FLAMBE, GFAS, GFED and QFED datasets for the Temperate North America region.

Appendix E. QFED file specification

Two global gridded (Level 3) products comprise the QFED dataset. The principal QFED product, Level 3a, contains daily FRP and pixel areas fields that can be used to calculate FRP densities. The Level 3a data is created and saved in separate NetCDF files for the MODIS/Terra and MODIS/Aqua instruments. The Level 3b product consists of biomass burning emissions for several pyrogenic species saved in separate NetCDF files. In versions 2.1, 2.2 and 2.4 of QFED the Level 3 products are created at $0.3125° \times 0.25°$ longitude-by-latitude (1152×721) spatial resolution. The Level 3 products in QFED-v2.4 are also available at $0.1° \times 0.1°$ spatial resolution.

E.1   QFED Level 3a (FRP) product

QFED versions 2.1 and 2.2

area Area of cloud free pixels over water and land in km^2.

frp_tf Fire radiative power of Tropical Forest fires in 10^6 W.

frp_xf Fire radiative power of Extra-tropical Forest fires in 10^6 W.

frp_sv Fire radiative power of Savanna fires in 10^6W.

frp_gl Fire radiative power of Grassland fires in 10^6W.

QFED version 2.4

land Land area (cloud free pixels over land) in km^2.

water Water area in km^2.

cloud Area of pixels obscured by clouds in km^2.

frp_tf Fire radiative power of tropical forest fires in 10^6 W.

frp_xf Fire radiative power of extra-tropical forest fires in 10^6 W.

frp_sv Fire radiative power of savanna fires in 10^6 W.

frp_gl Fire radiative power of grassland fires in 10^6 W.

fb_tf Predicted FRP density of tropical forests fires in 10^6 W km^{-2}.

fb_xf Predicted FRP density of extra-tropical forests fires in 10^6 W km^{-2}.

fb_sv Predicted FRP density of savanna fires in 10^6 W km^{-2}.

fb_gl Predicted FRP density of grassland fires in 10^6 W km^{-2}.

E.2 QFED Level 3b (emissions) product

QFED versions 2.1 and 2.2

biomass   Biomass burning emissions in $\mathrm{kg(constituent)\,s^{-1}\,m^{-2}}$.

QFED version 2.4

biomass   Biomass burning emissions in $\mathrm{kg(constituent)\,s^{-1}\,m^{-2}}$.

biomass_tf   Biomass burning emissions from tropical forest fires in $\mathrm{kg(constituent)\,s^{-1}\,m^{-2}}$.

biomass_xf   Biomass burning emissions from extra-tropical forest fires in $\mathrm{kg(constituent)\,s^{-1}\,m^{-2}}$.

biomass_sv   Biomass burning emissions from savanna fires in $\mathrm{kg(constituent)\,s^{-1}\,m^{-2}}$.

biomass_gl   Biomass burning emissions from grassland fires in $\mathrm{kg(constituent)\,s^{-1}\,m^{-2}}$.

Previous Volumes in This Series